

TR 2005305

### Proposition

accompanying the thesis:

*Morphodynamics of rivers with groynes*

by

Mohamed F. M. Yossef

Delft, 21 November 2005

1. Lowering the groynes along the Waal might be ineffective, after all. *This thesis.*
2. When evaluating the large-scale morphological impact of lowering the groynes, the effect of the sediment exchange between the groyne fields and the main channel can be ignored. *This thesis.*
3. Compared to the current performance of hydrodynamic models, the development in sediment transport modelling is lagging far behind.
4. Diffusion is a matter of scale; it should be always coupled with a definition of time and length scales.
5. Most of the uncertainty in medium and large-scale river bed morphology is in fact deterministic.
6. Laboratory experiments help understand processes rather than to get a final result; they answer the question of how things happen, rather than what will actually happen in reality. Whereas, field measurements capture a snap shot of reality; they answer the question of what has already happened, rather than how it has happened.
7. Numerical models are best suited to problems within a known solution space.
8. The relation between morphology and flow is similar to that between culture and environment in that they are both characterised by a strong feed-back mechanism.
9. The River Nile has shaped the character of the Egyptians of all times and the construction of the High Aswan Dam has caused a break in the millennia long cultural continuity by drastically altering the environment.  
*cf. Gamal Hamdan, (1980-84) "The Personality of Egypt" in 4 Vols., Cairo, 1980-84*
10. Sports are very enjoyable, but in a competitive environment they may become very stressful.

*These propositions are considered opposable and defensible and as such have been approved by the promoter Prof. dr. ir. H.J. de Vriend*

## Stellingen

Behorende bij het proefschrift:

*Morfodynamica van Rivieren met Kribben*

van

Mohamed F.M. Yossef

Delft, 21 november 2005

1. Uiteindelijk zou kunnen blijken dat verlaging van de kribben langs de Waal niet effectief zijn. *Deze thesis.*
2. Bij evaluatie van de grootschalige morfologische impact van verlaging van de kribben, kan de sedimentuitwisseling tussen de kribvakken en de hoofdgeul worden verwaarloosd. *Deze thesis.*
3. Ontwikkelingen in sedimenttransportmodellering lopen achter op die van hydrodynamische modellen.
4. Diffusie is een kwestie van schaal; het dient altijd te worden gekoppeld met een definitie van tijd- en lengteschaal.
5. De meeste onzekerheid bij het voorspellen van midden- en grootschalige morfologie van rivierbedden is in feite deterministisch.
6. Laboratoriumexperimenten helpen om processen te begrijpen en niet zozeer om een definitief resultaat te bereiken. Ze beantwoorden de vraag hoe dingen gebeuren maar niet wat in werkelijkheid zal gebeuren, terwijl veldmetingen een snap shot van de werkelijkheid vasthouden. Ze geven een antwoord op de vraag wat al gebeurd is en niet zozeer hoe het heeft plaatsgevonden.
7. Numerieke modellen zijn het meest geschikt voor problemen met een vooraf bekende oplossingsruimte.
8. De relatie tussen morfologie en stroming is vergelijkbaar met die tussen cultuur en milieu; beide zijn gekenmerkt door een sterk terugkoppelingsmechanisme.
9. De rivier de Nijl heeft het karakter van de Egyptenaar van alle tijden vormgegeven en de Hoge Aswan Dam heeft een breuk veroorzaakt in de millennia-lange culturele continuïteit door drastische verandering van het milieu.  
*cf.: Gamal Hamdan, (1980-84) "The Personality of Egypt" in 4 Vols., Cairo, 1980-84.*
10. Sport is erg gezellig, maar kan in een prestatiegericht milieu veel stress veroorzaken.

*Deze stellingen worden opponeerbaar en verdedigbaar geacht en zijn als zodanig goedgekeurd door de promotor Prof. dr. ir. H.J. de Vriend*

TR 200530

**Morphodynamics  
of  
rivers with groynes**

Cover photograph: a view from the Waal River, source: digital archive of Delft University of Technology, Faculty of Civil Engineering and Geosciences, Hydraulic Engineering Section.

Cover design: Hans van Bergem

# Morphodynamics of Rivers with Groynes

## *Morfodynamica van Rivieren met Kribben*

Proefschrift

ter verkrijging van de graad van doctor  
aan de Technische Universiteit Delft,  
op gezag van de Rector Magnificus, prof. dr. ir. J.T. Fokkema,  
voorzitter van het College voor Promoties,  
in het openbaar te verdedigen  
op 21 november 2005 om 10:30 uur

door

Mohamed Fathy Mohamed YOSSEF

Masters of Science in Hydraulic Engineering,  
UNESCO-IHE Delft

geboren te Giza – Egypte

Dit proefschrift is goedgekeurd door de promotor:  
Prof. dr. ir. H.J. de Vriend

Samenstelling promotiecommissie

Rector Magnificus	voorzitter
Prof. dr. ir. H.J. de Vriend	Technische Universiteit Delft, promotor
Prof. dr.-ing. habil. U.C.E. Zanke	Technische Universiteit Darmstadt
Prof. ir. J.K. Vrijling	Technische Universiteit Delft
Prof. dr. ir. G.S. Stelling	Technische Universiteit Delft
Dr. W.B.M. ten Brinke	RIZA, Arnhem
Dr. ir. E. Mosselman	WL   Delft Hydraulics
Dr. ir. W.S.J. Uijtewaald	Technische Universiteit Delft
Prof. dr. ir. A.E. Mynett	Technische Universiteit Delft, reservelid

Ir. G. J. Klaassen has provided substantial guidance and support in the preparation of this thesis.

This research was carried out within the framework of theme 1.3 (Intermediate-scale morphological developments in rivers due to human interventions) of the TU Delft research programme DIOC Water, and theme 3 (Coasts and Rivers) of the Delft Cluster joint research programme.

ISBN 90-407-2606-x

Copyright © 2005 by Mohamed Fathy Mohamed YOSSEF

*Printed by DUP Science*

DUP Science is an imprint of Delft University Press

All rights reserved. No part of the material protected by this copy right notice may be reproduced or utilised in any form or by any means, electronic, or mechanical, including photocopy, recording or by any information storage and retrieval system, without written permission of the publisher.

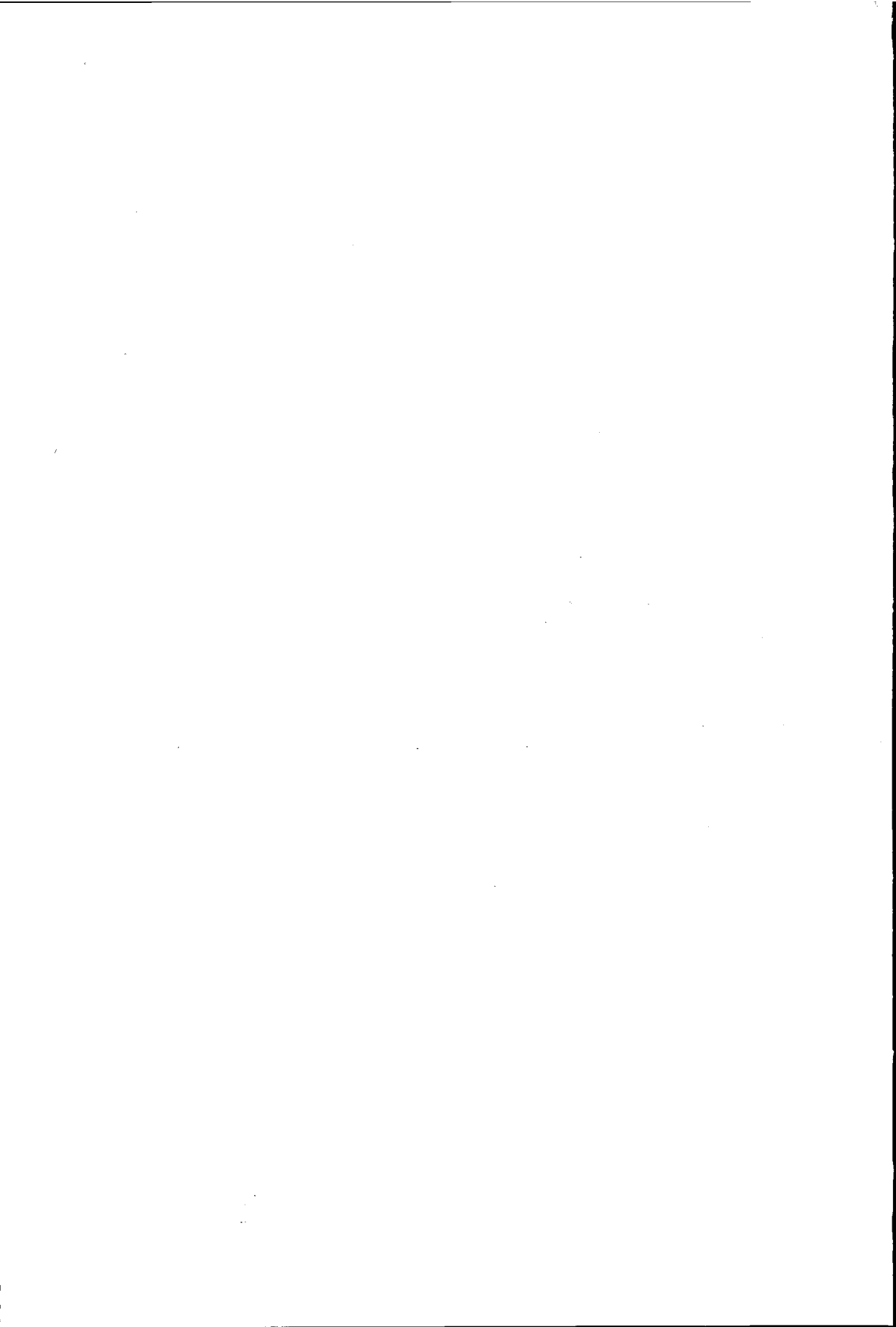
This thesis is also published in the “*Delft Hydraulics Select Series*”, No. 7/2005.  
ISBN 90-407-2607-8

Printed in the Netherlands

\* ... وَسَخَّرَ لَكُمُ الْفُلَ لِتَجْرِفَ فِي الْبَرِّ بِأَمْرِهِ وَسَخَّرَ لَكُمُ الْأَنْهَارَ \*

... it is He Who hath made the ships subject to you, that they may sail through the sea by His command; and the rivers hath He made subject to you.

Quran: 14:32





## ABSTRACT

In the framework of the project "*Ruimte voor Rijntakken*" (*Room for the Rhine Branches*), several measures have been devised to achieve a decrease of the water levels at peak discharges. A wide range of fourteen measures has been proposed, among which, lowering the existing groynes by some one to two metres. Lowering the groynes along certain reaches of the river will increase the flow area in addition to reducing the effective roughness in the groynes' region during high water conditions. However, if the groynes are lowered, the balance of hydrodynamic forces acting on the groyne fields will change, and there will be a morphological impact on the river system. To carry on with the proposed plan a thorough understanding to the effect of lowering the groynes on the morphology of the river is necessary.

To that end, the aim of this thesis was set to study the morphological interaction between the groyne fields and the main channel of a river; with the intention to address some concerns for the river manager. This thesis covers a range of scales. At the small scale level, the dynamics of the flow as well as the governing sediment exchange processes between the groyne fields and the main channel of a river were identified. At the intermediate scale level, the effect of the groynes on the navigation channel was addressed. At the large scale level, the effects of the groynes on the morphology of the whole river were considered. The study methodology comprised laboratory experiments, fixed-bed and mobile-bed; as well as numerical modelling, two-dimensional and one-dimensional.

Firstly, a fixed-bed flume experiment was carried out to investigate the dynamics of the flow near groynes and to study the effect of submergence level both on the formation of the mixing layer and on the resistance of the groynes. The results of the experiment revealed the difference in the turbulence characteristics between the emerged and submerged stages. When the groynes are not submerged, the flow inside the groyne fields can be characterised by a primary eddy that forms in the downstream part of the groyne field, a secondary eddy with an opposite sense of rotation, and a dynamic eddy that intermittently sheds from the tip of the upstream groyne. In the submerged stage, the flow in the groyne fields region can be characterised as a low velocity region that shows an alternate accelerating and decelerating pattern between flow over and around the groynes. The mixing layer between the main channel and the groyne fields differs in nature between the emerged and submerged flow stages. In the emerged situation, the mixing layer originates from the tip of the groyne and grows in width towards the next groyne downstream. Whereas, in the submerged situation, the mixing layer maintain a rather constant width due to the continuous generation of turbulence by the successive groynes. From the analysis of the effect of submergence, it was possible to derive a relation between the blockage by a groyne and its drag coefficient. This relation led to an expres-

sion of an effective Chézy coefficient that is representative to the resistance in the groyne region. The analysis of the effect of lowering the groynes has shown that the reduction in the water level for the design flood situation due to lowering the groynes is insignificantly small.

To predict the morphodynamic behaviour of the groyne fields as well as the main channel, a logical step would be to apply a numerical model. Accordingly, a two-dimensional depth-averaged process-based model coupled with Large Eddy Simulation, namely DELFT3D-MOR, was applied to study the intermediate-scale morphological effect of a series of groynes in a river. The primary objective of this step was to evaluate the morphodynamic behaviour and the sediment budget of the groyne fields under different flow conditions. This objective was not reached, as the reference situation did not yield the expected morphodynamic response in the groyne fields' region. Yet, on the bright side, we were able to reproduce the groyne-induced morphological features in the navigation channel. A modelling strategy was developed, in which an essential requirement is a correct representation of the time-dependent flow field.

A mobile-bed experiment was conducted in order to study the morphodynamic behaviour of the groyne fields, in addition, to provide insight into the mechanisms governing the sediment exchange process between the main channel and the groyne fields under different flow conditions. The results of the experiment provided information about the distribution of the sediment concentration in the channel transverse direction; the vertical suspended sediment concentration profiles in the main channel and inside the groyne fields; the bedform movements and the morphological development in the groyne fields at different flow stages. In all the tested cases, a net import of sediment into the groyne fields was observed. Moreover, we were able to conclude that the sediment transport mechanism into the groyne fields differs according to the flow stage. In an emerged situation, the sediment is mainly advected towards the groyne fields following the direction of the primary circulation cell; compared to transport by residual advection due to the large scale coherent structures in a submerged situation. The bed measurements revealed a decrease in the total deposition volume inside a groyne field as the submergence level increased. PIV technique was utilised to measure the bedform celerity, which can be interpreted to bed load transport. To the best of our knowledge, this was the first time to measure time-dependent bedform celerity of a mobile-bed simultaneously in two dimensions. From these measurements we have found a decreasing trend in the lateral sediment transport component into the groyne fields with increasing submergence.

In order to estimate the morphodynamic behaviour of a single groyne field for a larger time-scale, the different mechanisms that affect the sediment exchange between the river and its groyne fields were evaluated separately. The balance between the advective transport into groyne fields and navigation-induced erosion was considered for emerged groynes. The combination of advection due to large-scale coherent structures and diffusion through the mixing layer was considered for submerged groynes. The contributions of these mechanisms were evaluated and their associated morphological time-scales were estimated for conditions similar to the Waal River. The analysis has shown that lowering the groynes by e.g. 1.0 m would reduce the sediment supply rate to the groyne fields by approximately 20% during the submerged conditions.

Finally, to evaluate the large-scale morphodynamic behaviour of the whole river due to the interaction with the groyne fields, the behaviour of a single groyne was aggregated. To carry out this aggregation step we needed a modelling tool that is rather simple and possible to provide a complex set of boundary conditions. Thus, a one-dimensional model, namely SOBEK-River, was adopted for this final step. The morphodynamic behaviour of the groyne fields was used to develop corresponding boundary conditions in the form of lateral supply or extraction of sediment to the river from a region with morphologically active groyne fields. From the results of the model we were able to demonstrate that the primary morphological impact of lowering the groynes is due to the reduced discharge passing through the main channel. Due to lowering the groynes, a new equilibrium state will be reached. In the lowered groynes reach, the river will aggrade while getting steeper. The effect of the sediment exchange between the groyne fields and the main channel on the morphology of the main channel was found to be small and could be ignored. Eventually, this interaction will not affect the 'equilibrium' state of the main channel, but it will reduce the morphological time-scale and accelerate the aggradation process in the main channel. We finally concluded that lowering the groynes would cause a slow but persistent erosion of the groyne fields caused by the disturbance of the long-term balance between the erosion and deposition components.

Mohamed F.M. Yossef

November 2005



# CONTENTS

<b>Abstract</b>	<b>vii</b>
<b>Contents</b>	<b>xi</b>
<b>Chapter 1 Introduction</b>	<b>1</b>
1.1 Background-----	1
1.2 Problem definition-----	3
1.3 Objectives-----	3
1.4 Problem analysis-----	4
1.4.1 Scale of the problem .....	4
1.4.2 Forcing to the system .....	7
1.5 Outline of the Thesis-----	7
<b>Chapter 2 Background information</b>	<b>9</b>
2.1 Introduction-----	9
2.2 River Training – groynes-----	9
2.2.1 Types of groynes.....	10
2.2.2 Design Considerations for Groynes .....	10
2.3 Groynes in the Netherlands -----	13
2.3.1 Historical background .....	13
2.3.2 Characteristics of the groyne fields along the Waal River.....	16
2.4 Flow Near groynes-----	18
2.4.1 Emerged groynes.....	18
2.4.2 Submerged groynes .....	20
2.5 Effect of navigation-----	21
2.5.1 Water movement around a ship .....	21
2.5.2 Navigation-induced water motion near groynes .....	22
2.5.3 Navigation-induced erosion from groyne fields.....	25
<b>Chapter 3 Fixed-bed flume experiment</b>	<b>29</b>
3.1 Introduction-----	29
3.2 Experimental set-up-----	30
3.2.1 Geometry.....	30
3.2.2 Instrumentation .....	31
3.3 Experimental conditions and procedures-----	32
3.3.1 Series-A .....	32

3.3.2	Series-S .....	33
3.4	Data processing and Analysis .....	34
3.5	The dynamics of the flow .....	36
3.5.1	Velocity signals .....	36
3.5.2	Emerged groynes .....	39
3.5.3	Submerged groynes .....	41
3.6	Effect of the submergence level .....	43
3.7	Parameterisation of the flow near groynes .....	46
3.7.1	Velocity fluctuations .....	46
3.7.2	Mixing layer width .....	49
3.7.3	Flow periodicity .....	50
3.7.4	Coherence .....	50
3.8	Summary and conclusions .....	53
<b>Chapter 4</b>	<b>Mobile-bed flume experiment</b> .....	<b>55</b>
4.1	Introduction .....	55
4.2	Experimental setup .....	56
4.2.1	Model design .....	56
4.2.2	Experimental conditions .....	59
4.2.3	Model operation .....	61
4.2.4	Pilot tests .....	62
4.2.5	Measurements .....	62
4.3	Experimental results .....	67
4.3.1	Flow pattern .....	67
4.3.2	Sediment transport .....	69
4.3.3	Morphological features .....	74
4.4	Analysis and discussion .....	78
4.4.1	Transport mechanisms .....	78
4.4.2	The effect of submergence .....	80
4.4.3	Scale effect .....	82
4.5	Summary and conclusions .....	84
<b>Chapter 5</b>	<b>Synthesis of the small-scale behaviour</b> .....	<b>87</b>
5.1	Introduction .....	87
5.2	Emerged situation .....	88
5.2.1	Deposition in the absence of navigation .....	89
5.2.2	Navigation-induced erosion .....	91
5.2.3	Combined effect .....	93
5.3	Submerged situation .....	94
5.3.1	Modelling the flow near groynes .....	95
5.3.2	Transport by large-scale coherent structures .....	97
5.3.3	Diffusive transport .....	99
5.3.4	Effect of secondary flow .....	102
5.3.5	Combined effect .....	104
5.3.6	The effect of stage .....	105

5.4	Effect of lowering the groynes -----	108
5.4.1	Effect on flood level.....	108
5.4.2	Effect on sediment supply to the groyne fields .....	110
5.5	Conclusions-----	112
5.5.1	Effect of navigation.....	113
5.5.2	Morphological time-scales.....	113
5.5.3	Lowering the groynes.....	114
5.5.4	Further improvements.....	114
<b>Chapter 6</b>	<b>Numerical Modelling of a river with groynes</b>	<b>115</b>
6.1	Introduction-----	115
6.2	Relevance-----	116
6.3	Description of Delft-3D-----	116
6.3.1	Flow with HLES.....	117
6.3.2	Transport.....	120
6.3.3	Morphological update procedures .....	120
6.4	Model setup-----	122
6.5	Computational results-----	123
6.5.1	Flow pattern.....	123
6.5.2	Choice of sediment transport computation period $T_p$ .....	126
6.5.3	Morphological development .....	128
6.6	Qualitative comparison with field observations-----	131
6.6.1	Field observations.....	131
6.6.2	Comparison.....	133
6.7	Discussion-----	133
6.8	Conclusions-----	135
<b>Chapter 7</b>	<b>Large-scale morphology – case study</b>	<b>137</b>
7.1	Introduction-----	137
7.2	Schematisation-----	138
7.2.1	planform .....	138
7.2.2	Morphological representation of the groyne fields.....	138
7.3	Morphological modelling-----	140
7.3.1	Analytical equilibrium state models .....	140
7.3.2	Morphodynamic model .....	143
7.4	Effect of sediment exchange between the groyne fields and the main channel	144
7.4.1	The equilibrium state .....	144
7.4.2	Morphodynamic behaviour .....	147
7.5	Lowering the groynes-----	152
7.5.1	Effect of reduced discharge in the main channel.....	152
7.5.2	Effect of sediment exchange.....	153
7.6	Summary and Discussion-----	156
7.7	Conclusions-----	158

---

<b>Chapter 8 Conclusions and recommendations</b>	<b>159</b>
8.1 General-----	159
8.2 Conclusions-----	160
8.2.1 Hydrodynamics near a series of groynes .....	160
8.2.2 Morphological interaction between the river and its groyne fields ....	161
8.2.3 Modelling rivers with groynes .....	162
8.2.4 Groyne lowering.....	163
8.3 Recommendations-----	165
<b>Bibliography</b>	<b>167</b>
<b>Appendix A Results from the mobile-bed experiment</b>	<b>175</b>
A.1 Velocity-----	175
A.2 Suspended sediment-----	188
A.3 Bed Level-----	192
A.4 PIV-measurements-----	199
<b>List of Figures</b>	<b>207</b>
<b>List of Symbols</b>	<b>217</b>
<b>Acknowledgments</b>	<b>223</b>
<b>Curriculum Vitae</b>	<b>225</b>



# Chapter 1

## INTRODUCTION

### 1.1 BACKGROUND

The Netherlands is made up largely of sediments deposited by rivers and the sea. Although at present civil engineering works along the rivers and the coast prevent the lower areas from being flooded, the rivers and the sea still determine the Dutch landscape and they contribute significantly to its economy. In a densely populated country such as The Netherlands, water systems serve many purposes, which have to be combined so that conflicts are avoided. However, the combination of shipping interests and flood protection has resulted in a typical Dutch river landscape, in which rivers are embanked, while groyne perpendicular to the river banks keep the main channel in place and at the desired width and depth. Owing to such river regulations, the ecological value of the floodplains of the River Rhine in the Netherlands has decreased dramatically.

An ambitious plan named '*Living Rivers*' was promoted by the Dutch World Wide Fund for Nature (WWF, 1993). The plan has the objective to recover the natural river landscape that will lead to a return of river characteristic flora and fauna. Next to this plan, many initiatives and plans from different points of view, like navigation, nature and landscape have been published. However, safety remains the first priority, not to be hindered by any development. For example, the construction of flood plain forests will lead to an increased roughness of the river and to higher water levels upstream. It is possible to find engineering compensation by e.g. lowering the groyne. In this case, nature and safety would go hand in hand. Yet, the impact on the morphology in this case is unclear, which means that navigation might be hampered. This brief example emphasises that the river is a coherent system, in which every engineering measure has implications on all functions of the riverine area. Consequently, the decision to execute any measure must be supported by sound arguments based on an exploration of the potential impacts. In this way actors and stakeholders can be informed on the advantages and disadvantages of the measure and decide if the measure is socially desirable.

In view of that, several measures have been devised in the framework of the project "*Ruimte voor Rijnstakken*" (*Room for the Rhine Branches*) to achieve a decrease of the water levels at design discharges, by means of enlarging the river space. A wide range of

fourteen measures was mentioned in the '*Landscape Planning River Rhine*' report (LPR, 1996). One of those measures is lowering the existing groyne (Figure 1.1).

The rationale behind this proposal is that due to large-scale erosion of the low-water bed through the past decades, the groyne that were constructed between 1860 and 1920 are higher than strictly necessary for keeping the main channel at depth. Lowering the groyne along certain reaches of the river, an activity that requires a huge investment, will increase the flow area in addition to reducing the effective roughness in the groyne region during high water conditions. Thus, it increases the flood conveyance capacity of the river. The increased flood capacity would create space to restore some of the riverine nature, which would in turn, increase the effective roughness. This is important in the light of the policy objective to accommodate higher flood discharges without raising the dikes.

However, the areas between groyne, the groyne fields, are important elements in the River Waal and other Dutch branches of the River Rhine. They form zones of sediment storage with significant contribution to the overall sediment budget of the river. Erosion of the groyne fields may affect the stability of the groyne, or even lead to the disappearance of the beaches between the groyne. These beaches provide the sand for the natural formation of wind-blown dunes on the floodplains, a valuable habitat for riverine flora and fauna.

If the groyne are lowered, the balance of hydrodynamic forces acting on the groyne fields will change, and there will be a morphological impact on the river system. This impact may involve for example tilting of the entire river, opposite to the effect of the normalisation works in the first half of the previous century. It may also involve the necessity of dredging or other maintenance measures, so as to ensure the desired navigable depth. To carry on with the proposed plan to change the geometry of the groyne, a thorough understanding to the effect of groyne on the morphology of the river is necessary. The sediment exchange between the groyne-fields and the main channel needs to be better understood.

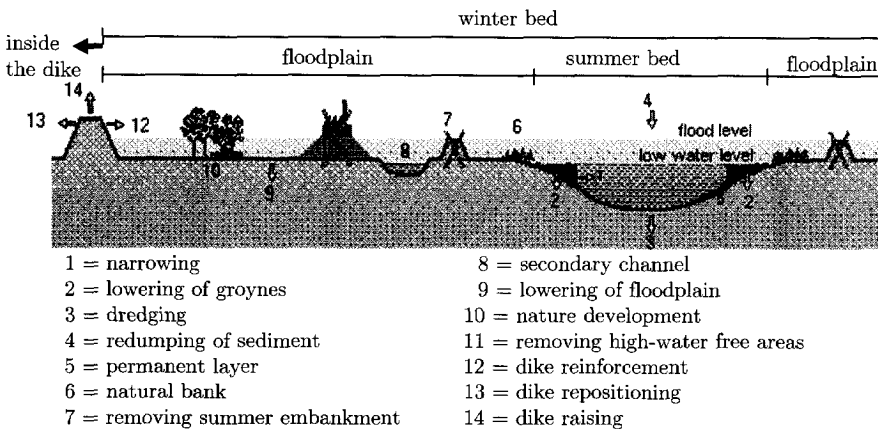


Figure 1.1: River engineering measures as proposed in *LRP* report to achieve a decrease of the water levels at peak discharges (source: LPR, 1996)

## 1.2 PROBLEM DEFINITION

Ten Brinke *et al.* (2001) estimated the sediment balance for the Waal River during the last three decades and particularly during the high water period of 1995. From the analysis of their findings, see Table 1.1, one can conclude that during high water conditions sedimentation in the groyne fields plays a major role in the total sediment balance of the river. However, in the long run there is no net erosion or deposition from/to the groyne fields. Thus, the amount of sediment that is deposited during floods must be released during normal and low flow conditions. The release of sediment from the groyne fields is probably due to the navigation-induced sediment transport.

Table 1.1: Sediment balance for the main channel of the Waal River during the last three decades (after Ten Brinke *et al.*, 2001)

Sediment source/sink	Volume x 1000 (m <sup>3</sup> /year)		
	1970 – 1990	1990 – 2000	Flood 1995
Input sediment (US)	+682	+507	+250
Output sediment (DS)	-761	-578	-270
Bed degradation	+489	+264	+573
Groyne fields erosion/deposition	---	---	-373
Floodplain deposition	-53	-53	-180
Dredging	-357	-140	0

± signs refer to gains and losses of sediment transported in the main channel

It is therefore surprising that the existing routine modelling practices ignore the morphological interaction between the main channel and the groyne fields (see for example Mosselman and Struiksmā, 1992; and Jesse and Kroekenstoel, 2001). This reflects a gap in our knowledge concerning the sediment exchange process between the groyne fields and the main channel. The present thesis is meant to fill at least part of this gap.

## 1.3 OBJECTIVES

The aim of this thesis is to study the morphological interaction between the groyne fields and the main channel of a river. We will endeavour to address some concerns for the river manager. These concerns range from the very local scale, such as bank erosion or undermining of groynes, via the intermediate spatial scale, such as the maintenance of the navigation channel, up to the scale of the whole river, such as the tilting of the river. At the small scale level, the governing sediment exchange processes between the groyne fields and the main channel of a river need to be identified. At the intermediate scale level, the effects of the groynes on the navigation channel is of great interest. At the large scale level, the effects of the groynes on the morphology of the whole river are to be considered.

Accordingly, the research objectives are divided into:

- Objectives related to the hydrodynamics:
  - to identify the flow pattern in the vicinity of groynes in detail,
  - to estimate the resistance of the groynes to the flow when they are submerged.
- Objectives related to the morphodynamics:
  - to identify the transport mechanisms that govern the sediment exchange process between the river and its groyne fields,
  - to quantify the sediment budget of a single groyne field.
- Objectives related to modelling:
  - to devise feasible strategies for detailed modelling of rivers with groynes, and
  - to be able to aggregate the detailed small-scale behaviour to the large-scale level.
- Objectives related to river management:
  - to quantify the effect of lowering the groynes on the design flood level,
  - to identify the effect of the morphological interaction between the main channel and the groyne fields, and
  - to identify the morphological impact of lowering the groynes,

## 1.4 PROBLEM ANALYSIS

### 1.4.1 Scale of the problem

We mentioned in the previous section some different scales. We will try here to elaborate the definitions of these scales. Following the classification of De Vriend (1999), the morphological process of a river could be represented by a hierarchy of scales. Assuming that to some extent these scale levels can be considered separately, they form a sort of cascade (Figure 1.2), in which the micro-scale level represents the small-scale bedforms, e.g. ripples and dunes. The meso-scale level is that of alternate bars and cross sectional-profile evolution. The macro-scale level is that of meander formation, up to longitudinal profile evolution of river reaches, e.g. in response to training works. Channel pattern formation at the scale of the river basin constitutes the mega-scale.

In this thesis, we will adopt a rather simplified classification from that of De Vriend (1999). This classification stems from some typical concerns for the river manager (see Table 1.2). The spatial and temporal domain will cover three different scales, i.e. small, intermediate, and large-scale. In this, the small-scale is a combination of the micro and meso-scales of De Vriend. The intermediate scale corresponds to the meso-scale, and the large-scale is equivalent to the macro-scale. Neither details of turbulence and sediment transport, which are the smallest of the micro-scale level, nor the mega-scale, will be discussed in this thesis.

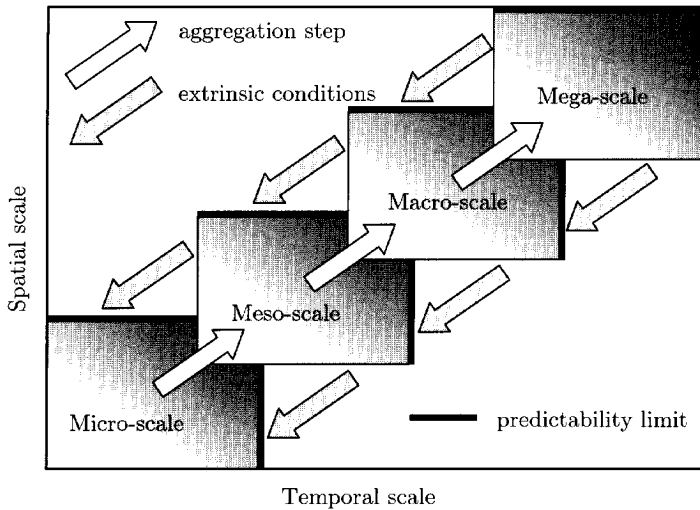


Figure 1.2: Scale cascade of morphological process according to De Vriend (1999)

Table 1.2: Identification of some management problems related to groynes, their scales and associated study tools

Management problem	Scale	Study tool
Bank erosion, undermining of groynes, resistance of groynes	Small	Physical models
Maintenance of the navigation channel	Intermediate	Process based model (Delft3D)
Tilting of the river	Large	Analytical and SOBEK

The small-scale analysis concerns the effects of the different hydrodynamic forcings on the behaviour of one or a few groyne-fields (*spatial distinction*), for a relatively short period of time (*temporal distinction*). The hydrodynamic part is investigated with a fixed-bed laboratory experiment. The sediment exchange process and the sediment budget of a groyne-field are studied in a mobile-bed laboratory experiment.

The intermediate-scale investigation studies the effects of a series of groynes on the morphology of the navigation channel. The aim is to provide a methodology that enables the river manager to take decisions concerning possible dredging activities. The study tool for this level is a process-based numerical model based on the DELFT3D software package (W1 | Delft Hydraulics, 2001a).

In the large-scale analysis, the impact on the whole river system is considered. The results from the small-scale analysis are then aggregated to form some kind of a forcing function to the large-scale stage. This function is supposed to be representative of the small-scale phenomena. A combination of an analytical model and a one-dimensional numerical model, namely SOBEK (W1 | Delft Hydraulics, 2001b), is utilised at this level.

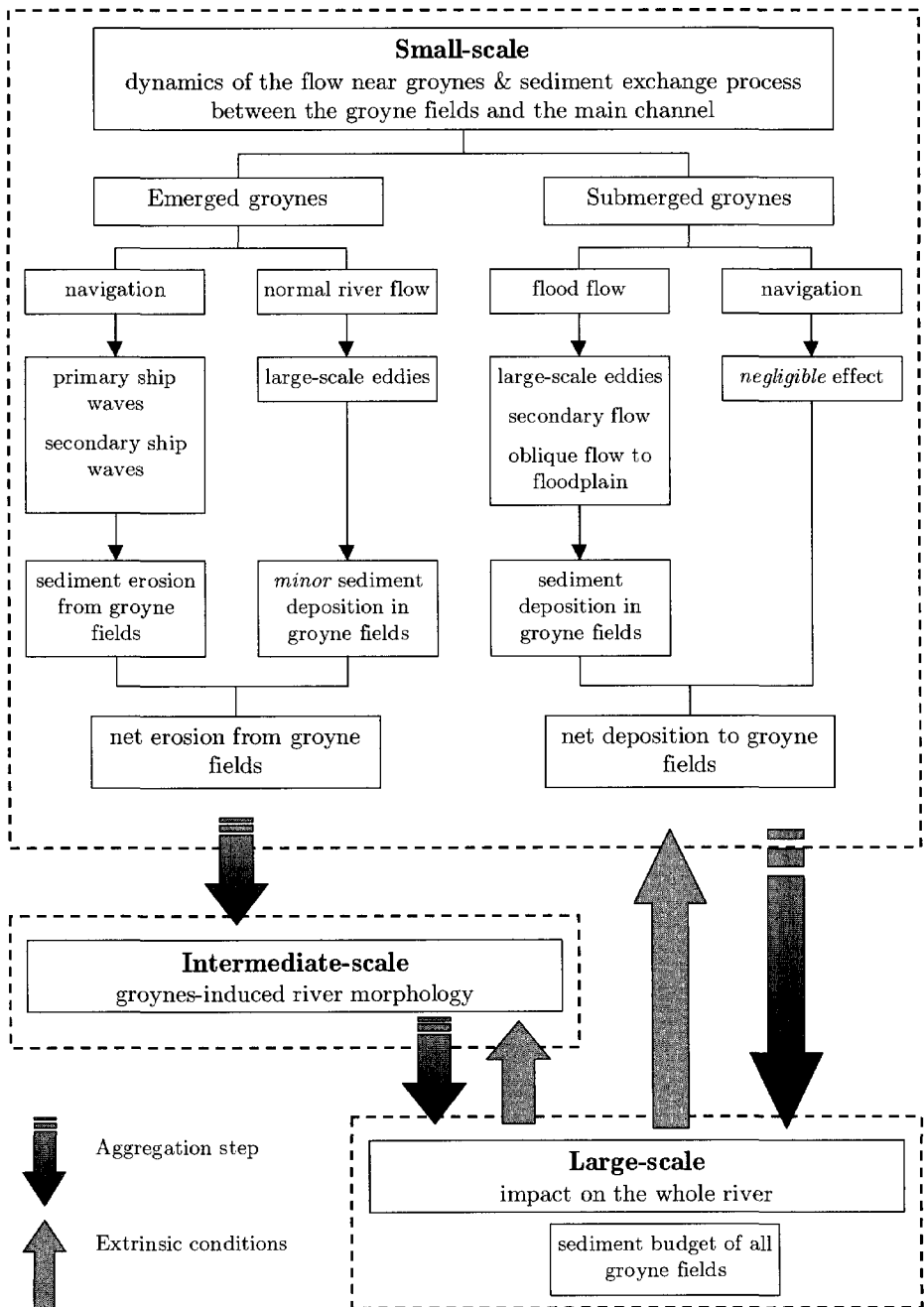


Figure 1.3: Overview of the various forcings and processes that affect the interaction between the groyne-fields and the main channel.

### 1.4.2 Forcing to the system

The hydrodynamic forcing that governs the interaction between the groyne fields and the main channel is the resultant of two components. The first is the effect of navigation, a factor that cannot be overlooked in a river like the Rhine, which is considered the backbone of the Northwest European waterways network. The other is the discharge-induced water motion. On the one hand, the groyne fields are filled with sediment during times of high discharge. On the other hand, the navigation-induced water motion is held responsible for eroding the groyne-field beaches; this effect is largest during low discharges. For an overview of the various forcings and processes that are affecting the interaction between the groyne-fields and the main channel, see Figure 1.3.

## 1.5 OUTLINE OF THE THESIS

The set-up of the thesis is presented in Figure 1.4. Chapter 2 gives some background information. It describes the different types of groynes, in addition to the characteristics of the groyne-fields along the Waal River. Chapter 3 describes a fixed-bed laboratory experiment for a river with groynes. In this chapter, the flow near groynes is described with emphasis on the dynamics of the flow and the resistance in the groynes region. In Chapter 4, the sediment transport in the vicinity of groynes is analysed and the mechanisms of transporting sediment to the groyne fields are highlighted. In Chapter 5, we synthesise the small-scale behaviour for a single groyne field. Chapter 6 focuses on the morphological modelling of a river with groynes using a 2DH process-based model (DELFT3D). Chapter 7 deals with the large-scale part of the problem. It uses a combination of analytical modelling and 1-D numerical modelling for a case study with schematised configuration that represents the Waal River. Finally, we draw some conclusions and recommendations in Chapter 8.

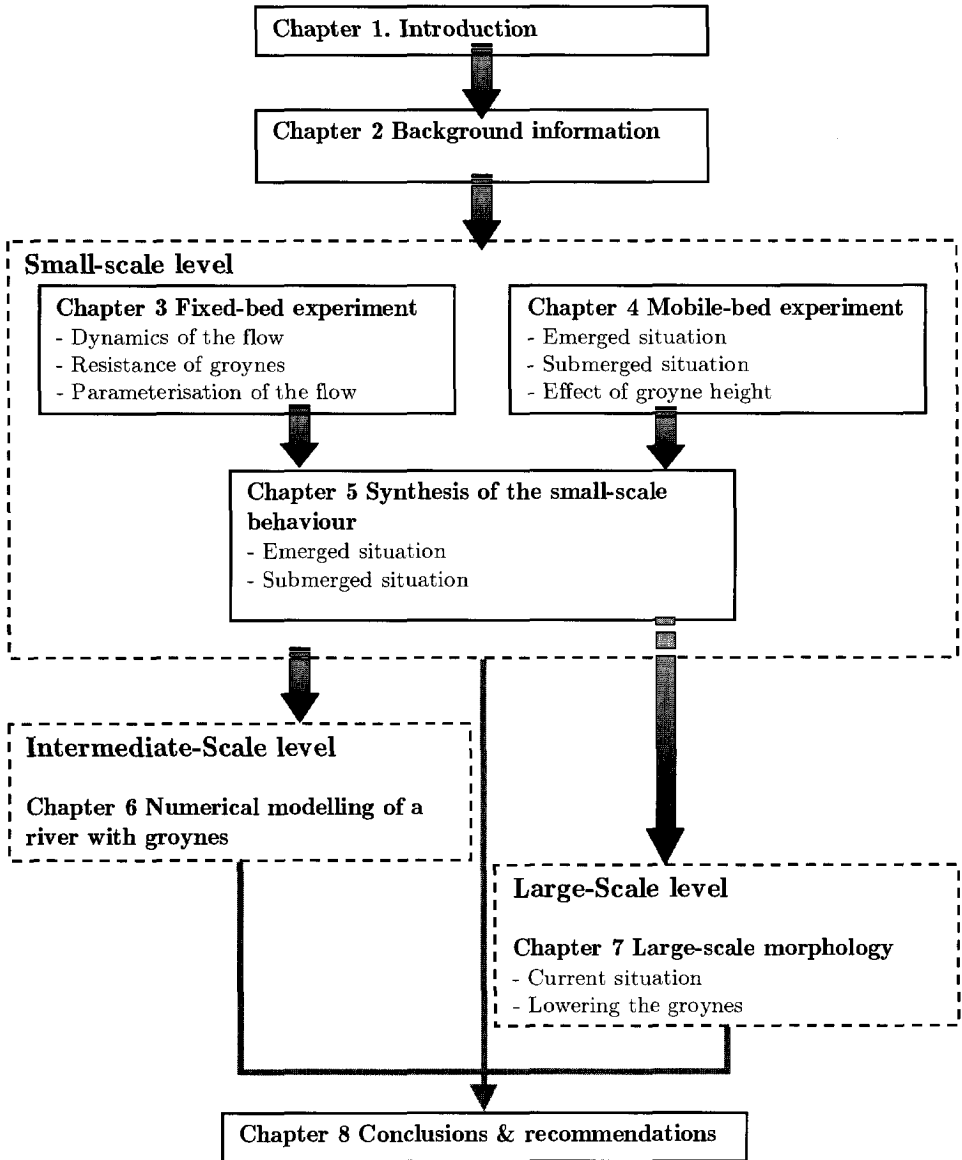


Figure 1.4: Graphical representation of the thesis layout.



## Chapter 2

### BACKGROUND INFORMATION

#### 2.1 INTRODUCTION

In this chapter, we present some of the background information that is required to proceed in studying the interaction between the main channel and the groyne fields in a regulated river. Firstly, in Section 2.2, we present some general aspects of groynes, and in Section 2.3 we describe the groynes in the Netherlands and the typical dimensions of the groyne fields found in the Waal River. Section 2.4, presents a brief survey of the available literature on the flow near groynes in the absence of navigation. Finally, Section 2.5, describes the effect of navigation on flow and sediment transport around groynes.

#### 2.2 RIVER TRAINING – GROYNES

The practice of river training dates back to the sixteenth century, when the Yellow River in China was trained by building embankments along its banks so that the flow would be confined to a single deep channel, which would transport the sediment load to the sea. Modern river-training practice, however, started in Europe in the nineteenth century, driven by the demands for additional safety due to ice jamming and to increase navigability associated with the industrial revolution.

Natural processes and/or human interventions may disturb the equilibrium between the sediment supply to the channel and its transport capacity. Training structures are then necessary to protect the channel against the changes that occur due to this disturbance. They can be classified as:

- Bed fixation and bottom vanes.
- Longitudinal structures, such as levees.
- Transverse structures, such as groynes.

Groynes, or spur-dikes, are small dams constructed at an angle to the flow, meant to deflect the flowing water away from critical zones. They are made of stone, gravel, rock,

earth, or piles, beginning at the riverbank with a root and ending at the regulation line with a head. They serve to maintain a desired channel for the purpose of flood control, improved navigation and erosion control.

### 2.2.1 Types of groynes

Various types of groynes can be distinguished according to their construction, action on stream flow and appearance. Przedwojski *et al.* (1995), claim that the following is necessary for a full description of groynes:

1- Classification according to the method and materials of construction:

Groynes may be permeable, allowing the water to flow through at reduced velocities, or impermeable, blocking and deflecting the current. Permeable groynes are fabricated from piles, bamboo or timbers, whereas impermeable groynes (also called solid groynes) are constructed using rock, gravel, gabions, etc.

2- Classification according to submergence stage:

Groynes may be designed either as submerged or as non-submerged under normal conditions. Which of the two types will be used is dictated by the design conditions. Usually impermeable groynes are designed to be non-submerged, since flow over the top of solid groynes may cause severe erosion along the shanks. Submerged groynes, on the other hand, may be designed permeable, depending on the degree of flow disturbance that is needed.

3- Classification according to the action on the stream flow:

Groynes may be classified as attracting, deflecting or repelling. Attracting groynes point downstream, they serve to attract the stream flow towards themselves and do not repel the flow towards the opposite bank. Deflecting groynes are generally short ones and used for local protection. They serve to change the direction of flow without repelling it. Repelling groynes point upstream. They serve to force the flow away from themselves.

4- Classification according to their appearance in planview:

Groynes may be built with different planview shapes. Examples are straight groynes, T-head, L-head, hockey stick, inverted hockey stick groynes, straight groynes with pier head, wing, or tail groynes.

### 2.2.2 Design Considerations for Groynes

The most important considerations involved in groyne design are planview shape, length, spacing, orientation to the flow, crest elevation and slope, cross-section, and construction materials (e.g. Richardson *et al.*, 1975; Alvarez, 1989; and Przedwojski *et al.*, 1995).

#### Planview shape & orientation

Of the abovementioned types of groynes, the straight ones are built under an angle to the bank that ranges from 70° to 120° (Klingeman *et al.*, 1984). They have a rounded

head to provide extra volume and area for scour protection at the outer end. T-head groynes are normally built under a right angle to the bank and they have straight shanks with a perpendicular head at the outer end. L-head, wing or tail groynes have different structures at the end, which generally leads to larger sediment deposits between groynes, less scour at their head and greater protection to the banks. L-head groynes are very effective in channelisation for navigation when the length of the head closes 45% to 65% of the gap between groynes. Hockey stick groynes have scour holes that are more extensive in area than T-head groynes.

Groynes may be oriented perpendicular to the flow, or inclined upstream or downstream. Each orientation affects the flow in a different way and results in a different deposition of sediment in the vicinity of the groyne. The so-called attracting groynes are pointing downstream to attract the flow towards itself, repelling or deflecting groynes are pointing upstream.

A groyne that is oriented upstream causes more deposition than a perpendicular one, not only downstream but also upstream of it, where an eddy is formed. Thus, the amount of deposition between groynes is largest in case of upstream inclined groynes. Groynes of this kind are therefore best suited for bank protection and sedimentation purposes. Groynes that are perpendicular to the flow protect a smaller area. Downstream facing groynes are not suitable for bank protection purposes, as they tend to attract the flow. The flow towards the root of the downstream groyne threatens the surrounding bank area, as well as the groyne itself. For the purpose of maintaining a deep navigable channel, on the other hand, perpendicular or downstream groynes perform best (Klingeman *et al.*, 1984).

### Spacing between groynes (S)

The spacing between groynes is measured at the riverbank between the groyne roots. It is related to river width, groyne length, flow velocity, angle to the bank, orientation to the flow, bank curvature, and purpose, but it is mostly expressed as a multiple of the groyne length. Richardson (1975) recommends a spacing of 1.5 to 6 times the upstream projected groyne length. In order to obtain a well-defined deep navigation channel, a spacing of 1.5 to 2 times the groyne length is recommended, whereas for bank protection the spacing is increased to 2 to 6 times the groyne length. There are, however, successful examples of bank protection with short groynes spaced at 10 to 100 times their length, but there the banks are protected with riprap or vegetation. If the spacing between groynes is too large, a meander loop may form between groynes. Long and widely spaced groynes may contract the flow resulting in channel degradation and bank erosion, thus causing a hindrance to navigation. If the groynes are spaced too close together, on the other hand, construction costs will be higher and the system would work less efficiently, not making full use of each individual groyne.

Mosselman (2000), presented a formula for the ideal spacing between groynes ( $S$ ) in terms of the main channel width ( $B_{mc}$ ), reading:

$$S \leq 2.5 k_1 k_2 k_3 B_{mc} \quad (2.1)$$

in which:

$k_1$  = correction factor for the groyne head type;  $k_1 = 1.0$  for ordinary straight groynes, and  $k_1 > 1.0$  for T-head and J-head groynes.

$k_2$  = correction factor for the alignment of the groynes system;  $k_2 = 1.0$  for straight alignments,  $k_2 > 1.0$  for convex alignments (inner bends), and  $k_2 < 1.0$  for concave alignments (outer bends).

$k_3$  = correction factor for the function of groynes ( $k_3 = 1.0$  for bank protection, and 0.5 for navigation).

### Length of the groynes (L)

Groyne length depends on location, purpose, spacing, and economics of construction. The total length of the groyne includes the anchoring length, referring to the part embedded in the bank, and the working length, referring to the part protruding into the flow. The length can be established by determining the channel width and depth desired. The working length is usually around a quarter of the mean width of the free surface; the anchoring length is recommended to be less than a quarter of the working length.

The maximum length of a groyne is equal to the distance between the bank and the river zone where no groyne encroachment is allowed. Such a zone should be determined in advance, as part of a river training strategy. Groynes intruding this zone may divert the river and trigger bank erosion at other locations over a large distance.

Laboratory experiments in Pakistan have shown that under bankfull flow conditions, a single groyne could protect bank lengths of 3 to 5 times the groyne projection length, implying that  $S/L \leq 3.0$  to 5.0 (Ghani and Gill, 1963). However, a stable eddy between the groynes contributes to a smooth guidance of the main flow if  $0.5 \leq S/L \leq 2.0$ . The latter condition is desirable for navigation, because it maintains a continuous deep channel along the face of the groyne battery (Eliasiewicz *et al.*, 1994). Yet, this requirement might be too strict, since a value of 3 to 3.5 for  $S/L$  along the Waal River seems to be satisfactory in practice.

### Crest elevation and base depth

The crest elevation of groynes depends on the purpose and possible problems due to overbank flow and ice. For bank protection, the crest should be at least as high as the bank. To avoid ice overtopping the crest elevation should be higher than the expected levels of ice. Crests may be either level or sloping downwards from the bank towards the end of the groyne. For bank protection, sloping-crested groynes are recommended by Alvarez (1989), with a slope of 0.1 to 0.25. They have the advantages of reducing scour at the groyne tip, requiring less material for construction and faster deposition of sediment between them. For navigation channel control, level-crested groynes work best normal to the flow or angled downstream, whereas sloping-crested groynes work best normal or angled upstream (Richardson *et al.*, 1975). The expected scour depth should be taken into consideration when determining the base depth of the groynes.

### Cross-section and Construction materials

The crest widths range from 1 to 6 m and side slopes from 1:1.25 to 1:5. The minimum crest width of 1 m is determined by the equipment used when placing the groynes. Wider crests generally make placing easier.

A wide range of materials is used for the construction of groynes, such as timber piles, tree trunks or branches, rock, soil, gravel, sandbags, riprap, prefabricated concrete elements, steel and wire, etc.

## 2.3 GROYNES IN THE NETHERLANDS

### 2.3.1 Historical background

The first major hydraulic engineering works since the Roman era were undertaken at the Rhine bifurcation in the early 1700s. Until then, channel corrections had been carried out and groynes, dams, and revetments had been built, but they served only local purposes such as the protection of dike sections. At the end of the 17<sup>th</sup> century, the Waal carried by far the greatest part of the Rhine discharge, probably over 95%. Water supply to the Nederrijn and the IJssel was so small that navigation was hardly possible.

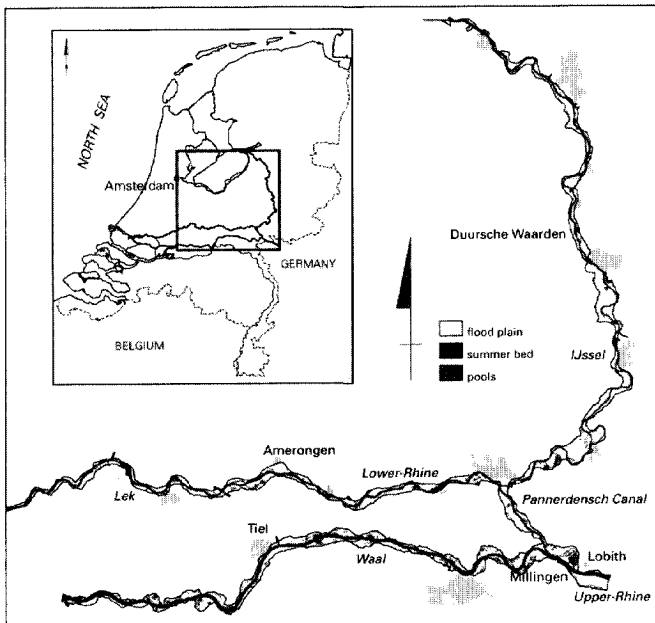


Figure 2.1: Rhine branches in the Netherlands – key-map

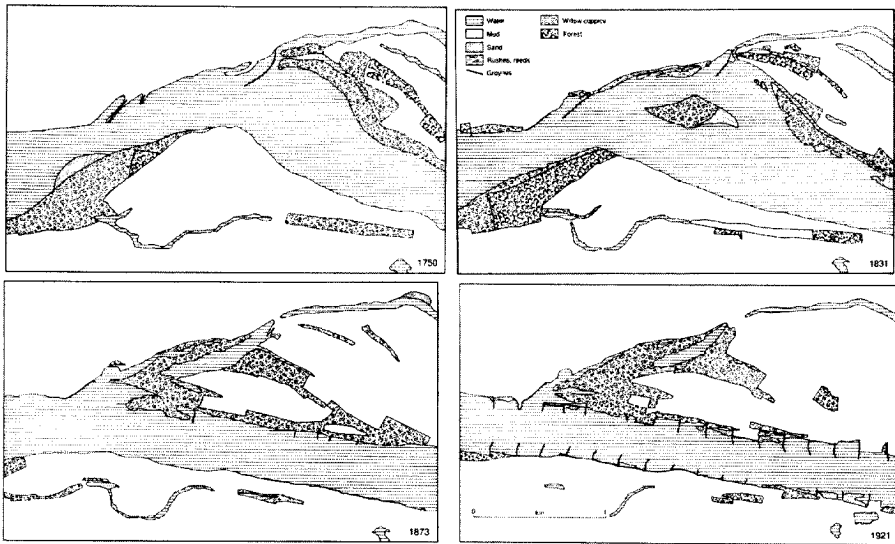


Figure 2.2: The Waal River near km 899-901 showing the channel changes over a period of about 200 years (source: Van Urk and Smit, 1989).

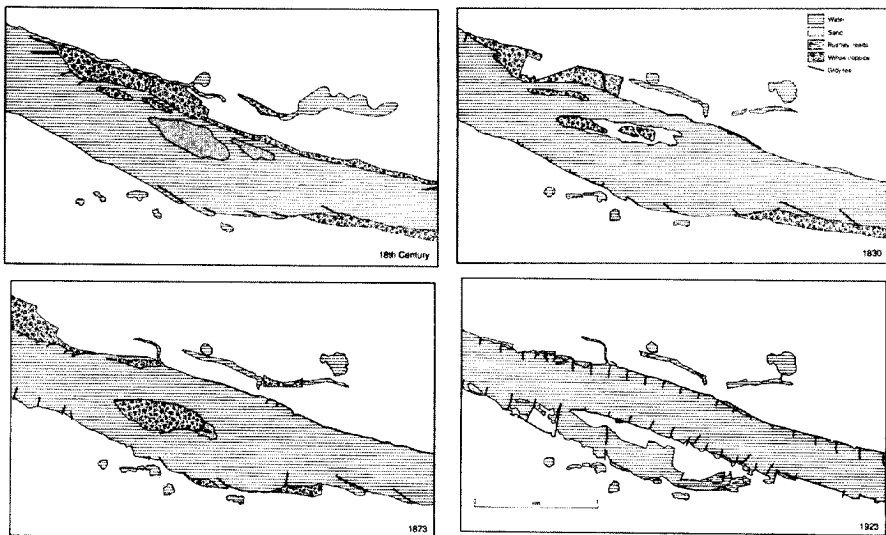


Figure 2.3: The Waal River near km 892-894 showing the channel changes since the 18<sup>th</sup> century (source: Van Urk and Smit, 1989).

Around 1775, the bifurcation of the Nederrijn and the IJssel was reconstructed by digging a new channel in the upper part of the IJssel. Since then, the IJssel received about one third of the discharge of the Pannerdensch Canal which in turn received about one third of the total Rhine discharge. The Waal carried the remaining two thirds of the flow. Stabilisation of the situation was achieved by moles, constructed under the supervision of Brunings, one of the first engineers to carry out accurate flow measurements in the river. Until the 1960s, the river bed of the Oude Rijn continued to function as a spillway for excess water, causing numerous floods in the region (Van Urk and Smit, 1989).

The works at the bifurcations improved the water distribution between the Rhine branches, but hazardous floods continued to occur. As administrative boards or water authorities with responsibility for integrated river management did not exist until the late 18<sup>th</sup> century, individual landowners built bank revetments and groynes to protect their land from erosion and to increase sedimentation. The resulting irregular array of groynes and the presence of many sandbars in the channel not only impeded flow, but in winters also led to the formation of ice dams. A formal ban on the irregular construction of groynes, proposed by the States of Gelderland in 1602 and finally adopted in 1715, had little effect by lack of enforcement.

In 1809 and 1820, large areas were inundated and in 1821 a government committee was appointed to make proposals for the solution of the problem. In 1825, the committee completed its report, which was published in 1827. Meanwhile, prominent engineers such as Blanken, Goudriaan and Krayenhoff, had published their views on the best solution. Their recommendations varied from the creation of new spillways by the partial removal of dykes, to the building of sluices, and to the construction of a totally new canal from the entry of the Rhine in the Netherlands through to the IJssel (Van Urk and Smit, 1989). These drastic plans were never executed. The solution finally adopted was outlined in a report submitted by inspectors Ferrand and Van der Kun of the newly formed Rijkswaterstaat (RWS). It proposed the removal of the sandbars and the constriction of the river's channels to accelerate flow.

Channel constriction was the solution that was finally adopted to increase the discharge capacity of the Lower Rhine. The effects of this channelisation are demonstrated best by a series of maps for a stretch of the river that was relatively unaffected before work started (Figure 2.2 and Figure 2.3). Because the wider River Waal had a stronger tendency to form multiple channels than the much narrower, strongly meandering River IJssel, the effect of channel constriction on the Waal was greater. The current situation of the Waal can be elucidated by Figure 2.4.

What the old maps do not show is the large-scale degradation process induced by these works. The degradation process in the Lower Rhine is complicated; it is mainly due to shortening of river bends, dredging activities, regulation of tributaries, and channel constriction by groynes. Near the entry point of the Lower Rhine into the Netherlands, bed degradation mainly occurred between 1925 and 1960. During that period the bed level came down by about 1.0 m (Van Urk and Smit, 1989). Ten Brinke and Gözl (2001) showed that this effect is still continuing, at least till 1995. The average bed degradation in the Lower Rhine branches since the end of the normalisation works ranges between 0.4 m and 2.2 m (see Table 2.1). Visser (2000) presented that the bed level of the Rhine branches has not yet reached its large-scale equilibrium state. The rate of degradation,

however, has slowed down considerably as compared the period right after the completion of the normalisation works.

Table 2.1: Average bed degradation in the different Rhine branches (after Visser, 2000)

River section	Rhine km	Period	Average degradation (m)
IJssel	878.5 – 1005	1938 - 1990	-0.40
Lek and Neder-Rijn	878.5 – 989	1933 - 1990	-0.90
Pannerden Canal	867.5 – 878.5	1926 - 1990	-2.20
Waal	867.5 – 952	1926 - 1990	-0.70
Boven-Rijn	857.5 – 867.5	1934 - 1990	-1.20

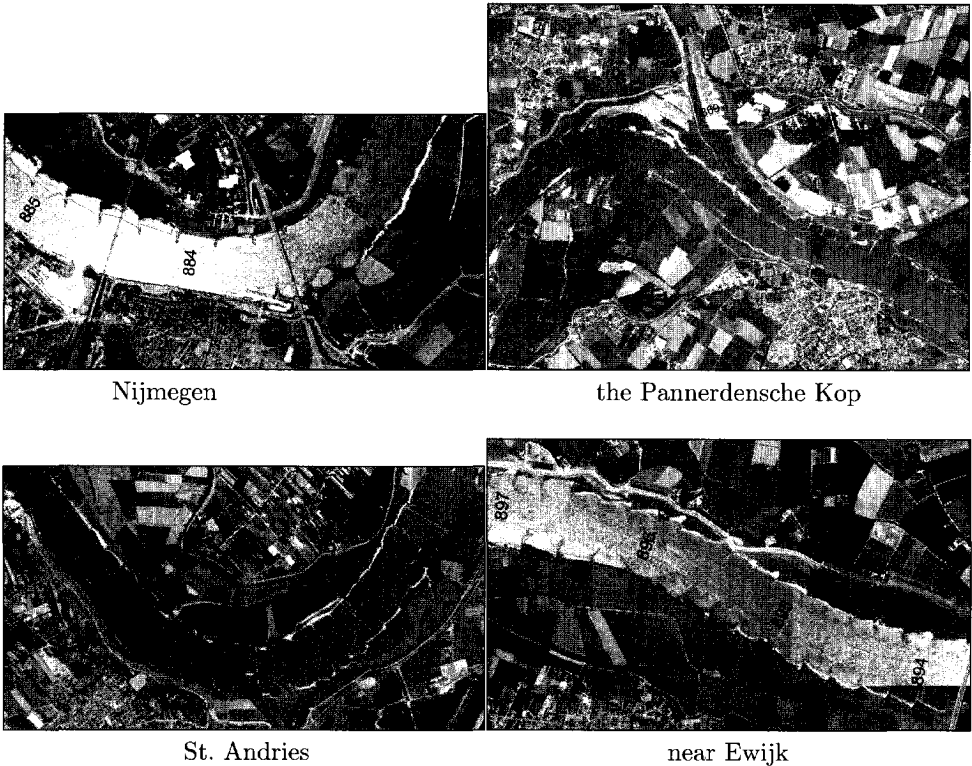


Figure 2.4: Aerial photographs showing the present situation for some locations along the Waal (courtesy of Rijkswaterstaat).

### 2.3.2 Characteristics of the groyne fields along the Waal River

Based on field measurements during the years 1996-1997 (Schans, 1998), the characteristics of the groyne fields along the Waal River are estimated and summarised in



Table 2.2. With reference to the definition sketch (Figure 2.5), the dimensions of the groyne fields can be defined as:

- $S$ : spacing between groynes (also the length of a groyne field  $L_{gf}$ )
- $L$ : groyne length
- $L_{gf,w}$ : groyne field length along the waterline
- $B_{mc}$ : river width between groynes (main channel width)
- $Y_{th}$ : distance between the normal line and the thalweg
- $G$ : orientation of a groyne (with respect to the line  $\perp$  thalweg)

Two more parameters are important for characterising the groyne fields, viz. the beach slope and the groyne field bed material size ( $D_{50}$ ). The bed material in the groyne fields generally consists of well-sorted sand with around 70% -by weight- between 250  $\mu\text{m}$  and 500  $\mu\text{m}$ . At sites that are more exposed to the current, the bed material is less well-sorted and an armour layer of gravel may be found. At these sites, more than 25% of the sediment is coarser than 2.0 mm and around 57% is between 125  $\mu\text{m}$  and 500  $\mu\text{m}$ .

Table 2.2: Characteristics of the groyne fields along the Waal River

Parameter	mean	min.	max.	standard deviation
$S$ : spacing between groynes [m]	198.2	50	420	37.7
$L$ : groyne length [m]	67.9	0	175	28.6
$L_{gf,w}$ : length along the waterline [m]	215.1	100	480	43.5
$Y_{th}$ : distance normal to thalweg [m]	129.8	10	320	93.6
$B_{mc}$ : main channel width [m]	279.5	252	412	35.2
$G$ : orientation of a groyne [deg.]	-8.0°	-30°	10°	8.7°
$D_{50}$ : bed material [ $\mu\text{m}$ ]	439.5	200	1300	264.5
Beach slope [--]	0.042	0.03	0.05	0.008

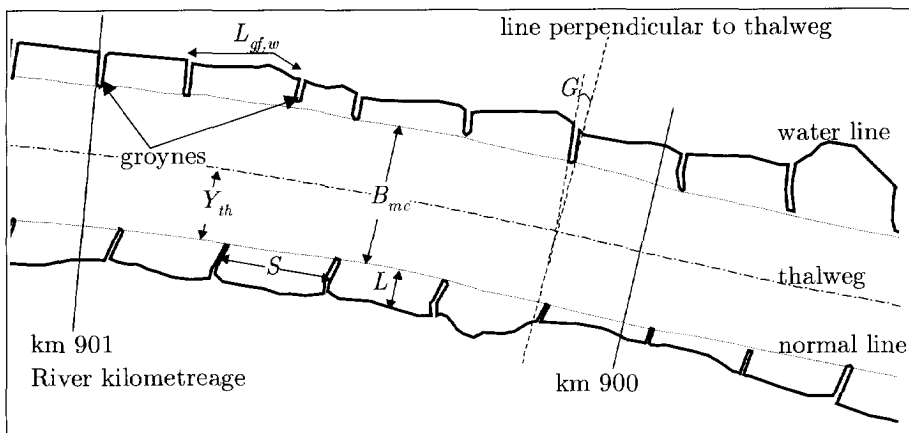


Figure 2.5: Definition sketch for the dimensions of arbitrary groyne fields.

Based on a previous analysis (Yossef, 2002), it was possible to assume the following values can be taken as representative for the groynes of the Waal River:

$$S \cong 200 \text{ m}$$

$$L \cong 60 \text{ m}$$

$$B_{mc} \cong 260 \text{ m}$$

$$G \cong 0^\circ$$

$$D_{50} \cong 350 \mu\text{m}$$

$$\text{Beach slope} \cong 1:25$$

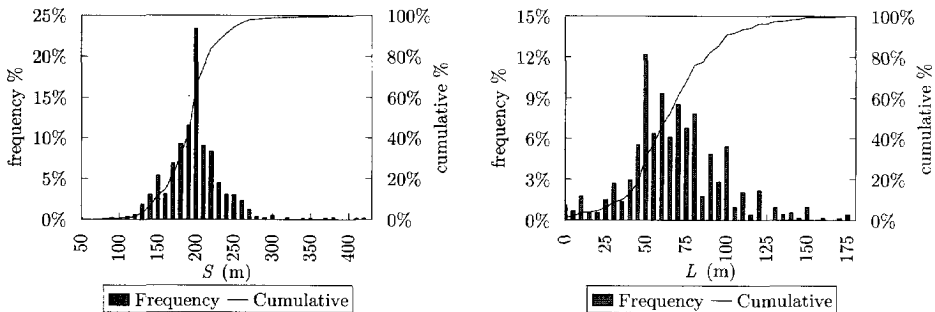


Figure 2.6: Statistical representations for the spacing between the groynes ( $S$ ), and the length of groynes ( $L$ ), in the Waal River.

## 2.4 FLOW NEAR GROYNES

The flow field differs significantly between the case of a single groyne and that of a series of groynes. This thesis focuses on groynes in series, for the flow pattern near a single groyne we refer to e.g. Ishii *et al.* (1983), Tingsanchali and Maheswarn (1990), Chen and Ikeda (1997), Ouillon and Dartus (1997).

### 2.4.1 Emerged groynes

Under conditions where the groynes are not submerged, the groyne fields are not really part of the flow conveying cross section of a river. Accordingly, the flow pattern in a groyne field does not directly contribute to the discharge in the main channel. Reducing the main stream velocity has little effect on the flow pattern itself, whereas lowering the water does affect the pattern (Uijtewaal *et al.*, 2001). Moreover, the flow pattern inside a groyne field may change with the change of its geometry, location along the river (inner bend, outer bend, straight part), and/or the groyne orientation (Przedwojski *et al.*, 1995). Klingeman *et al.* (1984) describe six types of eddy patterns between two groynes (Figure 2.7).

- Type one: the circulation pattern of this type is distinguished by the main flow that is deflected outside the groyne field, and a single eddy develops between the groynes.

This eddy is well developed and it prevents the main flow from penetrating into the groyne field.

- Type two: in this type, a second eddy appears but the main current is still deflected outside the groyne field.
- Type three: as the spacing between the groynes increases, the main current is directed into the groyne field creating a much stronger eddy near the upstream groyne.
- Type four: in this type, the upstream eddy is washed out and a single strong reverse current arises.
- Type five: in this type, the flow that is diverted by the upstream groyne is directed to the bank in the groyne field. Eddies form on both sides of this flow providing some protection to the bank.
- Type six: as the spacing between the groynes further increases, the downstream eddy disappears and the flow attacks the bank directly.

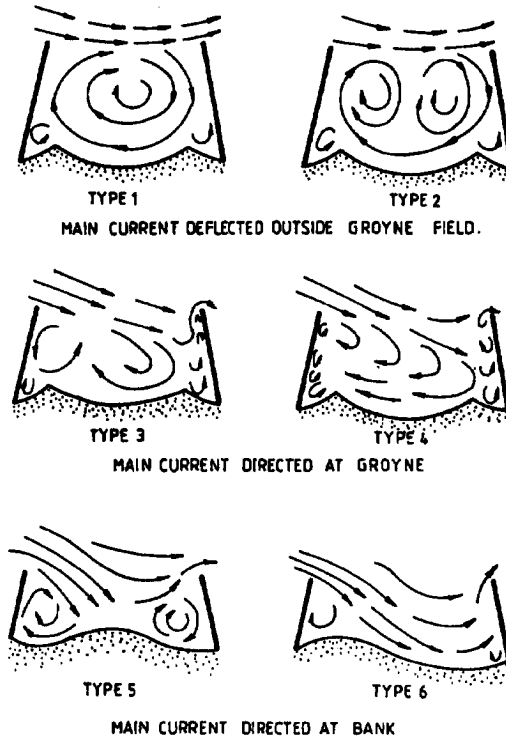


Figure 2.7: Different types of flow pattern in a groyne field, (source: Klingeman *et al.*, 1984).

The groyne field's length to width ratio determines the number and shape of eddies that emerge in the stagnant flow region (Uijttewaal, 1999; Muto *et al.*, 2000). An aspect ratio close to unity gives rise to a single eddy. A larger aspect ratio gives room for two stationary eddies, a large one, called primary eddy, in the downstream part of the groyne field, and a smaller secondary eddy near the upstream groyne. In a long groyne field with a length to width ratio of around six, the flow penetrates into the groyne field. The two eddies remain in a relatively stable position, while the main flow field starts to penetrate into the groyne field further downstream. In all cases, there is an eddy shedding intermittently from the tip of the groyne and migrating along the interfacial line between the main flow and the eddies. It eventually merges with the primary eddy.

The flow field is unsteady, even in the case of a steady discharge. Hence, there is a significant difference between the time-averaged and the instantaneous flow field. There is a strong time-dependent motion covering the entire groyne field, which can only be observed by looking at the instantaneous velocity field. The time-averaged velocity field has a different pattern that is difficult to explain in terms of flow dynamics, as a consequence of the averaging process.

Away from the tip of the groyne, the flow pattern between emerged groynes is predominantly two-dimensional. The small-scale three-dimensional turbulence plays a minor role in the mass and momentum exchange process between the groyne field and the main channel. Strong large-scale three-dimensional structures cannot develop due to the shallowness of water. The flow near the tip of the groyne is strongly three-dimensional (Krebs *et al.*, 1999).

#### 2.4.2 Submerged groynes

Reviewing the available literature revealed a lack of research dealing with groynes in submerged conditions. This may be due to the fact that there was little need to investigate submerged situations, since the groynes are mostly functioning under emerged conditions. Another reason might be the complexity and three-dimensionality of the problem, which require advanced measurement techniques and/or powerful three-dimensional computational methods. Few researchers have attempted to study the case of submerged groynes (see for example: Aya *et al.*, 1997; Peng *et al.*, 1997; Krebs *et al.*, 1999; Tomina-ga *et al.*, 2001).

Aya *et al.* (1997) report a sharp decrease in the water level between the upstream and downstream sides of the groynes. By implication, the water surface slope between two successive groynes is less than the slope in the main channel region.

Peng *et al.* (1997) compare three-dimensional numerical results with experimental results and conclude that the flow pattern in the case of submerged groynes shows strongly three-dimensional features behind groynes. On the upstream face of the groyne, the flow shows an upward motion because of the blockage effect. When the groynes are spaced far apart, the separating flow over the groyne reattaches to the bed, whereas too closely spaced groynes will prevent flow reattachment to the bed, thus keeping the bed shear stress at a low value.

Another important aspect of the flow pattern in the case of submerged groynes is the formation of a secondary flow structure. Both on top and behind the groynes, there is a secondary circulation that is directed from the bank towards the channel axis near the surface, and the other way around near the bed (Krebs *et al.*, 1999).

## 2.5 EFFECT OF NAVIGATION

In a river like the Rhine, which is considered the backbone of the Northwest European waterways network, navigation is a very important element affecting the morphology of both the groyne fields and the main channel. It ought to be taken into account when attempting to investigate the interaction between the groyne fields and the main channel.

### 2.5.1 Water movement around a ship

As a vessel sails through a waterway, it generates hydraulic disturbances in the form of waves and currents. The dominant hydraulic disturbances associated with a moving ship are the drawdown, return current, propeller jets, and secondary waves. The drawdown and the return current together form the *primary* water movement. The ship-induced waves and the associated orbital motion form the *secondary* water movement. The size of the vessel with respect to the waterway along with its speed dictates the magnitude of these forces and their effects on the environment (Hochstein and Adams, 1989; Bhowmik *et al.*, 1995).

As the vessel displaces water during its forward motion, it causes a drop in the water level alongside known as the drawdown. The drawdown begins near the bow and rebounds near the stern, producing a single forced wave with a duration in the order of 40 to 120 seconds, depending on vessel length and speed. This drawdown can cause dewatering of shallow areas along the shoreline during vessel passage.

The maximum return current is produced adjacent to the barges and typically closer to the stern. As the ship sails upstream, return currents cause a temporary increase in ambient current velocities. As the ship sails downstream, the return current causes a decrease in ambient current velocities and under low flow conditions, may even create temporary reversal of the ambient flow. Currents associated with the propeller jets are three-dimensional and disturb the flow locally. The characteristics of these jets are a function of hull shape, propeller type and size, engine power of the vessel, etc. Thrust, alignment to the bank and rudder angle affect the potential flow impingement on the bed or the banks. Under normal cruising conditions, propeller jet effects are limited to the navigation lane behind the ship.

Beginning at the corners of the lead barges of a tow, waves diverge from the sides of the tow. As transverse stern waves intersect with this diverging wave, secondary waves are formed which propagate away from the tow at an angle toward the shoreline. These waves are rather constant in amplitude and have short periods (1 to 5 s). For high-speed vessels, they can have significant wave heights and often dominate the hydraulic disturbances produced by the vessel. Transverse wave height decreases with increasing distance

from the stern and has wave periods in the order of 2 to 5 seconds. The influence of waves will decrease as the return current and the water-level depression are stronger. Thus, the smaller and faster ships are usually responsible for bank erosion due to the secondary waves, while the larger and slower ships cause erosion due to the return current.

### 2.5.2 Navigation-induced water motion near groynes

In the previous section, the basic components of navigation-induced water motion were introduced for an ideal case of a ship sailing near the centreline of a rectangular channel. In a natural river, the situation is more complex, due to a number of factors, such as side slope effects, eccentric sailing course and natural irregularities. Groynes complicate the estimation of navigation-induced water motion even further.

Some attempts have been made to understand the navigation-induced water motion and its effect on the sediment motion from the beaches of the groyne fields, prior to the introduction of the six-barge pushtow units to the River Waal. Field measurements during a trial year were carried out (Havinga *et al.*, 1984), as well as laboratory experiments (W1 | Delft Hydraulics, 1987). The dimensions of the different pushtow formations are given in Table 2.3. A simple computation method for the navigation-induced water motion in a groyne field, including the wave propagation through the groyne field, is described in detail by Termes *et al.* (1991).

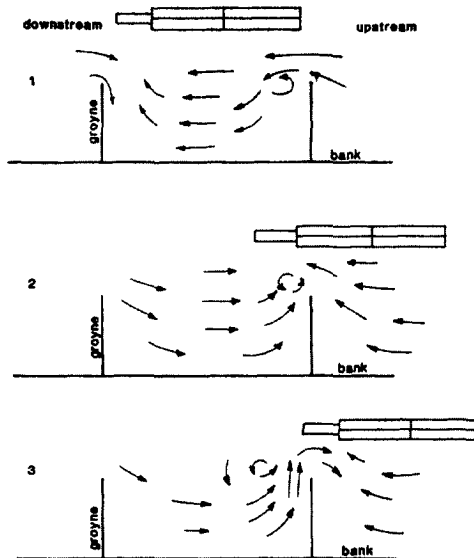


Figure 2.8: Flow pattern in a groyne field during passage of a pushtow unit, (source: Brolsma, 1988).

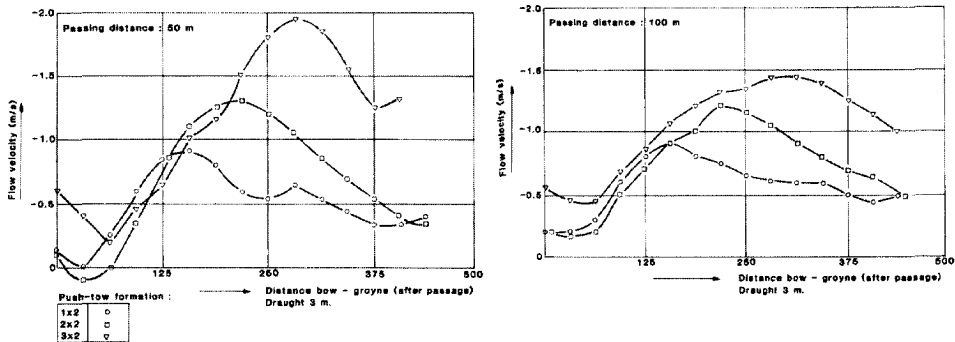


Figure 2.9: Flow velocities during a pushtow passage (source: Brolsma, 1988)

Figure 2.8, shows three important stages during the passage of a pushtow sailing upstream. The return current is maximal immediately after the bow passes a groyne. The return current is furnished by water from the upstream groyne field and the groyne field alongside. An eddy develops at the groyne head and the small vortex at the downstream end of the groyne field apparently disappears entirely. As the push-boat passes by, the supply flow refills the groyne field. When the stern of the push-boat passes the particular groyne field, the supply flow is forced to flow out of the groyne field by the upstream groyne, perpendicular to the axis of the fairway. The natural eddy immediately downstream of the groyne is transported downstream by the main current.

Table 2.3: Dimensions of different pushtow formations

Formation	2×2	3×2	2×3
Length (m)	193.0	229.5	193
Breadth (m)	22.8	22.8	34.2
Draught (m)	2.7	2.7	2.7

The magnitude of the velocities in the complex ship-induced water movement depends on ship dimensions, draught, unit speed, distance between pushtow and groyne, dimensions of the groyne field and the river discharge. In a physical model study performed by WL | Delft Hydraulics (1987; also see Brolsma, 1988), the navigation-induced water motion for three different formations, namely (3×2), (2×2), and (1×2) were investigated (see an example of the results in Figure 2.9). In addition, field measurements during the trial year 1984, to study the effect of (2×2), (3×2), and (2×3) formations on the flow in groyne fields, were carried out (Havinga *et al.*, 1984). Important conclusions from this work are:

- The increase in return and supply flows can be expected to cause larger velocities, mainly just downstream of the groynes. Therefore, an increase in ship speed, dimensions and draught will increase the flow velocity near groynes.
- The horizontal flow velocities increase almost linearly with an increase of the relative navigation speed for all formations tested.

- The model results demonstrate the effect of the passing distance, where the velocities increase with decreasing distance between the ship and the groyne tip.

The experiments showed that the maximum current velocities in small groyne fields are less than in large groyne fields, because of the smaller effect of the supply flow.

- From the field measurements, the current velocity in the groyne field was recorded during the passage of all three formations. The (2×2) formation produced a maximum return current of 1.10 m/s, 2 to 3 times higher than that with no navigation. The wide formation (2×3) had a lesser effect than the long one (3×2), but they both produced a higher current velocity than the (2×2) formation. The long formation yielded an increased current magnitude to 1.6 m/s, and the wide formation increased the current only to 1.25 m/s.
- The drawdown was also reported by Havinga *et al.* to be almost the same for the three above-mentioned formations: about 27 cm near the tip of the groyne, and about 20 cm near the bank.
- The field experiments further indicated that, whereas pushtows tended to produce a considerable increase in the flow in the groyne field, the largest self-propelled ship (about 2000 tons) had very little effect.

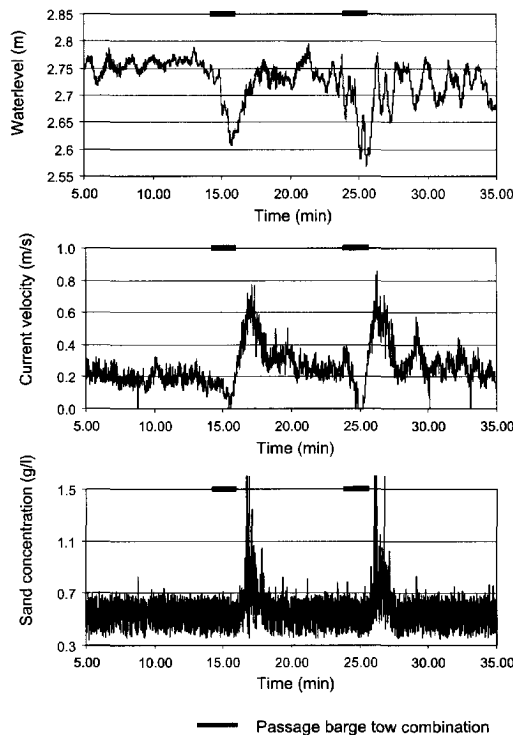


Figure 2.10: Example of the field records showing the navigation effect on current velocities, water level, and sediment concentration, (after: Ten Brinke, 2003).



- When the river discharge increases, the river cross section also increases. This increase causes a relative reduction of the return current and supply flow caused by navigation. Thus, a reduction of the navigation-induced flow velocities occurs. In addition, the relative draught (blockage) decreases, which is also a factor in favour of reducing the navigation effect.

Recent field measurements by Ten Brinke *et al.* (1999) also recorded the effect of a push-tow passing a groyne field. They reported that the water level depression can reach up to 20 cm, in addition to a return current of some 0.85 m/s. This current is strong enough to resuspend the sediment of the groyne field. An example of the result showing the effect of navigation on current velocity, water level and suspended sediment concentration is shown in Figure 2.10, where we can see that the peaks of these quantities coincide with the passage of push-tow units. These results are in analogy with those obtained from the field measurements by Havinga *et al.* (1984).

### 2.5.3 Navigation-induced erosion from groyne fields

One of the earliest investigations concerning the morphological changes in groyne fields was carried out in 1977 by Bruin (see Havinga *et al.*, 1984). Groyne field erosion in the reach Hulhuizen-Zaltbommel of the River Waal amounted to  $3\text{--}4 \times 10^6 \text{ m}^3$  during the period 1960–1976 (i.e. 17 years), based on photos at low water conditions. This eroded sediment is equivalent to an average lateral supply of sediment to the main channel of  $1.0 \times 10^{-7} \text{ m}^2/\text{s}$  from its sides, along the whole length of that reach (65 km).

During the field measurements carried out by Havinga *et al.* (1984), it was noticed that only push-tow units cause a sufficient increase in flow velocity to bring the sediment inside the groyne fields into motion. To have an idea about the sediment transport volume from a single groyne field due to a ship passage, we will use the information about the Hulhuizen-Zaltbommel reach given in Table 2.4. Utilising that erosion is fully due to push-tow units, we can then deduce that a single groyne field loses about  $0.14 \text{ m}^3$  of sand per passage. In that specific reach, the net changes in the river bed level between the normal lines during the period 1960 through 1976 is known to be negligibly small. During that period, the bottom level in the reach Hulhuizen–Nijmegen (15 km) dropped by around 0.20 m, and in the reach Nijmegen–Zaltbommel (57 km) a bottom rise of around 0.06 m took place.

Table 2.4: Some information about Hulhuizen-Zaltbommel reach

Distance Hulhuizen-Zaltbommel	65 km
Number of groyne fields	560
Frequency of push-tow units	8/day
Groyne fields erosion (1960-76)	$4 \times 10^6 \text{ m}^3/17 \text{ years}$

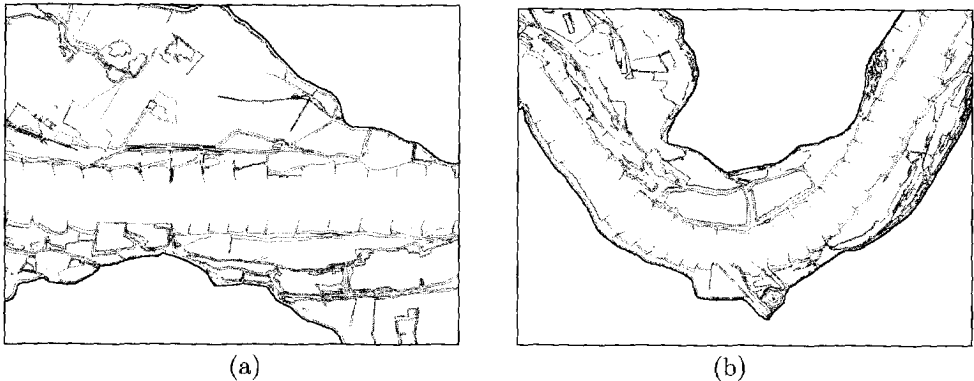


Figure 2.11: A straight part of the River Waal (a) near Druten; and a curved part (b) near St. Andries.

Havinga *et al.* (1984) measured the sediment concentration and the flow velocity during a ship passage near Druten (Figure 2.11a). They were aiming to quantify the effect of increasing the capacity by introducing six-barge pushtow units to the navigation fleet. Based on these measurements, they concluded that for pushtow units, the duration of the period with sediment export from the groyne fields is about 60 seconds, and that sediment outflow primarily takes place through the upstream 20 m of the groyne field. Furthermore, they estimated the sediment flux from a single groyne field to the main channel per passage, for the different pushtow formations. A summary of the results from Havinga *et al.* (1984) is presented in Table 2.5. These values would lead to an estimate of the erosion volume from the groyne fields of an order of magnitude higher than estimates by Bruin (see Havinga *et al.*, 1984) for the reach Hulhuizen-Zaltbommel. An additional conclusion from their study is the effect of the convoy configuration on the amount of sediment transport during its passage. With reference to Section 2.5, a long formation causes a much stronger return current during a longer period than a short formation. Consequently, the associated sediment flux from a groyne field is much larger for a long formation.

Moreover, these authors reported that the bottom material is generally at rest in the absence of navigation, since the velocity does not exceed 0.2–0.3 m/s. In addition, groyne fields are supplied with much less sediment from the main channel in periods without ship passages. This supply takes place across the downstream part, primarily due to the primary eddy.

De Haas and Van Essen (1987a) studied the groyne fields in a straight reach of the Waal River (near Druten, Figure 2.11a). Their results comply with the conclusion that there is a sediment supply from the river to the groyne fields in the absence of navigation. In this case, the measurements were carried out during a relatively high discharge condition (2000 to 3000 m<sup>3</sup>/s). Consequently, the estimated recharge of sediment was relatively high, i.e. in the order of  $3.6 \times 10^{-5}$  m<sup>3</sup>/s for each groyne field. Still the effect of navigation was higher, but no quantitative results could be obtained.

In addition to the study of a straight reach near Druten, De Haas and Van Essen (1987b) studied the groyne fields in a curved reach near St. Andries, where the groynes

are located in the outer bend (Figure 2.11b). In this case, no sediment recharge from the river was observed, only erosion. This is clear as the groyne fields are located already in the deep part of the cross section and the helical flow structure in a bend is in favour of eroding the groyne fields that are located in the outer bend.

Table 2.5: Sediment transport from a single groyne field due to navigation according to Havinga *et al.* (1984) (the effect of different formations)

Formation	Max. transport $10^6 \text{ m}^2/\text{s}$	Sediment out flux $\text{m}^3/\text{passage}$
2×2	9.8	0.035
3×2	19.6	0.070
2×3	12.0	0.040

In recent years, a series of studies concerning the morphodynamics of the groyne fields have been carried out by Rijkswaterstaat (e.g. Ten Brinke *et al.*, 1999; Ten Brinke *et al.*, 2001; Ten Brinke, 2003). Field measurements were carried out by Ten Brinke *et al.* (1999), where they measured the navigation-induced water motion and sediment transport in the area shown in Figure 2.11a. A sample result of these measurements is shown in Figure 2.10, in which it is clear that the turbidity peaks coincide with the passages of pushtow units. Based on the behaviour of two groyne fields in a straight reach, they estimated the average sediment transport from a single groyne field to be  $3 \times 10^{-3} \text{ m}^3/\text{s}$ , during 15% of the time. This was then used to estimate the sediment budget between the groyne fields and the main channel. For roughly 500 sandy groyne fields along the banks of the Waal, this would result in a total volume of  $7 \times 10^6 \text{ m}^3/\text{year}$  supplied to the main channel. They commented that this is far too high as compared with the river's yearly sand transport of  $0.5 \times 10^6 \text{ m}^3/\text{year}$ . This exaggerated estimation could be attributed to one or more of the following reasons:

- The study was carried out at a relatively low discharge, around  $1040 \text{ m}^3/\text{s}$  (mean discharge:  $1467 \text{ m}^3/\text{s}$ ). This means that the effect of navigation is relatively strong, as the effect of navigation increases with the decrease of the water level.
- The study area is in a straight reach of the river and the results cannot be generalised for the entire river. Since groyne fields behave differently according to their location along the river: a groyne field in an inner bend behaves significantly different from one in an outer bend or a straight reach.
- For the estimation of the total sediment volume, the total year was used as a base time, and the effect of the discharge variation was not considered. This leads to an overestimation of the exchange flux, since during relatively high discharges, the effect of navigation is negligible.

Ten Brinke *et al.* (2001) estimated the sediment balance for the Waal River during the last three decades and particularly during the high water period of 1995. From the analysis of their findings, see Table 1.1, one can conclude that during high water conditions sedimentation in the groyne fields plays an important role in the total sediment balance of the river. However, in the long run there is no net erosion or deposition

from/to the groyne fields. Thus, the amount of sediment that is deposited during floods must be released during normal and low flow conditions.

Table 2.6: Sediment balance for the main channel of the Waal River during the last three decades (after Ten Brinke *et al.*, 2001)

Sediment source/sink	Volume × 1000 (m <sup>3</sup> /year)		
	1970 – 1990	1990 – 2000	Flood 1995
Input sediment (US)	+682	+507	+250
Output sediment (DS)	-761	-578	-270
Bed degradation	+489	+264	+573
Groyne fields erosion/deposition	---	---	-373
Floodplain deposition	-53	-53	-180
Dredging	-357	-140	0

± signs refer to gains and losses of sediment transported in the main channel

The most up-to-date study is due to Ten Brinke *et al.* (2004), who revisited the estimates of the navigation-induced erosion from the groyne fields. They came out with two estimates for the erosion volume from the groyne fields. The first is based on the results from neural network modelling of the effect of navigation and the second is based on monitoring the bed level changes of the groyne field beaches during the period 1995-1998. The neural network modelling was based on an extended set of the measurements by Ten Brinke *et al.* (1999). This led to an estimate of the net sediment supply volume from the groyne fields of 200,000 m<sup>3</sup>/year. The estimate based on monitoring the beaches of the groyne fields was deduced from a relatively long monitoring period that included the effect of navigation at different discharge conditions. It even included some discharge conditions that would induce deposition to the groyne fields. Thus, it yielded a lower estimate for the net sediment supply from the groyne fields. This estimate amounted to only 90,000 m<sup>3</sup>/year.

The results of Ten Brinke *et al.* (2004) indicate that vessels less than 60 m had a minor effect on the morphodynamics of the groyne fields. Furthermore, the navigation-induced erosion is much stronger (nearly twice) on the south bank than on the north bank of the Waal. This difference is attributed to the significant difference between the characteristics of ships sailing near the south bank and those sailing near the north bank. Ships sailing upstream from Rotterdam to Germany are generally loaded, whereas they sail downstream generally empty. This leads to a significant difference in the underwater volume between ships sailing in either direction.

## Chapter 3

### FIXED-BED FLUME EXPERIMENT

#### 3.1 INTRODUCTION

The first step towards understanding the sediment exchange process between the main channel and the groyne fields of a river is to study comprehensively the details of the flow pattern near groynes.

The last few years have seen a number of experimental studies to investigate the details of the flow near groynes (e.g. Tominaga *et al.*, 2001; Uijttewaal *et al.*, 2001; Kurzke *et al.*, 2002). Cases much similar to groynes, viz. with embayments were studied by e.g. Kawahara *et al.* (1995), Muto *et al.* (2000) and Muto *et al.* (2002). Owing to the efforts of these researchers, the hydrodynamics of the flow near groynes have been gradually clarified. Yet, the dynamics of the flow near a series of groynes remain to be fully comprehended. To that end, fixed-bed flume experiments were carried out with the following main objectives:

- to investigate the dynamics of the flow and its associated time scale in the mixing layer between the groyne fields and the main channel,
- to study the effect of submergence level on the formation of the mixing layer,
- to obtain quantitative data on the mean velocity in the groynes region that enables us to model the effective resistance of groynes during submerged conditions.

The experiments presented in this chapter were financially supported by the Road and Hydraulic Engineering Division (DWW) of Rijkswaterstaat. The author participated in the design and preparation process, as well as in the measurements. The full test series covered four different types of groynes (see Berg and Uijttewaal, 2002; Uijttewaal *et al.*, 2002; Uijttewaal and Van Schijndel, 2004). In this thesis, however, only the standard groyne type as found in the Dutch River Waal is considered.

In this chapter, Section 3.2 discusses the experimental set-up in addition to the instrumentation and the measuring procedures. Section 3.3 explains the conditions and the procedures of the experiments. Section 3.4 briefly presents the data processing and data analysis procedures. Section 3.5 presents a number of characteristic results concerning the dynamics of the flow. The effect of the submergence level is presented in Section 3.6.

Section 3.7 proposes a parameterisation of the flow near groynes. Finally, we end this chapter with a summary and conclusions in Section 3.8.

## 3.2 EXPERIMENTAL SET-UP

### 3.2.1 Geometry

A physical scale model was built in the Laboratory for Fluid Mechanics of Delft University of Technology. The total model was 5 m wide and 30 m long. The model consisted of a schematic river reach, with dimensions based on the geometry of the Dutch River Waal scaled down to 1:40. In the lateral direction, the model represents half of the river width.

Figure 3.1 shows a schematic representation of the model set-up with indication to the fourth groyne field where the measurements were performed. The model bed is fixed and flat in the main channel; and it is sloping towards the bank in the area between the groynes. The groynes are located on a shallower part (Figure 3.2). The water is fed from the upstream side and the water level is controlled at the downstream side using a manually controlled tailgate.

In all test cases the Froude number ( $F_r$ ) was small (around 0.2) to guarantee subcritical flow, and the Reynolds number ( $R_e$ ) was guaranteed to be high enough to ensure fully developed turbulent flow in both the main channel region ( $R_e \cong 6 \times 10^4$ ) and the groyne fields region ( $R_e \cong 10^4$ ). In a preliminary test to determine the bed roughness, the groyne fields were closed off, yielding a 3.0 m wide rectangular channel. From this test, it was possible to estimate the roughness height ( $k_s$ ) of the concrete bed. It was found that on average  $k_s \cong 6.27 \times 10^{-4}$  m (Berg and Uijttewaai, 2002).

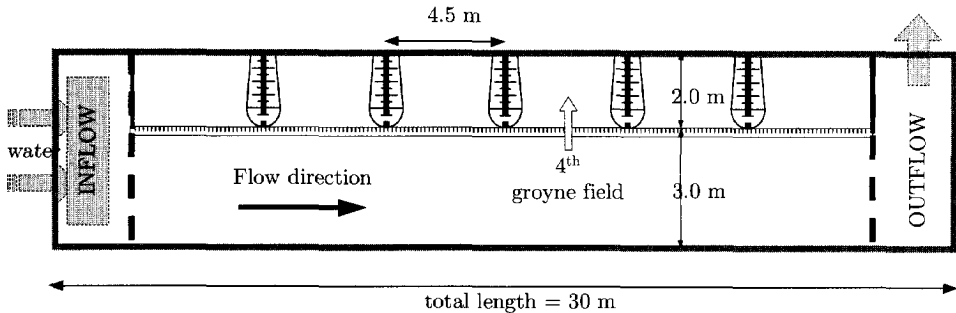


Figure 3.1: Experimental set-up with indication to the fourth groyne field where the measurements were taken; the set-up comprises five identical groynes. Co-ordinates are given in Figure 3.3.

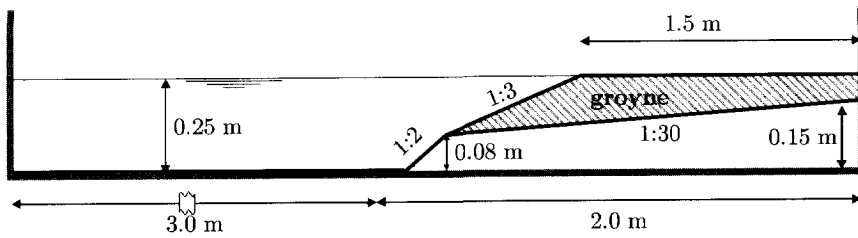


Figure 3.2: Cross-sectional view, showing the details of groyne type-A (not to scale).

In this thesis we will consider only one of the tested groyne types that represents the standard groyne as it is typically found in the Dutch River Waal. This groyne type (named: type-A) is a straight, impermeable structure perpendicular to the riverbank with a crest length of 1.5 m and with slopes of 1:3 on all sides (see Figure 3.2).

### 3.2.2 Instrumentation

Velocity measurements carried out during each test comprised different measurement techniques; we will focus here on the velocity measurements in the horizontal plane. Two different techniques were utilised, the first using electromagnetic flowmeters (EMF), and the second using particle-tracking velocimetry (PTV).

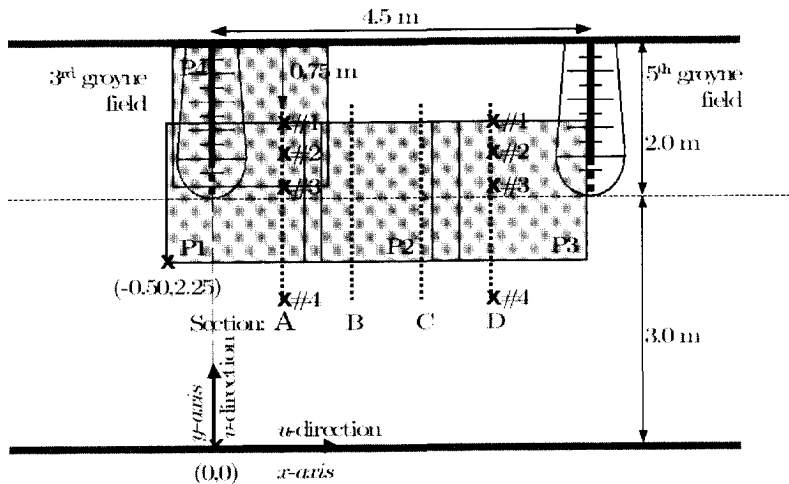


Figure 3.3: Measurement locations with respect to the co-ordinate system; shadow areas P1 to P4 indicate areas where PTV is applied. Points #1 to #4 are selected points for future illustration, sections A to D are located at 0.75, 1.50, 2.25, 3.50 m from the tip of the groyne.

Four electromagnetic flowmeters (EMF) were used, measuring  $u$ - and  $v$ -components of the velocity in the horizontal plane. The measurements covered the four sections A to D, in Figure 3.3. The sections extended over 2.6 m in the transverse direction and they were spaced at an equal distance of 0.75 m. Each section consisted of 12 points. At each point, velocities at two vertical elevations, located at 3.0 cm below the surface and 5.0 cm from the bottom, were recorded.

Particle-tracking velocimetry (PTV) is used to measure the instantaneous two-dimensional surface velocity, without causing any appreciable disturbance. It reveals the global structures of a complicated and/or unsteady flow field quantitatively. PTV was applied to measure the surface velocity in four areas of  $1.5 \times 1.5 \text{ m}^2$ ; these areas are indicated as P1 to P4 in Figure 3.3. Each time series lasted at least 5 minutes with a recording frequency of 30 Hz. Each frame contains about 2000 particles of 2 mm diameter, floating on the free surface. The velocities of these particles were determined using a PTV-algorithm (Bastiaans *et al.*, 2002). The unstructured data were then interpolated onto a uniform rectangular grid with a characteristic spatial resolution of 5 cm. This resolution is, however, not sufficient to resolve the full spectrum of turbulent fluctuations. The conclusions that are drawn from these experiments therefore only apply to the large-scale turbulence structures.

### 3.3 EXPERIMENTAL CONDITIONS AND PROCEDURES

In this Chapter, we present two test series. The first, named series-A, was carried out to study the dynamics of the flow near a series of groynes in different flow situations. The second test series, named series-S, was carried out to investigate the effect of the submergence level on the flow pattern in the vicinity of groynes.

#### 3.3.1 Series-A

This test series was dedicated to investigating the dynamics of the flow in the vicinity of a series of groynes in the two different flow stages; namely the emerged and submerged stages. The effect of flow stage is studied by changing the flow depth and keeping the main channel mean velocity constant at about 0.3 m/s. Three water levels were tested, the hydraulic conditions of which are given in Table 3.1. A water level of 0.25 m represented the emerged condition (case A1), two high water levels of 0.31 m and 0.36 m (cases A2 & A3), represented two submerged cases.

The aims of this series are summarised in the following points:

- to investigate the different turbulence time scales associated with the flow near groynes, with emphasis on large-scale structures,
- to identify the interaction process between the different turbulent structures,
- to investigate the differences in the turbulence pattern between the emerged and submerged groynes situations.



Table 3.1: Hydraulic conditions for the test cases of series-A

test	Q (m <sup>3</sup> /s)	Flow depth (m)
A1	0.248	0.248
A2	0.305	0.310
A3	0.381	0.357

As the emphasis of this series is on detecting the large-scale turbulence structures, both EMF and PTV techniques were used. The measurement locations covered the entire mixing layer from section-A to section-D. The sampling time was guaranteed to be long enough to ensure a full coverage of the largest turbulence structure; the total recording period for a single point was 600 seconds, with a sampling rate of 10 Hz. The inflow conditions were adapted to the expected profile far downstream such that beyond the first two groyne fields the flow can be considered as fully developed.

### 3.3.2 Series-S

This test series was dedicated to investigating the effect of submergence level on the resistance in the groynes region. In order to be able to investigate the effect of lowering the groynes it is important to assess the effect of different submergence levels on the flow in the groynes region. Accordingly, all test cases in this series were chosen so as to guarantee submerged flow conditions.

Twenty different cases were considered, as indicated in Table 3.2. The aims of this series are summarised in the following points:

- to investigate the shape of the transverse velocity profile under different blockage ratios,
- to investigate the resistance in the groynes region for the different blockage ratios.

The procedures for running this series were as follows; the downstream tailgate was adjusted to a certain level and the model was fed with water from the upstream side. From the inflow control valves, the discharge was reduced from the highest discharge to the lowest in a number of steps. Keeping the tailgate elevation constant and varying the discharge, we eventually vary both the water surface slope and the flow depth to produce different hydraulic conditions. The hydraulic conditions can be represented by Froude number ( $F_r = u/\sqrt{gh}$ ). Figure 3.4, shows the relation between the discharge and the Froude number for all test cases.

Table 3.2: Hydraulic conditions for the test cases of series-S.

Test	Q (m <sup>3</sup> /s)	Flow depth (m)			
		SA	SB	SC	SD
01	0.383	0.353	0.284	0.330	0.305
02	0.333	0.343	0.274	0.326	0.296
03	0.278	0.333	---	0.316	0.286
04	0.220	0.322	---	0.304	0.275
05	0.162	0.304	---	0.290	0.261
06	0.102	0.290	---	0.274	0.245

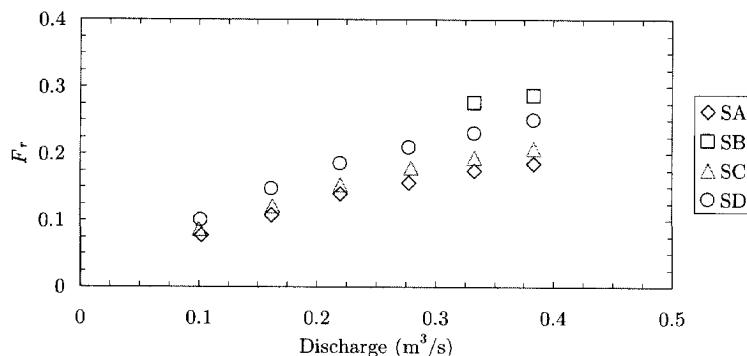


Figure 3.4: Relation between discharge, and Froude number ( $F_r$ ) for series-S (note that test SB has only two cases; see Table 3.2).

After a complete set of tests had been completed, the tailgate was set at a different elevation and the same procedures were repeated to establish a new set. Before carrying out the measurements, the flow was given enough time to adjust to the new discharge condition. In each test, the water level was measured and the horizontal velocity measured at 0.6 times the depth was recorded using EMF at section-C as in Figure 3.3.

### 3.4 DATA PROCESSING AND ANALYSIS

#### Statistical moments

The method of (central) moments is used for the computation of the basic statistical characteristics of the velocity records. The first moment of a data record of turbulent velocities  $u_i$  is an estimate of the mean velocity  $\bar{u}$ , and is computed with:

$$\bar{u} = \frac{1}{N} \sum_{i=1}^N u_i \quad (3.1)$$

With  $N$  as the number of samples, it is expected that this average converges to the true mean value as the number of samples increases. The velocity fluctuations  $u_i$  are obtained by subtracting the mean value  $\bar{u}$ , from the measured data  $u_i$ :

$$u_i = u_i - \bar{u} \quad (3.2)$$

The mean values of the various powers of  $n$  of  $u_i$  are known as the central moments, and are estimated by:

$$\overline{(u_i)^n} = \frac{1}{N} \sum_{i=1}^N (u_i)^n \quad (3.3)$$

The second central moment  $\overline{(u_i')^2}$  is equal to the variance of the velocity  $\text{VAR}(u_i)$ , and can be interpreted as a contribution of the velocity fluctuations in the  $u$ -direction to the turbulent kinetic energy per unit mass. It is more common to use the standard deviation  $\sigma$ , which is the square root of the variance and is expressed in velocity units. The standard deviation is identical to the turbulence intensity  $u'$  of a velocity component.

The third and the fourth central moments, normalised by the standard deviation, are known as the skewness  $S_K$ , and the flatness (kurtosis)  $F$ :

$$S_K = \frac{\overline{(u_i')^3}}{\sigma^3}; \quad F = \frac{\overline{(u_i')^4}}{\sigma^4} \quad \text{with } \sigma = \sqrt{\overline{(u_i')^2}} \quad (3.4)$$

The skewness is a measure of the lack of symmetry of the velocity distribution, and is connected with the convection of turbulent kinetic energy by turbulent motions. The flatness is large if the tails of the velocity distribution are relatively important, and is an indicator of the intermittency. In the case of the normal (Gaussian) distributed velocity data:  $S_K = 0$ , and  $F = 3$ . A positive skewness indicates a longer 'tail' of the distribution in the positive direction and the greater the kurtosis the flatter the distribution.

### Correlation functions and spectral analysis

A method to detect the different turbulent time scales in a velocity signal, is the determination of time correlations or autocorrelation function ( $R$ ), as function of the time shift ( $\tau$ ). The autocorrelation functions presented in this chapter are calculated for the mean-removed signal and normalised with its variance, according to the following expression:

$$R_{ii}(\tau) = \frac{\overline{u_i(t)u_i(t+\tau)}}{\overline{(u_i(t))^2}} \quad (3.5)$$

Another powerful tool to analyse the structure of turbulent flows is the energy density spectrum, obtained with the help of Fourier transformation. Based on the assumption that a time signal can be expressed as a superposition of sinusoidal functions, it is possible to transform any signal from the time domain to the frequency domain. The energy density spectrum ( $E$ ) gives the distribution of the turbulent energy over the different frequencies ( $f$ ). To suppress the variation of the estimated energy density spectra, the sampled time series were divided into a number of overlapping blocks (35% overlap). For each block, the energy spectrum was evaluated using FFT (*Fast Fourier Transform*). The final energy spectrum was obtained by averaging the spectra of the different blocks.

## 3.5 THE DYNAMICS OF THE FLOW\*

### 3.5.1 Velocity signals

In experiment series-A, velocity signals were measured in both the  $x$ - and the  $y$ -direction throughout sections A to D. Figure 3.5 shows a sample of the velocity records, taken at the centre of the mixing layer at section A. The signals presented give an impression of the amplitude and the time scale of the velocity fluctuations.

Upon comparison of the time signals of the  $u$ -, and  $v$ -components in each case, we can observe that in all three cases shown in Figure 3.5 the velocity fluctuations in the transverse direction are more pronounced than those in the streamwise direction. Furthermore, after a comparison between the time signals of the different cases, we can observe that the velocity fluctuations in the submerged condition generally have longer time scale than in the emerged condition.

Figure 3.6 presents the distribution in the transverse direction of the streamwise velocity  $\bar{u}$ , measured at sections A through D for the three test cases A1, A2 and A3. We can observe that the transverse velocity distribution in the emerged case Figure 3.6a, converges from section A to B, to reach a rather stable distribution at sections C and D. In the submerged cases (Figure 3.6b, c) the velocity distribution converges within a rather short distance, as it is nearly the same for sections B, C and D. This difference is due to the different nature of the mixing layer in case of emerged and submerged groynes.

Figure 3.7 presents a sample of the data extracted from the PTV-measurements in which the total turbulence intensity for the three test cases A1, A2, and A3 can be seen. The distribution of the total turbulence intensity gives an impression of the extension of the mixing layer in the different cases.

In the emerged stage (case A1) the mixing layer starts at the tip of the groyne and grows in width in the downstream direction. The total turbulence intensity and the transverse shear stress ( $\tau_{xy}$ ), have their maxima around 1.5 m from the tip of the groyne (see Figure 3.7a and Figure 3.8a).

Unlike the emerged stage, the mixing layer in the submerged stages does not originate from the tip of the groyne. It has a rather constant width that is generally larger than that in the emerged stage (see Figure 3.7b-c and Figure 3.8b-c). Moreover, after comparing between the two submerged cases A2 and A3, we observe that with increasing the submergence the magnitude of the total turbulence intensity as well as the transverse shear stress decrease, while the width of the mixing layer remains the same.

Distinguishing between the different time scales from the velocity signals is not a straightforward task. Therefore, more analysis is conducted and presented in the following two subsections, in which we will focus on the lateral velocity component, as it shows a clearer periodical behaviour and a clearer distinction between the emerged and submerged situations.

---

\* Excerpts from this Section were published as: YOSSEF, M. F. M., and UJTTEWAAL, W. S. J. (2003). "On the dynamics of the flow near groynes in the context of morphological modelling" in: *XXX IAHR Congress*, Thessaloniki, Greece, 361-368.

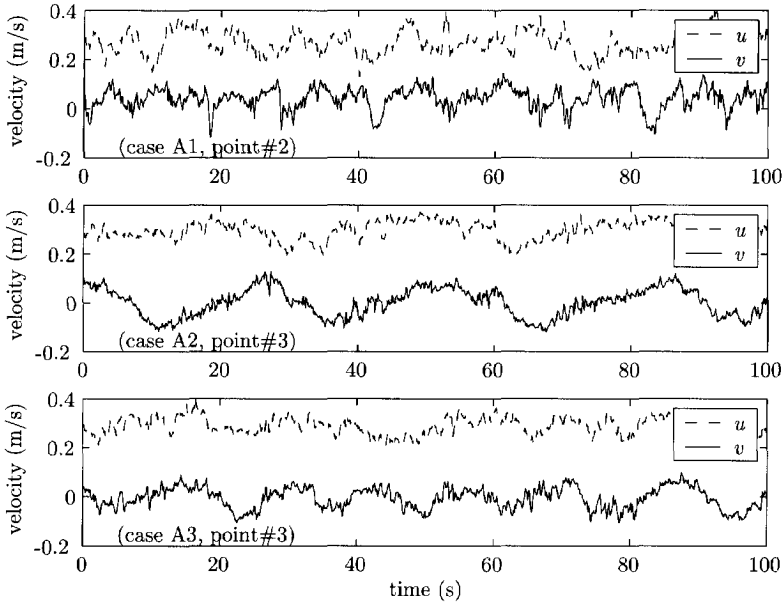


Figure 3.5: Sample time signals of the velocity records observed at section-A for cases (A1: emerged groynes), (A2 & A3: submerged groynes)

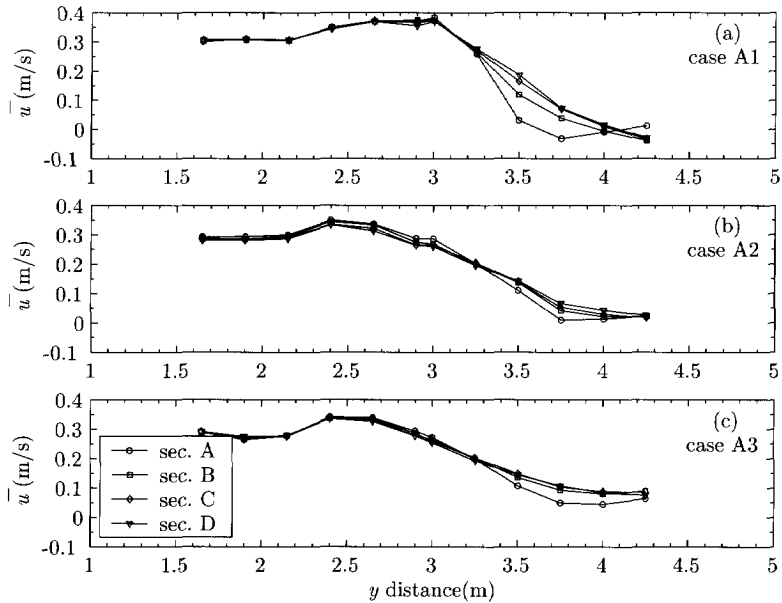


Figure 3.6: Velocity distribution in the transverse direction of ( $\bar{u}$ ), along sections A to D for cases (A1: emerged groynes), (A2 & A3: submerged groynes).

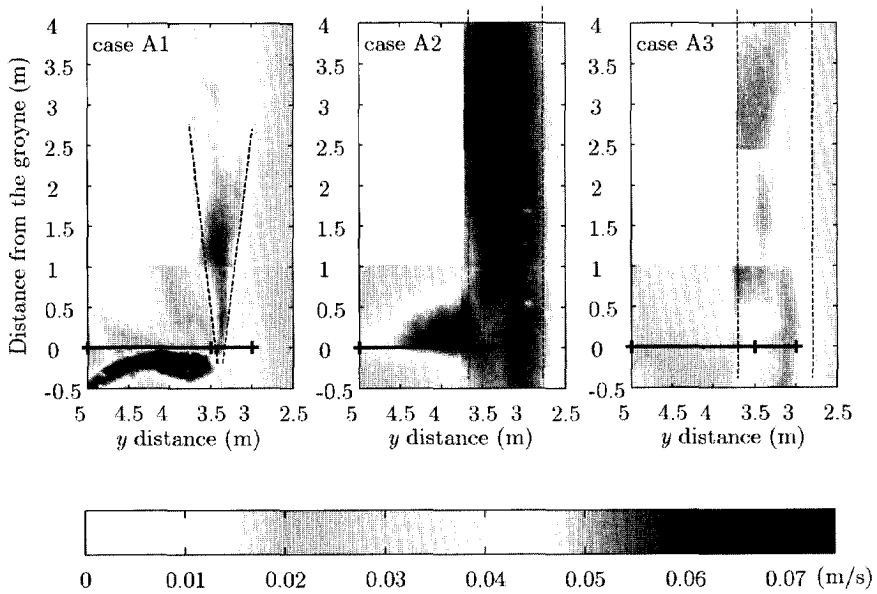


Figure 3.7: Total turbulence intensity  $\sqrt{u'^2+v'^2}$  extracted from PTV-data, for cases (A1: emerged groynes), (A2 & A3: submerged groynes); the solid line represents the crest of the groyne, dashed lines are imaginary lines for mixing layer shape.

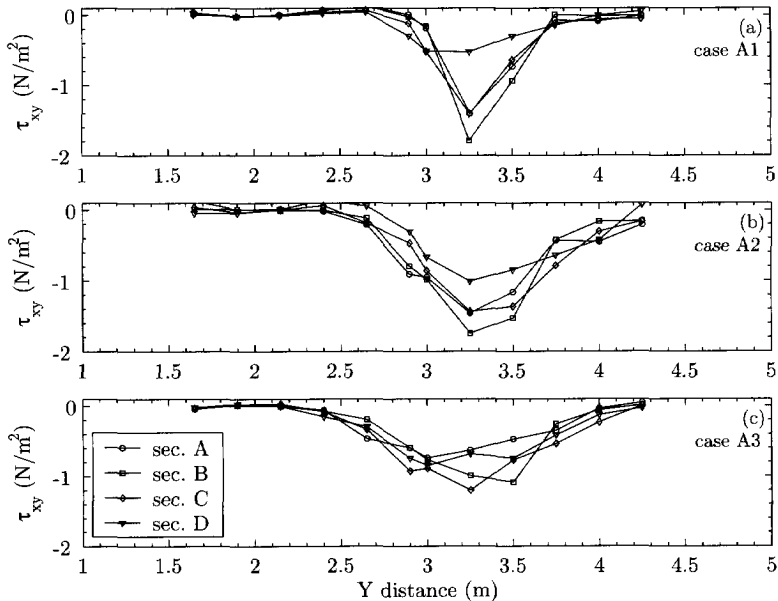


Figure 3.8: Transverse profiles of transverse shear stress  $\tau_{xy}$ , along sections A to D for cases (A1: emerged groynes), (A2 & A3: submerged groynes).

### 3.5.2 Emerged groynes

If the groynes are not submerged, the flow inside the groyne fields shows the circulation pattern as reported previously by Uijtewaal *et al.* (2001) for a similar aspect ratio (see Figure 3.9). This pattern is characterised by:

- a primary eddy that forms in the downstream part of the groyne field and covers nearly two thirds of its spacing; the velocity is usually about 30% to 40% of the main channel mean velocity.
- a secondary eddy driven by the primary one with an opposite sense of rotation and a much smaller flow velocity.
- a dynamic eddy that sheds regularly from the tip of the upstream groyne. This eddy migrates in downstream direction and merges with the primary one, which in return changes in size due to the interaction with the migrating eddy. After this eddy has travelled enough distance from the tip of the groyne, another eddy has room to form.

The whole circulation pattern is driven by the main stream via exchange of momentum through the interfacial mixing layer.

Figure 3.10, presents the autocorrelation functions of the transverse velocity for test case A1 (emerged groynes) measured at different locations. The large turbulence structures can be recognised through a correlation that extends over large time lags, the characteristic time of the modulation is related to the length-scale of the turbulent structure. Inside the groyne-fields (Figure 3.10a), we see the presence of positive and negative correlations at large time lags corresponding to large structures. Near the detachment point of the dynamic eddy (Figure 3.10b; section-A), we see a strong modulation with a shorter time span, corresponding to the dynamic eddy. At section-D, the autocorrelation shows the same characteristics as that inside the groyne field, implying that the same structure exists in these two points, evidently it is the primary eddy. In the main stream (see Figure 3.10d), the autocorrelations at large time lags are negligible. This suggests that only the small-scale turbulence structures corresponding to bottom-induced turbulence are present in the main stream far from the groynes.

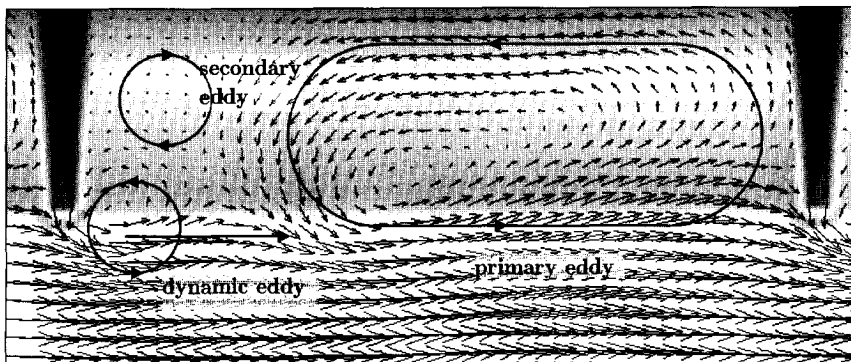


Figure 3.9: Flow pattern in a groyne field during emerged flow situation.

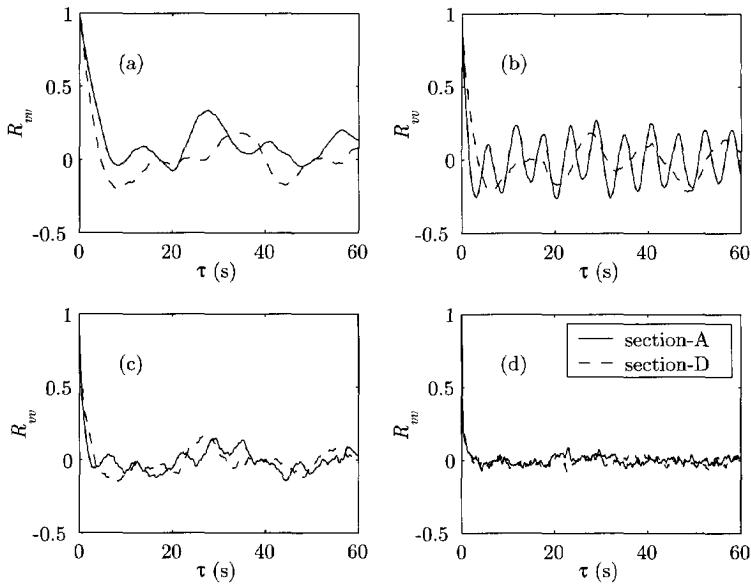


Figure 3.10: Autocorrelation functions of transverse velocity fluctuations ( $v'$ ) at sections A&D (case A1: emerged groynes); (a) point #1 inside the groyne field, (b) point #2, (c) point #3, (d) point #4 in the main channel.

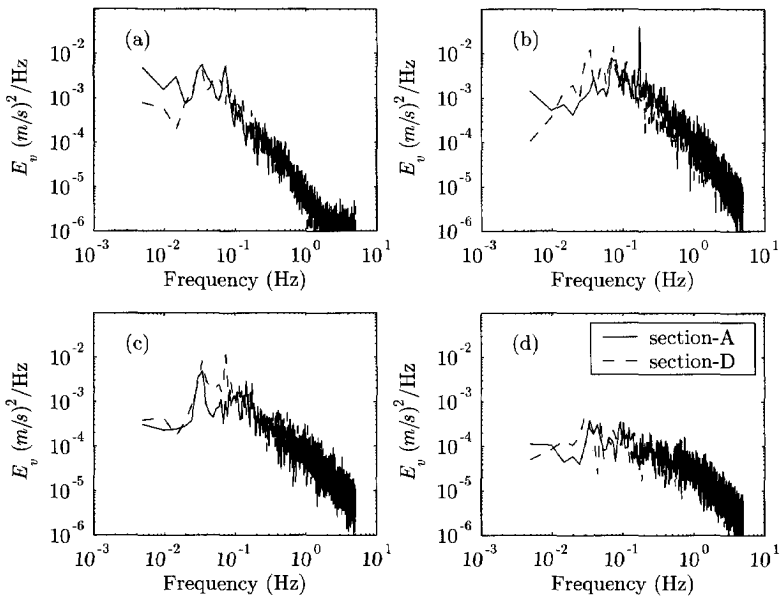


Figure 3.11: Energy density spectra of transverse velocity fluctuations ( $v'$ ) at sections A&D (case A1: emerged groynes); (a) point #1 inside the groyne field, (b) point #2, (c) point #3, (d) point #4 in the main channel.



Unlike a free mixing, which is characterised by a single dominant peak in the energy density spectrum (at a given location), the mixing layer due to a series of groynes contains more peaks. It consists of a number of frequencies superimposed on each other, due to the interaction between the shedding eddies from the groyne tips and the ones migrating from the upstream groynes, see Figure 3.11a,b,c. The same may be inferred from the autocorrelations presented in Figure 3.10a,b,c.

Inside the groyne fields (Figure 3.11a), two peaks can be observed in the energy density spectrum at section A. The peak at the higher frequency has faded away in section-D, where the lower frequency dominates. This can be interpreted as an increase of the length-scale of the eddy from section-A to section-D. The existence of the two peaks is due to the slow interaction between the primary and the secondary recirculation eddies.

In the point near the centre of the mixing layer (point #2), it can be seen from Figure 3.11b that near the groyne tip at section-A, in addition to the two peaks that are present at point #1, another sharp peak at a higher frequency is found. The presence of this peak is due to the dynamic eddy that sheds from the tip of the groyne at a high frequency; it appears only near the tip of the groyne and not at section-D. The same pattern can also be inferred from the autocorrelations presented in Figure 3.10b. The effect of the groynes further upstream is visible in the presence of the low-frequency peaks at section-A.

Point #3 at section-A is located just outside the mixing layer near the groyne, but still within the mixing layer of the upstream groyne. The energy density spectra at that point (Figure 3.11c) show the existence of only a low-frequency peak with a relatively low energy content at section-A, due to the mixing layer of the upstream groyne. At section-D, two peaks can be observed; the higher-frequency peak is due to the mixing layer that forms because of the nearby groyne and the low-frequency peak is due to the interaction with the migrating eddy from the upstream groyne. In the main stream (point #4), the large structures nearly disappear and only small-scale turbulence can be observed (see Figure 3.10d, and Figure 3.11d).

### 3.5.3 Submerged groynes

When the groynes are submerged, the flow in the groyne fields region does not show the circulation pattern as observed in the emerged condition, yet it can be characterised as a low-velocity region. The momentum transfer by the water flowing over the groynes is sufficient to balance the momentum transfer through the mixing layer, that otherwise would have caused a recirculating flow. It should also be noted that, as the groynes are submerged, the flow over the groynes hinders the horizontal recirculation, causing it to disappear beyond a relatively low submergence level. Generally speaking, the flow pattern in the submerged stage shows an alternate accelerating and decelerating pattern between flow over and around the groynes.

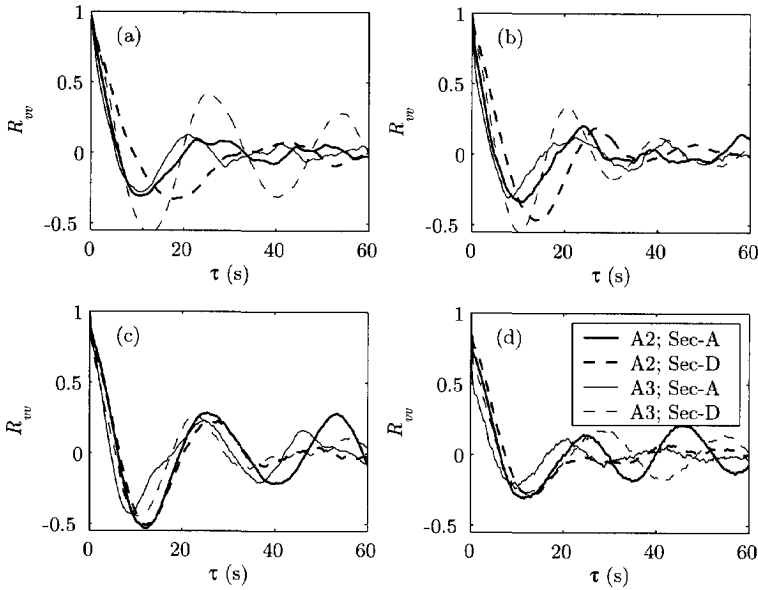


Figure 3.12: Autocorrelations function for velocity fluctuations in the transverse direction at sections A&D (cases A2, A3: submerged groynes); (a) point #1 inside the groyne field, (b) point #2, (c) point #3, (d) point #4 in the main channel.

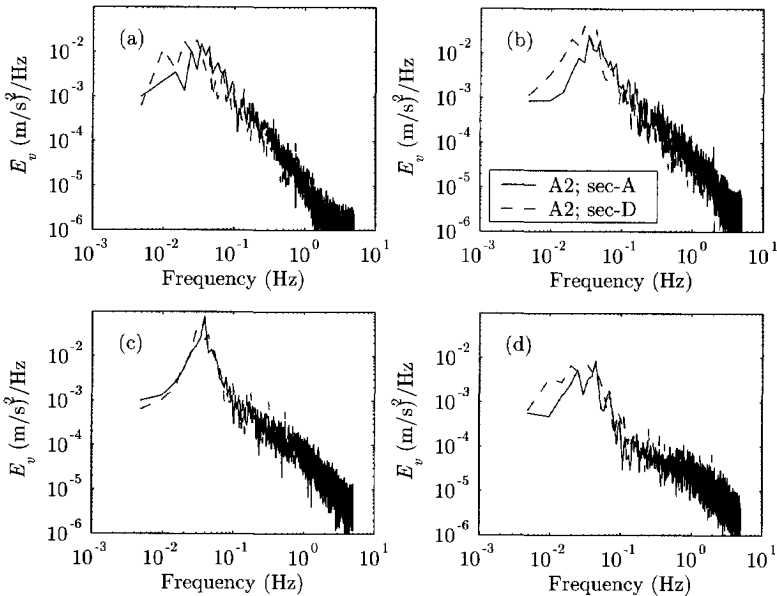


Figure 3.13: Energy density spectra at sections A, D (cases A2: submerged groynes); (a) point #1 inside the groyne field, (b) point #2, (c) point #3, (d) point #4 in the main channel.

It is obvious from Figure 3.12 that the turbulence characteristics in the submerged condition are different from the emerged condition. There is a very slow periodical behaviour with a time scale of around 25 seconds, which is present in all locations, see Figure 3.12a-d. This suggests a phenomenon that occupies the whole length of the groyne field. Yet, this phenomenon does not seem to have a free-surface signature, since no significant free-surface waves were observed.

The energy density spectra presented in Figure 3.13 shows a distinct single peak at a similar frequency for both sections-A and D, which means that the same fluctuation is present throughout the groyne field. From Figure 3.13d, one can observe the existence of large structures at point #4 far into the main stream. This means that for the submerged case the mixing region extends further into the main channel than in the emerged case.

### 3.6 EFFECT OF THE SUBMERGENCE LEVEL\*

With reference to the experiment series-S, the transverse velocity profile for different submerged flow conditions was measured. The measurements were chosen to take place along section-C to ensure that the upstream groyne is not affecting the velocity profile, in accordance with the findings from the Series-A as in Figure 3.6.

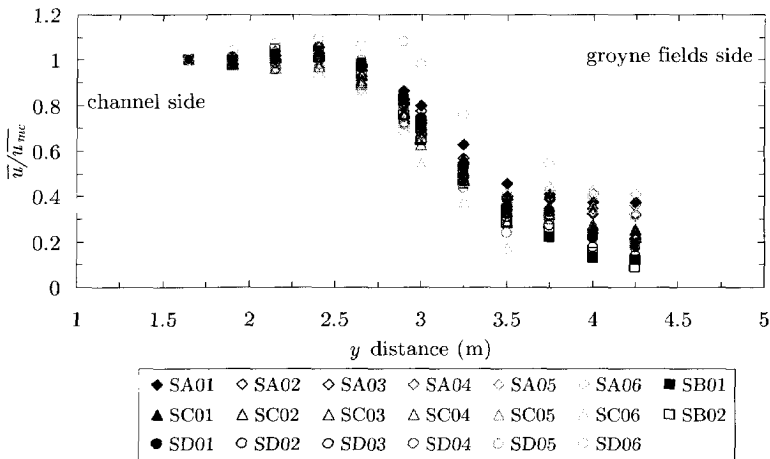


Figure 3.14: Transverse velocity profile for all test cases of series-S; velocities are normalised by the main channel velocity ( $\bar{u}_{mc}$ ).

\* Excerpts from this Section were published as: YOSSEF, M. F. M. (2004). "The effect of the submergence level on the resistance of groynes - an experimental investigation" In: *Advances in Hydro-science and -Engineering, Proc. of the 6<sup>th</sup> Int. Conf. on Hydro-science and -Engineering CD-ROM*, Brisbane, Australia.

Figure 3.14, shows that, although the mixing layer width is relatively constant in all cases, the mean velocity in the groyne region ( $u_{gr}$ ) varies between 10 and 40% of the main channel velocity ( $u_{mc}$ ). This variation is thought to be due to the different resistance that the groyne pose to the flow at different submergence ratios.

In literature, there are two ways of representing the groyne: as a submerged weir and as a large obstacle.

The first approach was used by Mosselman and Struiksmā, (1992); in this approach the discharge per unit width ( $q$ ) over a single groyne is represented in a weir form as follows:

$$q = \begin{cases} m_d \cdot (H_t - h_g) \cdot \sqrt{2g \cdot \Delta h} & \text{if } H_t > h_g \\ 0 & \text{otherwise} \end{cases} \quad (3.6)$$

where:

$m_d$  = discharge coefficient

$H_t$  = total water depth

$h_g$  = groyne height

$\Delta h$  = pressure drop over a groyne ( $\Delta h = S \cdot i$ ), in which  $S$  the spacing between two groyne and  $i$  the slope in the main channel region

It is assumed here that the losses in the groyne region are solely due to the groyne and the hydraulic gradient is zero between two successive groyne. This assumption could not be verified from the experiments, as no significant water level drop was observed over the groyne. Attempts have been made to measure  $\Delta h$  over a single groyne; yet, the low accuracy of the instruments made it impossible to obtain reliable readings with such a very small water level difference. Furthermore, it is assumed that the groyne-zone water level is equal to the main-channel water level immediately downstream of the groyne.

Using Eq. 3.6, it is possible to calculate the discharge coefficient ( $m_d$ ) for each test case. The calculated  $m_d$  in this approach was found to be more than unity in all test cases, which is in contradiction with the fact that the maximum value of  $m_d$  should not exceed unity for any type of weir. Therefore, the second approach is considered.

In this second approach, it is assumed that the resistance in the groyne region has two different sources: the bed resistance and the resistance due to the groyne. A formulation of the resistance of the groyne could follow the form of a drag resistance (see for example, Aya *et al.*, 1997). Accordingly, the momentum balance for a unit area in the groyne region away from the mixing layer can be written in the following form:

$$ghi = \underbrace{\frac{g}{C_{base}^2} u_{gr}^2}_{\text{bed resistance}} + \underbrace{\frac{1}{2} C_D \left( \frac{h_g}{S} \right) u_{gr}^2}_{\text{groyne resistance}} \quad (3.7)$$

where  $i$  is the local water surface slope,  $h$  is the local flow depth,  $C_{base}$  is the base Chézy coefficient in the main channel calculated as:  $C_{base} = 18 \log(12h/k_s)$ ,  $h_g$  is the groyne height,  $S$  is the spacing between two groyne and  $C_D$  is a representative drag coefficient for the groyne that accounts for the resistance of the groyne and is a function of both the hydraulic conditions and the blockage that a groyne poses to the flow.

Note that Eq. 3.7 can be rearranged to express the effective Chézy roughness coefficient ( $C_{effective}$ ), which is representative of the resistance in the groynes region, in terms of the base Chézy coefficient, drag coefficient of the groynes and the spacing between them. This definition takes the following form:

$$C_{effective} = \sqrt{\frac{1}{\frac{1}{C_{base}^2} + \frac{1}{2g} C_D \left(\frac{h_g}{S}\right)}} \quad (3.8)$$

It could be written as well in the following dimensionless form,

$$\frac{g}{C_{effective}^2} = \frac{g}{C_{base}^2} + \frac{1}{2} C_D \left(\frac{h_g}{S}\right)$$

Having measured the velocity and flow depth, and with the bed roughness height determined as mentioned before, it is possible to calculate the slope in the main channel for every test case. Assuming that the water surface slope in the groynes region is similar to that in the main channel, all parameters in Eq. 3.7 but  $C_D$  are known, whence  $C_D$  can be estimated for every test case. The result is plotted in Figure 3.15 showing the relation between the calculated  $C_D$  and the blockage ratio ( $h_g/H_i$ ).

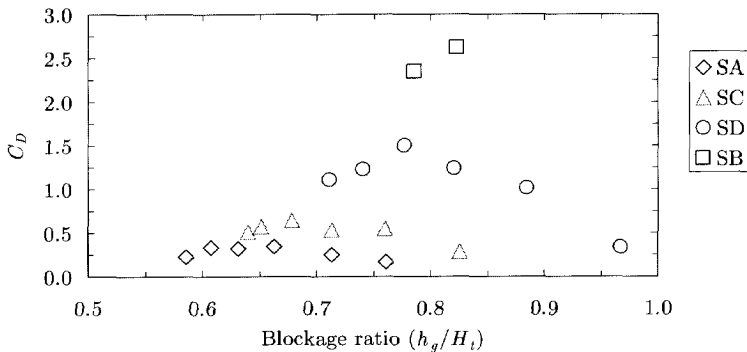


Figure 3.15: Relation between drag coefficient and submergence stage of a groyne, for all test cases of series-S; legend indicates the different test cases (see Table 3.2).

The plots shown in Figure 3.15 include the effect of the different hydraulic conditions in each test case. To eliminate this effect, the values of the estimated  $C_D$ , shown in Figure 3.15, are divided by ( $F_r^2$ ). The result is shown in Figure 3.16, from which it can be observed that the calculated ( $C_D/F_r^2$ ) exhibits an obvious increasing tendency against ( $h_g/H_i$ ); except for the point estimated from test case (SD06) which has a blockage ratio near unity.

Taking into consideration that the flow over a groyne can also be represented as flow over a weir, the relation between the resistance of a groyne and the blockage ratio would be better represented by a power relation of the form:

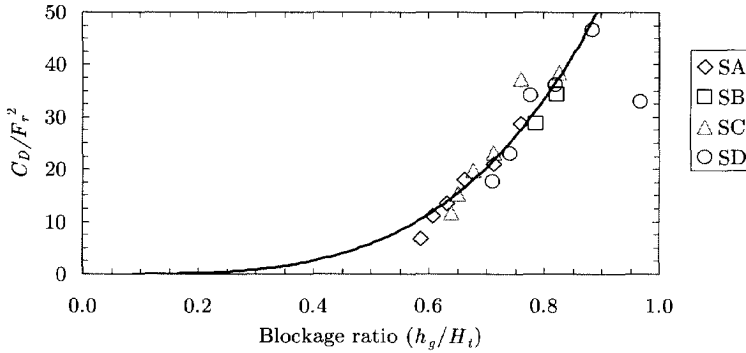


Figure 3.16: Relation between the blockage by a groyne and its drag coefficient normalised by  $F_r^2$ ; solid line is a data fit line for  $[y = a_1 x^{a_2}]$ , with  $a_1 = 76.4$ , and  $a_2 = 3.7$ ; legend indicates the different test cases (see Table 3.2).

$$\frac{C_D}{F_r^2} = a_1 \left( \frac{h_g}{H_t} \right)^{a_2} \quad (3.9)$$

where  $a_1$  and  $a_2$  are constants and  $F_r$  is calculated for the main channel region.

Having estimated the effect of groynes on the roughness in the groynes region for different blockage ratios, it is now possible to account for the effect of lowering the groyne on the effective roughness in the groynes region and further on the design flood level. This is going to be elaborated further in Section 5.4.1.

## 3.7 PARAMETERISATION OF THE FLOW NEAR GROYNES

### 3.7.1 Velocity fluctuations

In Section 3.5, attention was paid to the dynamics of the flow. It was shown that large-scale velocity fluctuations in both horizontal directions are present, and that the velocity shows a periodical behaviour. Modelling the velocity with a periodical function with prescribed amplitude, period and phase difference is a logical choice. The velocity signal associated with large-scale motion is therefore assumed to take the following form:

$$\begin{aligned} u &= \bar{u} + \hat{u} \cdot \sin(\omega \cdot t) \\ v &= \bar{v} + \hat{v} \cdot \sin(\omega \cdot t - \phi_0) \end{aligned} \quad (3.10)$$

– where:

- $\bar{u}, \bar{v}$  = time averaged velocity
- $\hat{u}, \hat{v}$  = amplitude of fluctuations
- $\omega$  = the peak frequency (rad/s);  $\omega = 2\pi/T_p$ , with  $T_p$  as the wave period

–  $\phi_0$  = phase difference between  $u$  and  $v$  in radians

The amplitude in this formulation has to comply with the turbulence intensity of the full signal. Applying the definition of turbulence intensity to a sine-function, we can write the amplitude as a function of the turbulence intensity, (substituting  $u'$  for  $\sqrt{u'^2}$  and  $v'$  for  $\sqrt{v'^2}$ ),

$$\hat{u} = \sqrt{2} u' \quad (3.11)$$

From the velocity measurements it was possible to quantify the turbulence intensities  $u'$ , and  $v'$  at different locations across the mixing layer. It should be mentioned here that the measured  $u'$  and  $v'$  represent all the velocity fluctuations i.e. the large-scale and the small-scale. However, an assessment of the contribution of the large-scale fluctuations to the total turbulence intensity is made by applying a low-pass filter to the original velocity signal. The turbulence intensity of the low-frequency side of the spectrum refers to the large-scale fluctuations. The cut-off frequency is chosen at 1.0 Hz, based on the assumption that the length-scale of the small-scale turbulence 'at most' equals the water depth. The results show that in the mixing layer the contribution of the small-scale turbulence fluctuations is not significant and the large-scale turbulence intensity is nearly equal to the total (Figure 3.17). Henceforth, the total turbulence intensity will therefore be used as an indication of the large-scale turbulence.

The large-scale velocity fluctuations are proportional to the velocity deficit across the mixing layer (see, for example, Uijttewaai and Booij, 2000; Van Prooijen, 2004), i.e. it is possible to write  $u'$  in the following form:

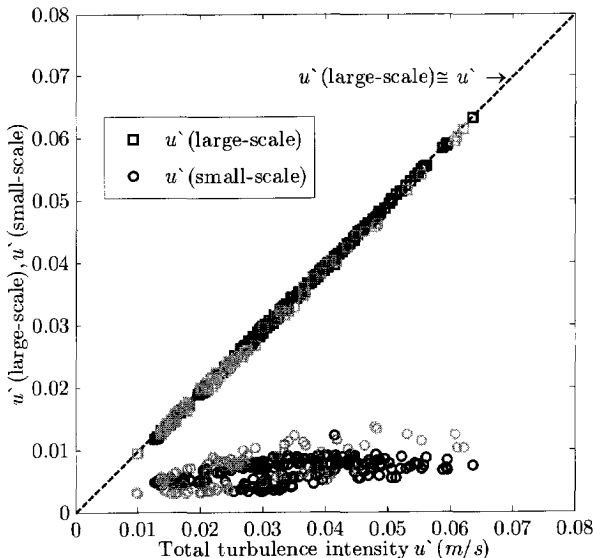


Figure 3.17: Comparison between the total turbulence intensity  $u'$  and the large-scale and small-scale turbulence intensities, separated at a cut-off frequency of 1.0 Hz.

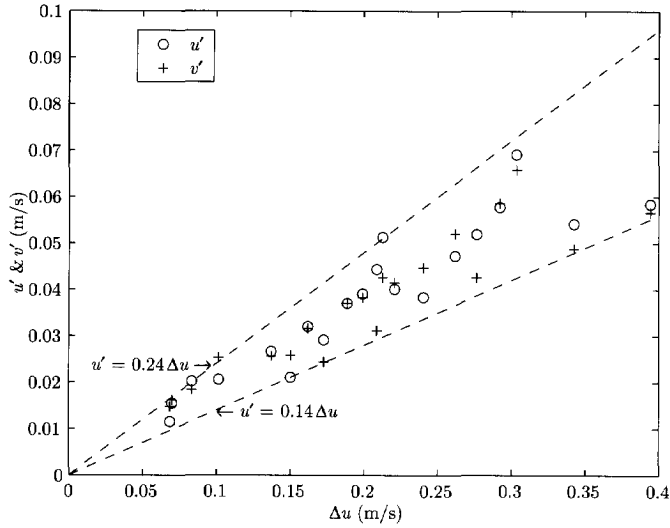


Figure 3.18: Relation between turbulence intensity  $u'$  at the centre of the mixing layer and the velocity deficit  $\Delta u$  for all test cases.

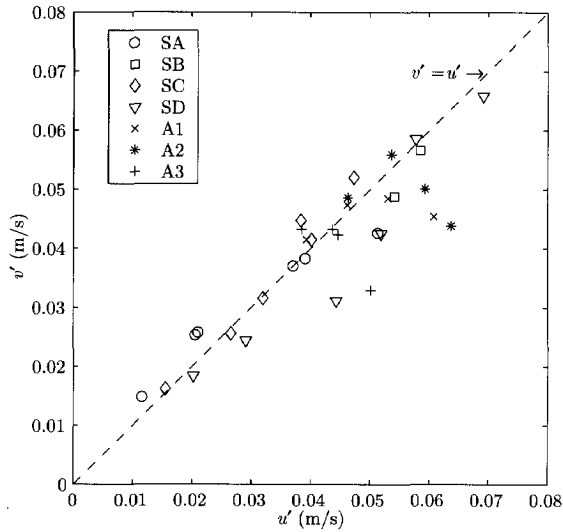


Figure 3.19: Relation between  $u'$  and  $v'$  in the centre of the mixing layer for all test cases.



$$\hat{u} = \beta_1 \cdot \Delta u \quad (3.12)$$

with  $\Delta u = u_{mc} - u_{gf}$ , and  $\beta_1$  is a constant.

The results of all experiments, as shown in Figure 3.18, indicate a value of  $\beta$  in the range of 0.14 to 0.24. The average value of  $\beta_1$  is about 0.18. Havinga (pers. comm., 2001) found a value of 0.14 for the mixing layer between the main channel and the floodplain in a straight compound channel without groynes.

Since the velocity fluctuations in the transverse direction,  $\hat{v}$ , are not by definition identical to those in the streamwise direction,  $\hat{u}$ , we attempt to describe the relation between  $\hat{v}$  and  $\hat{u}$  as:

$$\hat{v} = \beta_2 \cdot \hat{u} \quad (3.13)$$

with  $\beta_2$  as a constant.

The constant  $\beta_2$  is reported to be in the range between 0.5 and 1.0 for free mixing layers (Uijtewaal and Booij, 2000). Figure 3.19 shows that in the present case the constant  $\beta_2$  is rather close to unity. Hence, for simplicity the constant  $\beta_2$  is set to unity.

### 3.7.2 Mixing layer width

Due to the velocity difference between the main channel and the groynes region, a mixing layer develops along the interface between the two regions. The width of the mixing layer,  $\delta$ , can be defined as the width of the maximum slope in the lateral velocity profile (Uijtewaal and Booij, 2000), i.e.

$$\delta = \frac{\Delta u}{(du/dy)_{\max}} \quad (3.14)$$

From the velocity measurements, it is possible to estimate the maximum gradient and the velocity deficit, from which the mixing layer width can be calculated.  $\delta$  was found to be nearly constant at a value of  $1.0 \pm 0.1 m$  in all submerged flow cases. It may be significant to point out that, while  $\delta$  remained constant, the maximum velocity gradient was getting steeper with increasing  $\Delta u$ .

On the basis of this observation, one may assume that the mixing layer width is primarily related to the geometry of the groynes, but this needs further confirmation. From the results of the full test programme (Berg and Uijtewaal, 2002), a wider mixing layer was observed for more mildly sloping groynes. Hence, we may assume that  $\delta$  is related to the length of the groyne side slope:

$$\delta = \beta_3 m_1 h_g \quad (3.15)$$

where  $m_1$  is the groyne side slope, and  $\beta_3$  is a constant, according to the experiment, has an average value of 1.25.

### 3.7.3 Flow periodicity

The Strouhal Number is a dimensionless parameter that is useful for analysing oscillating flow problems. The Strouhal Number ( $St$ ) can be expressed as:

$$St = f_r \frac{\mathcal{L}}{\mathcal{U}} \quad (3.16)$$

where

$$\begin{aligned} f_r &= \text{dominant frequency} \\ \mathcal{L} &= \text{length-scale,} \\ \mathcal{U} &= \text{velocity-scale, } \mathcal{U} = 0.5(u_{mc} + u_{gf}) \end{aligned}$$

A distinct peak was observed in the energy density spectra of the velocity signals. We attempt here to describe the observed periodicity ( $T_p = 1/f_r$ ), in terms of the mixing layer width as a characteristic length-scale ( $\mathcal{L} = \delta$ ), and the average advection velocity as a characteristic velocity-scale ( $\mathcal{U} = 0.5(u_{mc} + u_{gf})$ ), i.e. we will write  $T_p$  in the following form:

$$T_p = \frac{1}{St} \frac{\delta}{0.5(u_{mc} + u_{gf})} \quad (3.17)$$

with  $St$  as a constant that we can estimate by analysing the results of the experiments.  $St$  was found to be in the range from 0.12 to 0.18, compared to a value of 0.20 in the case of vortex shedding from a circular obstacle in a fully turbulent flow (see for example Chen and Jirka, 1995).

### 3.7.4 Coherence

In order to assess whether the large turbulence structures in the case of the submerged groynes are transferring momentum across the mixing layer, cross-spectra have been calculated using  $u'$  and  $v'$  data measured at some points across the mixing layer. In addition to the amplitude of the energy density spectra for the different frequency components, the phase relation between  $u'$  and  $v'$  has been obtained.

Figure 3.20 shows an example from a point near the centre of the mixing layer, in which we can observe that the peak of the cross energy spectrum between  $u'$  and  $v'$  has its maximum at the same frequency for  $u'$  and  $v'$ ; this implies that there is a significant momentum transfer at this frequency. The phase relation shows that the phase difference between  $u'$  and  $v'$  equals zero in the low frequency side, whereas at the higher frequencies, the phase angles are distributed randomly. The point beyond which the phase relation becomes random is related to the transition to the high-frequency side of the peak. The phase difference at the frequency of the peak equals zero, which indicates that the fluctuating components are in phase; this means that the mass transfer is maximal.

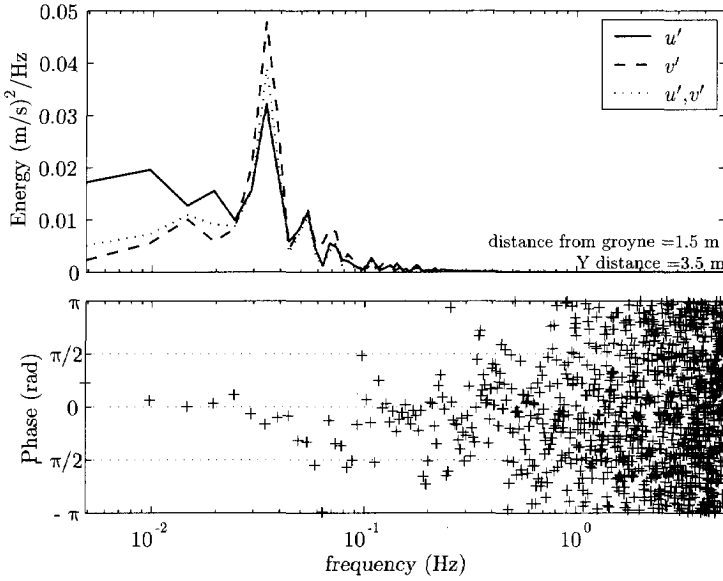


Figure 3.20: Cross-energy spectra (upper panel) for velocity fluctuations and phase relation (bottom panel) for  $u'$  and  $v'$  components ( $u',v'$  is the cross-spectra); near the centre of the mixing layer.

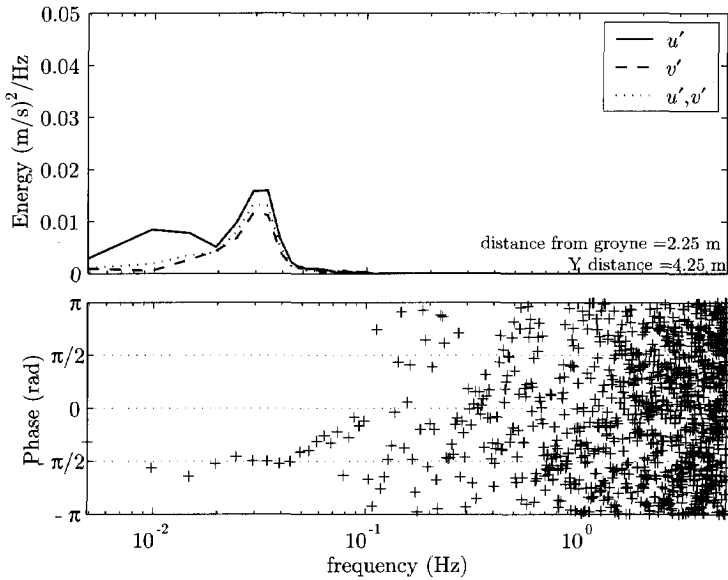


Figure 3.21: Cross-energy spectra (upper panel) for velocity fluctuations and phase relation (bottom panel) for  $u'$  and  $v'$  components at a point on the boundary of the mixing layer inside the groyne fields ( $u',v'$  is the cross-spectra).

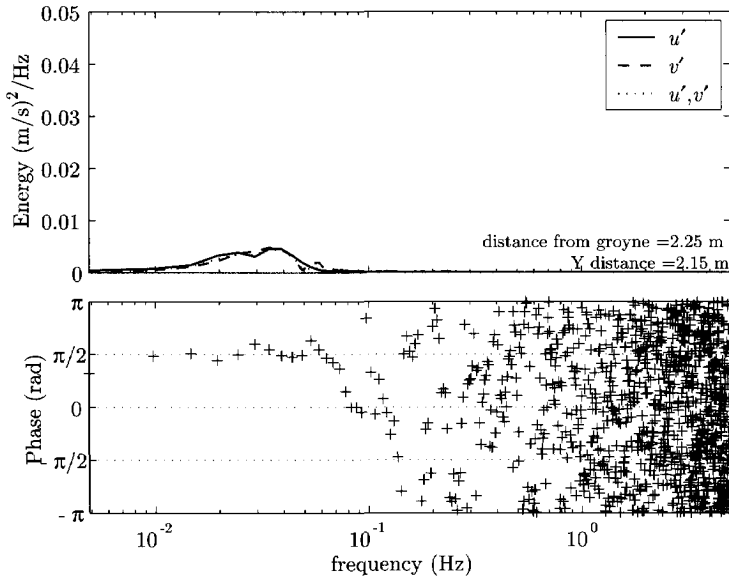


Figure 3.22: Cross-energy spectra (upper panel) for velocity fluctuations and phase relation (bottom panel) for  $u'$  and  $v'$  components at a point on the boundary of the mixing layer from the main channel side ( $u'$ ,  $v'$  is the cross-spectra).

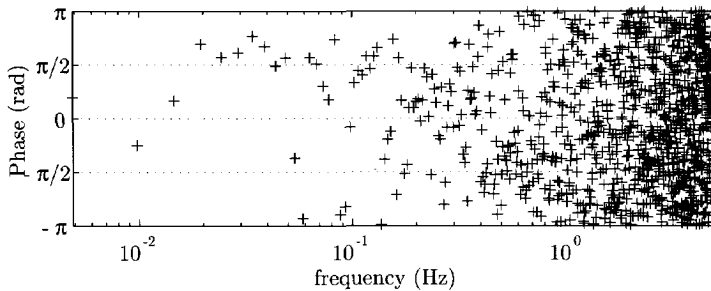


Figure 3.23: Example of a random phase relation between  $u'$  and  $v'$  outside the mixing layer.

In the points at the boundaries of the mixing layer, the peak amplitude is much smaller than in the centre. Still, we can observe that the peak of the cross spectrum has its maximum at the same frequency for  $u'$  and  $v'$ . However, the phase relations at these points show that the phase difference between  $u'$  and  $v'$  equals  $-\pi/2$  for a point on the boundary of the mixing layer from the groyne fields' side (see Figure 3.22), and equals  $\pi/2$  for a point on the main channel side (Figure 3.23). This means that the mass transfer in these regions is minimal. For comparison, the phase relation outside the mixing layer is depicted in Figure 3.23, where the phase relation is random for all frequencies.

### 3.8 SUMMARY AND CONCLUSIONS

This chapter concerns the results of the velocity measurements in a fixed-bed model that is representative of a river with groynes with typical dimensions as found in the Dutch River Waal. The effect of the flow stage was studied by changing the flow depth.

The measurements provide insight into;

- the flow pattern in the vicinity of groynes,
- the shape and the extent of the mixing layer during the different flow stages,
- the dynamic behaviour of the velocity along the mixing layer between the main channel and the groyne fields,
- and the effect of the submergence ratio on the effective resistance in the groynes region

Firstly, when the groynes are not submerged, the flow inside the groyne fields can be characterised by a primary eddy that forms in the downstream part of the groyne field, a secondary eddy driven by the primary one with an opposite sense of rotation, and a dynamic eddy that frequently sheds from the tip of the upstream groyne. The whole circulation is driven by the main stream via exchange of momentum through the interfacial mixing layer.

In the submerged stage, the flow in the groyne fields region does not show the circulation pattern as observed in the emerged condition, yet it can be characterised as a low velocity region that shows an alternate accelerating and decelerating pattern between flow over and around the groynes.

Secondly, the mixing layer between the main channel and the groyne fields differs in nature between the emerged and submerged flow stages. In the emerged situation, it originates from the tip of the groyne and grows in width towards the next groyne downstream. In the submerged situation, it has a rather constant width. This constant width is due to the continuous generation of turbulence by the successive groynes, which retain the total turbulence intensity (Figure 3.7) and the transverse shear stress (Figure 3.8), at high level.

Thirdly, from the observations on the dynamics of the flow we can conclude that,

- large-scale velocity fluctuations are found in all test cases,
- time scales vary with the flow stage and the location within the groyne field;
- the submerged cases show a different turbulence pattern from the emerged case. The point with the highest turbulence energy content moves from the normal line (point#2) in the emerged condition to a point further in the main channel (point#3) when the groynes are submerged, and
- the large-scale velocity fluctuations  $u'$  &  $v'$ , are nearly in phase in the centre of the mixing layer (Figure 3.20), and they have a phase difference of  $\pm\pi/2$  for the points on the boundaries of the mixing layer (Figures 3.21 and 3.22). For the points far from the mixing layer, there is a random phase relation between  $u'$  and  $v'$  (Figure 3.23).

Finally, from the analysis of the effect of submergence, it was possible to establish a relation between the blockage by a groyne and its drag coefficient. This relation led to an

expression of an effective Chézy coefficient that is representative of the resistance in the groynes region (Eq. 3.8). Such an expression allows for estimating the conveyance capacity of the groynes region and hence the effect of lowering the groynes.

In order to estimate the conveyance capacity of the groynes region, two methods were considered to represent the groynes. The first used a weir-formulation and the second used a drag-formulation. The difference between the two approaches lies in assuming in the former case that the water surface slope is zero (horizontal surface) between the groynes and that in the latter case it is equal to the water surface slope in the main channel. Besides, in the case of a weir-formulation, by definition, the flow control-section lies on top of the groynes, whereas it lies between the groynes in the latter case. Having the flow control-section on top of the groynes makes the estimate of the discharge capacity of the groynes region sensitive to changes in the crest level of the groynes. Using a drag-formulation, on the other hand, reduces the sensitivity of the conveyance capacity of the groynes region to the exact height of the groynes. Since the flow control-section in this case is not affected by changes in the groyne, only the drag coefficient in this case is a function of the groyne geometry. Moreover, due to the momentum exchange along the normal line, the slope in the groynes region is more likely to be similar to that in the main channel. Thus, a drag-formulation seems preferable.

Note that both methods of representing the groynes (weir or large obstacle) could be calibrated to reproduce a given situation. However, when attempting to evaluate the effect of changing the geometry of the groynes, they will deviate from one another. In general, a weir representation will yield a more pronounced effect than a drag formulation.

The aforementioned observations have the following consequences for the modelling procedures in the case of a river with groynes:

- It is important to use a model that has the capacity to resolve large time dependent turbulence structures, for example by large eddy simulation.
- The choice of a representative time for transport computations should cover the large-scale structures. A single or an average flow field would not necessarily yield the same result as a long time sequence. The accuracy of the transport model is expected to increase if it covers a long time sequence, but, on the other hand, the computation time will also increase.
- Both the magnitude and the direction of the sediment transport are expected to depend on the large-scale motion. The sediment transport rate is proportional to the velocity to a certain power (3-5). The transport direction will be strongly affected by the contribution of the fluctuating lateral velocity component that has a mean value zero, but a relatively large amplitude.
- When schematising the river with groynes in a one-dimensional model, the groynes section must have an equivalent roughness coefficient that is a function of both the blockage ratio and the Froude number. Consequently, if the groynes are lowered, the effective roughness in the groynes region will be reduced.

## Chapter 4

### MOBILE-BED FLUME EXPERIMENT\*

#### 4.1 INTRODUCTION

The sediment balance for the Waal River during the last three decades and particularly during the high water period of 1995, as estimated by Ten Brinke *et al.* (2001), emphasises the role that groyne fields play in the total sediment balance of the river. With our present modelling capabilities, we are unable to include this role in large-scale morphological predictions (see Mosselman and Struiksmā, 1992; Jesse and Kroekenstoel, 2001). In fact, even on the small-scale level the groyne fields sedimentation/erosion is not reproduced adequately (see Yossef and Klaassen, 2002; Rupprecht, 2004). This is due to a gap in our knowledge concerning the sediment exchange process between the groyne fields and the main channel. To include the contribution of the groyne fields in the overall sediment balance of the river we need to further understand the sediment exchange processes. To that end, mobile-bed experiments were carried out.

The primary objective of the experiments presented in this chapter is to investigate the role of the groyne fields in the river's total sediment balance. Moreover, they are to provide insight into the mechanisms governing the sediment exchange between the main channel and the groyne fields. With the knowledge gained, we hope to answer the following questions:

- What is the sediment budget of the groyne fields during different flow conditions?
- Moreover, what is the effect of lowering the crest level of the groynes on this sediment budget?

Furthermore, we will attempt to establish a relation between the discharge stage, represented by the submergence level of the groynes, and the erosion/deposition.

The analysis of the formation and development of local scour around the groynes is not a primary objective.

---

\* Excerpts from this chapter were published as: YOSSEF, M. F. M., and DE VRIEND, H. J. (2004). "Mobile-bed experiments on the exchange of sediment between main channel and groyne fields" *In: River Flow 2004 - Proc. of the 2nd Int. Conf. on Fluvial Hydraulics*, Naples, Italy, 127-133.

Firstly, Section 4.2 presents the experimental design, conditions, instrumentation, and the measurements procedures. Secondly, Section 4.3 presents the results of the velocity measurements, suspended sediment concentrations, bedforms movements, and bed levels. We end this chapter with a discussion in Section 4.4 and a summary and conclusions in Section 4.5.

## 4.2 EXPERIMENTAL SETUP

### 4.2.1 Model design

For a proper scaling of the experiment, some dimensionless aspects are of particular importance to guarantee a proper representation of the flow characteristics. For example:

- the spacing to length ratio,  $(S/L)$ , which governs the flow pattern in the horizontal plane.
- the spacing to height ratio,  $(S/h_g)$ , which governs the flow pattern in the vertical plane.
- the side slopes of the groynes, which govern the flow pattern in the vertical plane and the vortex formation.

#### Spacing–length ratio $(S/L)$

The  $(S/L)$  ratio determines the number and shape of the horizontal eddies that form along the normal line and inside the groyne fields (Uijtewaal, 1999). An aspect ratio close to unity gives rise to a single eddy. A larger aspect ratio, i.e. between 2 and 4, gives room for two eddies: a large one called primary eddy that forms in the downstream part of the groyne-field, and a smaller secondary eddy emerging intermittently near the upstream groyne. An extremely long groyne-field leads to the penetration of the main flow into the groyne-field. In the River Waal, the  $(S/L)$  ratio is about 3. This means that the dimensions of the experiment should be in the range of  $(S/L = 2 \text{ to } 4)$ . Considering the available space in the laboratory, a value of  $S/L = 3.1$  has been chosen.

#### Spacing–height ratio $(S/h_g)$

As the  $(S/L)$  ratio controls the flow pattern in the horizontal plane, the  $(S/h_g)$  ratio governs the flow pattern in the vertical plane. If the groynes are spaced far apart, the flow that separates from the upstream groyne reattaches to the bed. Too close groynes will prevent the flow reattachment to the bed, thus keeping the bed shear stress low (Peng *et al.*, 1997). A reasonable estimate of the extension of the separation zone at the lee-side of a groyne can be deduced from the case of a backward-facing step. For turbulent flow with high Reynolds number, the separation region extends  $(7 \pm 0.5)$  times the step height, (see for example Kim, 1978; Nakagawa and Nezu, 1987).

In the River Waal  $S/h_g \cong 28$ , i.e. the flow reattachment to the bed takes place. This condition should be guaranteed in the experiment. To guarantee the flow reattachment to the bed,  $(S/h_g)$  should not be less than 7.5, and preferably be equal to 28, so as to fully



represent the prototype situation. However, the space available in the laboratory prevented such a large ( $S/h_g$ ) ratio. Three values of  $S/h_g$  were tested; they were  $S/h_g = 16$ , 20, and 26.5, respectively.

### Side slopes

In a flume test, it is much more handy to use vertical groynes rather than sloped-face groynes. Nevertheless, Lauchlan (2004) reports a significant difference between the sediment transport over a vertical weir and over a sloped weir, a situation that is to some extent similar to the transport over a groyne. In addition, the dynamics of the flow and the strength of the eddies detaching from the tip of the groynes strongly depend on the slope (Uijttewaal *et al.*, 2002). In prototype groyne slopes are typically 1:3 (vertical to horizontal). A 1:3 groyne slope is therefore more representative of reality.

### Dimensions

A physical scale model was built in the Laboratory for Fluid Mechanics of Delft University of Technology. The dimensions of the model were based on those of the River Waal (see Section 2.3.2) and tuned to the space available in the laboratory. The model consisted of a schematised straight river reach, with a geometrical undistorted scale of 1:100 with respect to the Waal River. The working length of the model measured 26.85 m, and the width of the model was 2.0 m. In the lateral direction, the model represented half of the river width with groynes at one side (see Figure 4.1).

The model included nine identical groynes (Figure 3.1). The first one was positioned 6.0 m from the model entrance following three wooden pseudo groynes that were meant to let the inflow of water and sand adapt before reaching the first groyne. The groynes were equally spaced 2.0 m from each other, they had a crest length  $L = 0.65$  m, a crest height of 0.25 m measured from the concrete bottom of the flume, and side slopes of 1:3 in all directions. The model dimensions are summarised in Table 4.1 (see also Figure 3.1 and Figure 3.2).

Table 4.1: Summary of the dimensions for the proposed experiments

Parameter	dimension	unit	
Groyne height ( $H_g$ )	0.25	m	measured from the concrete bottom
Groyne length ( $L$ )	0.65	m	crest length
Groynes spacing ( $S$ )	2.00	m	distance between crests
Spacing to length ratio ( $S/L$ )	3.08	---	
Spacing to height ratio ( $S/h_g$ )	16-27	---	function of sand layer thickness

$h_g = H_g$  - thickness of sand layer

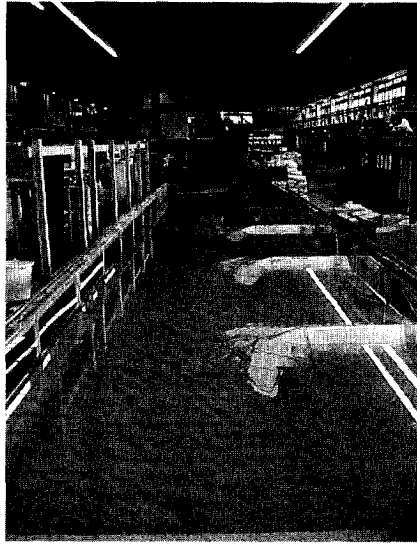


Figure 4.1: Picture of the flume looking upstream.

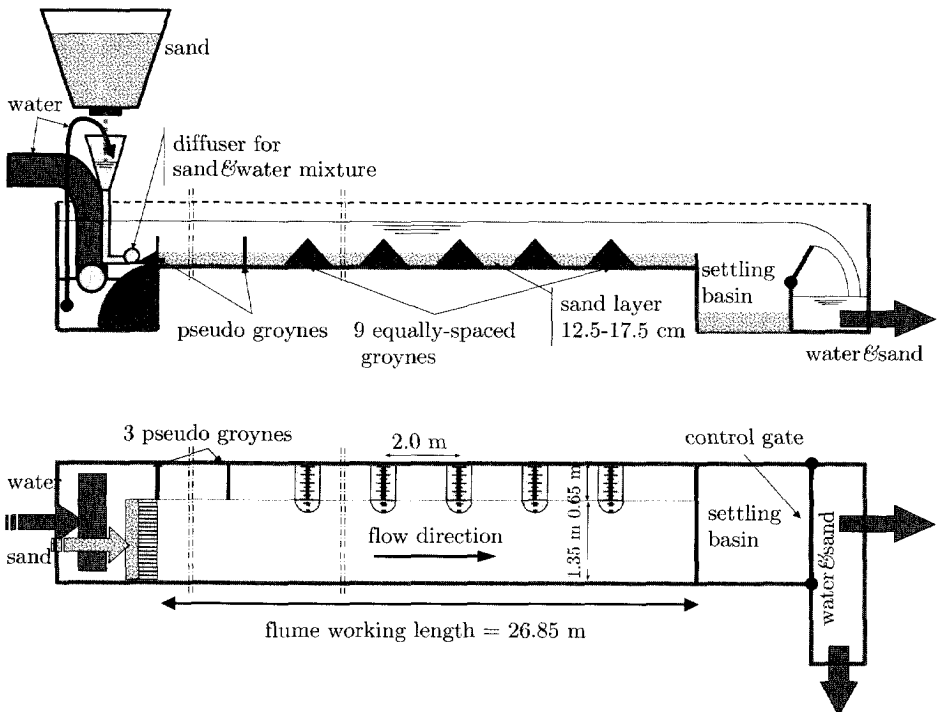


Figure 4.2: Schematic drawing for the experimental set-up; upper panel is a side view, lower panel is a top view (drawing is not to scale).

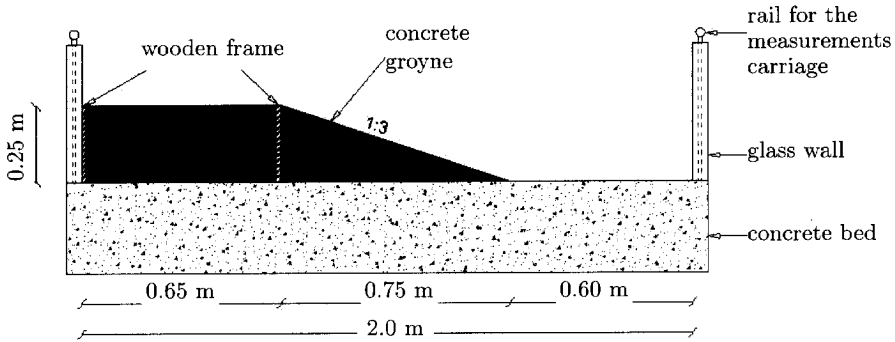


Figure 4.3: Cross-section view through a groyne; empty flume.

### 4.2.2 Experimental conditions

The hydraulic and sediment transport conditions were set to ensure that both bed-load and suspended-load transport take place in all test cases; see Yossef (2003) for further details.

Different conditions were tested by changing both the flow depth and the crest level of the groynes. The crest level was controlled by changing the reference level via the thickness of the sand layer in the whole flume. In this way, it was possible to test three different crest levels (cases G1, G2, and G3). For each of them, four different submergence levels were tested. The submergence ratio ( $h/h_g$ ) ranged from 1.0 (marginally emerged groynes) to 2.0 (submerged groynes), where  $h$  is the water depth and  $h_g$  is the groyne height measured from the sand bed.

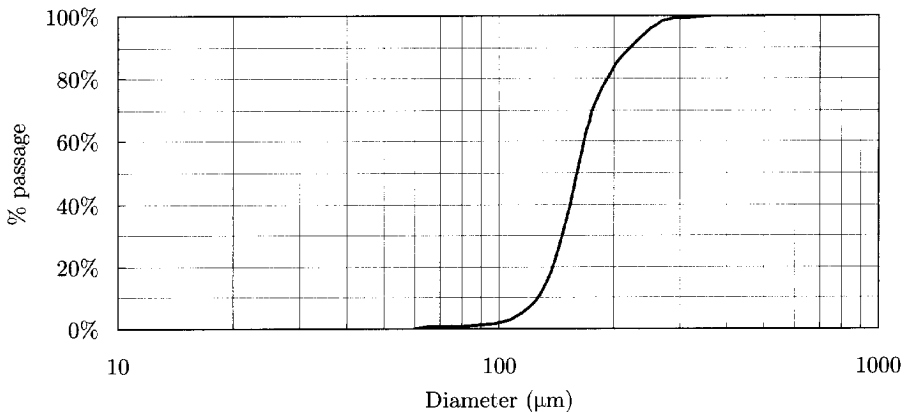


Figure 4.4: Particle size distribution curve.

Nearly-uniform quartz sand was used in all tests; the particle size distribution is shown in Figure 4.4. The sand had a median grain size  $D_{50} = 0.164$  mm, and a geometric standard deviation  $\sigma_g = 1.23$ . The thickness of the sand layer varied from 0.125 m (case G1) to 0.175 m (case G3).

For all test cases, the particle mobility parameter (Sheilds parameter)  $\theta$  (Eq. 4.1) was set at a value of 0.23, and the suspension number  $Z$  (Eq.4.2), at a value of 1.87 to guarantee a suspended sediment profile over the whole water column.

$$\theta = \frac{u^2}{C^2 \Delta D_{50}} \quad (4.1)$$

$$Z = \frac{w_s}{\beta \kappa u_*} \quad (4.2)$$

where

$C$  = Chézy coefficient.

$\Delta$  = relative specific weight of the sediment under water; for quartz sand,  $\Delta = 1.65$ .

$w_s$  = particle fall velocity; for  $D_{50} = 0.164$  mm,  $w_s = 0.019$  m/s.

$\kappa$  = von Kármán constant;  $\kappa = 0.4$ .

$\beta$  = factor  $\geq 1.0$ , ( $\beta = 1$  was used).

The hydraulic conditions were chosen to fulfil the sediment transport requirements of constant mobility and suspension in all test cases. In all the test cases, the Froude number ( $Fr$ ) was small enough to ensure sub-critical flow (maximum = 0.28), and the Reynolds number ( $Re$ ) was high enough to ensure fully developed turbulent flow in both the main channel region ( $Re_c \cong 1.8 \times 10^4$ ) and the groyne fields region ( $Re_c \cong 0.5 \times 10^4$ ). Table 4.2 contains a detailed description of the test programme undertaken, including the hydraulic and sediment transport conditions for each case.

Table 4.2: Experimental programme including test conditions

Test name	$h_g$ [m]	$h/h_g$ [-]	$h$ [m]	$\bar{u}_{mc}$ [m/s]	$Q_w$ [m <sup>3</sup> /s]	$Q_s$ [kg/hr]	$Re$ [-]	$Fr$ [-]
G1i		1*	0.125	0.277	0.058	29.03	11 250	0.27
G1a	0.125	1.4	0.175	0.298	0.088	33.54	15 626	0.23
G1b		1.7	0.213	0.310	0.111	36.29	19 737	0.21
G1c		2.0	0.250	0.320	0.134	38.67	23 970	0.20
G2i		1*	0.100	0.263	0.044	26.22	7 895	0.27
G2a	0.100	1.4	0.140	0.284	0.067	30.51	11 924	0.24
G2b		1.7	0.170	0.296	0.085	33.14	15 089	0.23
G2c		2.0	0.200	0.306	0.103	35.42	18 352	0.22
G3i		1*	0.750	0.245	0.031	22.81	5 523	0.29
G3a	0.750	1.4	0.105	0.266	0.047	26.82	8 385	0.26
G3b		1.7	0.128	0.278	0.060	29.29	10 639	0.25
G3c		2.0	0.150	0.288	0.073	31.43	12 967	0.24

\* Emerged groynes

### 4.2.3 Model operation

Water was supplied to the flume through an inflow pipe connected to a diffuser that discharges into the upstream distribution basin (Figure 4.5). The discharge adjustment and daily operation were controlled via two separate valves mounted on the supply pipe; an upstream valve that was used to adjust the test discharge and a downstream one that was used for daily operation. At the downstream side of the flume, water was discharged through the settling basin over a tailgate into the suction basin of the downstream pumps. The tailgate was used to control water levels along the flume. Utilising two pumps, the water was discharged back to the laboratory flow system through a long-enough settling basin to guarantee that only clear water reaches the laboratory system.

As shown in Figure 4.5, the sand supply system consisted of two parts. The first part is a container filled with dry sand, at the bottom of which a wooden plate was fitted. The plate has an opening to allow sand flow. Different plates were prepared in accordance with the required sand supply rates. The second part of the sand supply system consisted of a funnel in which the sand is mixed with water. A submerged pump supplies the water to the funnel from a point downstream of the water supply diffuser. The sand-water mixture enters the model through a 1.35 m-wide diffuser. In order to shorten the required adaptation length for the equilibrium suspended sediment profile, the diffuser was positioned in such a way that the sediment is supplied in the lower part of the water column.

In the downstream side, most of the sediment was collected in the settling basin. A small part remained in suspension through the downstream pumps; this sediment settled in another long settling basin to prevent it from reaching the flow system of the laboratory. The volume of this sediment was very small and was not included in the total sediment balance after each test.

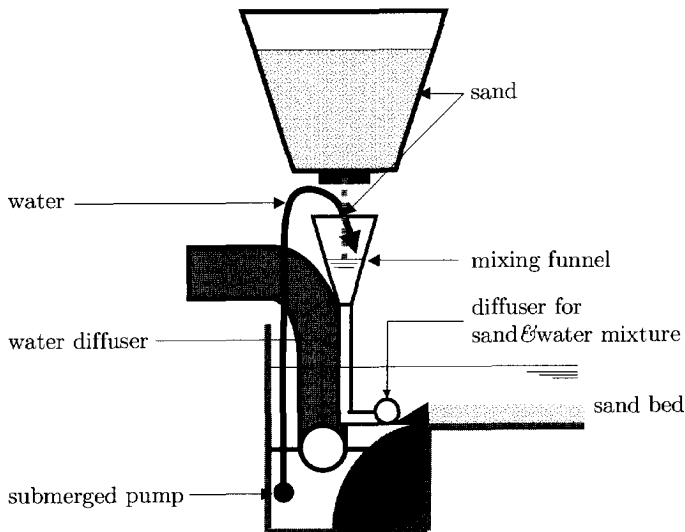


Figure 4.5: Details of the inflow section.

Special attention was paid to starting up the model, in order to avoid wash-out of existing bedforms. The start-up of the model was done in the following order:

- adjust the tailgate at its highest level,
- fill the model with water at a low discharge,
- increase the discharge slowly to reach the design discharge, and in the meantime adjust the capacity of the downstream pumps,
- adjust the water to the assigned water level in the test section by adjusting the tailgate, and finally
- switch on the sand supply system.

#### 4.2.4 Pilot tests

In order to set up the main test programme, it was necessary to estimate the expected time and length scales of the processes in the main channel region and within the groyne fields. In addition, the estimate of the sediment supply rate showed a large discrepancy between the two sediment formulae used (Van Rijn, 1984a and Engelund & Hansen, 1967). Existing knowledge provided only rough estimates of these scales. Therefore, it was decided to conduct a pilot test before the start of the main experimental programme, with the following objectives:

- to identify the morphodynamic processes due to the presence of groynes, both in the main channel and in the groyne fields sections,
- to quantify the morphological time scales of the different processes, and accordingly define the time scales of the experiment,
- to quantify the sediment supply rate,
- to get acquainted with the different instruments and to test the operational procedures of the model.

Two pilot tests were performed; one with emerged groynes and one with submerged groynes. The former case had the same conditions as case G1i, and the latter was similar to case G1c. Based on the results from the pilot test, it was decided to:

- limit the duration of each experiment to 40 hours, as the morphological changes in the groyne fields have become minor after that time span,
- modify the diffuser of the sand feeding system to prevent clogging of sand when applying a high feeding rate, and
- add six electrical switches on the rails to mark the passage of the movable carriage, in order to better determine its location.

#### 4.2.5 Measurements

Several quantities were measured during every test: bed profiles, suspended sediment concentration, flow velocity, water level, and bedform movement via video recording. Table 4.3 provides an overview of the measurements and equipment used during the experiment.

To make sure that the sediment concentration profile was fully adapted to the flow, the measurements were taken far from the inflow section, between the fifth and the eighth groyne. The test section and the coordinate system are shown in Figure 4.6.

Velocity, water level fluctuation, and bed profiles were acquired using DASyLab32 data acquisition system. Both velocity and bed profile measuring devices were mounted on a movable carriage (Figure 4.7). The carriage could move on two rails to scan the area between groynes 5 and 8. The speed of the carriage ranged from 0.0315 to 0.39 m/s, but bed level measurements were always taken while the carriage was moving on its minimum speed.

Table 4.3: Summary of measurements and equipment used during the experiment

Measurement	Measuring equipment	Number of		
		instruments	Location	times
Bed features	Bed profile followers (PROFO)	3	Between gr. 5 & 8	4 @ 10, 20, 30 and 40 hrs
Suspended sediment	Transverse suction system (TSS)	4	2 sections S1 & S2	1 @ 10 hrs
Velocity	Electromagnetic flow meters (EMF)	2	2 sections S1 & S2	1 @ 10 hrs
Water level	Wave gauges & static	2	U.S. & D.S.	variable
		2	U.S-D.S gr. 3	
Bedforms migration	Video camera	1	Between gr.5 & 6	continuous

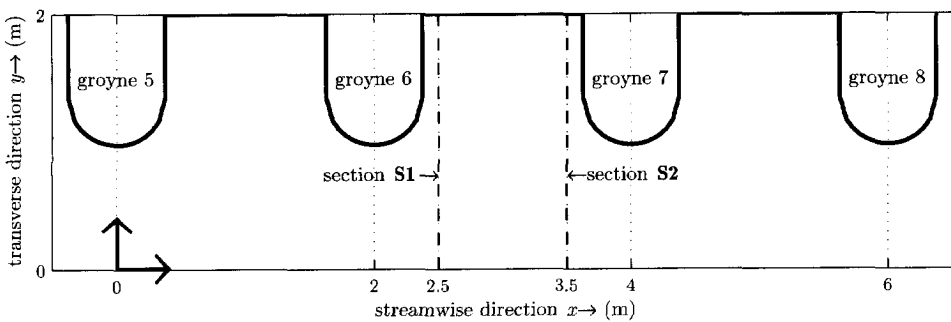


Figure 4.6: Test section and coordinate system.

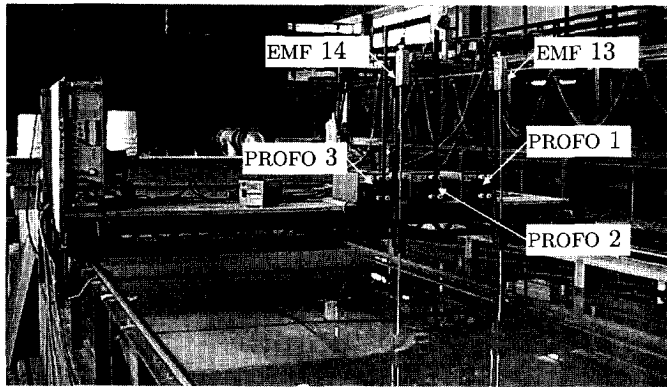


Figure 4.7: Movable carriage with two EMF units, and three bed profilers

### Bed profiles

The bed topography was measured by means of three electronic bed-level profile followers (PROFOS); type: PV-07, range: 55 cm (full scale), sensitivity: 0.635 V/cm, manufactured by WL| Delft Hydraulics. The measurements covered the area between the fifth and the eighth groynes with 6.0 m active measuring length. The measured profiles were spaced at 0.05 m, starting at 0.2 m from the sidewall of the flume, and ending 0.2 m away from the other wall, i.e. covering a total width of 1.60 m. The sampling rate of the PROFOS was 10 Hz, which means that with the carriage speed of 0.0315 m/s the spatial resolution of the bed readings in the longitudinal direction was  $3.15 \times 10^{-3}$  m. A reference reading was always taken before the start of every test, and measurements were taken at 10, 20, 30, and 40 hours from the start. The measured profiles were calibrated then interpolated on a  $2.5 \times 2.5$  cm<sup>2</sup> grid.

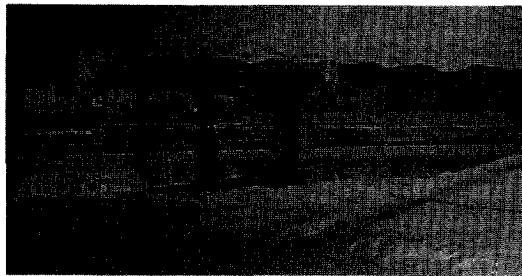


Figure 4.8: Bed profile followers (PROFOS) in action.

### Suspended sediment concentration

Time-averaged suspended sediment concentration profiles were determined by means of a transverse suction system (TSS). The system used in this experiment was a syphon sampling system consisting of 4 arrays of 5 intake-tubes of 3 mm internal diameter, (Figure 4.9). The intake tubes were spaced at 5 cm with the lowest intake-tube positioned 2 cm above the crest level of the local bedform.



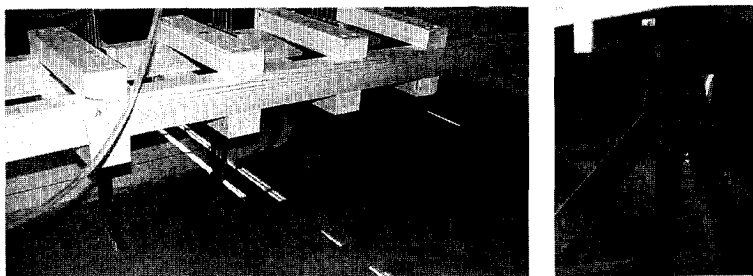


Figure 4.9: Suspended sediment sampling using transverse suction system (TSS).

The measurements were carried out in two cross-sections, namely S1 and S2 (Figure 4.6). Section S1 was located at 0.50 m downstream of groyne #7 and S2 at 0.50 m upstream of groyne #8. The measurements covered four points in the lateral direction. They were located at  $y = 0.85, 1.10, 1.35$  and  $1.60$  m consecutively. The vertical positions were 2, 7, 12, 17, and 22 cm above the highest ripple. For low water levels, the exposed nozzles were not used. From every sampling point 5.0 litres of water was collected. The samples were collected in 20 buckets. The submerged weight of the collected sand was determined and the concentration was then calculated.

### Velocity and water levels

Velocity measurements were conducted in two transverse profiles at the same location as the concentration measurements S1 and S2. The spacing between the measuring points was 5 cm. Utilising two electromagnetic flowmeters EMF13 and EMF14, the velocities were measured at  $0.6h$  from the water surface, so as to represent the depth-averaged velocity. Each measurement lasted 240 seconds, to cover a number of large-scale turbulence structures, with a frequency of 10 Hz.

The water level measurements aimed at evaluating the slope in the main channel and in a single groyne field. Measurements were taken in two points in the main channel, one near the inflow and the other near the outflow boundary. Moreover, two wave gauges were mounted upstream and downstream of groyne #3 to measure the water level drop over a single groyne.

### Bedform migration

The area between groyne #5 and groyne #6 was continuously monitored using a standard video camera. Initially, it was intended to use the video recordings for visual observations and to generate accelerated animations to help understand the sediment transport processes. Recent developments of the PIV-technique\*, however, made it possible to derive quantitative information from the otherwise qualitative video recordings.

The video camera was connected to a PC, which controlled the timing and the frame grabbing. The recording lasted throughout each test, at a rate of one frame per minute (0.0167 Hz). The recorded frames were later corrected for distortions utilising calibration

---

\* Particle Image Velocimetry

parameters that were derived from a still-picture of a square grid (Figure 4.10). A standard PIV-technique was then applied (LAVISION PIV SYSTEM), using cross-correlation between two successive images to estimate the bedform celerity. The celerity was determined using an adaptive multi-pass cross-correlation method with decreasing interrogation window size, starting with  $32 \times 32$  pixels and ending with  $16 \times 16$  pixels with 50 % overlap, which leads to a final resolution of  $8 \times 8$  pixels. This is equivalent to vector field spacing of  $\Delta x = \Delta y = 2.57$  cm.

Between the steps of the multi-pass cross-correlation, vectors were checked in two steps. First, a quality criterion that removes vectors with low correlation peaks in which, vectors that have a peak ratio factor (ratio between the height of the correlation peak and the height of the noise peak) less than 1.5 are removed. Second, a median filter with possibility to select a second correlation peak was used to reject large discrepancies between neighbouring vectors. The deviation of a central vector, compared to the root mean square value of the surrounding vectors, should not exceed a factor of 2. If this value is exceeded, the vector is rejected and the vector with the second highest correlation peak is checked against the same criterion and inserted if acceptable. The resulting vectors still contain some errors that require further postprocessing before the final vector field is obtained. The vectors were checked again, using a median filter that removes vectors with a deviation more than 1.3 times the root mean square value of the surrounding vectors and an absolute vector range of  $\pm 10$  pixels ( $\pm 3.21$  cm/min).

According to the area of interest, the frequency of the images used was varied; in the main channel, the bedform celerity is highest, hence, the maximum possible number of images (one per minute) was applied. In areas with lower bedform celerity, the number of frames was reduced to one per 10 minutes, so as to allow for accurate detection of the slower changes. The celerity was initially given in pixel per image; later it was converted to (m/s), using the same correction factors as before. For every test, the time-dependent celerity was estimated and then averaged over a long period, in order to eradicate out-layers. In this way, a quantitative picture was established for the magnitude and direction of the bedform celerity.

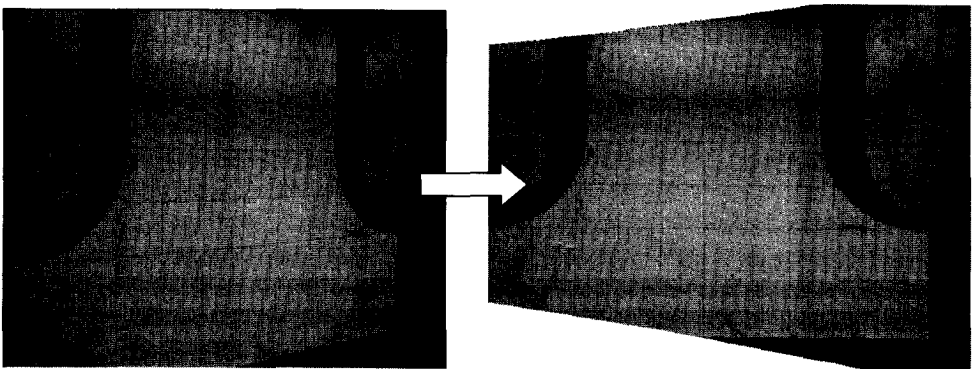


Figure 4.10: Image correction using a square grid with a spacing of 0.20 m; a pre-processing step.

From the celerity and the dimensions of the bedforms, the sediment transport rate could have been deduced. However, in this experiment, only the average dimensions of the ripples were measured at the end of each test and the results were not accurate enough to be processed further. Therefore, no attempt was made to quantify the sediment transport rate by bedform tracking.

## 4.3 EXPERIMENTAL RESULTS

### 4.3.1 Flow pattern

Since a fixed-bed experiment has been carried out before (see Chapter 3), detailed velocity measurements were not taken in this experiment. The flow dynamics have been elucidated in Chapter 3. In this experiment, the depth-averaged velocities were measured along sections S1 and S2 in one point at  $0.6h$  from the water surface (Figure 4.11). In some cases, the velocities were measured in two points of the water column at  $0.2h$  and  $0.8h$ , in order to identify secondary flow. For completeness and future use, the results of all velocity measurements are given in Appendix A.1.

#### Emerged groynes

During the first few hours of a test, the observed flow pattern did not differ much from the observations described in Chapter 3 (cf. Uijttewaai *et al.*, 2001; Yossef and Uijttewaai, 2003). The flow inside the groyne fields showed unsteady behaviour characterised by a primary circulation cell in the downstream part of the groyne field, a secondary circulation cell driven by the primary one with an opposite rotating direction, and a dynamic eddy that intermittently sheds from the tip of the upstream groyne. Moreover, smaller-scale vortices are generated near the tip of the groynes; they migrate in the flow direction and follow the primary circulation cell deep into the groyne field. The whole circulation is driven by the main stream via exchange of momentum through the mixing layer.

Along with the morphological development, the flow pattern showed minor changes. With the development of the scour hole, the dynamic eddy stretches in the vertical direction following the newly formed scour hole. After the development of the deposition region inside a groyne field, the interaction between the groyne field and the main channel is hindered and the primary circulation cell slows down, which ultimately leads to the disappearance of the secondary circulation cell.

#### Submerged groynes

In this case, the flow in the groyne fields does not show the circulation pattern as observed in the emerged condition. Yet, the groyne fields can be characterised as low-velocity regions. The momentum loss by the water flowing over the groynes is sufficient to balance the momentum input through the mixing layer. The mixing layer in this situation has a constant width. The total turbulence intensity across the mixing layer decreases as the submergence ratio increases.

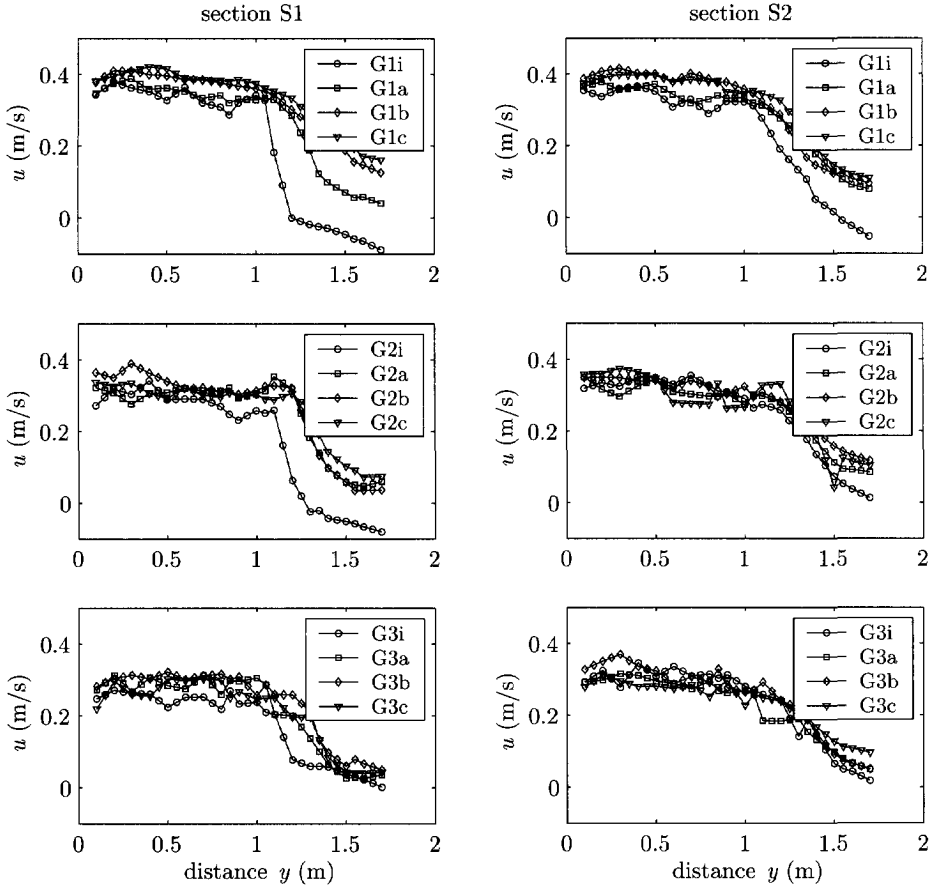


Figure 4.11: Distribution of depth-averaged velocity in the transverse direction  $y$ , for all cases in G1, G2 and G3 (1<sup>st</sup>, 2<sup>nd</sup> and 3<sup>rd</sup> row consecutively), measured at section S1 (left column) and section S1 (right column).

In the case of very shallow submergence (Cases .a), the flow pattern showed some of the characteristics of the flow in the emerged situation. It should be noted, however, that the flow over the groynes hinders the horizontal recirculation, suppressing it completely if the submergence ratio is high enough (Cases .b & .c). Generally speaking, the flow in the submerged state shows an alternately accelerating and decelerating pattern between flow over and around the groynes (cf. Yossef and Uijtewaal, 2003).

Some researchers report observing a secondary flow structure during submerged conditions (eg. Peng *et al.*, 1997; Krebs *et al.*, 1999). This secondary flow occurs along the normal line with the flow directed towards the groyne fields near the bed and towards the main channel near the water surface. In this experiment, some secondary-flow-like behaviour was observed from dye visualisations, but it could not be identified from the velocity measurements.

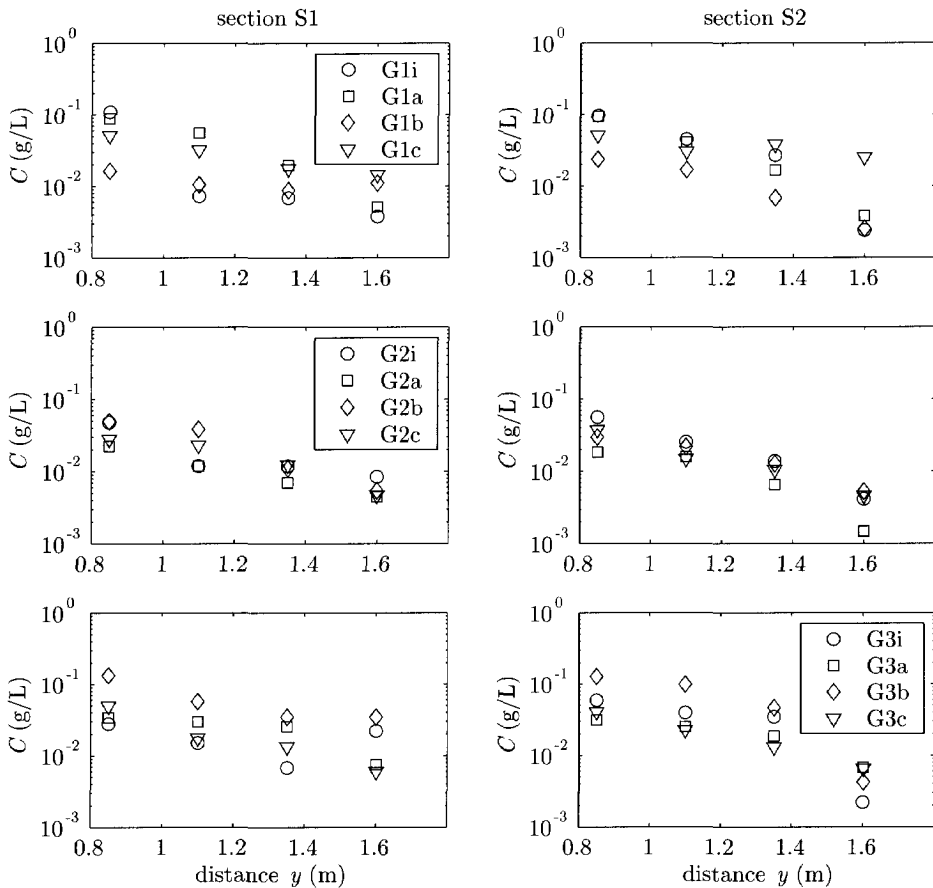


Figure 4.12: Distribution of depth-averaged suspended sediment concentration in the transverse direction  $y$ , for all cases in G1, G2 and G3 (1<sup>st</sup>, 2<sup>nd</sup> and 3<sup>rd</sup> row consecutively), measured at section S1 (left column) and section S1 (right column).

Except for a slight decrease in turbulence intensity near the tip of the groynes, no significant changes in the flow pattern were observed in response to the bed changes.

### 4.3.2 Sediment transport

Information about the sediment transport was deduced from the concentration measurements and from the bedforms migration measurements. Results from these measurements are described and discussed in the following two subsections.

#### Suspended sediment concentration

Time-averaged suspended sediment concentrations have been measured at four locations along sections S1 and S2, each time from five depth points distributed over the water

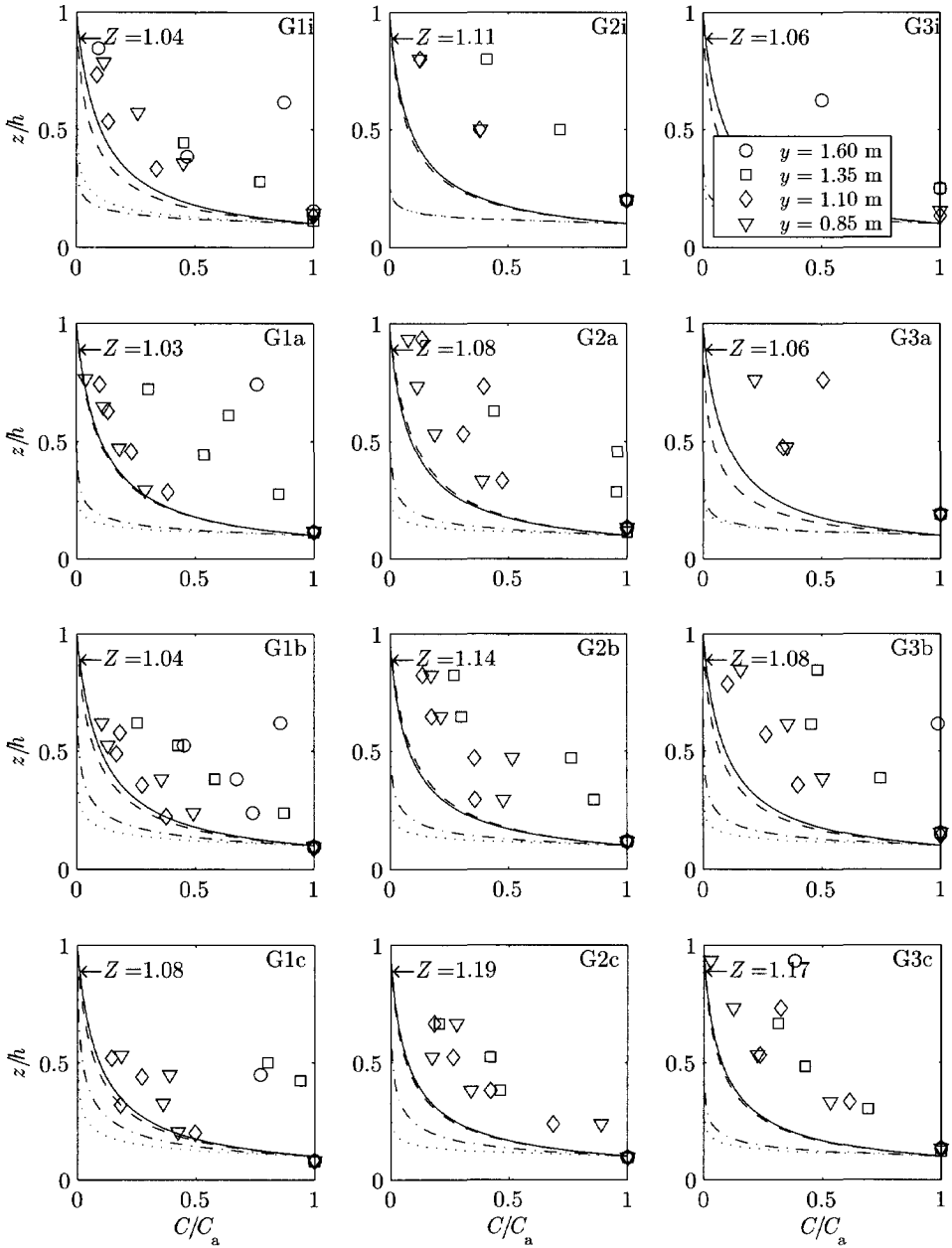


Figure 4.13: Suspended sediment concentration profiles for all cases. Profiles are measured at transverse locations indicated by legend. Lines represent equilibrium (Rouse) concentration profiles at different values of suspension number  $Z$  (deduced from measured velocity), solid-lines represent profiles at  $y = 0.85$  m (main channel), dotted-lines represent profiles at  $y = 1.60$  m (groyne field), dashed-lines at  $y = 1.10$  m, and dash-dot-lines at  $y = 1.35$  m.

column. The distributions of the depth-averaged suspended sediment concentration in the transverse direction are given in Figure 4.12 and the vertical profiles are given in Figure 4.13.

The distributions of the depth-averaged suspended sediment concentration given in Figure 4.12 show that the concentration drops exponentially in the transverse direction. The gradient ( $dc/dy$ ) based on measured concentrations is considerably less than that based on the equilibrium concentrations deduced from the measured velocities. This indicates that the measured concentration in the flow entering the groyne fields is unable to follow the rapid decrease of the equilibrium concentration.

The transverse distributions in the measured sections S1 and S2 are comparable. This implies that the transport to the groyne fields is distributed ‘rather’ evenly along the whole length of the normal line. The same conclusion could be inferred from the shape of the mixing layer in the case of submerged groynes, as observed in the fixed-bed experiment presented in Chapter 3. Similar behaviour has been detected from measurements in the Elbe River (cf. Sukhodolov *et al.*, 2002; Sukhodolov *et al.*, 2004).

The vertical profiles of the suspended sediment concentration for all cases are given in Figure 4.13 where it is compared with the equilibrium (Rouse) concentration profiles for values of the suspension number  $Z$  estimated from measured properties. Solid lines represent profiles in the main channel and dotted-lines represent profiles inside the groyne field.

The equilibrium profiles exhibit lower concentrations inside the groyne fields and seem to form a lower envelope of the data points. This indicates that equilibrium had not yet been reached. The flow is still loaded with sediment transported from the main channel and the concentration cannot follow the rapid decrease of the equilibrium concentration as the flow enters the groyne fields.

### Bedform movement

Images have been recorded in an area covering part of the main channel and the region between groynes #5 and #6. The images were processed using a standard PIV-technique as explained in Section 4.2.5. In this way, we were able to generate vector fields that give quantitative information about the time-dependent bedform celerity, which is indicative of the bed load transport. An example is given in Figure 4.14, where we see large variations between the vector fields due to the dynamics in the mixing layer. The area near the groyne tip exhibited the strongest variations. Frequently, sediment (bedforms) is advected towards the groyne fields (Figure 4.14, frames 3 to 6). The time-dependent vector fields were averaged over a long period (60 minutes) to produce time-averaged pictures; complete results are given in Appendix A. An example is given in Figure 4.15, where the celerity in the streamwise direction  $u_{bf,x}$  (Figure 4.15, upper right panel) and transverse direction  $u_{bf,y}$  (Figure 4.15, lower left panel) were extracted from the complete vector field presented in Figure 4.15 (upper left panel).

For comparison, the celerity based on the EMF-velocity measurements were calculated using the transport formula  $m u^n$  (Engelund & Hansen, 1967). The celerity in the streamwise direction  $u_{bf,x}$  calculated with PIV, has the same order of magnitude with that based on EMF velocity measurements (see Appendix A.4). However, the gradient in the trans-

verse direction ( $du_{bf,x}/dy$ ) is milder than ( $du^n/dy$ ). This suggests the transport in the mixing layer to be greater than calculated from a sediment transport formula. The celerity in the transverse direction  $u_{bf,y}$  contained a large scatter in the results. This was due to several factors, the most important of which was the error in the correction procedures of the image-distortion (Figure 4.10). Accordingly, only indicative conclusions can be drawn from these results.

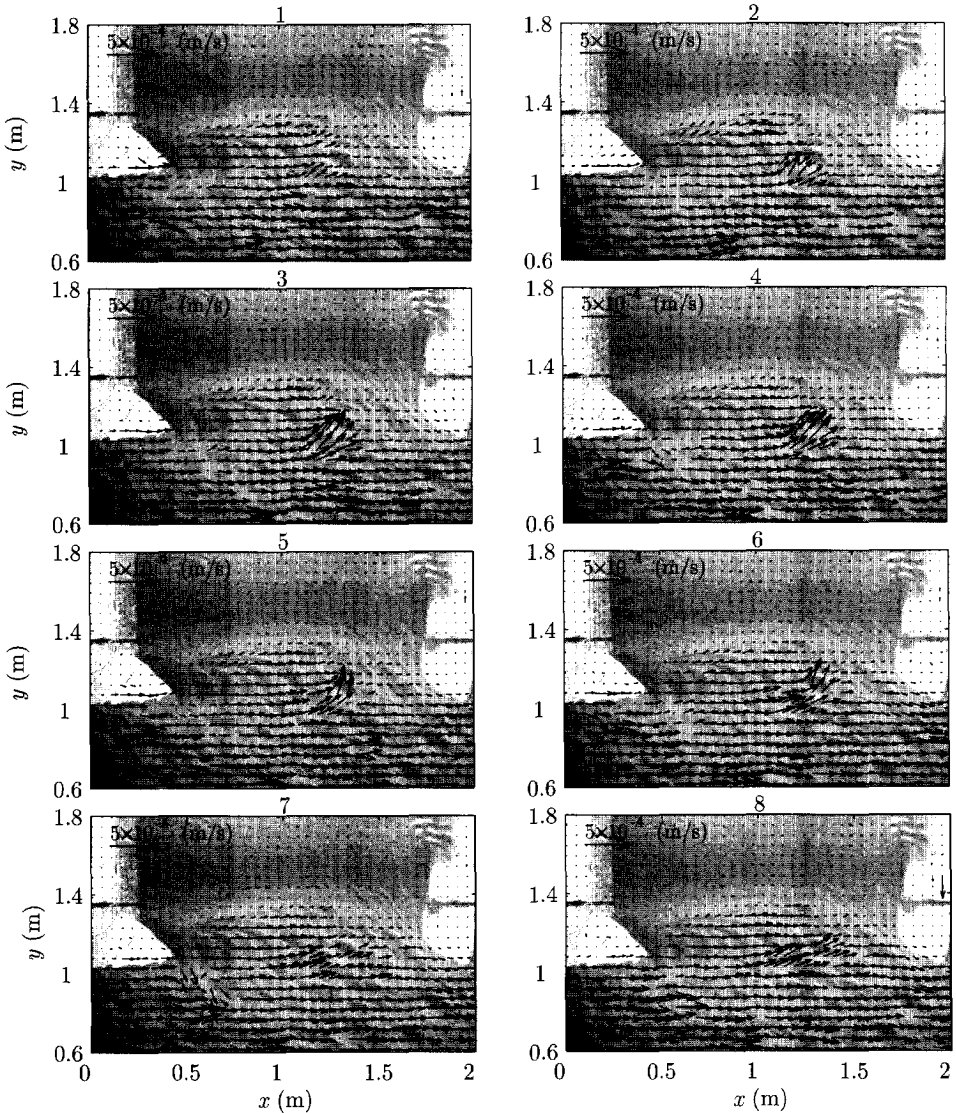


Figure 4.14: Bedforms celerity computed over eight consecutive minutes from case G3i; background is an unprocessed reference image.



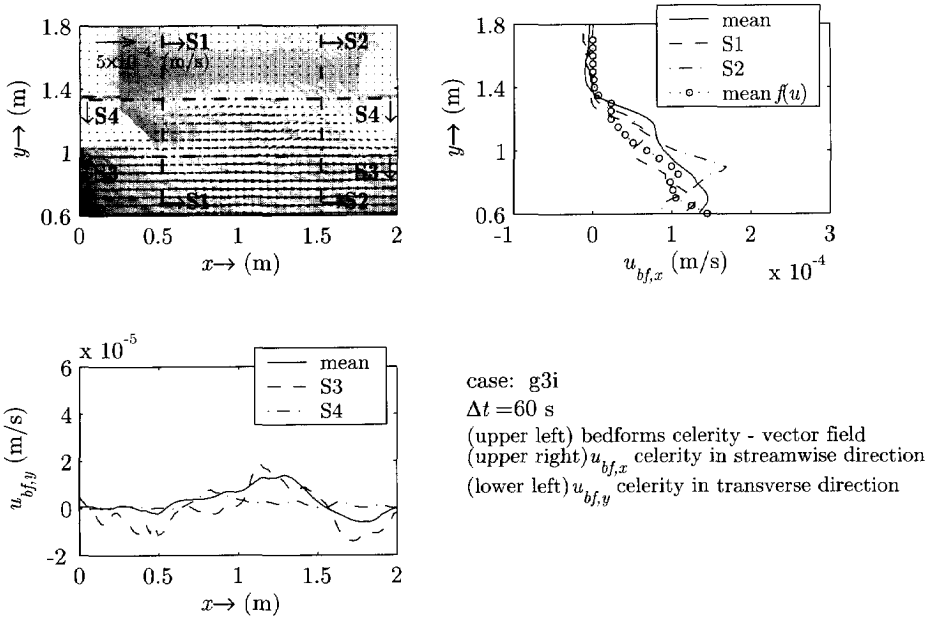


Figure 4.15: Time-averaged bedform celerity computed from images taken with image-interval of 60 s, o-points in upper right panel is  $u_{bf,x}$  resulting from EMF velocity measurements; background is an unprocessed image; case G3i. Complete results are given in Appendix A.4.

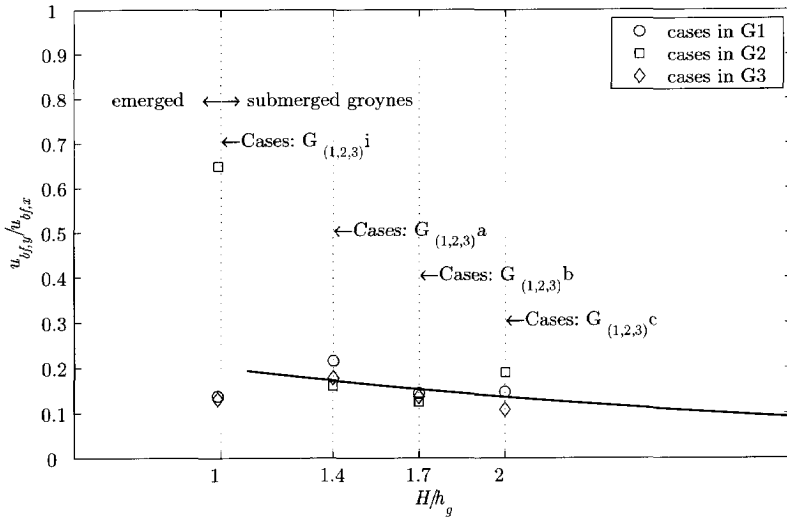


Figure 4.16: Behaviour of  $u_{bf,y}/u_{bf,x}$  versus the submergence ratio  $h/h_g$  deduced from the vector fields of all test cases;  $u_{bf,y}$  is across the normal line and  $u_{bf,x}$  is in the main channel. The solid line is an indicative exponential decay function.

Firstly, the estimated bedform celerity gives an impression of the relation between the transport rate in the main channel and that in the mixing layer and further into the groyne fields. Figure 4.16 illustrates the behaviour of  $(u_{bf,y}/u_{bf,x})$ , which is not exact, yet representative of the transport rate into the groyne fields, compared with that in the main channel. It shows that  $(u_{bf,y}/u_{bf,x})$  is a decreasing function of the submergence ratio, which indicates that, for the same transport rate in the main channel, the transport to the groyne fields decreases as the submergence increases.

Secondly, the analysis of the results given in Appendix A.4, gives an idea of the sediment supply to the groyne fields for the different cases. Generally speaking, the sediment transport to the groyne fields in the cases of emerged groynes takes place across the downstream part of the normal line. If groynes are submerged, the transport to the groyne fields takes place along the whole normal line.

Finally, the bedform migration in the main channel accelerates near the tips of the groynes and decelerates between the groynes. This is because the streamlines are converging around the groyne tips and diverging afterwards.

### 4.3.3 Morphological features

For all the cases considered, two typical features were observed. The first was the development of a scour hole near the tip of each groyne; the second was sediment deposition inside the groyne fields. The morphological time-scale for the development of the scour holes was rather short compared to the total duration of each experiment. In each of the tested cases, both scour and deposition patterns looked similar near all groynes except near the first and the last ones. Nevertheless, significant differences were found between the emerged and submerged cases.

#### Emerged groynes

In situations with emerged groynes, the sediment import into the groyne fields takes place across the downstream part of the normal line. The sediment is transported from the main channel towards the groyne following the primary circulation cell and settles down on its way, forming a deposition region in the downstream part of the groyne fields.

An example of the temporal development in morphology and the erosion/deposition pattern, which is estimated by subtracting the bed level from the initial bed level, is presented in Figure 4.17. It shows that the morphological features are similar in all three groyne fields, indicating that flow and transport are fully developed in the test section. The development of the scour hole has a rather short time-scale; it is fully developed after some 10 hours (Figure 4.17 first row). The deposition process has a much longer time-scale, which indicates that the deposition is not resulting from the sand eroded from the scour hole; it must have been supplied from the main channel.

Figure 4.18 is derived from Figure 4.17 by averaging the measured bed levels over a single groyne field. Figure 4.18 (upper right panel) gives the distribution of the deposited material in the transverse ( $y$ ) direction. Notice the deposition ridge at the entrance of the groyne field. Apparently, this ridge results from the early development of the scour hole. Note that its peak is almost fully developed after 10 hours.

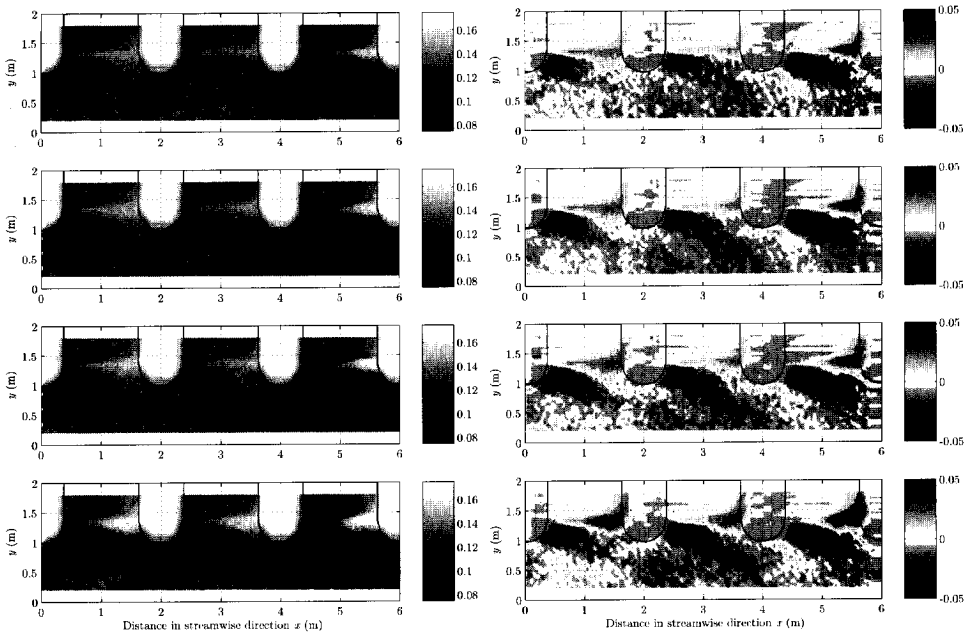


Figure 4.17: Bed level (left column) and erosion/deposition pattern (right column) measured after: 10, 20, 30 and 40 hours consecutively (from top to bottom) – Case G1i (emerged groynes).

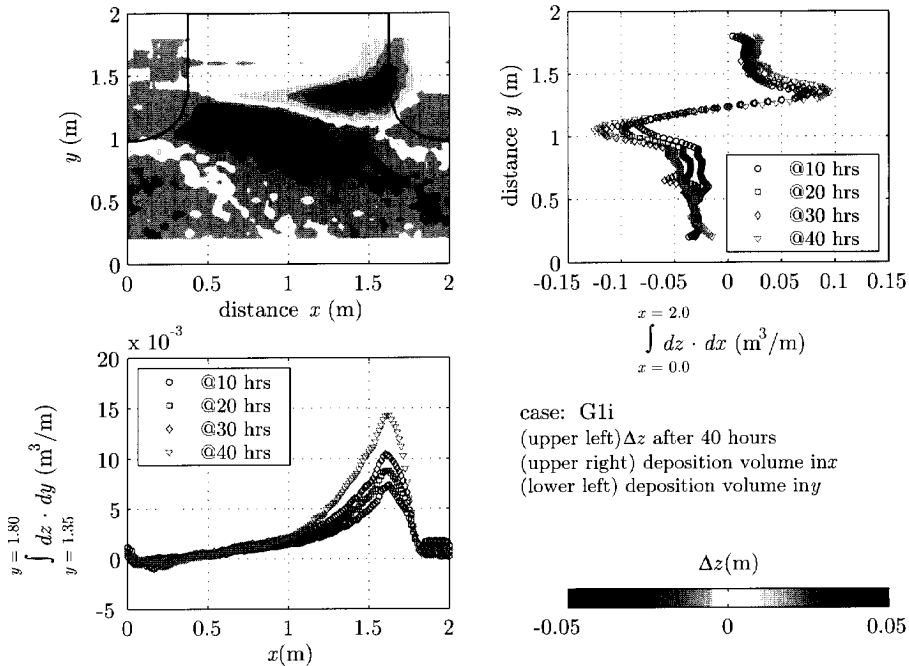


Figure 4.18: Erosion/deposition pattern after 40 hours, averaged over one groyne field; Case G1i (emerged groynes).

The scale effect is an additional factor that contributes to the occurrence of such a ridge close to the normal line. In the model, the velocity drops below the critical velocity (for initiation of motion) within a rather short distance, a situation that is not likely to occur at the same location in the prototype. There, this ridge is expected to be smoothed out and shifted further into the groyne field.

Figure 4.18 (lower left panel) gives the distribution of the deposited material in the streamwise ( $x$ ) direction, from which we can see that most of the deposition takes place towards the downstream end of the groyne field. The deposition volume after 40 hours is much higher than that after 10 hours. This indicates, once more, that the sediment eroded from the scour hole does not contribute much to the deposition volume.

The scour hole alignment follows the direction of displacement of the dynamic eddy (see Figure 4.17 and Figure 4.21). It is oblique to the flow direction and makes an angle of about  $30^\circ$  with the normal line. In a later stage, the scour had a feedback onto the flow by stretching the dynamic eddy in its direction.

### Submerged groynes

In situations with submerged groynes, the sediment deposition inside the groyne fields takes place across most of the length of the normal line (apart from the part closest to the groyne tip, see Figure 4.19). The sediment is transported from the main channel towards the groyne through the mixing layer. Due to the high turbulence intensity, the sediment concentration in the mixing layer remains high (comparable to the concentration in the main channel). Consequently, the sediment exchange through the mixing layer is significant. The alignment of the ripples near the sidewall in the middle of the groyne fields near the sidewall indicates that some sediment is transported over the groynes (Figure 4.22). In a long enough channel, there will be no net contribution to the sediment balance in a groyne field, since the same amount is transported over every groyne. The areas downstream and upstream of the groynes are free from bedforms because the transport over the groynes is considerably low, also due to flow separation (in the vertical) in these regions.

An example of the temporal development is presented in Figure 4.19. Similar to the emerged situations, the scour hole is almost fully developed after 10 hours, whereas deposition continues for a longer time, indicating that the deposition region cannot be fully attributed to the sand eroded from the scour hole.

Figure 4.20 (upper right panel) gives the distribution of the deposited material in the transverse direction. It shows the existence of a deposition ridge, the location of which is shifted slightly towards the bank as compared with the emerged situation. Again, the scale-effect is likely to play a role in the shape and location of this ridge. Unlike the emerged case, the deposited material is more distributed over the length of the normal line (Figure 4.20 lower left panel).

In the submerged cases, both the depth and the alignment of the scour hole depends on the water level. The maximum scour depth decreases as the submergence level increases. In all submerged cases, the observed depth of scour was less than that in the emerged cases. The alignment of the scour hole also changes with the water level. It rotates

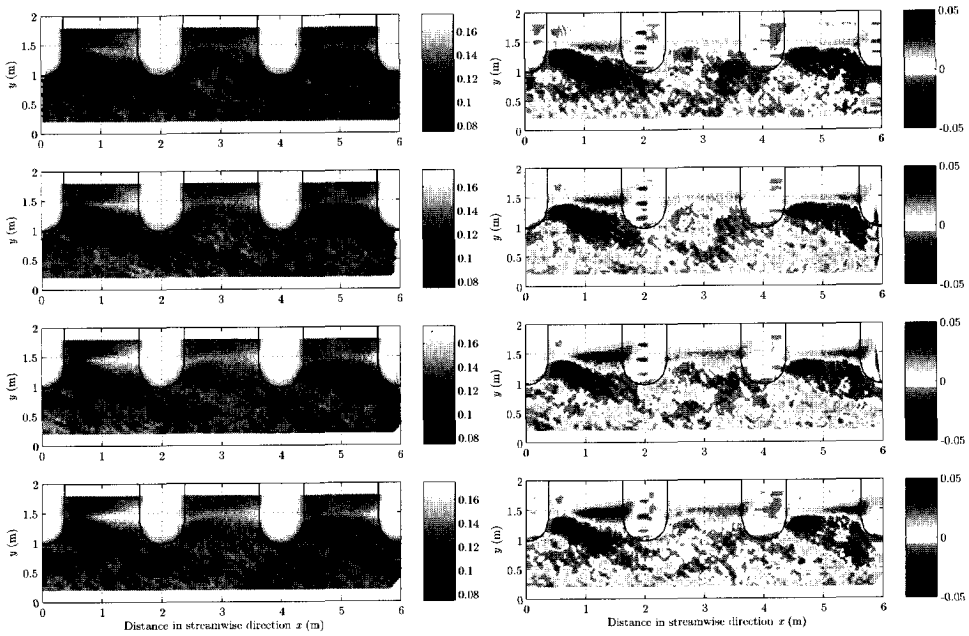


Figure 4.19: Bed level (left column) and erosion/deposition pattern (right column) measured at: 10, 20, 30 and 40 hours consecutively (from top to bottom) – Case G1a (submerged groynes).

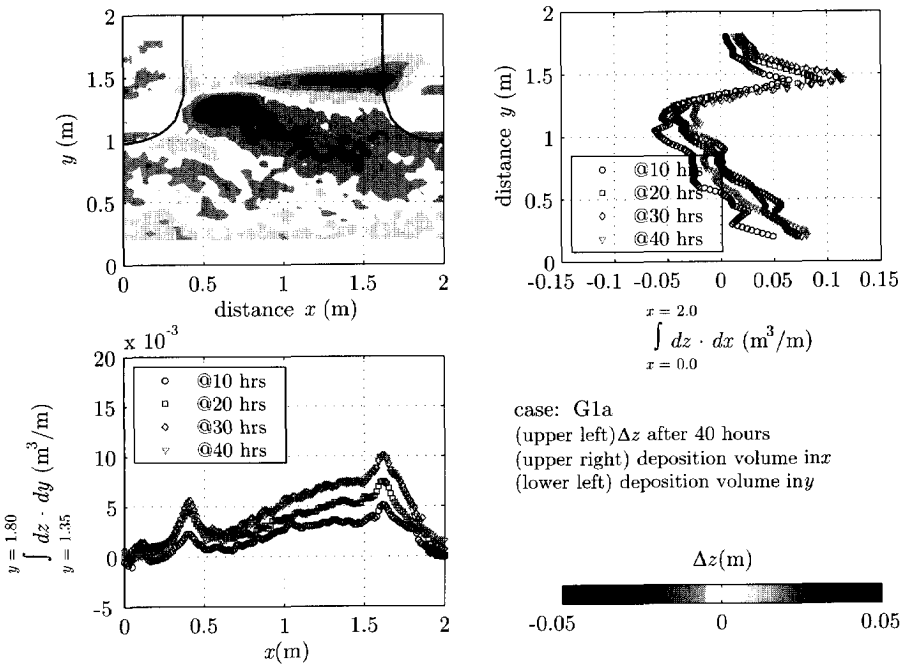


Figure 4.20: Erosion/deposition pattern after 40 hours, averaged over one groyne field; Case G1a (submerged groynes).

towards the bank as the submergence level increases (see Appendix A.3). Similar behaviour has been observed in the real-life rivers (Sukhodolov *et al.*, 2002) and in the laboratory (Kuhnle *et al.*, 1999).

## 4.4 ANALYSIS AND DISCUSSION

### 4.4.1 Transport mechanisms

In situations with emerged groynes, the footprint of the flow pattern was clearly visible in the morphology. As indicated in Figure 4.21, the sediment import into the groyne fields takes place through the downstream part of the normal line. The sediment is advected from the main channel towards the groyne fields following the direction of the primary circulation cell. Along with the drop of the velocity, the sediment tends to settle. The alignment of the ripples near the wall deep inside the groyne field is opposite to the main flow direction, but complies with the flow direction inside the groyne fields. The size of the ripples near the wall may have been exaggerated in the experiment due to the effect of the smooth sidewall. Still, this indicates that the effect of the primary circulation cell is extending through the width of the groyne field. The area in the middle of the groyne field, which coincides with the centre of the primary circulation cell, as well as the area in the upstream upper corner, which coincides with the secondary circulation cell, are both free from bedforms.

In the submerged cases, the flow near the groynes does not give rise to 'pure' advective transport, as the mean flow is not directed towards the groyne fields. Nevertheless, a significant sediment transport has been observed from the main channel to the groyne fields that cannot be solely attributed to turbulent diffusion. This transport is attributed to transport by large coherent structures that develop in the mixing layer. One might argue that from a large-scale perspective this is a kind of diffusive transport. In any case, the processes involved are not diffusive in nature.

In the present context, we make a distinction between small-scale (three-dimensional) and large-scale (two-dimensional) turbulence. The former induces diffusive transport and the later residual advective transport. The time-scale of this residual advective transport is similar to that of the large-scale coherent flow structures. Although the mass balance of water is conserved within a groyne field, the advective sediment transport by large coherent structures does not necessarily have a zero average. This is due to the non-linear relation between transport capacity and flow velocity, in addition to the difference in concentration between the main channel and the groyne fields. The non-linear relation between transport and velocity causes a net transport towards the groyne fields if the large-scale fluctuating velocity components ( $u'$  &  $v'$ ) are in phase (additional elaboration in Chapter 5). The difference in concentrations between the main channel and the groyne fields is such, that the inflow to the groyne fields is loaded with sediment from the high-concentration side (main channel), and the outflow part carries no or little sediment as it comes from the low-concentration side (groyne fields). Thus, continuous accumulation of sediment inside the groyne fields takes place.



Figure 4.21: Morphological features for emerged groynes with indications to the flow pattern (dashed-lines); picture taken at the end of case G1i.

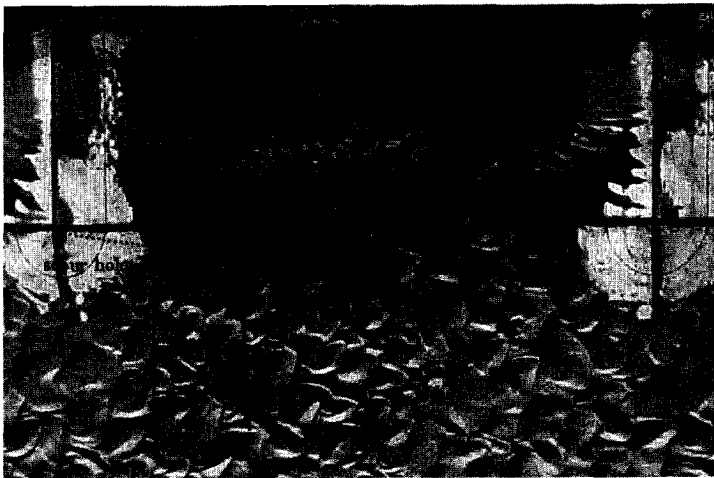


Figure 4.22: Morphological features for submerged groynes; picture taken at the end of case G1c.

As we have mentioned before (Section 4.3.1), some secondary-flow-like features were observed from the dye visualisations. Though it was not detected by the EMF measurements, secondary flow could be an additional mechanism that causes the flow near the bed to be directed towards the groyne field, transporting the sediment from the main channel into the groyne field.

Suspended sediment concentrations measurements revealed that the measured (absolute) reference concentrations were always higher than theoretically calculated. Moreover, the normalised vertical concentration profiles were found to be higher than the theoretically based equilibrium profiles which appeared as a lower-limit envelope for the measured

profiles (Figure 4.13). The transverse distribution of the depth-averaged concentration exhibits a slower decay than the theoretically estimated equilibrium concentration.

Furthermore, bursting events were repeatedly observed visually along the path of the small-scale dynamic eddies. These eddies detached from the tip of the groynes and they were advected along following the direction of the primary circulation cell, thus, carrying sediment towards the groyne fields.

Obviously, the area near the groynes and along the normal line exhibits high turbulence intensity in addition to large-scale coherent structures that form because of the existence of the groynes. According to Nezu and Nakagawa (1993) the coherent structures consist of both the large-scale vortical motions and bursting motions, which they identify as *the double structure of turbulence*. They could not find an answer to the questions of how large-scale vortical motions interact with bursting motions and how strongly the former motions are involved in the reoccurrence of the latter. This question remains for further 'basic' research. Nonetheless, the large-scale motion forms a high-shear layer near the bed. This high-shear layer triggers the suspension of sediment. Thus, the suspended sediment reference concentration increases as well as the vertical concentration profile. Consequently, the transverse distribution of the suspended sediment concentration will change, leading to additional transport towards the groyne fields.

#### 4.4.2 The effect of submergence

When the groynes are not submerged, there is no effect of the submergence ratio ( $h/h_g$ ), which is by definition less than unity. The effect in these situations is attributed to the flow depth only, which increases the transport into the groyne fields as it increases. The morphological features and the erosion/deposition pattern look quite similar for the three tested emerged cases (G1i, G2i, and G3i), with some differences in the magnitude of changes.

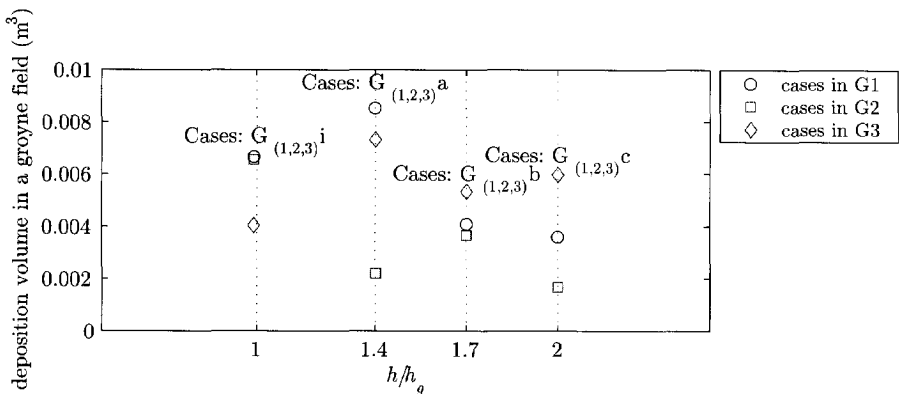


Figure 4.23: Deposition volume inside a single groyne field after 40 hours for all tested cases.



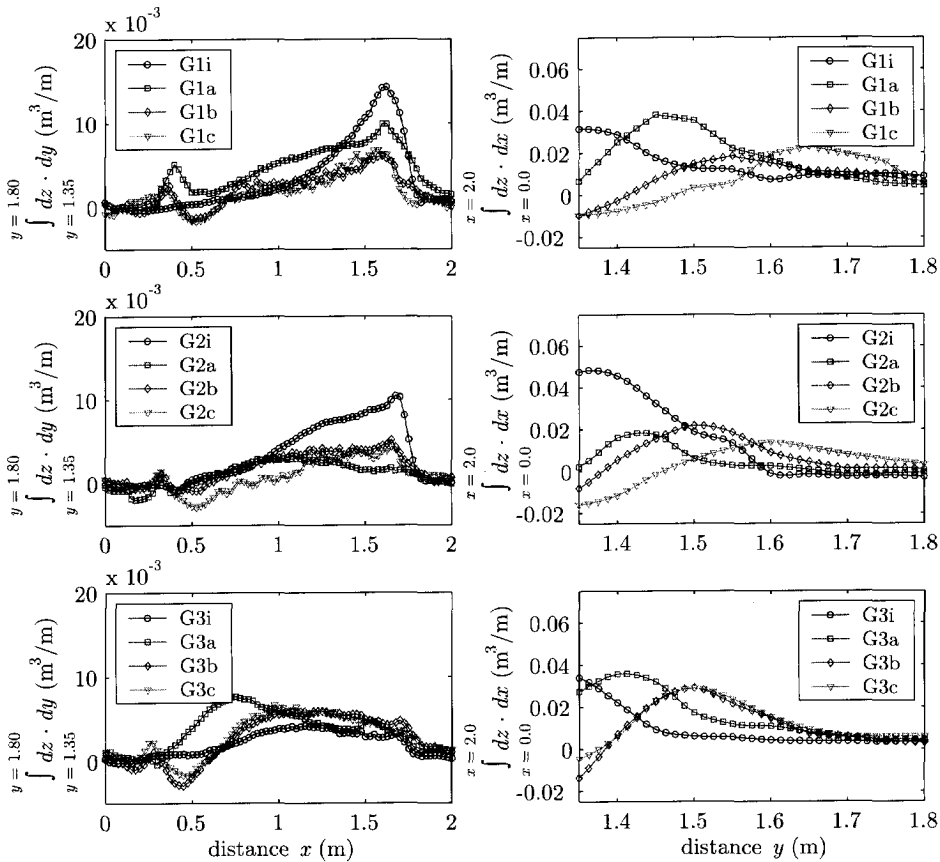


Figure 4.24: Distribution of deposited material inside groyne fields per unit length (left column) and per unit width (right column), grouped by submergence ratio.

When the groynes are submerged, the morphological features as well as the magnitude of the changes depend on the submergence ratio. With increasing submergence, the characteristics of the mixing layer change, such that the turbulent intensity as well as the velocity gradient across the mixing layer decrease. This in its turn weakens the large-scale coherent flow structures that contribute most to the sediment exchange between the main channel and the groyne fields. For very deep submergence, the velocity gradient across the mixing layer will be too weak to trigger large-scale coherent structures. Consequently, the volume of sand deposited in a groyne field decreases with the increase of submergence (Figure 4.23). Besides, the location of maximum deposition shifts further towards the bank as the submergence ratio increases (Figure 4.24, right column).

Though the picture given in Figure 4.23 shows some scatter in the deposited volume of sand in a groyne field, it conforms to the results from the PIV-measurements as presented in Figure 4.16. The scatter in measured volumes is due to differences between the actual hydraulic conditions and the original design conditions, (cf. the different values of the suspension number,  $Z$ , in Figure 4.13).

The alignment of the scour hole also responds to the increased submergence, viz. by rotating towards the groyne fields. The cases of low submergence, the scour hole intrudes into the main channel, whereas for deep submergence it is rather aligned to the flow direction and fully impounded inside the groyne fields. Prototype observations have shown bi-directional alignment of scour holes, which could be explained by the formation of two scour holes at two different flow stages, e.g. a normal flow condition (emerged groynes) and a flood (submerged groynes). The difference in alignment is attributed to the path of eddies shedding from the tips of the groynes. The maximum scour depth decreases with increasing the submergence ratio, which is attributed to the lower turbulence intensity that goes hand in hand with increasing submergence. Note that in the case of very deep submergence the effect of the groynes vanishes.

Apparently, the height of the groynes on its own has no effect on the sediment exchange between the main channel and the groyne fields. A comparison between different groyne heights at the same submergence ratio did not reveal a clear trend.

#### 4.4.3 Scale effect

In order to translate the findings from the experiments to prototype conditions, we first need to highlight some aspects related to scale effects.

Firstly, the experiments were carried out at a geometrical scale of 1:100, based on a Froude similarity to represent conditions similar to the Waal River. However, as customary for mobile-bed experiments, the sediment size was not scaled with the same scaling criterion. Hence, the velocity had to be exaggerated (tilted model) to induce bed load as well as suspended load transport (see for example De Vries, 1993). Ettema and Muste (2004) studied the effect of exaggerated velocities in the case of a single groyne. They report that an exaggerated velocity leads to an increased vorticity of eddies shedding from the groyne. This increased vorticity is advected relatively further in the model than in the prototype. It further enhances the turbulence intensity in the mixing layer. Increased vortical motion and turbulence generation would result in an over-estimation of the sediment entrainment in the mixing layer and consequently the transport to the groyne fields.

Secondly, due to the typical geometry involved, there is a velocity gradient between the main channel and the groyne fields. This gradient causes the velocity to drop below the critical velocity just inside the groyne fields. The location at which this takes place is different in the model and in the prototype. This causes the deposition material to settle in the model relatively close to the normal line, as was shown in Section 4.3.3.

Finally, the smooth sidewall in the model initiates some bed changes near the wall. This was not significant in our case and had no consequences on the interpretation of the results.

With respect to the above-mentioned aspects, mobile-bed experiments are best to be used for comparative studies. Both the qualitative and quantitative results of the experiments are valuable. However, when attempting to upscale the quantitative results to the prototype conditions, special attention should be paid; this step is best to be done via modelling of the captured mechanisms (see Chapter 5). Nonetheless, we attempt to

upscale the results here in order to have an indication of the order of magnitude of the measured quantities with respect to the prototype.

The scale factor of the morphological changes in the experiment is calculated according to the Delft method (see Jansen *et al.*, 1979; De Vries, 1993), as given below.

$$n_{tm} = \frac{n_h \cdot n_L}{n_D^{3/2} \cdot n_\Delta^{1/2}} \tag{4.3}$$

where  $n_X$ , refers to the scale relation of the parameter  $X$  ( $n_X = X_{prototype}/X_{model}$ ),  $tm$  the morphological time-scale,  $h$  the vertical length-scale,  $L$  the horizontal length-scale,  $D$  the sediment size, and  $\Delta$  the sediment specific density.

Eq. 4.3 yields a morphological time-scale of 480 on average; i.e. one hour in the model is equivalent to 20 days in the prototype. The morphological changes measured with a step of 10 hours in the model can be considered equivalent to changes in the prototype after 200 days and the total duration of the experiment of 40 hours is equivalent to some 2.2 years in real life. From Eq. 4.3 we can further calculate the scale factor of the sediment transport rate  $n_{Q_s}$  as:

$$n_{Q_s} = n_L \cdot n_D^{3/2} \cdot n_\Delta^{1/2} \tag{4.4}$$

which yields  $n_{Q_s} \cong 1500$ , from which we can upscale the measured deposition volumes in a single groyne field given in Figure 4.23, to the prototype conditions; the result is given in Figure 4.25. For a groyne field with dimensions of  $200 \times 60 \text{ m}^2$ , the average measured deposition volume ( $Q_s = 0.5 \times 10^{-4} \text{ m}^3/\text{s}$ ) is equivalent to an increase of the groyne fields' bed level by around 0.13 m/year. It is clear that this is too much, yet expected as we have indicated previously.

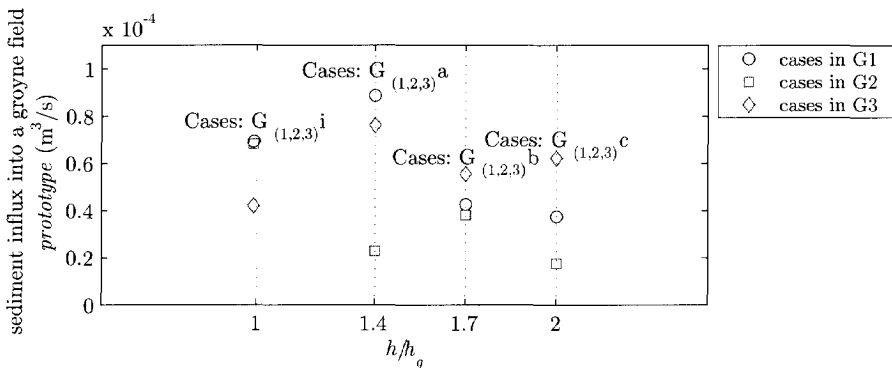


Figure 4.25: Sediment influx into a single groyne field upscaled to prototype condition.

## 4.5 SUMMARY AND CONCLUSIONS

In this chapter we discussed the results of a mobile-bed experiment of a river with groyne dimensions found in the Dutch River Waal. The effect of flow stage was studied by changing the flow depth and the effect of lowering the crest level of the groynes was studied by changing the thickness of the sand layer in the whole flume.

The measurements provided information about:

- the distribution of the depth-averaged velocity in the transverse direction,
- the distribution of the sediment concentration in the transverse direction,
- the suspended sediment concentration profiles in the main channel and inside the groyne fields.
- the bedform movements, and
- the morphological development in the groyne fields at different flow stages.

The findings from this Chapter lead to the following conclusions:

- In all tested cases, there is a net import of sediment into the groyne fields. In this way, the trivial equilibrium situation is a completely filled-up groyne field. Nevertheless, in the case of the Rhine, erosion of the groyne fields due to navigation-induced sediment transport yields a state of dynamic equilibrium (this is going to be discussed further in Chapters 5 & 7).
- The mechanism of sediment transport into the groyne fields differs according to the flow stage. In the emerged situation, the sediment is mainly advected towards the groyne fields following the direction of the primary circulation cell. In the submerged situation, the sediment is transported to the groyne fields across the whole length of the normal line, primarily by residual advective transport by large-scale coherent structures. Diffusion through the mixing layer and secondary flow circulation play a minor role in this case.
- Groyne height does not have an effect on its own on the deposition volume into the groyne fields; it is primarily the submergence ratio that plays an important role. The results from the bed level measurements showed a decrease in the total deposition volume inside a groyne field as the submergence level increases. The experiments were conducted for constant sediment mobility in all cases; this condition is violated in the prototype. The lower flow stages in the prototype have lower sediment mobility and vice versa.
- In general, mobile-bed experiments are best to use for comparative studies or to identify governing processes. Upscaling the results to the prototype requires special attention. Direct upscaling of the results of the experiments using scaling-laws yielded an overestimation of the deposition volume inside the groyne fields. This step is best carried out with a model that includes the processes captured in the experiment.
- The vertical concentration profiles deviated from equilibrium. The equilibrium 'Rouse' profiles appeared to form a lower envelope to the actual profiles. Apparently, the vertical concentration profiles in the vicinity of groynes are not governed by dif-

fusion. There is additional sediment entrainment in this region, due to the existence of vortical motions and high turbulence intensity.

- From the observations of the bedform celerity, we found a decreasing trend in the celerity (sediment transport) component into the groyne fields with increasing submergence. The PIV-technique we have utilised to measure bedform celerity is a powerful tool for quantifying instantaneous bedform movement (ripples in this case) on a fully mobile bed. To the best of our knowledge, this is the first time that time-dependent bedform celerity of a mobile-bed has been measured simultaneously in two dimensions. This method is suited for laboratory conditions with concentrations low enough to allow sufficient visibility. In principle, it can also be used to quantify bed-load transport rates, if it can be coupled with a technique to measure the height of the bedforms; e.g. via a stereoscopic technique using two cameras measuring simultaneously from two different angles. Results obtained with the PIV-technique could be further improved, for example by minimising the error in the image correction step by mounting cameras vertically over the area of interest, or by using special high resolution cameras.
- During the last phase of the design and instrumentation of such experiments, pilot tests proved to be vital. During the daily operation, attention has to be paid to starting up the model as explained in Section 4.2.3.
- Conducting this type of experiments proved to be not an easy task, and definitely not a cheap one. Several parameters need to be controlled simultaneously; water supply and discharge, sediment supply and collection, and various measurements, all running at the same time. A single test runs for 40 hours, which is a week and needs another week's preparation. Nevertheless, when it comes to understanding the relevant processes, laboratory experiments remain indispensable and worth the effort.



## Chapter 5

# SYNTHESIS OF THE SMALL-SCALE BEHAVIOUR

### 5.1 INTRODUCTION

In this chapter, we endeavour to analyse the different mechanisms that affect the sediment exchange between the river and its groyne fields, and to evaluate the contribution of each mechanism separately. Moreover, we attempt to aggregate these contributions for larger time scales, in order to evaluate the morphological response of a single groyne field (small spatial scale). Figure 5.1 gives an overview of the mechanisms governing the sediment exchange between the groyne fields and the main channel of a river. A distinction is made between the emerged and the submerged flow stages.

When the groynes are emerged, the ambient flow conditions in the absence of navigation cause a net sediment import into the groyne fields. On the other hand, the navigation-induced water motion causes a net export of sediment from the groyne fields. The small-scale dynamic eddies near the tip of the groyne give rise to local scour, whereas the large-scale circulation between the groynes transports sediment from the main channel into the groyne fields. Secondary ship waves stir the sediment in the shallow groyne fields and primary ship waves generate a significant outflow velocity that transports sediment towards the main channel. These mechanisms are analysed in Section 5.2.

When the groynes are submerged, the effect of navigation vanishes as the cross sectional area of the water body is now much larger compared to the cross sectional area of the passing vessel. The exchange of sediment between the main channel and the groyne fields can be attributed to the combined effect of:

- advection by the flow from the main channel into the floodplain,
- the large-scale turbulence structures,
- diffusion through the mixing layer, and
- the effect of secondary flow due to streamline curvature.

These mechanisms are analysed in Section 5.3.

In Section 5.4 we further discuss the effect of lowering the groynes both on the design flood level and on the sediment exchange between the groyne fields and the main channel. We finish this chapter with some conclusions in Section 5.5.

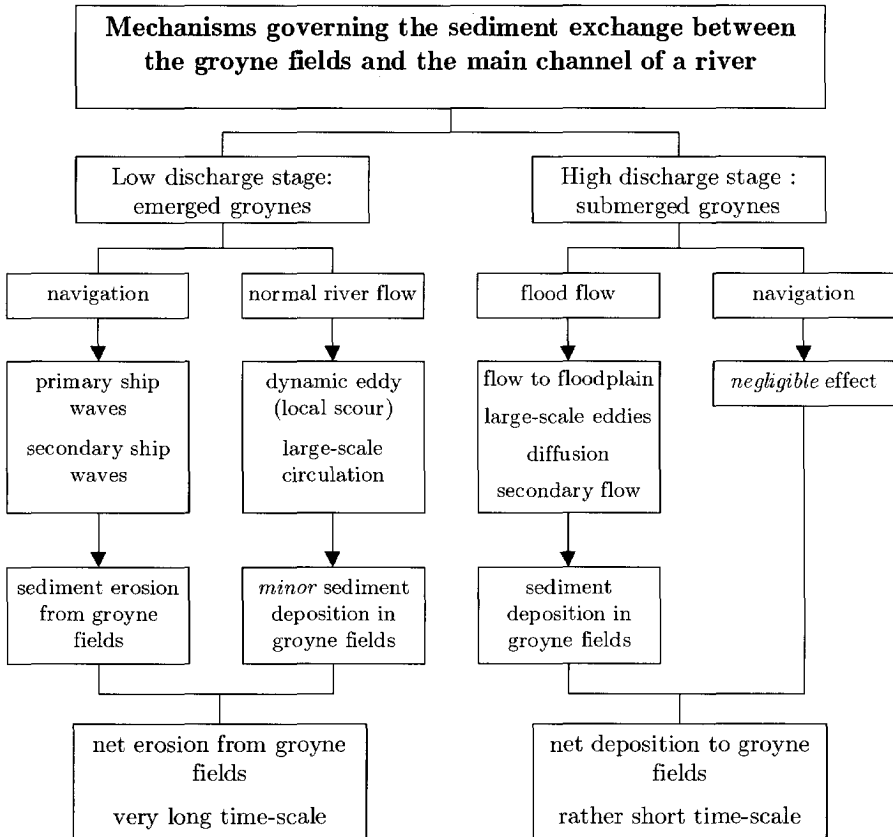


Figure 5.1: Mechanisms governing the sediment exchange between the groyne fields and the main channel of a river.

## 5.2 EMERGED SITUATION

When the groynes are not submerged, the bed level in the groyne fields is determined by the balance between deposition of sediment caused by the circulation pattern and navigation-induced erosion. In the following sections, we try to evaluate each of these contributions and their combined effect.



### 5.2.1 Deposition in the absence of navigation

As deduced from the mobile-bed experiments, sediment is mainly advected towards the groyne fields following the circulation pattern of the primary eddy. The transport takes place through the downstream part of the groyne fields. The velocity in this part has an advective component towards the groyne fields. The total sediment influx to a single groyne field can be written in the following form,

$$Qs_{in} = \int_0^{L_{gf}} \int_{z_{gf}}^{z_w} v_{in} \cdot c \cdot dz dx \quad (5.1)$$

where  $v_{in}$  is the inflow velocity,  $c$  is the concentration in the mixing layer,  $z_w$  is the water level,  $z_{gf}$  is the bed level of the groyne fields, and  $L_{gf}$  is the length of the groyne fields.

We will assume that, due to the high turbulence intensity in the mixing layer, the concentration is always in equilibrium with the local flow conditions, such that:

$$c = \frac{m \cdot u_{mix,c}^{n-1}}{h} \quad (5.2)$$

where  $u_{mix,c}$  is the velocity in the centre of the mixing layer ( $u_{mix,c} \cong 0.5 u_{mc}$ ),  $h$  is the local depth,  $n$  is the power of the flow velocity in the sediment transport formula, and  $m$  is the constant of proportionality in the same formula.

From the analysis of the results of the numerical computations given in Chapter 6, we can estimate an approximate distribution for the inflow velocity along the normal line. This distribution can be described in terms of the maximum inflow velocity  $v_{in,max}$  and the active inflow length  $L_{r1}$ , by a parabolic function as given in Eq. 5.3 (also see Figure 5.2). The distribution of the outflow velocity for  $0 < x < (L_{gf} - L_{r1})$ , is not relevant as we assume that there is no sediment transport from the groyne fields. We indicate that it is negative in order to satisfy the continuity equation. The maximum inflow velocity can also be presented as a fraction of the velocity in the main channel, i.e. ( $v_{in,max} = \alpha_1 \cdot u$ ). Laboratory measurements (e.g. Berg and Uijtewaal, 2002; Uijtewaal *et al.*, 2002; Yossef and Uijtewaal, 2003), and numerical simulations (e.g. Yossef and Klaassen, 2002; Van Schijndel and Jagers, 2003; Rupprecht, 2004), indicate that  $\alpha_1$  is in the order of 0.3.

$$v_{in} = \begin{cases} -\frac{2}{3} v_{in,max} \cdot \frac{L_{r1}}{L_{gf} - L_{r1}} & 0 < x < (L_{gf} - L_{r1}) \\ v_{in,max} \cdot \left[ 1 - \left( \frac{x - (L_{gf} - 0.5L_{r1})}{0.5L_{r1}} \right)^2 \right] & (L_{gf} - L_{r1}) < x < L_{gf} \end{cases} \quad (5.3)$$

With an active inflow length  $L_{r1} = L_{gf}/3$ , we can reduce Eq. 5.1 to;

$$Qs_{in} = \frac{2}{9} \alpha_1 u \cdot L_{gf} \cdot (z_w - z_{gf}) c_{in} \quad (5.4)$$

where  $c_{in}$  is constant if  $u_{mix}$  is constant along the normal line, and  $\alpha_1 \cong 0.3$ .

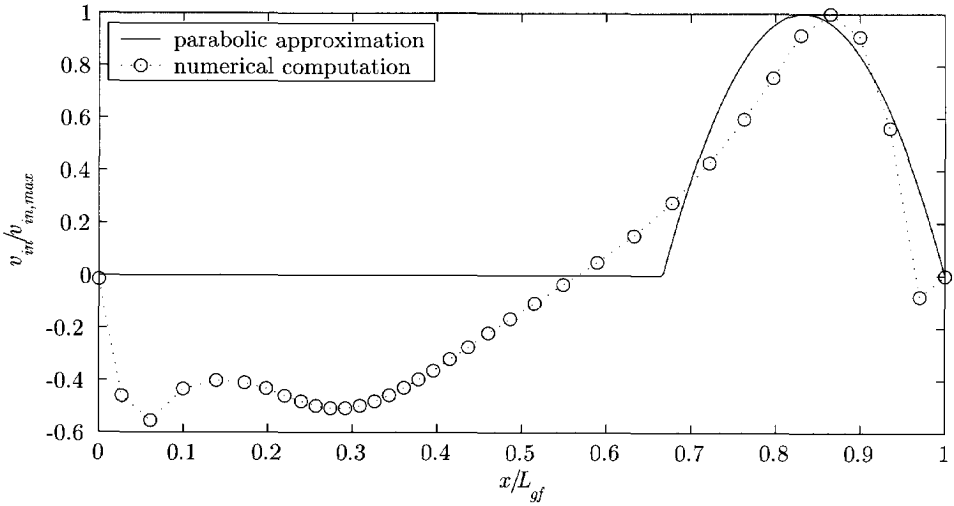


Figure 5.2: Distribution of time-averaged inflow velocity  $\overline{v_{in}(x)}$  during emerged condition; comparison between result from numerical computation for emerged groynes (Rupprecht, 2004), and Eq. 5.3.

Utilising this definition in combination with typical values as found in the River Waal at a discharge of  $1400 \text{ m}^3/\text{s}$ , we arrive at an estimate of the sediment flux into a single groyne field in the emerged situation of  $Q_{s_{in}} = 1.4 \times 10^{-5} \text{ m}^3/\text{s}$ . This is equivalent to an inflow of sediment of  $q_{s_{in}} = 0.07 \times 10^{-6} \text{ m}^2/\text{s}$  per unit length of the morphologically active groynes region. In the absence of navigation, this would result in a monotonous increase of the bed level in the groyne fields by approximately  $0.06 \text{ m/year}$ . However, feedback from the bed level to the sediment supply rate would lead to equilibrium. Assuming a first-order relaxation model, we can describe the time-dependent bed development of the groyne fields. In this case, the temporal variation of  $z_{gf}$  is given by:

$$\frac{\partial z_{gf}}{\partial t} = \frac{1}{T_{mor}} \cdot (z_{gf,e} - z_{gf}) \quad (5.5)$$

in which  $T_{mor}$  is a characteristic adaptation time-scale, and  $z_{gf,e}$  is the equilibrium bed level. We define  $T_{mor,1}$  as the time needed to fill the groyne fields with sediment with the initial sediment transport rate  $Q_{s_{in,0}}$ , and  $z_{gf,e1}$  is an upper-limit equilibrium bed level if groyne fields are filling up.

$$T_{mor,1} = \frac{(1-p) \cdot B_{gf} \cdot L_{gf} \cdot |z_{gf,e1} - z_{gf,0}|}{Q_{s_{in,0}}} \quad (5.6)$$

where  $p$  is the porosity and  $B_{gf}$  is the width of the groyne field.

Applying this expression leads to an estimate of the morphological time-scale for deposition process of  $T_{mor,1} = 47 \text{ years}$ . Note that the solution of Eq. 5.5 takes the form,

$$z_{gf} = z_{gf,e1} - (z_{gf,e1} - z_{gf,0}) \cdot e^{\frac{-t}{T_{morph.1}}}$$

where subscripts (0, e) refer to initial and equilibrium conditions consecutively.

For the time ( $t \rightarrow \infty$ ), the solution is  $z_{gf} = z_{gf,e1}$ , which in this case occurs when the groyne fields are completely filled with sediment to the floodplain level  $z_{fp}$ , i.e. ( $z_{gf,e1} = z_{fp}$ ). This may take place in rivers that have no or low, navigation load, or in cases where the sediment is so fine that it leads to a reduced morphological time-scale.

### 5.2.2 Navigation-induced erosion

For the River Rhine, which is considered to be the backbone of the North western European waterways network, the primary objective of groynes is to provide a fairway of sufficient depth and width (Figure 5.3). The draught of the barges and push-tow units determines the depth criterion, whereas the width of the units and the number of navigation lanes govern the width of the channel. For the River Waal, the most important branch of the River Rhine in the Netherlands, a depth of 2.5 m and a width of 150 m have to be guaranteed during 95% of the time. Further projects are ongoing to enlarge the available dimensions to 2.8 m and 170 m respectively.

Research related to navigation-induced sediment transport is limited to rivers with heavy traffic such as the Mississippi River, the Elbe River, or the Rhine River. Several studies were carried out for the Mississippi River by the US Corps of Engineering, but they focused on situations without groyne fields (e.g. Maynard, 2000; Copeland *et al.*, 2001; Parchure *et al.*, 2001). A list of these studies can be found in USACE (2004). Few studies have examined the effect of navigation on the hydrodynamics and morphodynamics of



Figure 5.3: Pushtow unit in the River Waal near Ewijk, sailing downstream; (courtesy: Wim Uijttewaal, 2004)

the groyne fields (e.g. WL | Delft Hydraulics, 1987; Brolsma, 1988; Ten Brinke *et al.*, 1999; Ten Brinke, 2003; Sukhodolov *et al.*, 2004). Observations from prototype show that navigation strongly influences the hydrodynamics in the groyne fields. The magnitude of velocity fluctuations generated during and after a ship passage greatly exceeds the level of natural velocity fluctuations. The increase in magnitude of velocity fluctuations leads to an increase in the bottom shear stress, and thus to suspension of deposited sediment.

Primary ship waves force an additional outflow velocity, which transports sediment out of the groyne fields. The outflow velocity  $v_{out}(x)$ , has a maximum value ( $v_{out,max}$ ) near the tip of upstream groyne (with respect to the sailing direction), and reduces exponentially with the distance towards the downstream groyne (WL | Delft Hydraulics, 1987). The velocity  $v_{out}(t)$  changes as well, as the sailing unit passes the groyne field. According to the results from laboratory experiments (Brolsma, 1988),  $v_{out}(t)$  can be represented by a parabolic function which first increases then decreases in time. This representation is given in Figure 5.4, and can be described as:

$$v_{out}(x, t) = v_{out,max} \cdot \left[ 1 - \left( \frac{t}{0.5 T_s} - 1 \right)^2 \right] \cdot \exp\left( \frac{x - L_{gf}}{L_{r2}} \right) \quad (5.7)$$

where  $v_{out,max}$  is the maximum outflow velocity from a groyne field,  $L_{r2} \cong 0.2 L_{gf}$  is the active outflow length, and  $T_s \cong 200$  s, is the time of the increased velocity which approximately equals the time that a sailing unit takes to pass a groyne field.

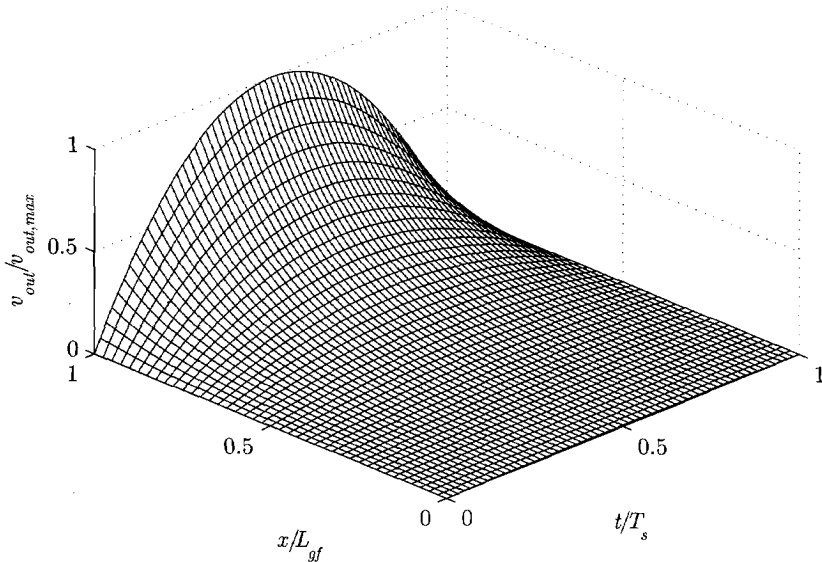


Figure 5.4: Distribution of the outflow velocity from a groyne field during a ship passage.

By integrating the sediment transported across the normal line and over the passage time of a vessel, the navigation-induced sediment efflux ( $Qs_{out}$ ) from a single groyne field can be presented in the following form:

$$Qs_{out} = \alpha_2 f_s \int_0^{T_s} \int_0^{L_{gf}} m v_{out}^n dx \cdot dt \quad (5.8)$$

with  $f_s$  as the frequency of navigation [ $s^{-1}$ ] and  $\alpha_2$  as a calibration coefficient to account for the effect of the return flow.

Utilising this definition in combination with typical values as found in the River Waal, we could estimate the navigation-induced sediment efflux. Using the following values:  $\alpha_2 = 1.0$ ,  $f_s = 4$  ship/hour,  $v_{out,max} = 1.0$  m/s,  $T_s = 200$  s,  $D_{50} = 0.5$  mm, and  $L_{gf} = 200$  m; we find that  $Qs_{out}$  equals  $7.1 \times 10^{-5}$  m<sup>3</sup>/s. Subtracting the inflow component  $Qs_{in}$  yields a net erosion rate of  $5.7 \times 10^{-5}$  m<sup>3</sup>/s during emerged conditions. This is equivalent to a degradation in the bed level of the groyne fields by 0.25 m/year, which is relatively high compared to the findings of ten Brinke (2003) of 0.18 m/year for groyne fields along the southern bank (loaded ships), and 0.13 m/year for groyne fields along the northern bank (empty ships). The results of ten Brinke (2003) were based on neural network analysis of field measurements, and we consider it to be more accurate.

Hence, from here on, the calibration coefficient  $\alpha_2$ , is set to a value of 0.7 yielding a value of  $Qs_{out}$  that equals  $4.97 \times 10^{-5}$  m<sup>3</sup>/s. In the same manner as in the previous section, we utilise a first-order relaxation model to represent the degradation process of the groyne fields due to navigation effect. In this case, the morphological time-scale is defined as:

$$T_{mor,2} = \frac{(1-p) \cdot B_{gf} \cdot L_{gf} \cdot |z_{gf,e2} - z_{gf,0}|}{Qs_{out,0}} \quad (5.9)$$

where  $T_{mor,2}$  is the time needed to empty the groyne fields from sediment, and  $z_{gf,e2}$  is a lower-limit equilibrium bed level if they are completely eroded. In this case equilibrium occurs when the bed level inside the groyne fields equals that of the main channel i.e.  $z_{gf,e2} = z_{mc}$ .

Applying this expression, we reach an estimate to the morphological time-scale of the erosion process  $T_{mor,2} = 13$  years, which is much shorter than the morphological time-scale of the deposition process.

### 5.2.3 Combined effect

The morphological time-scales of both erosion and deposition processes,  $\mathcal{O}(\text{years})$ , are much larger than the time-scale of the transport process,  $\mathcal{O}(\text{minutes})$ . Thus, the combined effect of navigation and flow can be evaluated by estimating the net sediment transport rate ( $Qs = Qs_{in} - Qs_{out}$ ). The temporal variations of  $z_{gf}$  can be written as:

$$z_{gf} = z_{gf,c} - (z_{gf,c} - z_{gf,0}) \cdot e^{-\frac{t}{T_{mor,E}}} \quad (5.10)$$

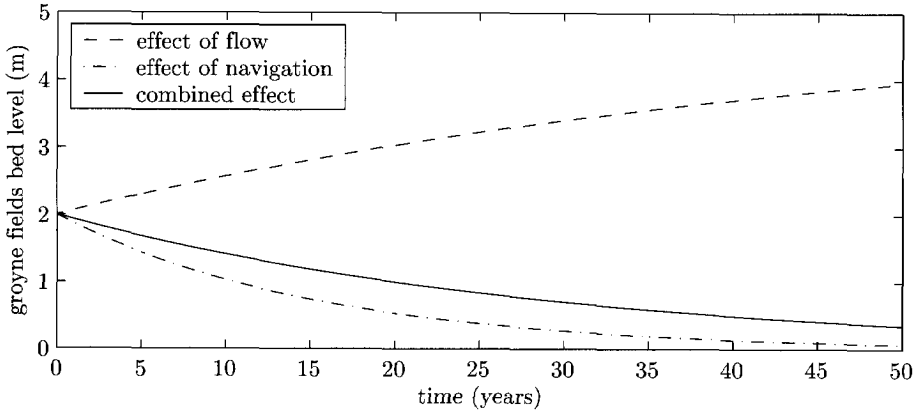


Figure 5.5: Bed development of a groyne field during emerged situation for conditions similar to the Waal River (no floods were considered), measured from main channel level.

with  $T_{mor,E}$  defined as:

$$T_{mor,E} = \frac{(1-p) \cdot B_{gf} \cdot L_{gf} \cdot |z_{gf,e} - z_{gf,0}|}{|Qs_{in} - Qs_{out}|} \quad (5.11)$$

and  $z_c$  defined as:

$$z_c = \begin{cases} z_{c1} = \min(z_w, z_{fp}) & \text{if } Qs_{in} > Qs_{out} \\ z_{c2} = z_{mc} & \text{if } Qs_{in} < Qs_{out} \end{cases} \quad (5.12)$$

Employing typical values in the same manner as in the previous sections, we estimate the temporal variations of the bed level in the groyne fields and its associated time-scale. The result is presented in Figure 5.5 where we can see that the effect of navigation is dominant in this situation leading to a continuous degradation in the groyne fields. The morphological time-scale of which, was found to be 22 years. This is a rather long period considering that the return period of an average flood that would alter this trend is much shorter.

### 5.3 SUBMERGED SITUATION

The sediment transport in the submerged situation may be attributed to a combination of the effects of:

- advection by non-parallel flow (e.g. oblique flow into floodplain),
- residual transport due to large-scale coherent structures,
- diffusion through the mixing layer, and
- the effect of secondary flow.

The first mechanism of transport was considered to be outside the scope of this thesis and was not tested in two experiments presented in Chapter 3 and Chapter 4; hence, it will not be addressed here. The contribution of the other mechanisms will be evaluated in the following sections.

### 5.3.1 Modelling the flow near groynes

In accordance with the findings from the fixed-bed experiment presented in Chapter 3 and as discussed in Section 3.7, the flow near the groynes is modelled as follows (see Figure 5.6):

- 1- The velocity inside the groyne fields is calculated using the Chézy formula:

$$U_{gf} = C_{gf} \sqrt{(h - z_{gf})} i \quad (5.13)$$

- 2- The shear layer between the river and the groyne fields is treated as a free mixing layer. The velocity distribution in the transverse direction across the mixing layer follows a self-similar profile as in conventional mixing layers, e.g. the error function (Uijtewaal and Booij, 2000) or a hyperbolic tangent (Van Prooijen, 2004), (Figure 5.6a; cf. Figure 3.6 and Figure 3.14):

$$U_{mix}(y) = U_{mix,c} + \frac{1}{2} \Delta U \tanh\left(\frac{y_c - y}{\frac{1}{2} \delta}\right) \quad (5.14)$$

Note that the exact nature of the profile does not change the result significantly.

- 3- The large-scale velocity fluctuations in the mixing layer are represented by a ‘perfect’ sine-wave (Figure 5.6b; cf. Figure 3.5); consequently the velocity signals of  $u$  and  $v$  take the following form,

$$\begin{aligned} u &= \bar{u} + \hat{u} \cdot \sin(\omega t) \\ v &= \bar{v} + \hat{v} \cdot \sin(\omega t - \phi_0) \end{aligned} \quad (5.15)$$

- 4- The velocity fluctuations are in phase ( $\phi_0 = 0$ ) in the centre of the mixing layer and out of phase ( $\phi_0 = \pm \pi/2$ ) outside the mixing layer (Figure 5.6c; cf. Figures 3.20, 3.21 & 3.22):

$$\phi_0 = \frac{\pi}{2} \tanh\left(\frac{y_c - y}{\frac{1}{2} \delta}\right) \quad (5.16)$$

- 5- The amplitude of the fluctuations is maximum in the centre of the mixing layer and negligible outside the mixing layer (Figure 5.6d; cf. Figure 3.8):

$$\hat{u} = \sqrt{2} \cdot \beta_1 \cdot \Delta u \cdot \left[ 1 - \tanh\left(\frac{y_c - y}{\frac{1}{2} \delta}\right)^2 \right] \quad (5.17)$$

- 6- The width of the mixing layer is constant in  $x$ -direction, and can be calculated according to Eq. 3.15.
- 7- The wave period  $T_p$  is calculated a function of the mixing layer width and the velocity in the centre of the mixing layer and can be calculated according to Eq. 3.17.

The symbols in the above expressions are defined as follows:

- $i$  = free surface slope in the main channel
- $C_{sf}$  = Chézy coefficient in the groyne region calculated according to the procedures given in Section 3.6 (see Eq. 3.8).
- $U_{mix,c}$  = depth-averaged velocity in the centre of the mixing layer
- $\Delta U$  = velocity difference across the mixing layer, ( $\Delta U = U_{mc} - U_{sf}$ )
- $y_c$  =  $y$  co-ordinate of the centre of the mixing layer
- $\delta$  = width of the mixing layer
- $\bar{u}, \bar{v}$  = time-averaged velocity in streamwise, and transverse direction, respectively,
- $\hat{u}, \hat{v}$  = amplitude of fluctuations of  $u$  and  $v$ , respectively,
- $\omega$  = peak frequency (rad/s);  $\omega = 2\pi/T_p$ , with  $T_p$  as the wave period in seconds,
- $\phi_0$  = phase difference between  $u$  and  $v$  in radians,
- $\bar{v} = 0$ ; as we consider that there is no net flow to/from the groyne fields.

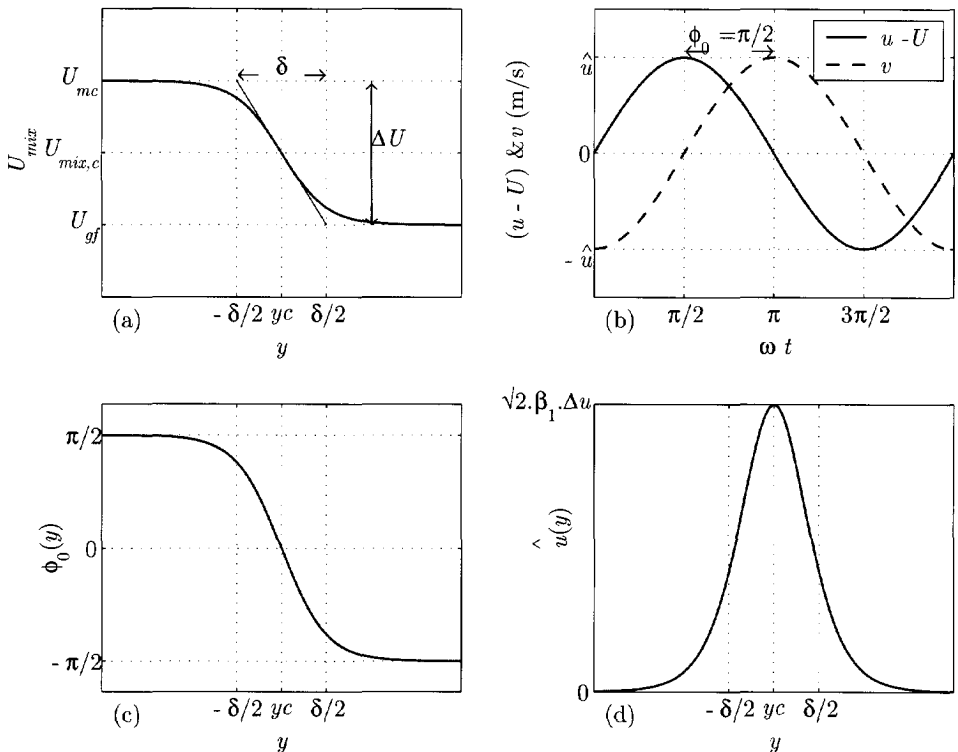


Figure 5.6: Representation for the mixing layer due to groynes. (a) distribution of the velocity in the transverse direction, (b) large-scale velocity fluctuations  $u$  and  $v$  with  $\pi/2$ -phase difference (c) distribution of the phase difference angle (d) distribution of the amplitude of fluctuations.



### 5.3.2 Transport by large-scale coherent structures

Utilising a power-law sediment transport formula ( $qs = m \cdot u^n$ ), we can compute the sediment transport rate associated with the velocity signal given in Eq. 5.15. The transverse sediment transport component due to large-scale flow structures  $qs_{y,LS}$  can be expressed as:

$$qs_{y,LS} = qs \cdot \sin(\alpha_s) \quad (5.18)$$

where:

- $qs$  = the sediment transport rate ( $m^2/s$ )
- $\alpha_s$  = the direction of the sediment transport

The sediment transport rate is calculated according to:

$$qs = m(u^2 + v^2)^{\frac{n}{2}} \quad (5.19)$$

For a horizontal bed and in the absence of secondary flow, the sediment transport follows the direction of the bed shear stress ( $\alpha_s$ ) given by:

$$\alpha_s = \alpha_\tau = \tan^{-1}\left(\frac{v}{u}\right) \quad (5.20)$$

Ignoring the bed slope can be justified by the fact that sediment in this region is mostly in suspension.

The net sediment flux to/from the groyne fields is then evaluated by integrating the sediment transport over one wave period across the normal line, which may be considered the centre of the mixing layer. The average sediment transport rate to the groyne field can be estimated as follows:

$$\overline{qs_{y,LS}} = \frac{1}{2\pi} \int_0^{2\pi} qs_{y,LS} d(\omega t) \quad (5.21)$$

We may further split Eq. 5.21 into two terms, each representing the transport in half a wave period, which is equivalent to an inflow and an outflow contribution to the net sediment flux. Such a distinction allows us to account for the difference in sediment concentration between the main channel region and the groyne fields region. We use a weighing factor to represent that effect.

$$\overline{qs_{y,LS}} = \frac{1}{2\pi} \left( \underbrace{\beta_m \cdot \int_{\phi_0}^{\pi+\phi_0} qs_y d(\omega t)}_{\text{inflow}} + \underbrace{\beta_{out} \cdot \int_{\pi+\phi_0}^{2\pi+\phi_0} qs_y d(\omega t)}_{\text{outflow}} \right) \quad (5.22)$$

where  $\beta_m$  and  $\beta_{out}$  are weighing factors for the effectiveness of sediment transport to/from the groyne fields. A simple representation to the values of  $\beta_m$  and  $\beta_{out}$  can be reached by comparing the adaptation length-scale of suspended sediment transport ( $L_{a,s} = \mathcal{H}\mathcal{U}/w_s$ ) with the distance along the path of a streamline entering (for  $\beta_m$ ), or leaving (for  $\beta_{out}$ ),

the groyne fields. Typical values for  $\beta_{in}$  and  $\beta_{out}$  were found to equal 0.7 and 0.6, respectively.

Notably, the net sediment flux according to this model is determined by the phase difference between the two horizontal velocity components. In general, if  $u$  and  $v$  are in phase ( $\phi_0 = 0$ ) or in antiphase ( $\phi_0 = \pm\pi$ ), the net sediment flux is maximal. For a velocity  $v$  with +ve sign directed towards the groyne fields, if  $\phi_0 = 0$ , the flux is directed into the groyne fields and if  $\phi_0 = \pm\pi$ , it is directed outwards. Furthermore, if  $\phi_0 = \pm\pi/2$ , both the inflow and outflow components in Eq. 5.22 are equal and of opposite direction. Figure 5.7 gives a graphical representation of the effect of the phase difference angle  $\phi_0$  on the transverse component of sediment transport; from which we can use  $q_{s_r}$  as a reduction factor to  $q_{s_{y,LS}}$  for values of  $\phi_0$  at the centre of the mixing layer other than  $\phi_0 = 0$ .

From the results of the fixed-bed experiments, the phase difference in the centre of the mixing layer as evaluated for all the tested cases ranged from  $\phi_0 = 0$  to  $\pi/4$ , with an average value of  $\phi_0 = 0.65$  rad. Accordingly, the corresponding reduction factor to the net transport in the transverse direction has a value 0.8 (see Figure 5.7).

Now, with the knowledge of the flow properties in the main channel we can estimate the sediment transport rate from the main channel to the groyne fields by large-scale coherent structures during the submerged flow situation. An example is given in Figure 5.8 where we can see the distribution of  $q_{s_{y,LS}}$  in the transverse direction, from which we will consider that whatever crosses the centre of the mixing layer i.e.  $q_{s_{y,LS}}(y = y_c)$  ends up in the groyne fields.

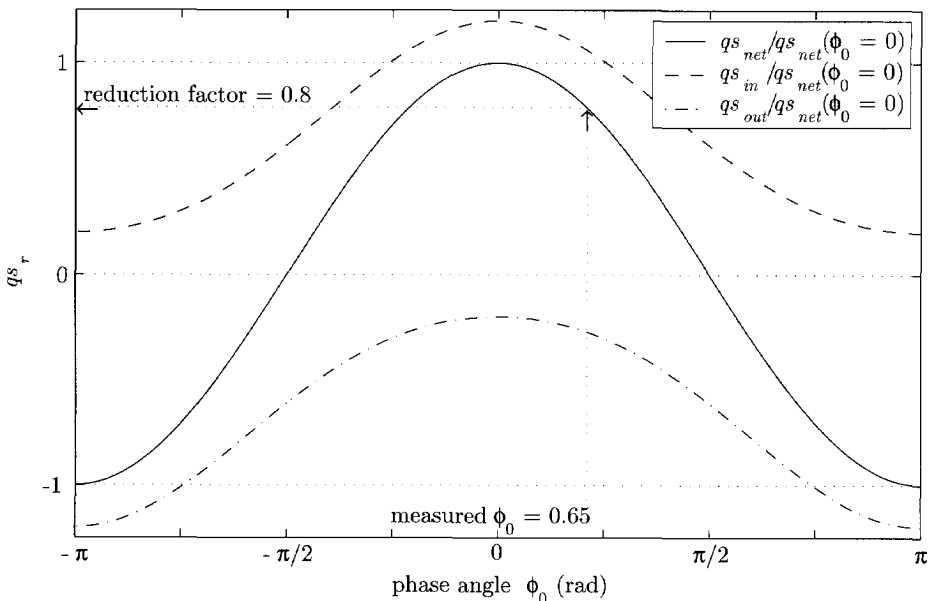


Figure 5.7: The effect of the phase difference ( $\phi_0$ ) between  $u$  and  $v$  on the transverse component of the sediment transport ( $q_{s_{net}}$ ,  $q_{s_{in}}$ ,  $q_{s_{out}}$ ); values are divided by  $q_{s_{net}}(\phi_0 = 0)$ .

### 5.3.3 Diffusive transport

The transverse component of the depth-averaged equation for suspended sediment transport can be written in the form:

$$qs_y = \underbrace{h \cdot \bar{v} \cdot c}_{\text{advection}} - \underbrace{h \cdot \varepsilon_s}_{\text{diffusion}} \cdot \frac{\partial c}{\partial y} \quad (5.23)$$

with  $\varepsilon_s$  as the sediment mixing coefficient,  $v$  is given by Eq. 5.15, and  $c$  is the depth-averaged value of concentration.

Moreover, we relate the concentration to the flow properties via:

$$c = \frac{m \cdot U_{mix}^{n-1}}{h} \quad (5.24)$$

In a straight channel, the mean depth-averaged transverse velocity component  $\bar{v}$  equals zero, i.e. the corresponding advective sediment transport component vanishes. Note that the transport by large-scale coherent structures does not necessarily vanish, as was shown in the previous section. The second term in the right-hand side of Eq. 5.23 represents the diffusive component of sediment transport in the transverse direction. In order to evaluate the diffusive transport term, we need a definition for the horizontal mixing coefficient ( $\varepsilon_s$ ). The sediment-mixing coefficient is related to the eddy viscosity as follows:

$$\varepsilon_s = \phi_s \cdot \beta_s \cdot \nu_t$$

The factor  $\phi_s$  represents the damping effect of the sediment particles on the turbulence structure of the fluid. It is assumed to be dependent on the local sediment concentration. For small concentrations,  $\phi_s = 1.0$  (Van Rijn, 1987). The factor  $\beta_s$  is a proportionality factor that describes the difference in the diffusion of a single sediment particle and the diffusion of a fluid particle. Often, it is argued in literature that the mixing of sediment is not completely analogous to that of water and therefore  $\beta_s$  deviates from unity. Three different theories can be found in literature;  $\beta_s > 1$ , i.e. sediment is diffused at a higher rate than water (e.g. Van Rijn, 1993; Nielsen and Teakle, 2004),  $\beta_s < 1$ , leading to diffusion of sediment at a lower rate (e.g. Muste and Patel, 1997), and  $\beta_s = 1$ , which means that sediment and water are diffused in the same rate (Sisternans, 2002). Sisternans (2002) compared the different theories and concluded that  $\beta_s = 1.0$  is the most appropriate value. The sediment mixing coefficient is therefore taken equal to the horizontal eddy viscosity ( $\varepsilon_s = \nu_t$ ).

Moreover, we adopt the definition of van Prooijen (2004) in which the horizontal eddy viscosity is split into two components, small-scale and large-scale as defined in Eq. 5.25. We further assume that the sediment mixing coefficient is analogous to the eddy viscosity and can be split into two components, as well, one for the small scale ( $\varepsilon_{s,SS} = \nu_{t,SS}$ ) and one for the large scale ( $\varepsilon_{s,LS} = \nu_{t,LS}$ ).

$$\nu_t = \underbrace{\alpha_{v,SS} h u_*}_{\nu_{t,SS}} + \underbrace{\alpha_{v,LS}^2 \delta^2}_{\nu_{t,LS}} \frac{du}{dy} \quad (5.25)$$

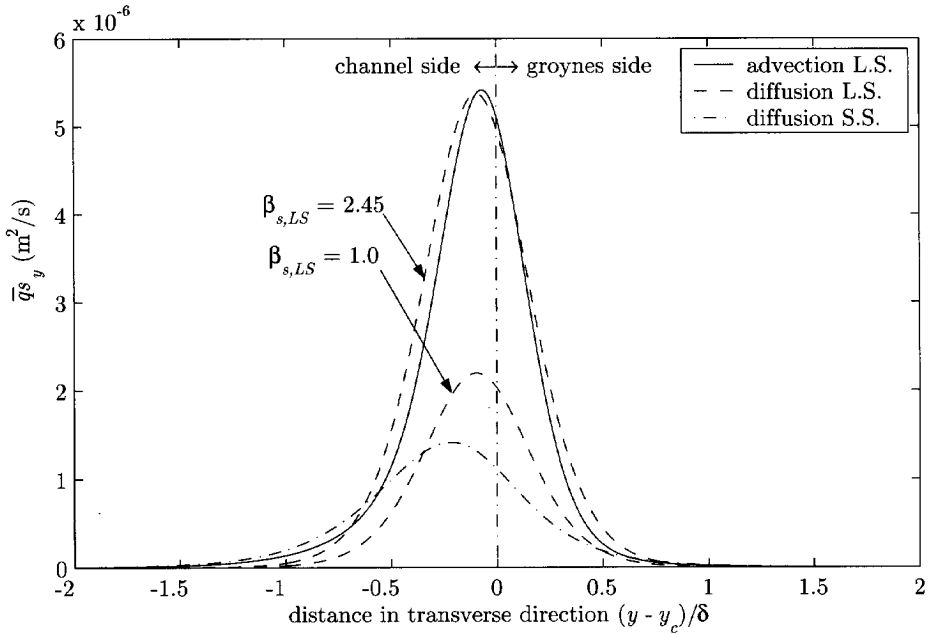


Figure 5.8: Sediment transport rate to the groyne fields due to advection by large-scale coherent structures (solid line), diffusion by small-scale turbulence (dash-dot line), and diffusion by large-scale turbulence for two different values of  $\beta_{s,LS}$  (dash lines); distribution in the transverse direction corresponding to a discharge of  $3000 \text{ m}^3/\text{s}$  in the Waal River.

where:

$\alpha_{\nu,SS}$  = coefficient for small-scale turbulence;  $\mathcal{O}(10^{-1})$ ,

$\alpha_{\nu,LS}$  = coefficient for large-scale turbulence; ( $\alpha_{\nu,LS} = 0.088\text{--}0.124$  for free mixing layer),

$u_*$  = shear velocity,

$\frac{du}{dy}$  = velocity gradient in the transverse direction.

Utilising Eqs. 5.24 & 5.25, we can write the contribution of the diffusive transport term in Eq. 5.23 as follows:

$$q_{s_y, \text{diff}} = \underbrace{-h \cdot \varepsilon_{s,SS} \cdot \frac{\partial c}{\partial y}}_{\text{small-scale}} - \underbrace{h \cdot \varepsilon_{s,LS} \cdot \frac{\partial c}{\partial y}}_{\text{large-scale}} \quad (5.26)$$

It is essential to note that the definition of  $\nu_t$  given in Eq. 5.25 includes the effect of the large-scale coherent structures. Consequently, the diffusive transport by large-scale coherent structures, of which the effect has already been accounted for by evaluating their advective transport contribution as described in the previous section, appears in Eq. 5.26. In order to avoid double counting, we should omit the large-scale component of the diffusive transport (2<sup>nd</sup> term in Eq. 5.26) and evaluate only the diffusive transport based on

the small-scale turbulence. Accordingly, the diffusive transport term is evaluated as follows:

$$qs_{y,diff} = -h \cdot \varepsilon_{s,SS} \cdot \frac{\partial c}{\partial y} \quad (5.27)$$

Results corresponding to a situation similar to the Waal River with a discharge of  $3000 \text{ m}^3/\text{s}$  are presented in Figure 5.8, where we can see that the advective transport by large coherent structures is nearly four times greater than the diffusive transport. We can further observe that the diffusive transport by large-coherent structures (with  $\beta_{s,LS} = 1.0$ ) is much less than the advective transport.

Here, one might argue that in a non-eddy-resolving approach we could use additional diffusion in the mixing layer to account for the additional transport due to large-scale coherent structures. As we see from Figure 5.8, it appears that we can mimic the advective transport by large-scale coherent structures using a diffusion concept through scaling-up the sediment mixing coefficient  $\varepsilon_{s,LS}$ . This can be achieved by increasing the value of the large-scale component of the eddy viscosity  $\nu_{t,LS}$ , e.g. by enhancing the coefficient  $\alpha_{\nu,LS}$  in Eq. 5.25. However, for a correct momentum exchange the value of  $\alpha_{\nu,LS}$  should not differ much from what is found in literature ( $\alpha_{\nu,LS} \cong 0.1$ ), i.e. this increase should affect only the sediment mixing coefficient, implying that  $\varepsilon_{s,LS} > \nu_{t,LS}$ . This brings us back to the choice of a value of  $\beta_s$  higher than unity that should only be effective to  $\varepsilon_{s,LS}$ , which we will therefore call it  $\beta_{s,LS}$ . Values of  $\beta_s$  larger than unity were reported by Tooby *et al.* (1977), and confirmed by Nielsen (1992) where he demonstrated that the effect of eddies which indeed exist within large-scale coherent structures cause sediment particles to spiral away and to be thrown out of the eddies, yielding  $\beta_s$  values higher than unity.

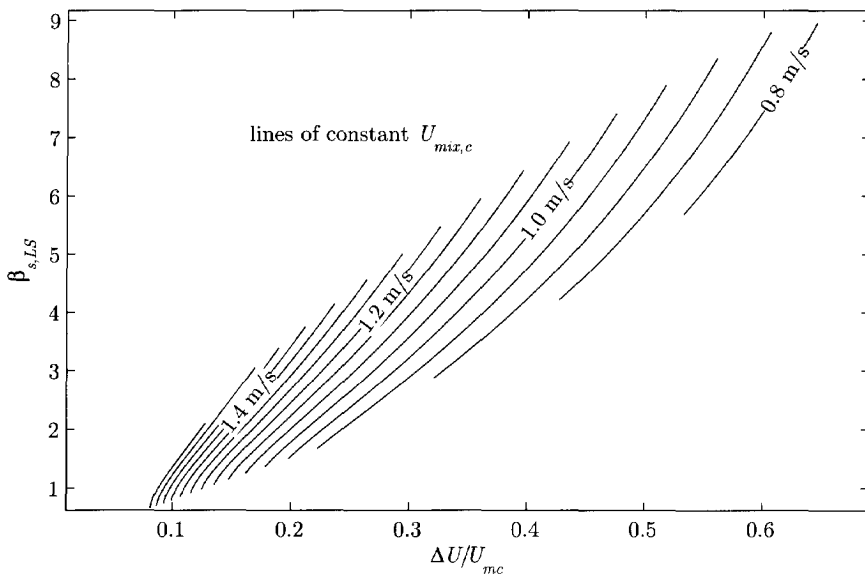


Figure 5.9: Behaviour of  $\beta_{s,LS}$  ( $qs_{diff,LS} = qs_{y,LS}$ ) versus normalised velocity difference for different values of  $U_{mix,c}$ .

To evaluate the behaviour of  $\beta_{s,LS}$  for different hydraulic conditions, we equate the sediment transport rate by large-coherent structures at  $y = y_c$  based on advection as given in Section 5.3.2 with that based on diffusion as given in Section 5.3.3. From Figure 5.9 we see that for a constant  $U_{mix,c}$  there is an increasing tendency of  $\beta_{s,LS}$  as velocity difference across the mixing layer increases. This is rational, as the intensity of the eddies in a mixing layer is directly connected to the velocity gradient across the mixing layer ( $\Delta U/\delta$ ); note that  $\delta$  is constant in our case. With the knowledge of the velocity in both the main channel and groyne fields region, Figure 5.9, can be utilised to predict the value of  $\beta_{s,LS}$ . In the example of Figure 5.8, we can see that the distribution in the transverse direction for transport into the groyne fields by large-scale coherent structures based on diffusion is now similar to that based on advection, if  $\beta_{s,LS} = 2.45$ .

### 5.3.4 Effect of secondary flow

Due to the oscillating velocity in the mixing layer between the main channel and the groyne fields, streamlines are curved, giving rise to curvature-induced secondary flow. To quantify the intensity of this secondary flow ( $I_s$ ) we utilise the expression of the velocity given in Eq. 5.15 to estimate the parametric equations of the streamline.

$$\begin{aligned} x(t) &= \int u dt = \bar{u} \cdot t + \frac{\hat{u}}{\omega} (1 - \cos(\omega t)) \\ y(t) &= \int v dt = -\frac{\hat{v}}{\omega} \cos(\omega t - \phi_0) \end{aligned} \quad (5.28)$$

The time-dependent secondary flow intensity  $I_s$  can be described by an advection-diffusion equation that takes the following form (WL | Delft Hydraulics, 2001a):

$$\frac{\partial}{\partial t} h I_s + \frac{\partial}{\partial x} (h I_s u) + \frac{\partial}{\partial y} (h I_s v) = h \left[ \frac{\partial}{\partial x} \left( D_h \frac{\partial I_s}{\partial x} \right) + \frac{\partial}{\partial y} \left( D_h \frac{\partial I_s}{\partial y} \right) \right] - \frac{h(I_s - I_{s,c})}{T_a} \quad (5.29)$$

with  $D_h$  = horizontal diffusion coefficient,  $I_{s,c}$  = local equilibrium value of  $I_s$  given by:

$$I_{s,c} = \frac{h}{R_s} \sqrt{u^2 + v^2}$$

$R_s$  = the radius of curvature given by:

$$R_s = \frac{(u^2 + v^2)^{\frac{3}{2}}}{u \frac{dv}{dt} - v \frac{du}{dt}}$$

$T_{a,s}$  = adaptation time-scale of secondary flow given by:

$$T_{a,s} = \frac{I_{a,s}}{\sqrt{u^2 + v^2}}$$

$L_{a,s}$  = adaptation length-scale of secondary flow given by:

$$L_{a,s} = \frac{1 - 2\alpha}{2\kappa^2 \alpha} h$$

with  $\alpha = \min[0.5, g^{1/2}(\kappa C)^{-1}]$ , where  $\kappa$  is the Von Kármán's constant and  $C$  is the Chézy coefficient.

The effect of the secondary flow on the sediment transport appears as a correction to the direction of the bed shear stress, which now deviates from the depth-averaged flow direction. The corrected direction of the bed shear stress is calculated using the following expression:

$$\alpha_{\tau,s} = \tan^{-1} \left( \frac{v - \alpha_l I_s \frac{u}{\sqrt{u^2 + v^2}}}{u + \alpha_l I_s \frac{v}{\sqrt{u^2 + v^2}}} \right) \tag{5.30}$$

in which,  $\alpha_l = \frac{2}{\kappa^2} E_s \left[ 1 - \frac{1}{2} \frac{\sqrt{g}}{\kappa C} \right]$ , with  $E_s$  as a tuning parameter (here we take  $E_s = 0.5$ ).

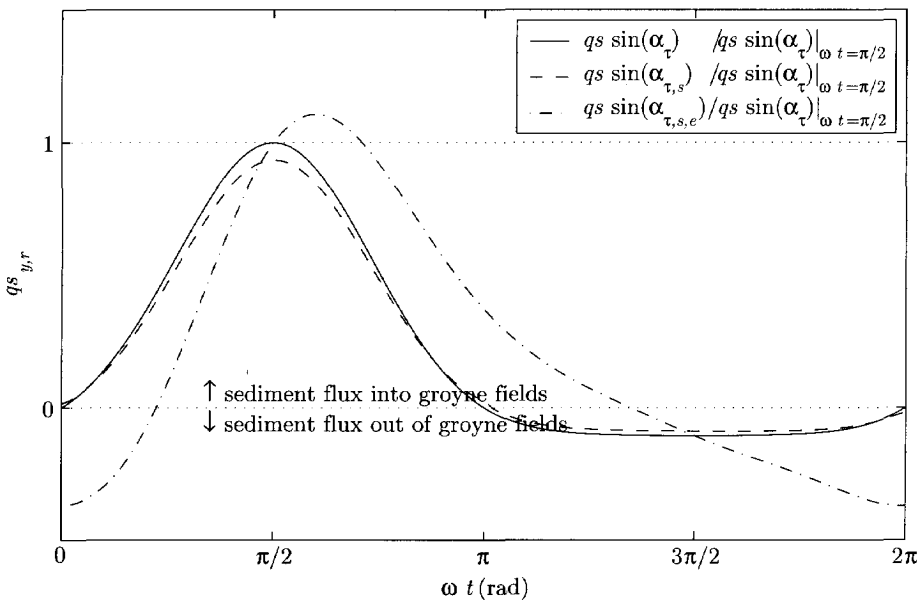


Figure 5.10: Comparison between the transverse component of the sediment transport over one wave period with and without secondary flow correction; values are calculated for  $\phi_0 = 0$ . Dash-dot line is the corrected transport using equilibrium values of secondary flow intensity.

Eq. 5.29 is solved numerically. The implication on the transverse sediment exchange is evaluated by comparing the advective transport by large-scale coherent structures as given by Eq. 5.18 using the corrected bed shear stress angle ( $\alpha_s = \alpha_{r,s}$ ), with that using depth-averaged flow direction ( $\alpha_s = \alpha_r$ ). This comparison is given in Figure 5.10, where we can see that the secondary flow reduces the transverse component of the sediment flux in both directions; around 5% for the inflow part and around 15% for the outflow part. The difference between the inflow and outflow parts is due to the difference in the gradient of the equilibrium secondary flow intensity. This reduction is due to the fact that the streamlines are curved in a way that will always produce secondary flow in the direction opposite to the transverse velocity component.

Due to the difference between the contribution of the inflow and outflow fluxes, the reduction of the inflow part is more significant than that of the outflow part; Consequently, the net sediment flux to the groyne fields is reduced by around 4%. Accordingly, we can conclude that the secondary flow is not a mechanism that is increasing the sediment transport to the groyne fields. In fact, it is rather reducing the net sediment transport to the groyne fields. It would be increasing the net sediment transport to the groyne fields only if we assume that there is an equal contribution for the inflow and the outflow fluxes i.e. when  $\phi_0 = \pm\pi/2$ ; in this case the flux to the groyne fields is minimal anyhow.

It is worth mentioning that, due to the relatively long adaptation length-scale, thus time-scale, of the secondary flow intensity, the secondary flow intensity  $I_s$  stays far from its equilibrium value,  $I_{s,e}$ . A first estimate to the bed shear stress angle ( $\alpha_{r,s,e}$ ) using equilibrium secondary flow intensity ( $I_{s,e}$ ) would have yielded a significantly different sediment transport to the groyne fields (see Figure 5.10). This emphasises the importance of including the adaptation process in models of this type of transport phenomena.

### 5.3.5 Combined effect

In the three previous sections, we have estimated the contribution of each of the mechanisms transporting sediment into groyne fields in a straight reach. These mechanisms were; advection by large-scale coherent structures, diffusion through the mixing layer, and the effect of secondary flow that is incorporated as correction to the direction of the advective sediment transport component. The effects of these mechanisms are added to reach the total sediment transport into the groyne fields per unit length of the normal line.

$$qs_y = \underbrace{qs_{y,LS}}_{\substack{\text{corrected for;} \\ \phi_0 \neq 0 \\ \text{secondary flow}}} + \underbrace{qs_{y,diff}}_{\substack{\text{small-scale} \\ \text{Eq. 5.27}}} \quad (5.31)$$

From the results of the mobile-bed experiment, we were able to identify that sediment inflow to the groyne fields takes place across a segment of the normal line that measures around  $\frac{2}{3}$  of the length of the groyne fields. Thus, the effective sediment transport rate to a single groyne field equals,

$$Qs_y = \frac{2}{3} L_{gf} qs_y \quad (5.32.)$$



Again, we use a first-order relaxation model to describe the time-dependent bed development of the groyne fields. In this case, the morphological time-scale is defined as,

$$T_{mor,S} = \frac{(1-p) \cdot B_{gf} \cdot L_{gf} \cdot |z_{gf,e3} - z_{gf,0}|}{Qs_{y,0}} \quad (5.33)$$

where  $T_{mor,S}$  is the time needed to fill the groyne fields with sediment, and  $z_{gf,e3}$  is an upper-limit equilibrium bed. In this case equilibrium occurs when the bed level inside the groyne fields equals that of the floodplain i.e. ( $z_{gf,e3} = z_{gf,e1} = z_{fp}$ ).

Applying this expression, we reach an estimate to the morphological time-scale of the deposition process during the submerged situation that is largely dependent on the hydraulic conditions. For conditions similar to the Waal River and depending on the magnitude of the flood,  $T_{mor,S}$  ranges from one to five years. This is much shorter than the time-scale of the erosion process during the emerged condition. However, one must not forget that the total duration of floods is much shorter than that of low flow conditions.

### 5.3.6 The effect of stage

As we have mentioned in the previous section, the sediment deposition into the groyne fields and its associated morphological time-scale is strongly dependent on the hydraulic conditions. To analyse its behaviour during different submergence conditions, we employ a schematic case that is representative to the situation as in the Waal River.

To start with, we presume a three-sections compound channel consisting of a 260 m wide main channel, two 60 m wide groyne fields with 200 m spacing between the groynes, and two 500 m wide floodplains (Figure 5.11). The bed level of the floodplains and the crest level of the groynes are both at 7.0 m above the bed level of the main channel. The bed level of the groyne fields is 2.0 m above the main channel.

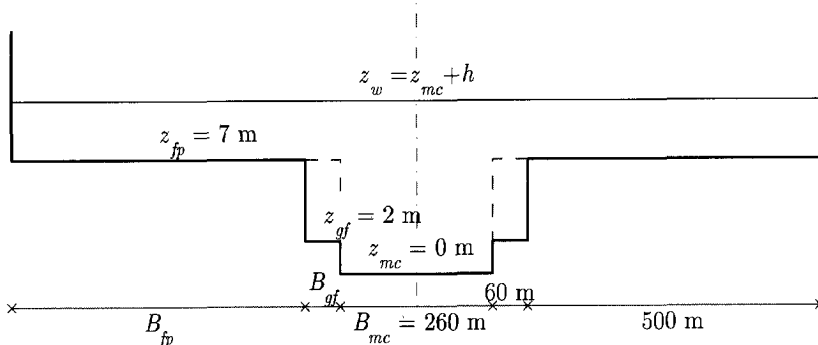


Figure 5.11: Schematic cross section.

The bed roughness of the main channel and the floodplain are represented by constant Chézy coefficient of  $40 \text{ m}^{1/2}/\text{s}$  and  $25 \text{ m}^{1/2}/\text{s}$ , respectively. The resistance in the groynes region is represented by a Chézy coefficient that is calculated according to Eq. 3.8, (Section 3.6). The slope of the main channel is assumed to be constant ( $i = 1.0 \times 10^{-4}$ ). We further consider that the discharge  $Q$ , and the height of the groynes  $h_g$ , are given quantities. Accordingly, we can compute the discharge distribution between the three sub-channels as well as the velocity in each of these sub-channels. Utilising the procedures given in the previous sections, we can further estimate the sediment supply rate to the groyne fields ( $qs_y$ ) for different combinations of  $Q$  and  $h_g$ .

Figure 5.12(upper row) demonstrates the behaviour of the sediment supply rate to the groyne fields ( $qs_y$ ) as a function of the discharge  $Q$  (Figure 5.12a), and the submergence ratio  $h/h_g$  (Figure 5.12b). Figure 5.12(lower row) shows the behaviour of  $qs_{y,r}$ , which is the transport into the groyne fields normalised by the sediment transport rate in the main channel, such that  $qs_{y,r} = qs_y / qs_{mc}$ . Figure 5.13 gives a more comprehensive picture of the behaviour of  $qs_y$  and  $qs_{y,r}$ .

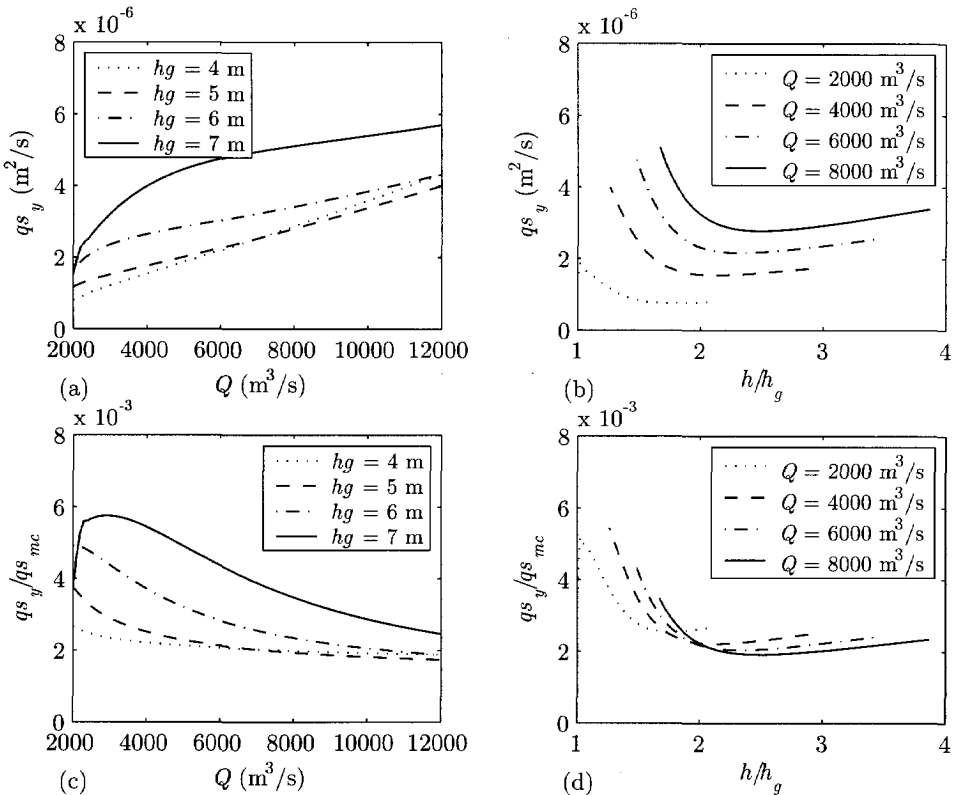


Figure 5.12: Sediment transport rate to the groyne fields versus (a) the river discharge, and (b) the height of the groynes; normalised by the transport rate of the main channel (c) & (d).

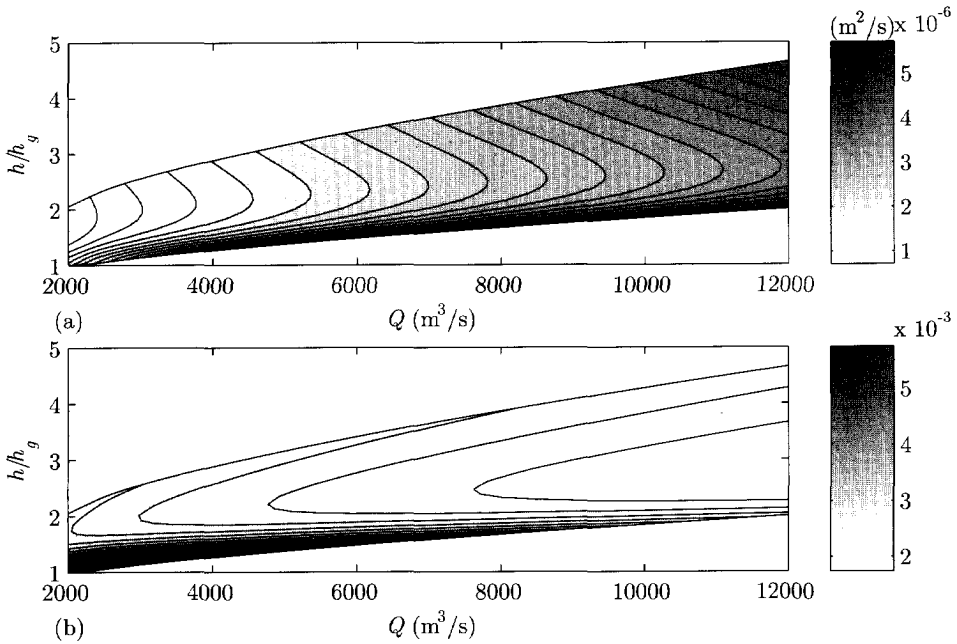


Figure 5.13: Contour plot for (a)  $qs_y$  and (b)  $qs_{y,r} = qs_y/qs_{mc}$ , versus the discharge ( $Q$ ), and the submergence ratio ( $h/h_g$ ).

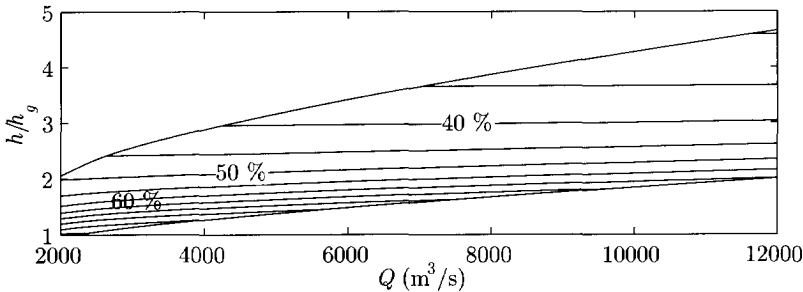


Figure 5.14: Relative contribution of advective transport to the total sediment influx to the groyne fields.

From Figure 5.12a, we can see that for a given groyne height the sediment input into the groyne fields increases as the discharge increases; i.e. a higher flood yields a higher deposition volume inside the groyne fields (Figure 5.13a). However,  $qs_{y,r}$ , as represented in Figure 5.12c, shows a different behaviour that can be characterised by an initial increase followed by a decline in  $qs_{y,r}$  with peak point that moves towards a lower discharge value as the groyne height decreases (i.e. increase in submergence ratio  $h/h_g$ ) see Figure 5.13b. The initial increase in  $qs_{y,r}$  is due to the initial rapid increase of the mean velocity in the centre of the mixing layer with respect to the main channel velocity. Then, the decline of  $qs_{y,r}$  takes place as the velocity in the groyne fields region further increases leading to a

decrease in the velocity gradient across the mixing layer that in turn reduces the mixing between the main channel and the groyne fields. This effect is most pronounced in the case of low groynes where the transport by large coherent structures decreases for large submergence ratios while transport by diffusion becomes dominant (see Figure 5.14).

The effect of relative submergence  $h/h_g$  is illustrated in Figure 5.12b and Figure 5.12d. From Figure 5.12b we can see that for a given  $Q$  the sediment supply rate to the groyne fields initially descends steeply as the submergence level increases. Subsequently, it increases again, but less steeply, as  $h/h_g$  further increases. A similar behaviour can be observed for  $qs_{y,r}$  (Figure 5.12d), yet in this case the lines for the different discharges are closer to one another.

This behaviour can be explained by considering the relative contribution of advection and diffusion separately (Figure 5.14). The declining part of  $qs_y$  is attributed to the reduction in the advective component of the sediment influx. By increasing the submergence, the velocity in the groyne fields increases. Consequently, the velocity gradient across the mixing layer and hence the intensity of the large-scale coherent structures decreases. Further increase in submergence increases the velocity in the centre of the mixing layer that leads to increasing the contribution of the diffusive transport. The line of 50 % in Figure 5.14 distinguishes between the range of dominant advective transport and dominant diffusive transport, from which we see that, at low submergence levels ( $h/h_g \lesssim 2$ ) advection by large coherent structures is more dominant than diffusion. Furthermore, we see that the contour lines in Figure 5.14 are almost parallel to the horizontal axis, implying that the discharge hardly plays a role in the relative contribution of either mechanism.

## 5.4 EFFECT OF LOWERING THE GROYNES

Lowering the groynes will affect both the hydrodynamics and the morphodynamics of the river. The effective resistance in the groynes' sub-channel will decrease as a result of lowering the crest level of the groynes. Thus, it will increase the conveyance capacity of the river. The changes in the hydrodynamics will have consequences on the morphodynamics of the main channel, as well as on the exchange of sediment between the main channel and the groyne fields. Here, we evaluate the effect of lowering the groynes on the design flood level and on the exchange of sediment between the main channel and the groyne fields.

### 5.4.1 Effect on flood level

The discharge through the groynes region will increase as a result of lowering the groynes. Accordingly, the normal flow depth will decrease leading to a reduction in the flood level. Utilising the schematic cross-section in Figure 5.11 in combination with the definition of the groynes' resistance given in Section 3.6, we can reconstruct the stage-discharge relation of the river for different groynes' crest levels. Figure 5.15 gives an idea about the effect of lowering the crest level of the existing groynes on the normal flow

depth. We can see that the effect of lowering the groynes is very significant for low floods. For example if we lower the height of the existing groynes from  $h_g = 7.0$  m to 6.0 m (i.e.  $\Delta h_g = 1.0$  m), the flow depth corresponding to a flood of  $3000 \text{ m}^3/\text{s}$  will be reduced by some 12.0 cm.

The motive behind lowering the groynes is to gain additional safety against floods without increasing the height of the existing dikes. Thus, the reduction in water level due to lowering the groynes is only relevant for the design flood condition. From Figure 5.15 we can see that the effect of lowering the groynes on the design flood level is in the order of few centimetres. Lowering the groynes by 1.0 m will reduce the water level of the design flood by approximately 4.0 cm. In fact, the maximum possible water level reduction by lowering the groynes is only 6.0 cm.

The insensitivity of the water level to groynes lowering under design flood conditions is due to the fact that the blockage by groynes in this case is relatively small. The resistance of the groynes is represented by a drag formula that is a function of the blockage.

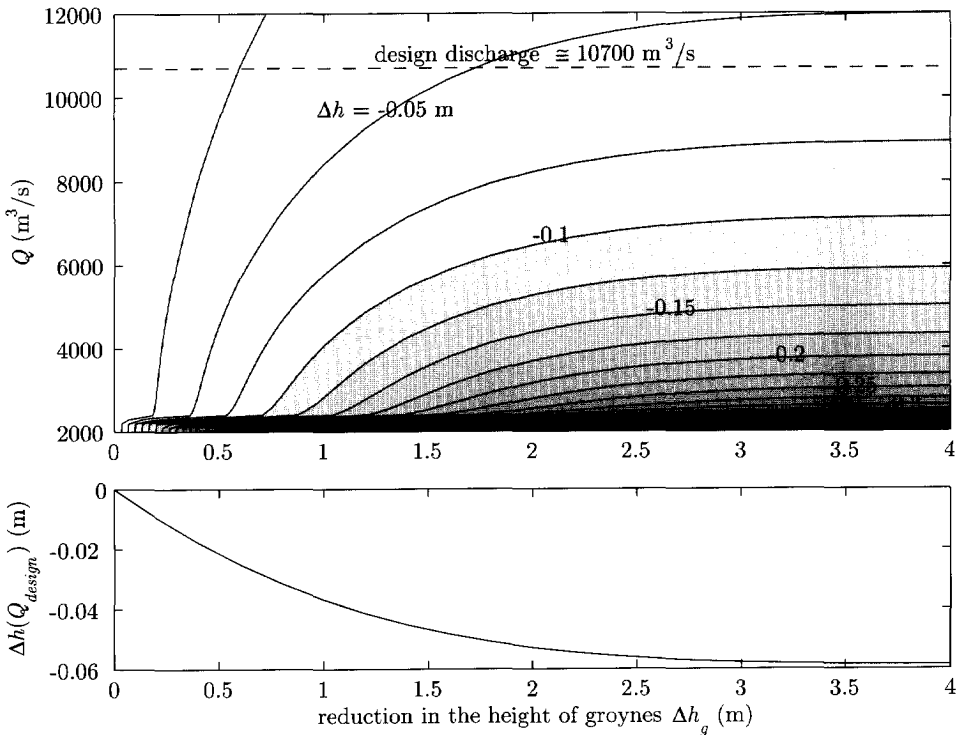


Figure 5.15: Effect of lowering the groynes; (upper panel) contour plot of the change in flow depth  $\Delta h = h(h_{g, new}) - h(h_{g, 0})$  as a function of  $Q$ , and  $\Delta h_g$  (the reduction of the groynes height from its current situation of  $h_g = 7$  m); (lower panel)  $\Delta h$  for the design discharge.

In the design flood situation, the blockage by the groynes is small; accordingly, the value of the effective Chézy coefficient in the groyne fields region is already very close to that of the main channel (see Eq. 3.8). Hence, it is insensitive to changes in the blockage ratio.

#### 5.4.2 Effect on sediment supply to the groyne fields

As we have demonstrated in the previous section, lowering the groynes will increase the velocity in the groynes region. This will reduce the velocity gradient across the mixing layer. Consequently, the exchange of sediment between the main channel and the groyne fields will be altered. Figure 5.16 gives an idea about the behaviour of  $qs_y$  and  $qs_{y,r}$  as a function of the height of the groynes  $h_g$  and the discharge  $Q$ . It shows that lowering the groynes gives an analogous effect to increasing the submergence ratio.

Although we can detect minima of  $qs_y$  and  $qs_{y,r}$  (dashed lines in Figure 5.16), lowering the groynes by one or two metres will always reduce the sediment influx to the groyne fields. To evaluate the effect of lowering the groynes, we calculate the relative change in the sediment supply rate to the groyne fields  $\Delta qs_{y,r}$  as a function of  $Q$ , and  $\Delta h_g$ :

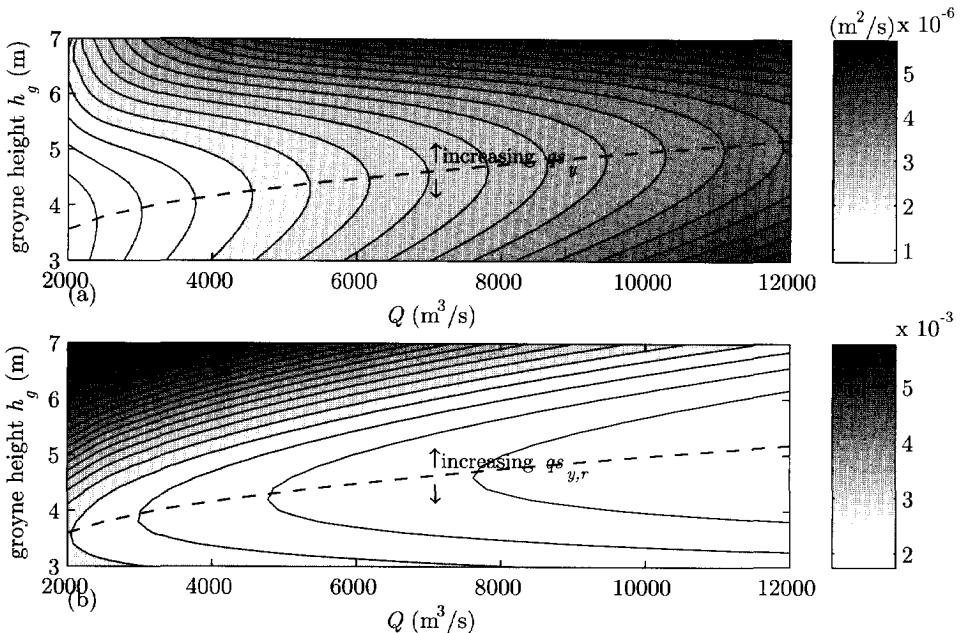


Figure 5.16: Contour plot for (a)  $qs_y$  and (b)  $qs_{y,r} = qs_y/q_{smc}$ , versus the discharge ( $Q$ ), and the height of the groynes ( $h_g$ ).

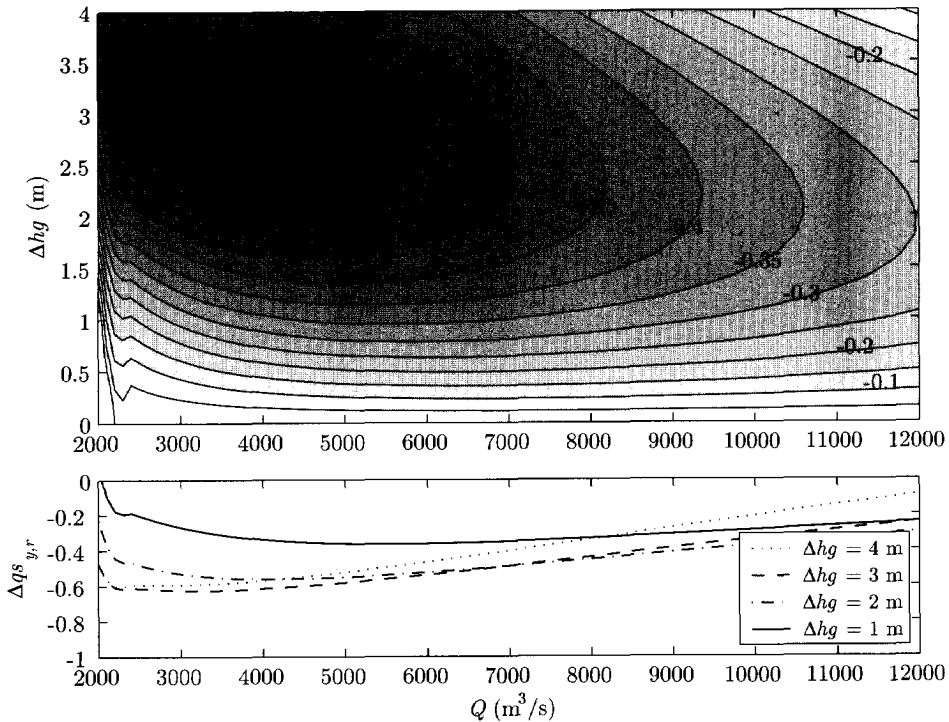


Figure 5.17: Effect of lowering the groynes; (upper panel) contour plot of the change in relative sediment supply rate to groyne fields  $\Delta q_{s,y,r}$  as a function of  $Q$ , and  $\Delta h_g$ ; (lower panel)  $\Delta q_{s,y,r}$  for some chosen values of  $\Delta h_g$ .

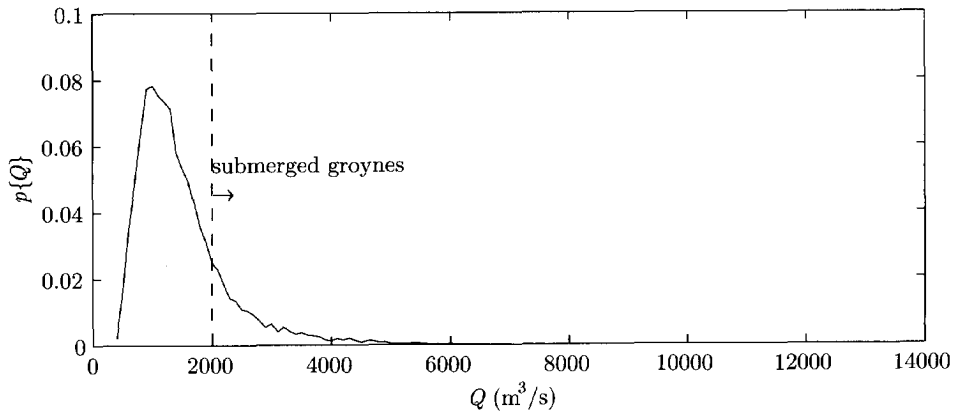


Figure 5.18: Discharge of the River Waal; probability density  $p\{Q\}$  estimated from daily records in the period from 1945 to 1997 (with  $dQ = 100 \text{ m}^3/\text{s}$ ).

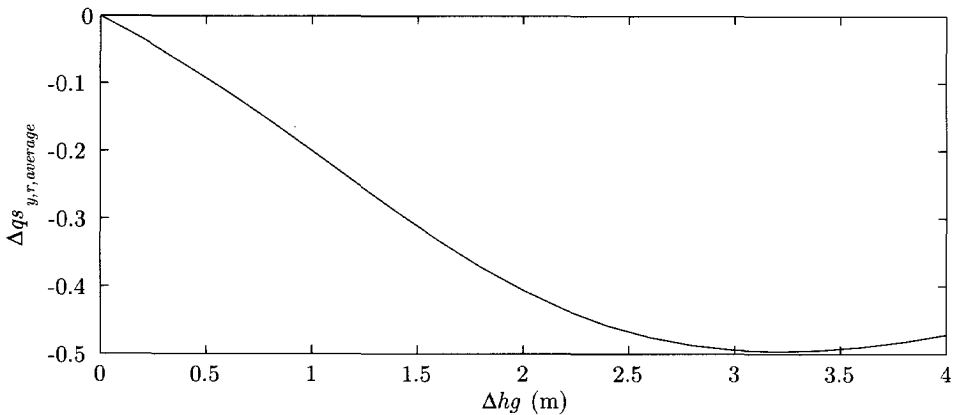


Figure 5.19: Relative change in sediment supply to the groyne fields due to lowering the groynes.

$$\Delta q_{s_{y,r}} = \frac{q_{s_y}(h_{g,ncw}) - q_{s_y}(h_{g,0})}{q_{s_y}(h_{g,0})} \quad \text{with } h_{g,0} = 7.0 \text{ m}$$

The result is given in Figure 5.17 where we can see that reducing the groynes reduces the sediment supply rate to the groyne fields by values that can reach some 60 % if we lower the groynes by 3.0 m. Lowering the groynes by 1.0 m will reduce the sediment flux to the groyne fields by a value that may reach 30 % of its original value. The extent of this reduction depends on the discharge (Figure 5.17).

To estimate the effective reduction in the sediment supply due to lowering the groynes, we need to determine the weighted-average of  $\Delta q_{s_y}$ . ( $\sum p_i \Delta q_{s_y,i}$ ) Employing the historical records of the discharge of the River Waal, we are able to deduce its probability density  $p\{Q\}$  (Figure 5.18) which we then utilise to estimate the weighted-average of  $\Delta q_{s_y}$ . The result is presented in Figure 5.19 from which we see that lowering the groynes by 1.0 m leads to a total reduction of 20 % in the sediment supply to the groyne fields.

## 5.5 CONCLUSIONS

In this chapter, the sediment exchange process between the main channel and the groyne fields of a river has been investigated. The following mechanisms have been analysed:

- Emerged situation
  - Advective transport in the absence of navigation
  - Navigation-induced erosion from groyne fields
- Submerged situation
  - Advective transport due to large-scale coherent structures,
  - Diffusive transport through the mixing layer
  - the effect of secondary flow was evaluated and found to be not significant



The contributions of all mechanisms were evaluated and their associated morphological time-scales were estimated for conditions similar to the Waal River. The following conclusions and recommendations could be drawn from the result of the analysis given in this chapter.

### 5.5.1 Effect of navigation

An analytical formulation was developed in Section 5.2.2 to estimate the effect of navigation. In this formulation, we used a representative outflow velocity ( $v_{out}$ ) from the groyne fields to represent the navigation-induced water motion. It is worth mentioning that the definition of  $v_{out}$  is far from trivial. A correct estimate of  $v_{out}$  should be a function of the ship speed, dimensions, draught, its sailing distance from the normal line, the groyne field dimensions, the wetted area of the navigation channel and the flow velocity. Nevertheless, based on fleet characteristics, one can distinguish classes of ships and define the frequency distribution corresponding to every class, whence it is possible to estimate the sediment efflux from the groyne fields ( $Q_{s_{out}}$ ). Alternatively, we can work with overall representative navigation characteristics: we define  $v_{out}$  and frequency  $f_s$  such that they yield the same  $Q_{s_{out}}$  as calculated from the full characteristics of the fleet. Note that the frequency of navigation is an important aspect that we need to consider when trying to assess the navigation-induced erosion from a groyne field. Due to secondary ship waves, sediment is kept in suspension until long after a vessel has passed the groyne field. The passage of a later vessel while sediment is still in suspension will cause more sediment to be transported out of the groyne field (cf. Sukhodolov *et al.*, 2004).

An accurate identification of the navigation-induced erosion from the groyne fields is a difficult task that requires further attention. Field measurements carried out by ten Brinke (2003) revealed the complexity of identifying the effect of navigation due to the interaction between various elements that is inherent to real-life rivers.

### 5.5.2 Morphological time-scales

In situations with emerged groynes, deposition of sediment takes place due to the advective transport in the absence of navigation with a morphological time-scale estimated at 47 years for the Waal River (Section 5.2.1). Erosion takes place due to the navigation-induced water motion with a significantly smaller morphological time-scale (Waal: 13 years; see Section 5.2.2). The net response of the bed level in the groyne fields during the emerged condition depends on the balance between the two fluxes. Because the sediment efflux is generally greater than the influx, net erosion takes place with a morphological time-scale somewhere between the deposition and the erosion time scales (Waal: 22 years; see Section 5.2.2).

In the submerged situation, advective transport by large-scale coherent structures is generally more dominant than the diffusive transport. The morphological time-scale of the deposition process in this case was found to range from one to five years (Section 5.3.5). The effect of the stage was analysed, as well. For relative submergence  $h/h_g \leq 2$ , the sediment supply to the groyne fields decreases with the increase of  $h/h_g$ . This result

agrees with the observations from the mobile-bed experiments presented in Chapter 4 where we tested relative submergence levels upto  $h/h_g = 2$ .

Comparing the morphological time-scale of the erosion process with that of the deposition process makes little sense, because the equilibrium states for erosion or depositions only will probably never be reached. The ratio of the duration of periods of continuous erosion or individual flood events and relevant morphological time-scale is a more useful parameter. The duration of a flood is roughly 10% of the estimated morphological time-scale, which is the also the order of magnitude as the duration ratio for the erosion process. This indicates that the beaches of the groyne fields may will be in a state of dynamic equilibrium. The general tendency of erosion during the emerged situation and deposition during floods is confirmed by the field measurements reported by ten Brinke (2003).

### 5.5.3 Lowering the groynes

The reduction in the design flood level due to lowering the groynes was evaluated in Section 5.4.1. The result shows that this reduction amounts only to 4 cm. This is less than the estimates in the LPR-report (1996) which stated that "*Lowering the groynes with 0.5 and 1.0 m results in an average reduction of high water levels by between 0.05 and 0.10 m*". It is important to realise that, the estimates made in Section 5.4.1 were based on a schematic channel, not on a numerical model of the real-life river (as in the LPR-report). Moreover, in our case, the groynes were represented as large obstacles with a drag resistance, whereas, in the LPR-report the groynes were represented as submerged weirs. Apparently, the two ways of schematising the groynes deviate from one another.

Lowering the groynes by 1.0 m will reduce the sediment supply rate to the groyne fields by approximately 20% during the submerged conditions. It will inflict no change on the sediment exchange during the emerged situation, except for the small range of discharges on the edge between emerged and submerged situations.

### 5.5.4 Further improvements

From the findings of the analysis presented in this chapter, it is recommended to:

- carry out a detailed laboratory experiment to study navigation-induced erosion in groyne fields,
- carry out a desk study, and if necessary a laboratory investigation that focuses on the best representation of groynes in one-dimensional models during flood conditions, and
- study the effect of non-parallel flow (e.g. oblique flow into floodplain), on the sediment balance of the groyne fields.

## Chapter 6

# NUMERICAL MODELLING OF A RIVER WITH GROYNES\*

### 6.1 INTRODUCTION

In this chapter, we utilise a process-based model to study the intermediate-scale morphological effect of a series of groynes in a river. We attempt to evaluate the sediment budget of the groyne fields, as well as the morphological behaviour of the navigation channel in their vicinity. The aim is to provide a methodology that enables the river manager to take decisions concerning possible dredging activities.

As demonstrated in Chapter 3 for non-submerged groynes, the flow field is predominantly two-dimensional, with mainly horizontal eddies (cf. Krebs *et al.*, 1999; Nassiri *et al.*, 1999). The eddies shed from the tips of the groynes and migrate in the flow direction. These eddies have horizontal dimensions in the order of tens of meters and time-scales in the order of minutes. In the standard flow simulations, these motions are usually not resolved, due to a too coarse grid, too large time steps and, more importantly, the use of inadequate turbulence modelling. In order to reproduce the flow pattern near groynes correctly, using for example a  $\kappa$ - $\epsilon$  model, it is necessary to introduce substantial modifications (Tingsanchali and Maheswarn, 1990; Ouillon and Dartus, 1997; Peng *et al.*, 1997). Previous work, however, has shown the shortcomings of such an approach (Bijvelds *et al.*, 1999). We therefore try to simulate the quasi-2D turbulence and model the 3D turbulence with well-known closures. We apply a two-dimensional depth-averaged model, taking an eddy-resolving approach. This type of flow modelling is called horizontal large eddy simulation, further refereed to as HLES.

In this chapter, we will present the application of a 2DH-morphodynamic model coupled with HLES on a schematic case of a river with groynes. Numerical simulations of the experiments described in Chapter 3 (Van Schijndel and Jagers, 2003; Uijttewaai and Van Schijndel, 2004) showed large discrepancies between the experiments and the 2DH-Model

---

\* An excerpt from this chapter was published as: YOSSEF, M. F. M., and KLAASSEN, G. J. (2002). "Reproduction of groynes-induced river bed morphology using LES in a 2-D morphological model" In: *River Flow 2002 - Proc. of the Int. Conf. on Fluvial Hydraulics*, Louvain-la-Neuve, Belgium, 1099-1108.

results for the submerge case. Therefore, the submerged-groynes situation was not modelled. In this chapter, the groynes are emerged. Moreover, local scour near the tips of the groynes is not considered in detail, because sediment transport by the shedding vortices is insufficiently covered by the model.

## 6.2 RELEVANCE

For the River Rhine, which is considered the backbone of the Northwest European waterways network, the primary objective of groynes is to provide a fairway of sufficient depth and width. The draught of barges and pusher units determines the depth criterion, whereas the path width of the units and the number of required lanes govern the width of the channel. For the River Waal, the most important branch of the Rhine in the Netherlands, a depth of 2.5 m and a width of 150 m are required during 95% of the time. Projects are ongoing to enlarge the available dimensions to reach 2.8 m and 170 m, respectively. However, the very existence of groynes generates large-scale turbulence causing complex local morphological changes. These changes are characterised by a scour hole followed by a deposition area. The latter appear in the multi-beam soundings during dredging operations as red areas (colour convention to highlight the required dredging locations). Accordingly, they are often called '*groyne flames*'. These features usually extend some tens of meters towards the centreline of the navigation channel. During low flow conditions, they often determine the critical navigation depth and the locations where maintenance dredging is needed. It is of extreme importance to the river manager to predict which are the critical locations along the river that need dredging to meet the navigation requirements, and how frequently that needs to be done. To fulfil this need, it is important to predict the morphological development of groyne flames.

With the developments of morphodynamic models, it now appears that these models can be used to answer practical questions related to morphological developments. Yet, the commonly used models, when applied to a river with groynes, poorly reproduce the morphological development in the vicinity of groynes, as well as in the main channel. One of the possible causes is the presence of large-scale horizontal eddies (i.e. eddies with horizontal axis) that govern the local sediment transport (Liek, 2000; Rupprecht, 2004).

## 6.3 DESCRIPTION OF DELFT-3D

Simulations described in this chapter were carried out using the DELFT3D-MOR programme, which is part of the DELFT3D software package of WL | Delft Hydraulics. In this programme, five modules can be distinguished:

- 1- Main module (named: MORSYS): MORSYS, the steering module, controls the execution of the morphological process simulation. MORSYS essentially couples the DELFT-3D modules that describe the four principal physical processes (i.e. waves, flow, transport, and bottom changes) that constitute a morphodynamic system. The MORSYS module controls the order in which these processes are activated and the communica-

tion between the different modules. Depending on the nature of the simulation, different modules are executed in different order.

- 2- Waves module (named: DELFT3D-WAVE): The waves module is designed to simulate wave fields. This module was not used in this case.
- 3- Flow module (named: DELFT3D-FLOW): The flow module is a multi dimensional (2-D or 3-D) hydrodynamic simulation programme. In DELFT3D-MOR it is only used in 2DH (depth averaged) mode coupled with a parameterisation for curvature-induced secondary flow (quasi three-dimensional).
- 4- Transport module (named: DELFT3D-TRAN): There exist four different versions of the sediment transport module, dealing with, total-load transport, suspended-load transport, cohesive sediment transport, and graded sediment transport, respectively. In the total-load transport mode, the transport rate is given by a total-load transport formula, whereas in the suspended-load transport mode a distinction is made between bed load and suspended load. Unless otherwise indicated, the suspended-load sediment transport module has been applied in conjunction with the sediment transport formulae of van Rijn (1984a; 1984b).
- 5- Bottom module (named: DELFT3D-BOTT): In this module the bed level changes are computed from the sediment balance. Divergence in the sediment transport field result in local erosion or sedimentation.

In the next subsections we give a short description of the basic equations used by the flow, sediment transport, and bed level update modules. For additional information we refer to Struiksmā (1985), Struiksmā *et al.* (1985), Roelvink and van Banning (1994), Jagers (2003), Lesser *et al.* (2004) and WL | Delft Hydraulics (2001a).

### 6.3.1 Flow with HLES

The flow model is based on the depth-averaged shallow water equations, solved on a curvilinear grid (Stelling, 1984). In this approach, the vertical momentum equation is reduced to the hydrostatic pressure relationship, in which the vertical accelerations are assumed to be small compared to the gravitational acceleration and are not taken into account. The system of equations consists of the depth-averaged momentum equations and the continuity equation. The momentum equations in  $x$  and  $y$  directions are:

$$\frac{\partial u}{\partial t} + u \frac{\partial u}{\partial x} + v \frac{\partial u}{\partial y} + g \frac{\partial \zeta}{\partial x} - fv = -\frac{\tau_{b,x}}{\rho h} + \sum \frac{F_x}{\rho h} \quad (6.1)$$

$$\frac{\partial v}{\partial t} + u \frac{\partial v}{\partial x} + v \frac{\partial v}{\partial y} + g \frac{\partial \zeta}{\partial y} + fu = -\frac{\tau_{b,y}}{\rho h} + \sum \frac{F_y}{\rho h} \quad (6.2)$$

and the depth-averaged continuity equation is given by:

$$\frac{\partial \zeta}{\partial t} + \frac{\partial hu}{\partial x} + \frac{\partial hv}{\partial y} = 0 \quad (6.3)$$

where:

- $u, v$  = depth averaged water flow velocities in  $x$  and  $y$  directions [m/s];
- $\zeta$  = water level with respect to the reference level [m];
- $h$  = flow depth,  $h = \zeta - z_b$ ,
- $z_b$  = bed elevation measured from reference level [m];
- $t$  = time [s];
- $\rho$  = mass density of the fluid [kg/m<sup>3</sup>];
- $\tau_b$  = bed-shear stress [N/m<sup>2</sup>];
- $f$  = Coriolis parameter [s<sup>-1</sup>];
- $F$  = forcing due to turbulent momentum exchange, wind, waves, etc. [N/m<sup>2</sup>].

The bed shear stress components are modelled using the Chézy roughness coefficient ( $C$ ) as:

$$\tau_{b,x} = \frac{\rho g u \sqrt{u^2 + v^2}}{C^2} \quad \& \quad \tau_{b,y} = \frac{\rho g v \sqrt{u^2 + v^2}}{C^2} \quad (6.4)$$

and:

$$F_x = \frac{\partial \tau_{xx}}{\partial x} + \frac{\partial \tau_{xy}}{\partial y} + F_{x,external} \quad \& \quad F_y = \frac{\partial \tau_{xy}}{\partial x} + \frac{\partial \tau_{yy}}{\partial y} + F_{y,external} \quad (6.5)$$

with:

$$\tau_{xx} = 2\nu_H \frac{\partial u}{\partial x}, \quad \tau_{yy} = 2\nu_H \frac{\partial v}{\partial y}, \quad \text{and} \quad \tau_{xy} = \nu_H \frac{\partial u}{\partial y} + \nu_H \frac{\partial v}{\partial x} \quad (6.6)$$

in which  $\nu_H$  = horizontal eddy viscosity [m<sup>2</sup>/s].

In the conventional way of modelling, the horizontal eddy viscosity ( $\nu_H$ ) in this model is taken constant throughout the computational domain. However, when using this uniform eddy viscosity, the large horizontal eddies are not reproduced correctly. To resolve these eddies, the effect of the sub-grid turbulent motions needs to be described in terms of the model's dependent variables. In the version of DELFT3D-FLOW used herein, a recently developed Smagorinsky-type sub-grid scale (SGS) model for the horizontal eddy viscosity was applied (Uittenbogaard and Van Vossen, 2003). This SGS model, which includes damping by bed friction, produces a spatially and temporally varying horizontal eddy viscosity that in turn accounts for the direct energy loss by bed friction. Rather than spatial filtering, a simple temporal recursive high-pass filter is applied on the resolved velocity field. This filter removes the steady or slowly varying large-scale contributions to the strain rates that enter the SGS model.

The advantage of HLES is that the horizontal motion is described by the correct and well-established momentum equations for shallow-water flow. The applied SGS model is founded as follows:

$$\nu_H = \frac{1}{k_s^2} \left( \sqrt{(\gamma \sigma_T S^*)^2 + B^2} - B \right) \quad (6.7)$$

where;

$$k_i = \frac{\pi f_p}{\sqrt{\Delta x \Delta y}}; \quad f_p \leq 1 \quad (6.8)$$

$$\gamma = \frac{1}{2} I_\infty \sqrt{1 - \alpha^{-2}} \quad \text{and} \quad I_\infty = 0.844 \quad (6.9)$$

$$B = \frac{3}{4} \frac{g \overline{|U|}}{h C^2} \quad (6.10)$$

$$(S^*)^2 = 2 \left( \frac{\partial u^*}{\partial x} \right)^2 + 2 \left( \frac{\partial v^*}{\partial y} \right)^2 + \left( \frac{\partial u^*}{\partial y} \right)^2 + \left( \frac{\partial v^*}{\partial x} \right)^2 + 2 \frac{\partial u^*}{\partial y} \frac{\partial v^*}{\partial x} \quad (6.11)$$

where:

$k_i$  = truncation wave number

$f_p$  = spatial low-pass filter coefficient

$B$  = effect of bottom friction

$S^2$  = sum of the horizontal component of the strain rate tensor

$\gamma$  = numerical coefficient depending on the dimensionality of the turbulence (2D in this case), in which  $\alpha$  the slope in the log-log energy density spectrum  $E(k)$  (usually  $\alpha = 3$  or  $5/3$  holds)

$\sigma_T$  = turbulent Prandtl-Schmidt number, ( $\sigma_T = 0.5 \sim 1.0$ )

$h$  = water depth

$\Delta x$  = grid size in  $x$ -direction

\* = the asterisk denotes fluctuating flow variables.

The truncation wave number  $k_i$ , determines up to what length-scale of turbulence is modelled with the SGS model. The fluctuating flow variables are defined through a recursive high-pass filter operator utilising a user-defined relaxation time ( $\tau$ ). The choice of  $\tau$  depends on the time-scale of the largest eddies, and it is meant to distinguish between the fluctuations and the base flow.

For a proper HLES with DELFT3D-FLOW, the following time step ( $\Delta t$ ) limitations hold, (Uittenbogaard, 1999):

- Courant number  $\sigma_{BT}$  for surface waves (barotropic mode) should be less than  $4\sqrt{2}$ :

$$\sigma_{BT} = 2\sqrt{2} \frac{\Delta t}{\Delta \ell} \sqrt{gH} < 4\sqrt{2}$$

- Courant number  $\sigma_I$  for convection should be less than unity:

$$\sigma_I = U \frac{\Delta t}{\Delta \ell} < 1, \quad \text{and}$$

- an explicit integration of SGS stress.

$$\sigma_b = \nu_{SGS} \frac{\Delta t}{(\Delta \ell)^2} \leq \frac{1}{2}, \quad \text{with } \Delta \ell \text{ as grid size in flow direction}$$

### 6.3.2 Transport

After resolving the flow field, the sediment transport field is computed using the Van Rijn formulae, with separate expressions for bed load (Van Rijn, 1984a) and suspended load (Van Rijn, 1984b). The suspended sediment transport expression is used to derive the local equilibrium concentration field, which is employed to derive the local sediment concentration utilising depth-averaged advection-diffusion (Galappatti and Vreugdenhil, 1985).

$$\frac{\partial hc}{\partial t} + \frac{\partial uhc}{\partial x} + \frac{\partial vhc}{\partial y} - \frac{\partial}{\partial x} \left( \varepsilon_s h \frac{\partial c}{\partial x} \right) - \frac{\partial}{\partial y} \left( \varepsilon_s h \frac{\partial c}{\partial y} \right) = \frac{h(c_e - c)}{T_a} \quad (6.12)$$

where

- $c$  = depth-averaged concentration;
- $c_e$  = equilibrium depth-averaged concentration;
- $\varepsilon_s$  = sediment horizontal diffusion coefficient;
- $T_a$  = adaptation time for the vertical sediment concentration profile.

From the concentration field  $c$ , the suspended sediment transport rates in  $x$  and  $y$  directions are determined as:

$$\begin{aligned} Q_{s,x} &= huc - h\varepsilon_s \frac{\partial c}{\partial x} \\ Q_{s,y} &= hvc - h\varepsilon_s \frac{\partial c}{\partial y} \end{aligned} \quad (6.13)$$

The entrainment ( $E$ ) and deposition ( $D$ ) term ( $-E + D$ ) due to suspended load is then computed from the depth-averaged concentration field as:

$$(-E + D) = \frac{\partial Q_{s,x}}{\partial x} + \frac{\partial Q_{s,y}}{\partial y} - \frac{\partial hc}{\partial t} \quad (6.14)$$

Finally, the bed level changes are determined based on the gradient in the sediment transport field and takes the following form:

$$(1 - p) \frac{\partial z_a}{\partial t} + \frac{\partial Q_{s_b,x}}{\partial x} + \frac{\partial Q_{s_b,y}}{\partial y} = (-E + D) \quad (6.15)$$

where:

- $p$  = bed porosity,
- $z_a$  = bed level,
- $Q_{s_b,x}$ ,  $Q_{s_b,y}$  = bed load sediment transport components, and
- $Q_{s,x}$ ,  $Q_{s,y}$  = suspended load sediment transport components

### 6.3.3 Morphological update procedures

Morphological simulation in DELFT3D-MOR involves a combined simulation of currents, transport and bottom changes. The 'conventional' way of modelling river morphology



usually takes the structure shown in Figure 6.1(a), in which the flow field is computed to reach a 'steady state', i.e. the velocity difference between two consecutive time steps is less than a given threshold value. The sediment transport field is then computed and used to compute erosion and deposition rates, followed by a bed topography updating.

After this morphological update, the flow field has to be recomputed. Nevertheless, as long as the bed variations are small, the flow pattern will not change much. In this case, a frequently applied method to adjust the transport field for 'small' changes in the bed topography is called "continuity correction", in which the product of the velocity and the water depth is kept constant.

However, when the flow exhibits large fluctuations, averaging the velocity over a given period or taking the latest 'snapshot' of the velocity field would yield a different sediment transport from that computed from the instantaneous velocity records. Using an average velocity field would dampen the large-scale velocity fluctuations; thus, yielding a less pronounced lateral exchange. Using a snapshot velocity field would probably yield overestimation of the sediment transport in one direction and underestimation in the other.

In addition, when resolving the large eddies, the flow field in the mixing layer will never reach a formal 'steady state'. Therefore, the structure shown in Figure 6.1a cannot be applied. Instead, a structure similar to the one used in the case of tidally driven morphology is used, Figure 6.1b.

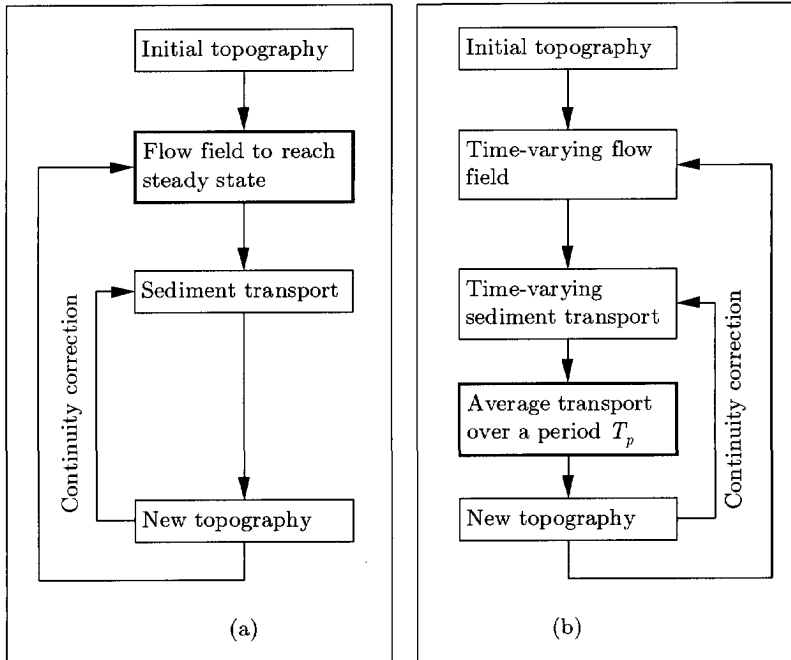


Figure 6.1: Structure of Delft3D-Mor; (a) conventional morphological procedures, (b) eddy resolving procedures.

In this method, the time-varying sediment transport is averaged over a representative time period ( $T_p$ ). In the tidal case, an obvious choice of this representative period is simply the tidal period. The choice of  $T_p$  when the flow fluctuations are driven by the large eddies is less obvious and requires some post-processing for the velocity field to estimate  $T_p$  before conducting the full morphological loop. The method to choose  $T_p$  is described in Section 6.5.2.

## 6.4 MODEL SETUP

The modelled area is a schematised straight river reach with groynes on both sides (see Figure 6.2 and Figure 6.3). The channel dimensions were chosen to represent the River Waal. The modelled reach is 2 km long with bed slope of  $1 \times 10^{-4}$ . The groynes length ( $L$ ) and spacing ( $S$ ) are 60 m and 200 m, respectively. These dimensions are typical of the River Waal as presented in Chapter 2 (cf. Schans, 1998). The main channel width is 250 m, the bed level difference between the main channel and the groyne-fields is 2.0 m, and the beach slope inside the groyne fields is 1:20, channel cross-section is shown in Figure 6.4. The sediment size was chosen 400  $\mu\text{m}$  for the whole field. A uniform grid size of 5 m was used throughout the model area.

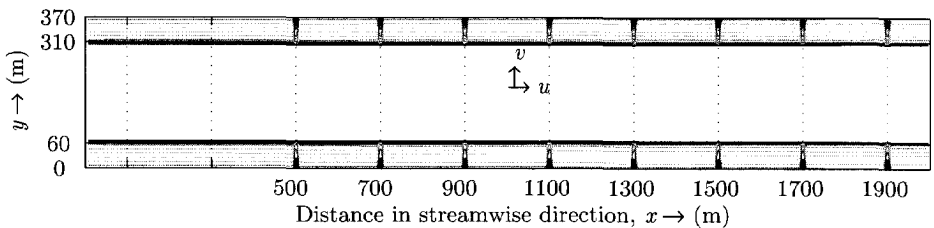


Figure 6.2: Model layout.

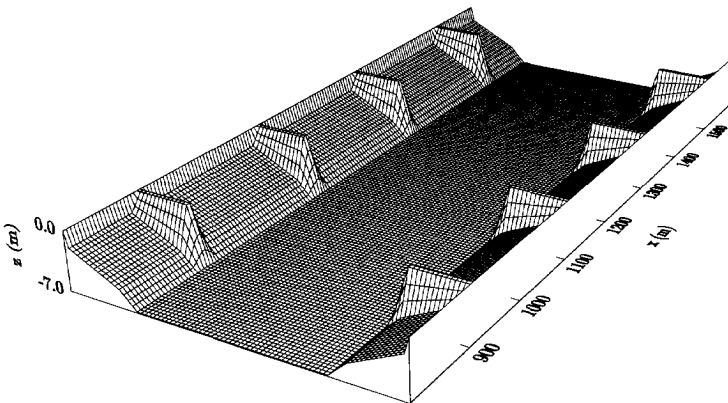


Figure 6.3: Overview of the model grid.

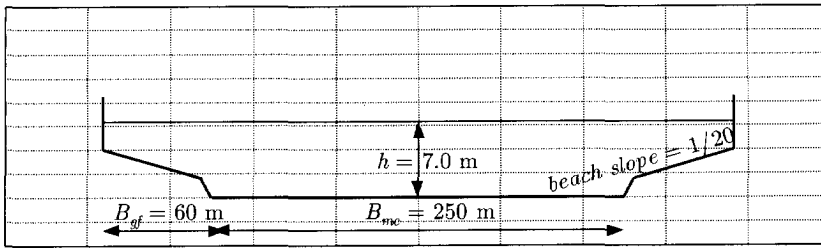


Figure 6.4: Channel cross-section through a groyne-field.

At the upstream boundary, a steady discharge of  $1500 \text{ m}^3/\text{s}$  was defined, and the downstream boundary condition was specified by a constant water level of  $7.0 \text{ m}$  measured from the channel bed. A constant Chézy roughness coefficient of  $45 \text{ m}^{1/2}/\text{s}$  was set for the entire domain. Despite the dominant effect of the bottom friction, the wall boundary condition has a significant effect on the structure of the recirculation pattern inside the groyne fields (see Nassiri *et al.*, 1999; Rupprecht, 2004). Three options are possible for the wall boundary in DELF3D-FLOW; free slip, no slip or partial slip condition. The wall boundary was set using a partial slip condition with a roughness height of  $0.1 \text{ m}$ .

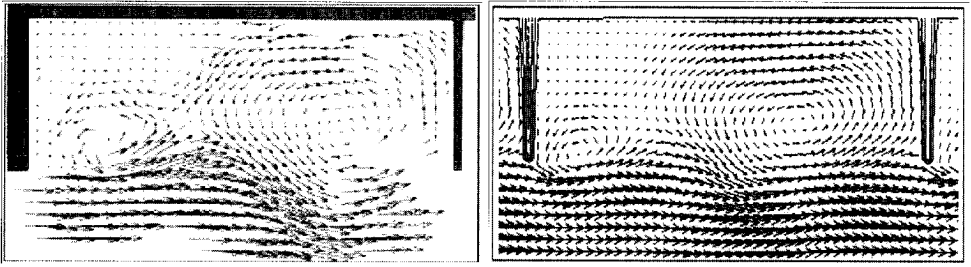
The groynes were represented in the model as depth points. To keep the groynes from eroding, the so-called *non-erodible* layer option was applied for the regions where erosion is not possible/wanted. The presence of a non-erodible layer reduces the magnitude of sediment transport over this layer. In all simulations, the groynes and their side-slopes were made non-erodible. For accuracy and stability purposes, a computational time step of 3 seconds was used for the flow module, but only every 30 seconds results were sent to the communication file between the different modules. Consequently, the sediment transport field was computed with a time step of 30 seconds. Morphological changes were computed with an automatic stepping mechanism that satisfied the Courant-Friedrichs-Lewy stability condition (Courant number based on bed celerity less than 0.9).

## 6.5 COMPUTATIONAL RESULTS

### 6.5.1 Flow pattern

The two panels in Figure 6.5 show the similarity between the computed instantaneous flow pattern and the measured pattern from an experiment with similar  $S/L$  ratio. Furthermore, the time variations of the flow as shown in Figure 6.6 agree well with the observations from the experiments as presented in Section 3.5. Note, however, that only the very large-scale structures were reproduced by the model.

Following the picture of the dynamic behaviour of the flow field, we can assert that the flow pattern exhibits a periodical behaviour. The most significant manifestation of this periodicity is found along the interfacial line between the river and the groyne-fields (the normal line). The velocity records were extracted from the results of the flow computation, the mean value of which was then subtracted to distinguish the fluctuating part.



(a)

(b)

Figure 6.5: Flow field in a groyne-field, snapshot picture; (a) experimental result (after Uijttewaal, 1999), (b) model results.

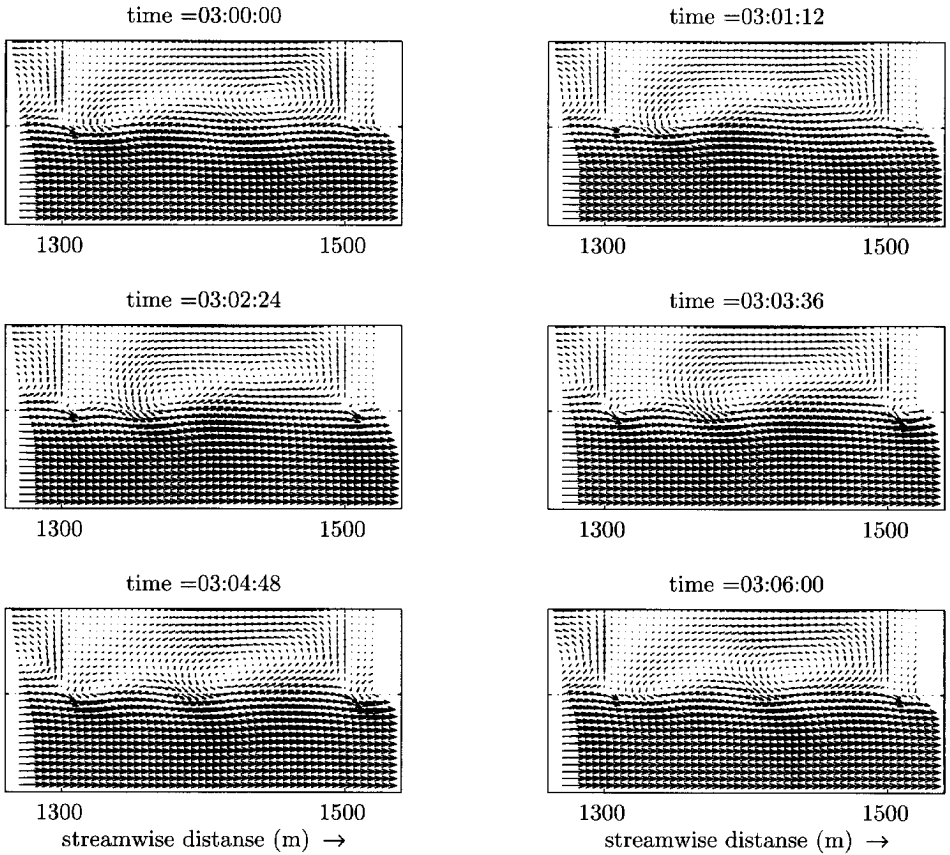


Figure 6.6: Computed time varying flow field in a groyne field (over a period of 6 minutes).

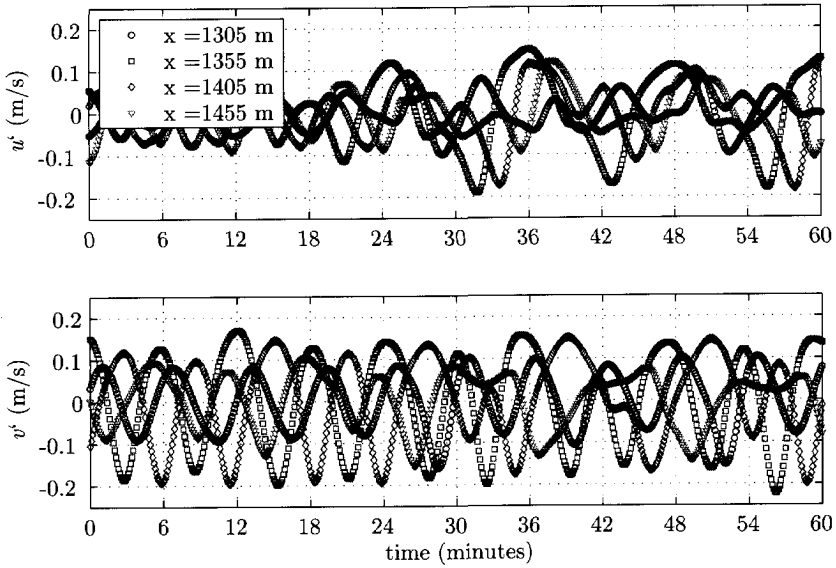


Figure 6.7: Velocity fluctuations for some points along the normal line,  $u$ -component (upper panel) and  $v$ -component (lower panel).

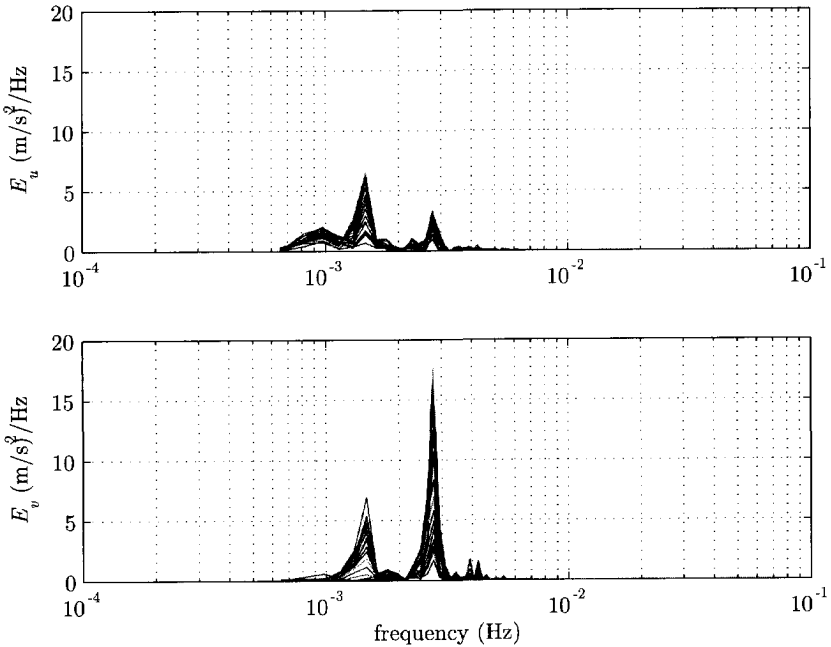


Figure 6.8: Energy density spectra for velocity fluctuations,  $u$ -component (upper panel) and  $v$ -component (lower panel).

The velocity fluctuations for some points along an arbitrary segment of the normal line (far from both boundaries) are given in Figure 6.7. The periodic nature of the velocity signals is now much clearer, yet remains to be quantified. Utilising a long time series of the velocity components  $u$  and  $v$ , it is possible to obtain the energy density spectra. The energy density spectrum gives the distribution of the turbulent energy over the different frequencies. For each of the observation points the energy density spectrum  $E$  was computed and the result is presented in Figure 6.8.

The energy spectra of the  $v$ -component of the velocity (Figure 6.8-lower panel) show a clear peak at a frequency of  $2.78 \times 10^{-3}$  Hz, (wave period  $t_{p1} \cong 6$  minutes), and a minor peak with much lower energy at a frequency of  $1.46 \times 10^{-3}$  Hz, ( $t_{p2} \cong 11.4$  minutes). For the  $u$ -component (Figure 6.8-upper panel), two peaks of comparable energy content occur at the same frequencies, with the low frequency (slow fluctuations) peak containing slightly higher energy. This could be attributed to the high mean velocity washing-out some of the higher frequency fluctuations. For the same reason, the overall energy content of peaks of the  $u$ -component is less than that of the  $v$ -component. None of the velocity components has energy at the high-frequency side of the spectrum. Clearly, this is due to numerical cut-off. The same dynamic behaviour, and the existence of two distinct peaks in the energy density spectra, was observed in the results of the fixed-bed model discussed in Chapter 3, (cf. Muto *et al.*, 2000; Uijttewaai *et al.*, 2001; Yossef and Uijttewaai, 2003).

### 6.5.2 Choice of sediment transport computation period $T_p$

As stated in Section 6.3.3, proper sediment transport modelling requires a careful choice of the period over which sediment transport is computed and averaged. The choice of the averaging period  $T_p$  should be in accordance with the wave period(s) deduced from the spectral analysis, i.e.  $T_p$  should cover at least one wave period ( $t_p$ ). As the peak at  $t_{p1}$  contains most of the turbulence energy, a manifold of  $t_{p1}$  should be used as a base choice for  $T_p$ . However, because of the existence of a second wave period at  $t_{p2}$ ,  $T_p$  should be extended to make sure that (at least) one cycle ( $t_{p2}$ ) is covered as well. Note, however, increasing  $T_p$  leads to a substantial increase in the total computational time, as the flow module (most time-consuming) also has to be run over this larger period.

The transport averaging-period was evaluated off-line (via post-processing the flow field) utilising the formula of Engelund and Hansen (1967). The time-averaged transport rates,  $Q_{s_x}$  and  $Q_{s_y}$ , were calculated using different values of  $T_p$ . Figure 6.9 gives a comparison between the transport rates computed based on different values of  $T_p$ , compared with the one based on a very long period of 60 minutes as a reference. The figure shows that the very short periods of 3 seconds and 3 minutes, both result in a very different transport pattern than the reference. When increasing  $T_p$ , we can still observe some deviations when using  $T_p = 6$  minutes ( $1 \times t_{p1}$ ), whereas, the deviation reduces with  $T_p = 12$  minutes ( $2 \times t_{p1}$ ), and practically disappears when using  $T_p = 24$  minutes ( $4 \times t_{p1}$ ). When using values other than a manifold of the dominant wave period deduced from the energy density spectra, we observe a lesser match with the results of the long averaging period (Figure 6.10), but the differences are less pronounced than in Figure 6.9. Accordingly, a transport averaging period of  $T_p = 4 \times t_{p1}$  (i.e. 24 min.) seems to be appropriate.

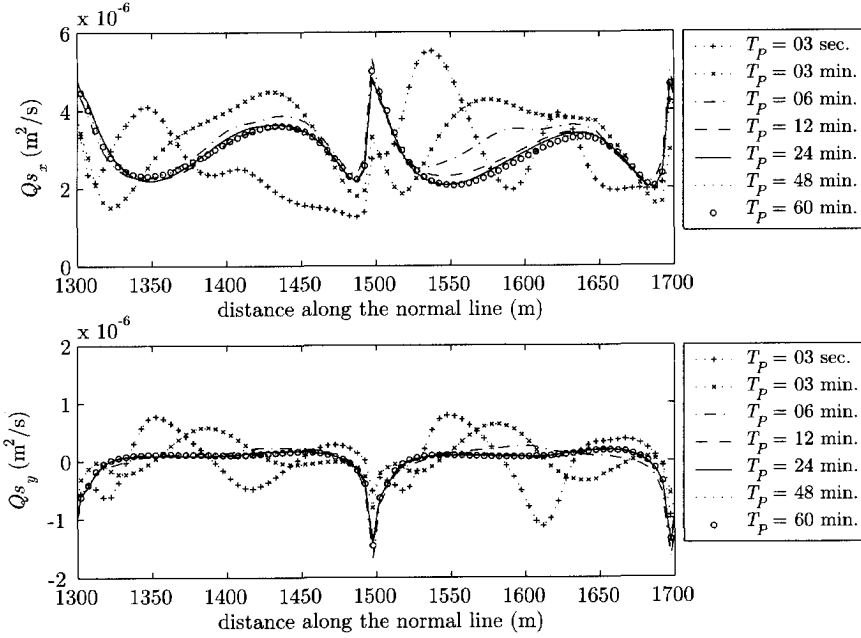


Figure 6.9: Comparison between sediment transport rate along the normal line using different values of  $T_p$  as averaging period. Streamwise component  $S_x$  (upper panel) and transverse component  $S_y$  (+ve  $S_y$ , is towards the groyne fields).

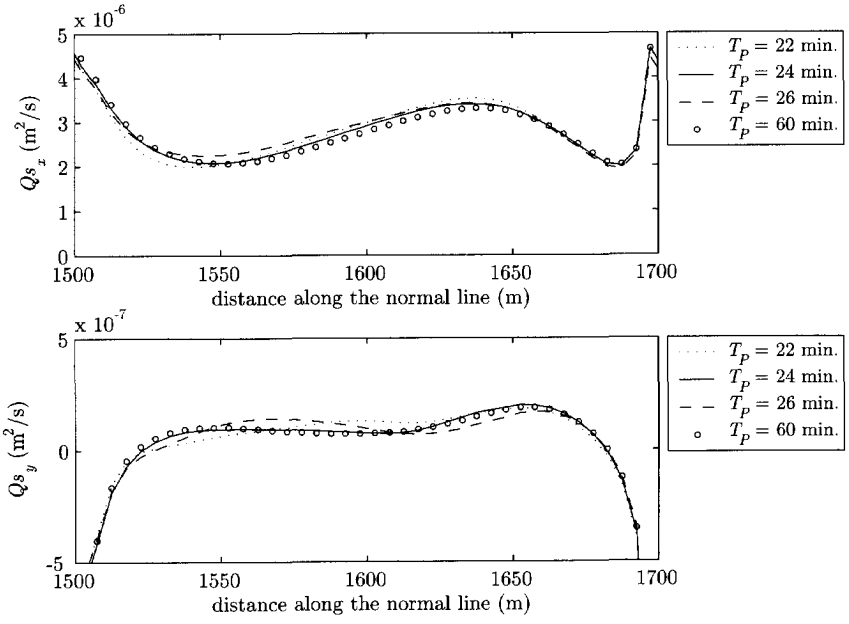


Figure 6.10: Comparison between sediment transport rate along the normal line using a multiple of  $t_p$  ( $T_p = 4 \times t_{pi}$ ), and  $T_p = 4 \times t_{pi} \pm 2$  minutes.

### 6.5.3 Morphological development

#### With HLES

Utilising the criteria mentioned in the previous section, a transport averaging period of  $T_p = 4 \times t_{p1}$  (i.e. 24 min.) was chosen. Now, we can carry out a complete morphological loop as indicated in Figure 6.1a. The resulting bed morphology after a period of two months is presented in Figure 6.11, where we can observe the typical pattern of an oblique scour hole near the tip of every groyne, followed by deposition in the subsequent area. This deposition area is the so-called groyne flame. In addition, we observe that there are differences in the morphological pattern formed near each groyne. This random component is due to the fact that the resolved eddies are 'to a certain extent' random. Due to the existence of dynamic eddies, some of the groyne flames have two apexes. However, as time proceeds they evolve to a single apex.

Shape and dimensions of the groyne flames are presented in more detail in Figure 6.12, where the morphological development is shown after a period of one and two months. Figure 6.12 (upper panel) shows that the basic shape of the flames is already present after one month. The deposition continues to reach a maximum after nearly 45 days (see Figure 6.14). After this period, the changes in shape continue, but the increase in the maximum deposition height is no longer significant.

The maximum deposition occurs at a distance of around 10 m from the normal line and could reach up to 1.5 m above the initial bed level in the main channel. The area with more than 0.5 m deposition height relative to the initial channel bed level extends over a distance that ranges from 20 to 50 m from the normal line.

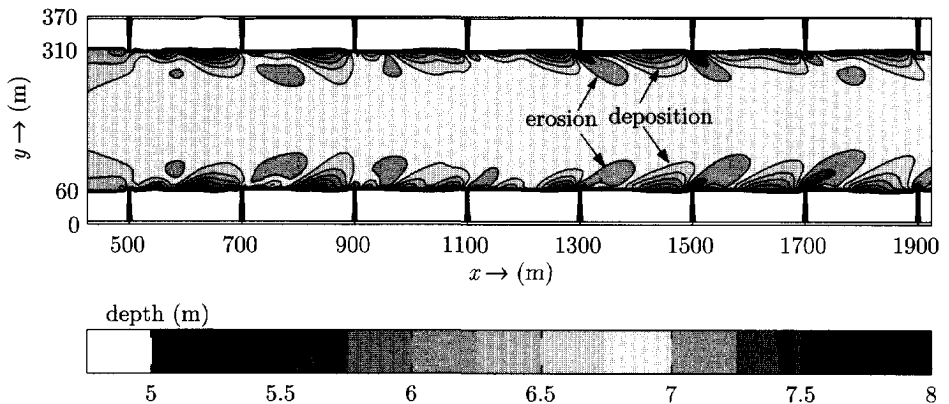


Figure 6.11: Bed topography after two months; (bed level is measured from water surface; flow from left to right).



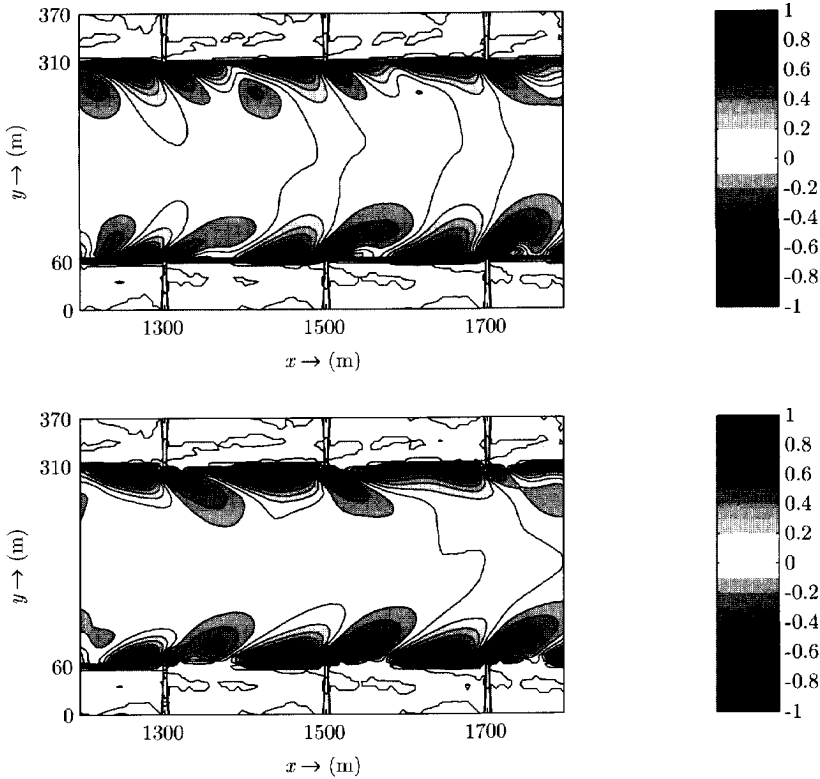


Figure 6.12: Erosion deposition pattern after one month (upper panel) and after two months (lower panel); (computation *with* HLES).

### Without HLES

For comparison, the same computations were carried out using the standard model with the eddy viscosity fixed at  $0.1 \text{ m}^2/\text{s}$  in the whole computational domain. We have to notice that, in this case, the large eddies are not resolved. Consequently, the flow pattern does not exhibit the same dynamic behaviour as observed in the computation with HLES. Hence, the averaging period ( $T_p$ ) does not have any impact on the computed sediment volume. Nevertheless, the same averaging period ( $T_p$ ) of 24 minutes was applied. The resulting morphology is presented in Figure 6.13.

We can still observe the same typical pattern of scour near the tip of the groynes and deposition in the subsequent area. Yet, the natural-looking randomness observed in Figure 6.12 is not present any more. The groyne flames look identical and the two sides of the channel look symmetrical. Moreover, the area characterised by 0.5 m deposition height after three months is only confined to the first 20 m from the normal line. Furthermore, the morphological time-scale in this case is much longer than that when using HLES (see Figure 6.14).

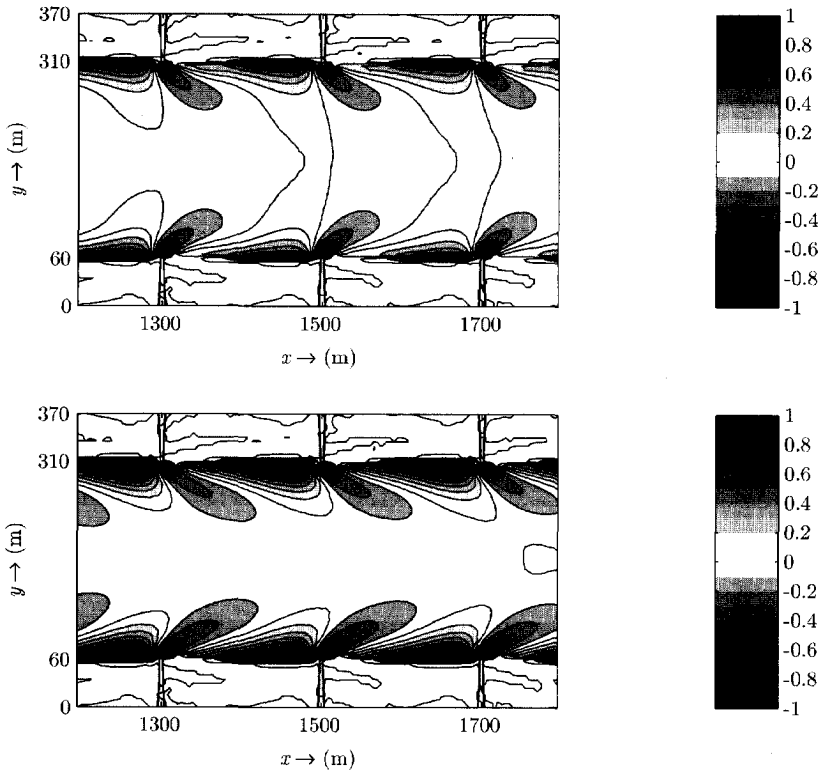


Figure 6.13: Erosion deposition pattern after: one month (upper panel), three months (lower panel); (computation *without* HLES).

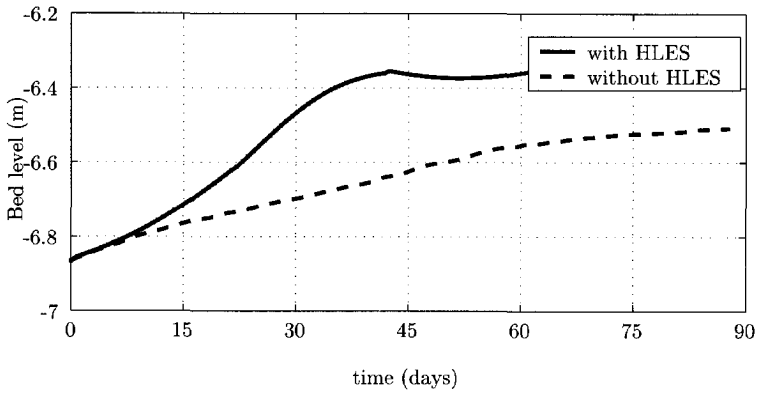


Figure 6.14: Comparison between bed level development with and without HLES, at the point with coordinates (1665,90).

## 6.6 QUALITATIVE COMPARISON WITH FIELD OBSERVATIONS

### 6.6.1 Field observations

The field data was obtained from the Directorate East Netherlands of Rijkswaterstaat (DON), through a project to monitor the morphological changes following dredging operations for maintaining the fairway (Taal, 1999, 2000). In this project, detailed measurements were carried out in several reaches of the River Waal. The navigation channel in the reach near Druten is almost straight and can be used for comparison with the presented simulations (Figure 6.15a). During the months August to November of the year 2000, the river discharge was invariably close to  $1500 \text{ m}^3/\text{s}$  (Figure 6.15b), which is similar to the discharge used in the simulations.

Maintenance dredging in this reach took place several times during the year 2000. The most relevant sequence of dredging and subsequent field measurements started on September 8<sup>th</sup>. The development of the navigation channel bed was monitored on September 19<sup>th</sup>, October 13<sup>th</sup> and November 22<sup>nd</sup>, i.e. after 11, 35, and 75 days respectively. The measured bed topography is presented in Figure 6.16, in which the development of the groyne flames is clearly visible. Because the river is slightly curved in this reach, the pattern near the southern bank (inner bend) is more pronounced than that near the northern bank (outer bend).

After 11 days, shallow areas were already present near the southern bank, (Figure 6.16a). After one month, the shape of the groyne flames became more pronounced, and we can as well distinguish that some had two apexes (Figure 6.16b). After a longer period, the groyne flames became more alike and they extended up to 40 m into the channel (Figure 6.16c). Estimating the morphological time-scale from these pictures is not straightforward. However, experience gained from many dredging operations shows that the recovery time of bed forms after dredging has strong relation to the river discharge (Klaassen and Sloff, 2000). In the case of the River Waal, the recovery time at a discharge of  $1500 \text{ m}^3/\text{s}$  is in the order of two months, which compares favourably with the time-scale of the numerical simulation using HLES.

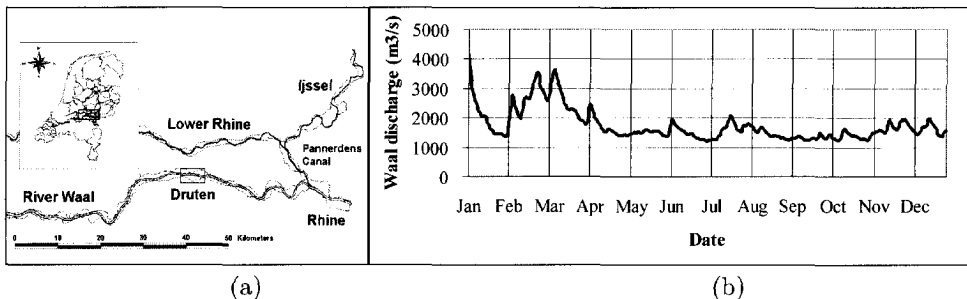
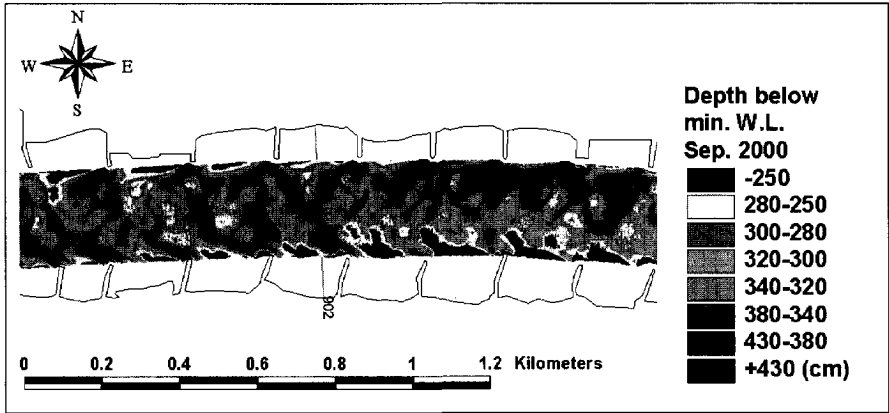
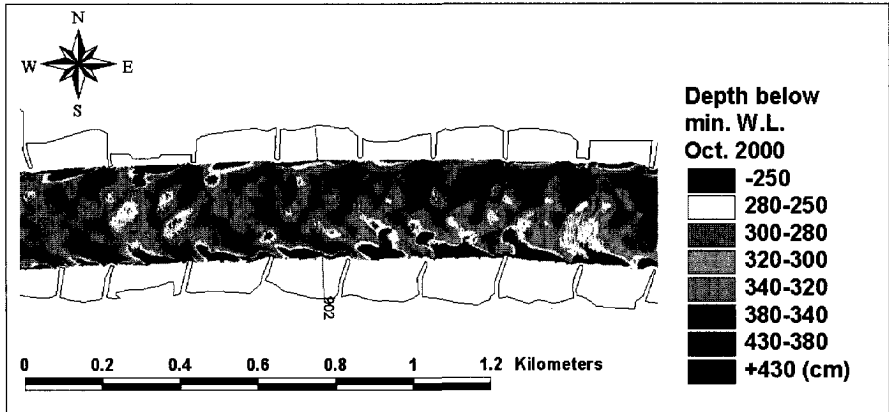


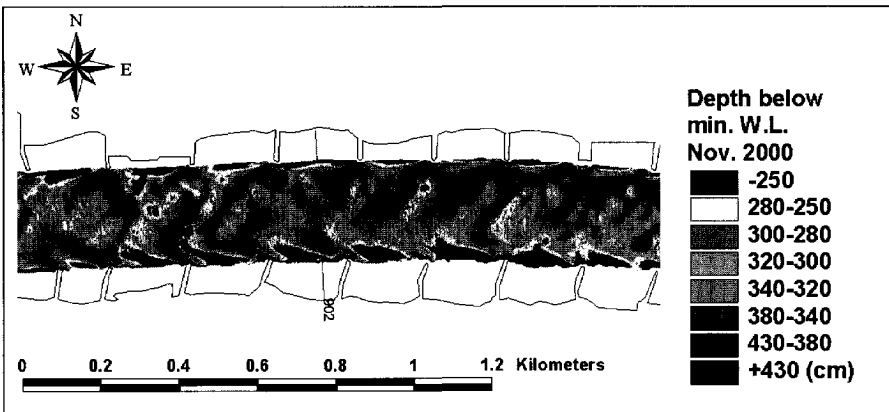
Figure 6.15: Key map for Rhine branches in the Netherlands (a); discharge record of the River Waal for year 2000 (b).



(a)



(b)



(c)

Figure 6.16: Bed morphology for the reach near Druten for three consecutive months (flow from East to West)

### 6.6.2 Comparison

Bearing in mind that simulations were carried out for a schematic situation, only a qualitative comparison between the model results and the field observations is possible. Considering two aspects viz. the shape of the groyne flames and the associated morphological time-scale, we observe:

- The development of the groyne flames starts with formations that sometimes have two apexes, which only after some time merge into one formation. This is only observable in the results of the model with HLES, the model without HLES yields a single deposition area at all times.
- In the early stage of their development, the groyne flames are not similar to one another, but similarity increases with time. This behaviour is visible in the field observations, as well as in the results when using HLES. The results of the model without HLES do not reveal this behaviour.
- The morphological development according to the model without HLES is much slower than observed in the field whereas, the development with HLES is comparable to that in the field.

Clearly, the strong velocity fluctuations that are resolved by HLES give rise to higher transport rates, hence to faster morphological development.

## 6.7 DISCUSSION

The primary objective of carrying out the simulations presented in this chapter was to evaluate the morphodynamic behaviour of the groyne fields under different conditions. This objective was not reached, as the reference situation presented here in did not yield any morphodynamic response in the groyne fields' region. As we have seen in Chapter 4, deposition in the groyne fields should take place under normal flow conditions. However, neither erosion nor deposition was observed in groynes region. This calls for an explanation, which we will attempt to give below.

For the case of a river with non-submerged groynes, DELFT3D-FLOW coupled with HLES resolves the hydrodynamics reasonably well and yields a good representation of the flow pattern in both the main channel and inside the groyne fields. The morphodynamic response in the main channel is comparable to what is observed in the field. The morphodynamic activity within the groyne fields, however, is largely under-predicted, such that there is practically no change from the given initial topography. This would not be too much of a problem if one is primarily interested in what happens in the main channel. However, when looking at the sediment exchange between the main channel and the groyne fields, and hence, the overall sediment balance, the problem appears.

Firstly, the flow pattern in the vicinity of emerged groynes implies that there should be an advective sediment transport component from the main channel towards a groyne field from its downstream part, following the direction of the primary circulation cell. This has been confirmed in the mobile-bed experiments presented in Chapter 4. Such a behaviour was not observed in the results of the simulations. One might argue that, this

is to be attributed to the existence of a step between the channel and the groyne fields which hinders the sediment flux. This is a valid argument, but, the same (no transport into the groyne fields) was concluded from the detailed simulations carried out by Rupprecht (2004) to simulate the same mobile-bed experiments without the existence of such a step.

Secondly, the sediment concentration in the main channel is relatively high as compared with that inside the groyne fields, which implies a contribution of sediment diffusion from the main channel to the groyne fields region. Nonetheless, the suspended sediment concentration dropped significantly in the transverse direction across the mixing layer while entering the groyne fields and hardly any sediment entered the groyne fields region. Increasing the sediment diffusion coefficient ( $\varepsilon_s$ ) did not improve the result; i.e. the sediment concentration inside the groyne fields did not increase. Moreover, when we further increased  $\varepsilon_s$  in entire computational domain, a completely unrealistic morphological pattern developed, in that the local scour holes near the tips of the groynes disappeared and a deposition ridge developed along the normal line. A more sophisticated way of increasing  $\varepsilon_s$  is to introduce a spatially varying diffusion coefficient that matches the regions of the increased turbulence intensity. The diffusion coefficient was deduced from the horizontal eddy viscosity ( $\nu_H$ ) resulting from the SGS-model. The time varying eddy viscosity was extracted, averaged out (off-line), and enhanced by a factor 5, then supplied to the transport module as a spatially varied diffusion coefficient field. Even, this did not result in major improvements with respect to the morphodynamics of the groyne fields.

For suspended sediment to be transported from the main channel region into the groyne fields region some factors are of importance, namely the reference sediment concentration in both regions, the adaptation time/length scales for the suspended sediment content, and the sediment transport capacity in the mixing layer.

The reference concentration as computed in DELFT3D-MOR is a function of the depth-averaged flow velocity. In the vicinity of the groynes and along the normal line, the velocity is lower than that in the main channel. Accordingly, the sediment transport capacity drops significantly over a rather short distance. Moreover, the velocity inside the groyne fields is close to (even below) the threshold of motion, leading to a transport capacity close to zero just inside the groyne fields. Hence, across the normal line a very steep gradient takes place, leading to the abrupt deposition of the entire bed-load.

The response of the suspended load to local equilibrium conditions as described in the previous paragraph, is delayed due to lag effects (see Eq. 6.12). The adaptation time and length scales as computed in Delft3D are functions of the velocity (for a given fall velocity and water depth). In the circulation zone inside the groyne fields, the velocity decreases considerably and falls below the validity range of the model of Galappatti and Vreugdenhil (1985). A very short adaptation length-scale is then applied. Consequently, the concentration drops over a short distance to the local equilibrium concentration, which is already very low across the normal line. Hence, similar to the bed-load, the entire suspended-load deposits just across the normal line.

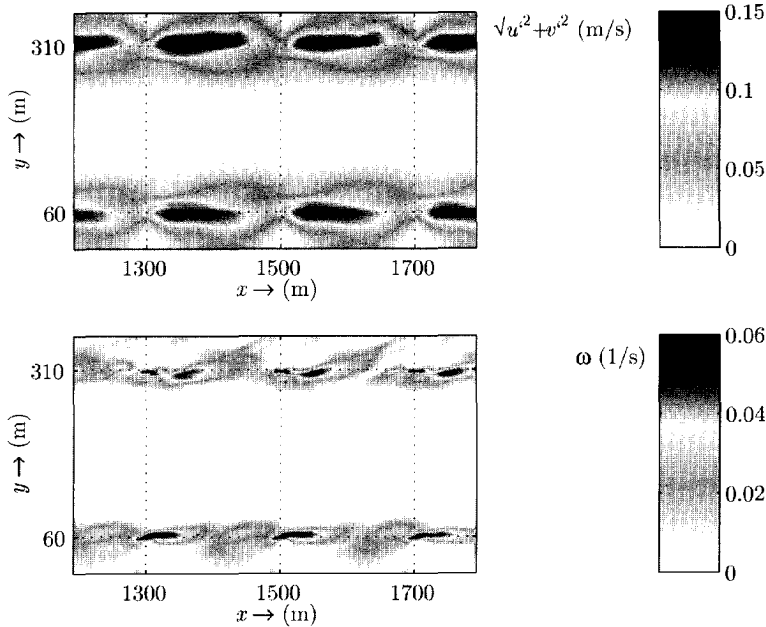


Figure 6.17: Distribution of: total turbulence intensity (upper panel), and vorticity (lower panel)

Noticeably, the area near the groynes and along the normal line exhibits high turbulence intensity as well as high vorticity, see Figure 6.17. Vortices shed from the tip of the upstream groyne and migrate in the downstream direction following the direction of the primary eddy. These vortices increase the sediment entrainment in their path (as observed from the mobile-bed experiments) causing higher sediment concentrations in the mixing layer that further extends following the path of the primary eddy. The applied/available sediment transport formula, however, ignores the increased turbulence level in the mixing layer, as well as the role of vortical motions that induce additional sediment entrainment in their path.

## 6.8 CONCLUSIONS

From this study we can conclude that it is possible to reproduce groyne flames in a river using a mathematical model that has the capacity to resolve large horizontal eddies. The first requirement to reproduce such a morphological pattern is a correct representation of time-dependent flow field. The flow field obtained from HLES compares well to that measured in a laboratory experiment for the case of emerged groynes.

The bed morphology computed when using HLES, as well as the associated time-scale, is similar to what has been observed in a field case. When using a mean-flow model without HLES, the bed morphology is less realistic and the morphological time-scale is much

larger. This slow development is the result of neglecting (or averaging) the strong velocity fluctuations associated with the time-varying eddy formation. This implies that large eddies which form at the interface between the main channel and the groyne fields are an important mechanism underling the typical groynes-induced bed pattern.

Further improvements to the model are required in order to reproduce the morphodynamic behaviour of groyne fields. Yet, this study has demonstrated the important role that 2D models with HLES can play in improving our predictive capabilities.

The shortcoming of the numerical model in reproducing the morphodynamics of the groyne fields is primarily due to the lack of a transport model that accounts for the increased turbulence level in the mixing layer, as well as the role of vortical motions in picking up sediment and keeping it in suspension for extended distances. With the current performance of the hydrodynamic model, it is time to invest in improving our sediment transport modelling to include vortical motion and increased turbulence level.



## Chapter 7

### LARGE-SCALE MORPHOLOGY – CASE STUDY

#### 7.1 INTRODUCTION

The estimates of the sediment balance for the Waal River during the last three decades, and particularly during the high water period of 1995, indicate that groyne fields erosion and sedimentation plays a role in the total sediment balance of the river (Ten Brinke *et al.*, 2001). During floods, a significant amount of sediment is deposited between the groynes. In the long run,  $\mathcal{O}(\text{decades})$ , no net erosion or deposition has been detected in the groyne fields. Accordingly, the amount of sediment that is deposited during flood conditions is released during normal to low flow conditions. This morphodynamic behaviour has been confirmed by observation of the temporal variation of the beaches between the groynes over shorter periods (Ten Brinke *et al.*, 2004). Currently, this morphological interaction between the groyne fields and the main channel is not included in our river modelling practice. In this chapter, we aspire to present a method to include such behaviour in models of large-scale river morphology. The technique is suitable for large-scale modelling with one- or two-dimensional models.

Large-scale models are generally characterised by a spatial scale of tens of kilometres and a temporal scale of a few decades (for the Rhine River). The nature of these models (coarse grid, larger than the spacing between groynes; disregarding transverse sediment exchange); the groyne fields are generally represented as morphologically inactive units. Here, we apply an analytical model and a one-dimensional model (Sobek of WL|Delft Hydraulics, 2001b) to some case studies to illustrate the applicability of the proposed method and further to analyse the effect of the morphodynamic behaviour of groyne fields on the morphology of the main channel.

In the first part of this chapter (Section 7.2), we present the schematisation used in the case studies. Secondly, we present the formulations of the models applied, viz. analytical equilibrium state models (Section 7.3.1) and SOBEK (Section 7.3.2). Thirdly, we show some results for the morphodynamic behaviour of the main channel under different possible conditions in Section 7.4 and Section 7.5. We end the chapter with a discussion and conclusions in Sections 7.6 and 7.7, respectively.

## 7.2 SCHEMATISATION

### 7.2.1 planform

The dimensions and the parameter settings of the case studies are based on the Dutch River Waal, which is a non-tidal lowland river with fixed planform. It is schematised as a compound channel with a 260 m wide main channel,  $2 \times 60$  m wide groyne fields with the groynes spaced at 200 m, and  $2 \times 500$  m wide floodplains (Figure 5.11). In a 1-D model this is represented by three sections, one for the main channel, one for the groyne fields and one for the floodplains. The bed level of the floodplain and the crest level of the groynes are taken at 7.0 m above the bed level of the main channel. The bed level of the groyne fields is 2.0 m above the main channel. The bed roughness of the main channel and that of the floodplain are represented by constant Chézy coefficients of  $40 \text{ m}^{1/2}/\text{s}$  and  $25 \text{ m}^{1/2}/\text{s}$ , respectively. The resistance in the groynes region is represented by a Chézy coefficient that is calculated according to Eq. 3.8 (see Section 3.6).

We further consider a reach length of 100 km with morphologically active groyne fields starting at km 30 measured from the beginning of the channel, and extending 50 km in the downstream direction. This is equivalent to the distance from Rhine km 887 to Rhine km 937 along the River Waal (cf. Ten Brinke *et al.*, 2004). Sediment transport take place only in the main channel region.

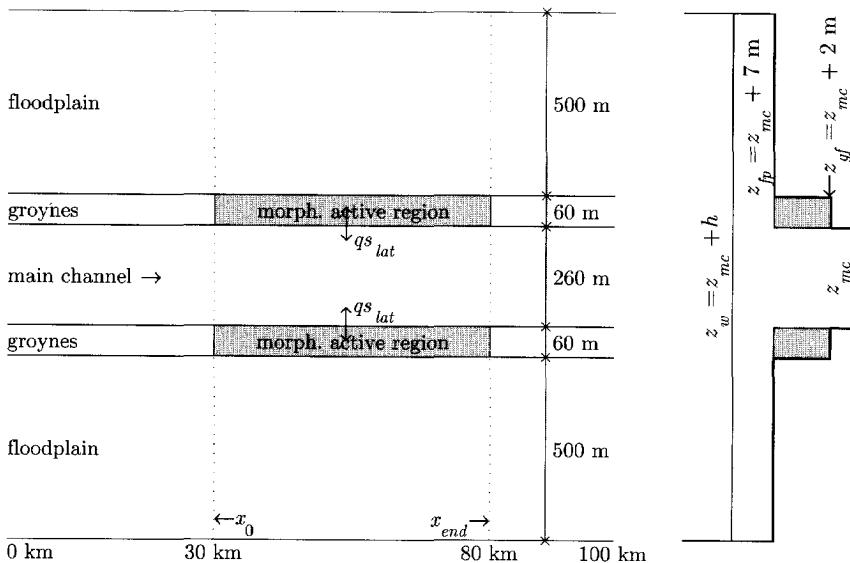


Figure 7.1: Schematic planform and cross section of the case study.

### 7.2.2 Morphological representation of the groyne fields

As we have discussed in Chapter 5, the beaches of the groyne fields are in a state of dynamic equilibrium. They experience erosion during emerged conditions, due to the effect of navigation, and deposition during submerged conditions. Accordingly, the groyne fields

are represented as a sediment source during normal to low-flow conditions, and as a sediment sink during high-flow conditions. This is treated in the model as lateral supply or extraction of sediment to or from the main channel. Still, the groyne fields are represented as a morphologically inactive region i.e. the bed levels between the groynes are not updated during computations. This simplification may give rise to an overestimation of the erosion rate from the groyne fields after a long period of continuous erosion, or vice versa. However, as we have discussed in Chapter 5, the morphological time scales of the development of the bed level in the groyne fields are long compared with the return period of floods; this simplification is therefore acceptable.

The impact of navigation is relatively strong at low discharges and decreases as the discharge increases. Hence, the navigation-induced erosion from the groyne fields gradually decreases with the increase of discharge. However, at very low discharges the fleet characteristics change significantly. A full and correct description of the navigation-induced erosion from the groyne fields as a function of the river discharge is problematic. Nevertheless, on the basis of the analysis of prototype behaviour given by Ten Brinke *et al.* (2004), we can estimate two different values for the erosion rate from the groyne fields. The first is based on the results from neural network modelling of the effect of navigation and the second is based on monitoring the bed level changes of the groyne field beaches during the period 1995-1998. The neural network modelling was based on measurements carried out during a relatively low discharge ( $Q = 1040 \text{ m}^3/\text{s}$ ). This led to net volume of sediment supply from the groyne fields of  $200,000 \text{ m}^3/\text{year}$ , over an active length of  $50 \text{ km}$  (i.e.  $q_{s_{lat}} = 0.13 \times 10^{-6} \text{ m}^2/\text{s}$ ). The estimate based on monitoring the beaches of the groyne fields was deduced from a long period that included the effect of navigation at different discharge conditions. It even included some discharge conditions that would induce deposition to the groyne fields. Thus, it yielded a lower estimate for the net sediment supply from the groyne fields. This estimate amounted to only  $90,000 \text{ m}^3/\text{year}$ , (i.e.  $q_{s_{lat}} = 0.06 \times 10^{-6} \text{ m}^2/\text{s}$ ). We will consider that the former estimate is on the high side and the later one is on the low side. In the absence of sufficient information, we will utilise an average value of  $q_{s_{lat}} = 0.1 \times 10^{-6} \text{ m}^2/\text{s}$  as representative of the effect of navigation during emerged conditions.

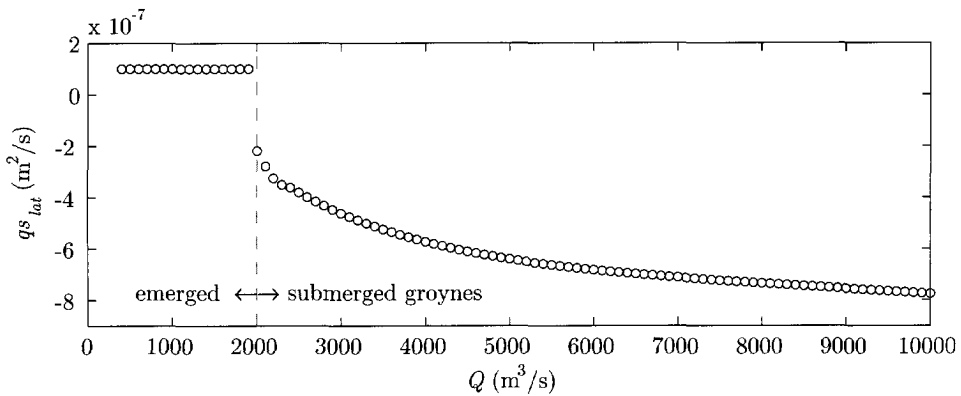


Figure 7.2: Schematic representation for the exchange of sediment between the groyne fields and the main channel as a function of the discharge.

Sediment extraction from the main channel to the groyne fields is determined according to the methodology presented in Section 5.3 (see Figure 5.12b) and calibrated to yield no net erosion or deposition from or to the groyne fields over the period 1970-2000 as observed from the field measurements (Ten Brinke *et al.*, 2001). The lateral sediment exchange rates ( $qs_{lat}$ ) as a function of the river discharge are depicted in Figure 7.2.

### 7.3 MORPHOLOGICAL MODELLING

#### 7.3.1 Analytical equilibrium state models

For a first analysis of the morphological effect of the interaction between the main channel and the groyne fields, we utilise a highly simplified model that describes the equilibrium state for a constant discharge. In the case of a constant discharge through a straight channel, the river bed will tend to reach an equilibrium state that is described by the following equations (see for example Jansen *et al.*, 1979).

$$u = C \sqrt{h i} \quad (7.1)$$

$$Q = B_{mc} \cdot h \cdot u \quad (7.2)$$

$$Qs = B_{mc} \cdot m \cdot u^n \quad (7.3)$$

This system of equations holds for each river reach where the model parameters are constant. In the equilibrium state, the flow is uniform and the water surface is parallel to the river bed. For an alluvial channel with fixed banks, constant discharge  $Q$ , and sediment load  $Qs$ , rearranging Eqs. 7.1 to 7.3 leads to the following expressions for the river equilibrium slope ( $i_c$ ) and depth ( $h_c$ ):

$$i_c = m^{\frac{3}{n}} B_{mc}^{\frac{n-3}{n}} C^{-2} Q^{-1} Qs^{\frac{3}{n}} \quad (7.4)$$

$$h_c = m^{\frac{1}{n}} B_{mc}^{\frac{1-n}{n}} Q Qs^{-\frac{1}{n}} \quad (7.5)$$

This reflects that the river tends to adjust its slope and depth to the supply of water and sediment at its upstream boundary. In the following sub-sections we will consider two situations. The first one describes the effect of including the sediment exchange between the groyne fields and the main channel of a river. In the second situation, we will consider the effect of the increased discharge through the groynes region after lowering the groynes.

#### Sediment exchange between the groyne fields and the main channel

Consider the emerged groynes situation, during which the groyne fields act as a source of sediment to the main channel. The same derivation holds for the submerged case, in which the groyne fields act as a sink of sediment, i.e. only the sign of  $qs_{lat}$  is different.

A continuous lateral supply of sediment from the groyne fields to the main channel will alter both the equilibrium slope and depth of the river. Assuming morphologically active groyne fields in the reach from  $x_0$  to  $x_{end}$ , with a constant lateral supply of sediment ( $qs_{lat}(x) = \text{constant}$ ). The sediment load in the river will change such that,

$$Qs(x) = \begin{cases} Qs_0 & \text{if } x < x_0 \\ Qs_0 + qs_{lat}(x - x_0) & \text{if } x_0 < x < x_{end} \\ Qs_0 + qs_{lat}(x_{end} - x_0) & \text{if } x > x_{end} \end{cases} \quad (7.6)$$

where  $Qs_0$  is the sediment influx from the upstream [ $\text{m}^3/\text{s}$ ],  $qs_{lat}$  the sediment supply from the groyne fields per unit length of the normal line [ $\text{m}^2/\text{s}$ ]. The new equilibrium slope and flow depth can be described as a function of  $Qs$  and  $x$ , as follows:

$$\frac{di_c}{dx} = \frac{di_c}{dQs} \cdot \frac{dQs}{dx} \quad (7.7)$$

$$\frac{dh_c}{dx} = \frac{dh_c}{dQs} \cdot \frac{dQs}{dx} \quad (7.8)$$

For the morphologically active reach, from Eqs. 7.4, 7.6, and 7.7 the slope  $i_c$  can be derived as

$$\frac{di_c}{dx} = \frac{3 \cdot Qs_r \cdot i_c}{n(1 + Qs_r \cdot (x - x_0))} \quad (7.9)$$

in which  $Qs_r = \frac{qs_{lat}}{Qs_0}$ . The depth  $h_c$  can be derived from Eqs. 7.5, 7.6, and 7.8, to yield

$$\frac{dh_c}{dx} = \frac{-Qs_r \cdot h_c}{n(1 + Qs_r \cdot (x - x_0))} \quad (7.10)$$

hence

$$i_r(x) = \begin{cases} 1 & \text{if } x < x_0 \\ (1 + Qs_r(x - x_0))^{\frac{3}{n}} & \text{if } x_0 < x < x_{end} \\ (1 + Qs_r(x_{end} - x_0))^{\frac{3}{n}} & \text{if } x > x_{end} \end{cases} \quad (7.11)$$

$$h_r(x) = \begin{cases} 1 & \text{if } x < x_0 \\ (1 + Qs_r \cdot (x - x_0))^{-\frac{1}{n}} & \text{if } x_0 < x < x_{end} \\ (1 + Qs_r \cdot (x_{end} - x_0))^{-\frac{1}{n}} & \text{if } x > x_{end} \end{cases} \quad (7.12)$$

$$\text{where } i_r = \frac{i_{c,new}}{i_{c,0}} \text{ and } h_r = \frac{h_{c,new}}{h_{c,0}}$$

Equations 7.11 and 7.12 describe the new equilibrium state of the river, with respect to its initial state, taking into account the sediment exchange between the groyne fields and the main channel. The behaviour of this case is analysed in Section 7.4.1.

### Reduced discharge in the main channel

Lowering the groynes is largely similar to lowering of the floodplain; a case that is investigated thoroughly by Van der Klis (2003) and Van Vuren *et al.* (2002). Both can be treated as a reduction of the discharge passing through the main channel (Figure 7.3a). Assuming that lowering of the groynes takes place in the reach from  $x_0$  to  $x_{end}$ , the equilibrium slope and flow depth will change only in that reach. Utilising Eqs. 7.4, 7.6, and 7.7, the change in slope and depth can be estimated as,

$$i_r = \frac{Q_{mc,0}}{Q_{mc,new}} \text{ and } h_r = \frac{Q_{mc,new}}{Q_{mc,0}}$$

In the above derivation the discharge was assumed to be constant. Yet, lowering the groynes will change the discharge distribution over the three sub-channels of the cross-section, hence the probability distribution of the discharge in the main channel (Figure 7.3b). Therefore, it makes sense to include the effect of discharge variations on the new equilibrium state. The derived equations can be extended rather easily to include such an effect. The variation of discharges can be characterised by the probability distribution  $p\{Q\}$ , which can be obtained by analysing the discharge time-series (Figure 7.3b). We follow the methodology presented by Jansen *et al.* (1979) that leads to the following definitions,

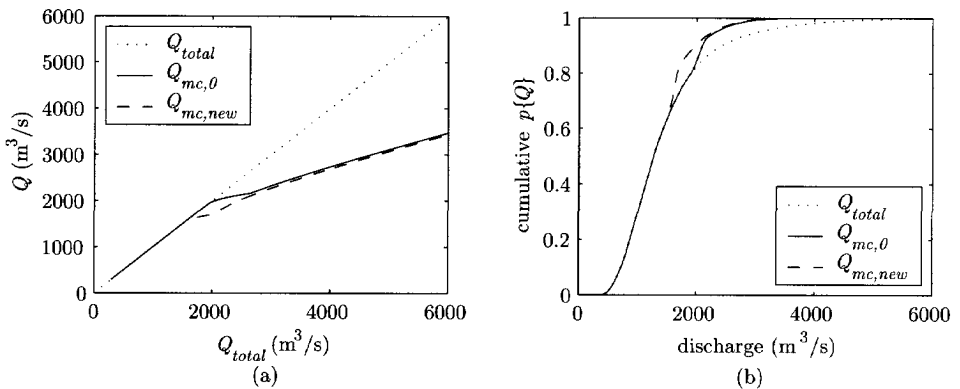


Figure 7.3: Comparison between the total discharge of the river and the discharge of the main channel (a), and cumulative probability distribution of the discharges (b); subscripts 0 and *new* refer to current situation and the situation with lowered groynes.

$$i_r = \left( \frac{\sum p_{i,0} Q_{i,mc,0}^{\frac{n}{3}}}{\sum p_{i,new} Q_{i,mc,new}^{\frac{n}{3}}} \right)^{\frac{3}{n}} \quad (7.13)$$

$$h_r = \left( \frac{\sum p_{i,new} Q_{i,mc,new}^n}{\sum p_{i,0} Q_{i,mc,0}^n} \right)^{\frac{1}{n}} \quad (7.14)$$

For the discharges of the Waal River measured between 1945 and 2005, this leads to values of  $i_r = 1.036$ , and  $h_r = 0.964$ . Note that the initial equilibrium flow depth in this case is estimated based on a 'dominant' discharge ( $Q_{D,h}$ ) defined as,  $Q_{D,h} = (\sum p_i Q_i^n)^{1/n}$ .

### 7.3.2 Morphodynamic model

Simulations described in this chapter were carried out using the SOBEC-River morphology module, which simulates the interactive cycle of water flow, sediment transport and bed level change. The flow module solves the one-dimensional de Saint Venant equations, which are a continuity equation and a momentum equation. They consecutively read:

$$\frac{\partial A_t}{\partial t} + \frac{\partial Q}{\partial x} = q_{lat} \quad (7.15)$$

$$\frac{\partial Q}{\partial t} + \frac{\partial}{\partial x} \left( \alpha_B \frac{Q^2}{A_f} \right) + g A_f \frac{\partial z_w}{\partial x} + \frac{g Q |Q|}{C^2 R A_f} = 0 \quad (7.16)$$

where  $A_t$  the total cross-sectional area including the storage area,  $A_f$  the cross-sectional flow area,  $Q$  the discharge,  $q_{lat}$  the lateral discharge added to the river per unit length,  $\alpha_B$  the Boussinesq coefficient (to account for the non-uniform velocity distribution in a cross-section),  $g$  the gravity acceleration,  $z_w$  the water level measured from a chosen reference level,  $C$  the Chézy coefficient, and  $R$  the hydraulic radius.

The sediment transport rate is estimated using an empirical sediment transport formula. Here, we use the formula of Engelund and Hansen (1967) which computes the total load transport rate in deposited volume per unit width and time,

$$qs = \frac{0.05}{(1-p)\sqrt{g} C^3 \Delta^2 D_{50}} u^5 \quad (7.17)$$

in which  $u$  is the average flow velocity in the main channel,  $p$  the porosity,  $\Delta$  the relative density of sediment and  $D_{50}$  nominal sediment size. Note that this formula can be simplified to  $qs = m \cdot u^n$ , with  $m$  constant and the exponent  $n = 5$ . The total sediment transport is then calculated by

$$Qs = B_s qs \quad (7.18)$$

in which  $B_s$  is the sediment transporting width. Here, sediment transport takes place only in the main channel i.e.  $B_s = B_{mc}$ .

Sediment transport gradients lead to changes in the cross-sectional profiles of the river. These changes are calculated by solving the mass balance equation for bed material,

$$\frac{\partial A_s}{\partial t} - \frac{\partial Q_s}{\partial x} = -q_{s_{lat}} \quad (7.19)$$

in which  $A_s$  is the sediment-transporting cross-sectional area, and  $q_{s_{lat}}$  is the lateral sediment supply, in deposited volume per unit river length and time. Changes in bed level ( $z$ ) can be calculated from the changes in the cross sectional area; an increase of  $A_s$  corresponds to a lowering of the bed level. For additional details on the model we refer to the technical manual of SOBEK (WL | Delft Hydraulics, 2001b).

## 7.4 EFFECT OF SEDIMENT EXCHANGE BETWEEN THE GROUYNE FIELDS AND THE MAIN CHANNEL

### 7.4.1 The equilibrium state

The analytical model gives a first impression of the effect of the sediment exchange between the groyne fields and the main channel on morphology of the main channel. This model does not reveal the morphodynamic behaviour of the river. However, it gives valuable information about the tendencies of changes and it can be utilised to study the sensitivity of the morphological changes to different parameters.

#### Case 1: constant supply of sediment from the groyne fields

We consider the case study of an emerged-groynes situation with a constant river discharge of  $1450 \text{ m}^3/\text{s}$ , to study the behaviour of the analytical model.

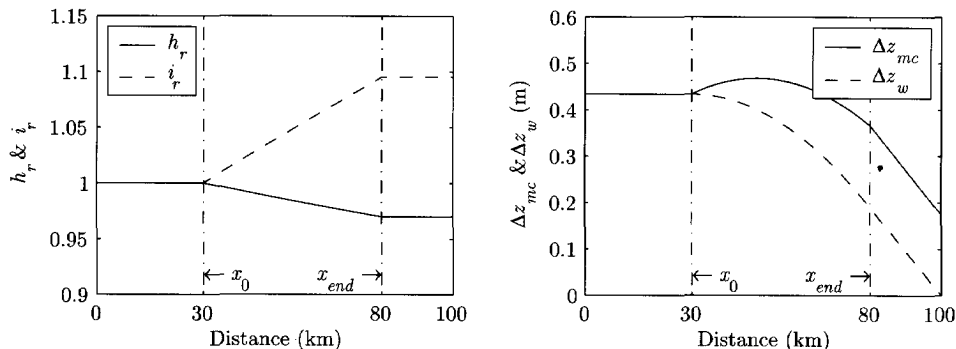


Figure 7.4: Changes in slope and depth due to sediment supply rate  $q_{s_{lat}} = 0.1 \times 10^6 \text{ m}^2/\text{s}$  from the groyne fields (left panel), and corresponding changes in bed and water levels (right panel).



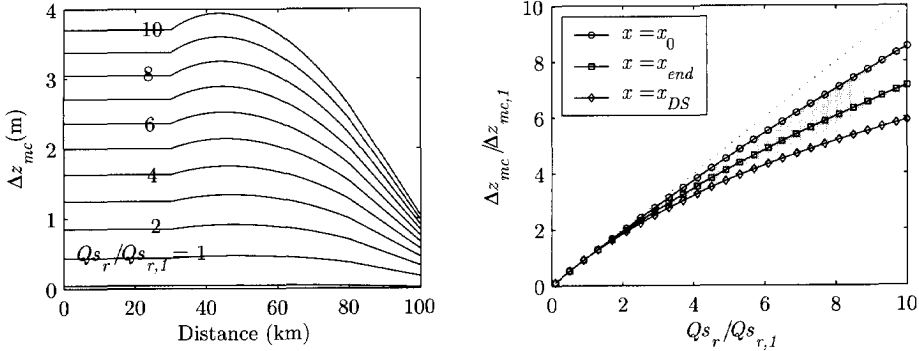


Figure 7.5: Sensitivity to changes in  $Q_{s_r}$ ; longitudinal profiles of  $\Delta z$  for different values of  $Q_{s_r}$  (left panel), and relative changes in  $\Delta z$  versus relative changes in  $Q_{s_r}$  at different locations along the river.

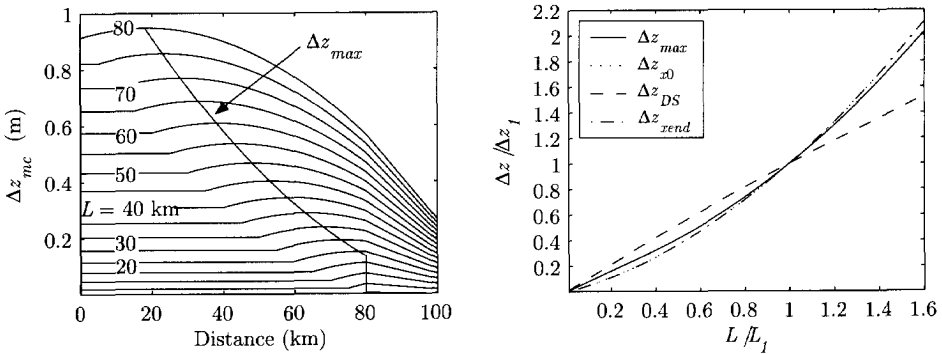


Figure 7.6: Sensitivity to changes in length of morphologically active reach ( $L = x_{end} - x_0$ ); longitudinal profiles of  $\Delta z$  (left panel) and effect on  $\Delta z$  at some locations along the river (right panel).

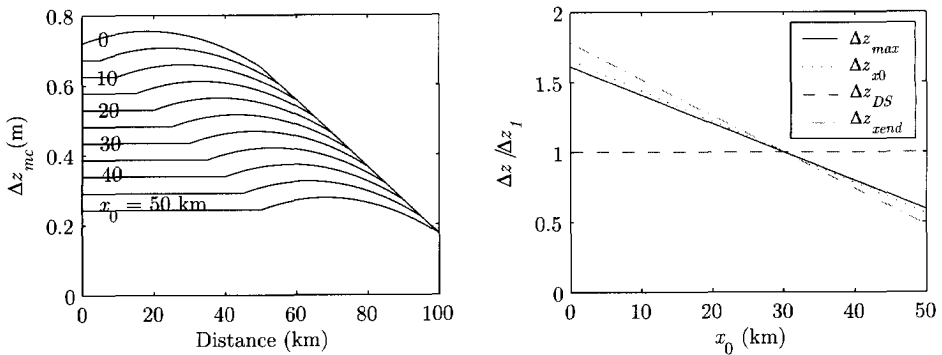


Figure 7.7: Sensitivity to changes in  $x_0$ ; longitudinal profiles of  $\Delta z$  (left panel), and effect on  $\Delta z$  at different locations along the river (right panel).

Since the emerged state implies that the flow is confined to the main channel, the groyne fields and the floodplain sections can be neglected in this case. The solution of Eqs. 7.11 and 7.12 which describes the new state of equilibrium, has the graphical representation given in Figure 7.4(left panel), from which we are able to distinguish three different regions along the river.

Upstream of point  $x_0$  which marks the start of the morphologically active groyne fields reach, neither the slope nor the flow depth go through any changes. Between points  $x_0$  and  $x_{end}$ , there is a gradual increase of  $Qs$ , which cause changes in both the slope and the flow depth; the slope gradually increases in the downstream direction while the flow depth decreases. Downstream of point  $x_{end}$ , the river responds as if it experiences a point source of sediment supply at point  $x_{end}$  with the cumulative lateral sediment supply from the reach ( $x_0 \sim x_{end}$ ). Accordingly, this reach develops a new steeper, yet constant slope and a shallower depth. Changes in slope and depth lead to changes in bed and water levels. An example of such changes is presented in Figure 7.4 (right panel) where we see that the bed level increase can reach some 0.43 m upstream of point  $x_0$ .

Three parameters affect the result of the model, viz. the lateral sediment supply rate, the length of the active region ( $x_0 - x_{end}$ ), and the location at which it starts. The sensitivity to these parameters is presented in Figure 7.5, Figure 7.6, and Figure 7.7 consecutively and could be summarised as follows:

- Changes in the sediment supply rate in the order of  $\pm 100\%$  have an equivalent, nearly linear, effect on  $\Delta z$ ; for higher changes of  $Qs$ , non-linearity appears (Figure 7.5).
- $\Delta z$  is slightly more sensitive to increasing the length of the morphologically active region. Extending that length by e.g. 50%, increases the maximum  $\Delta z$  by 83%; whereas, reducing it by the same amount reduces  $\Delta z$  by some 60% (Figure 7.6).
- Starting the active region at a more upstream location increases  $\Delta z$ , as the effect of the steeper slope downstream of  $x_{end}$  extends over a longer distance;  $\Delta z$  varies linearly with changes in  $x_0$  (Figure 7.7).

The temporal development to reach equilibrium was evaluated by applying the numerical model to the same case. The ‘equilibrium state’ resulting from the numerical simulation coincided with that resulting from the analytical model (Figure 7.8a). A representative morphological time-scale for the deposition process was estimated by assuming that bed development follows a relaxation model that takes the form,

$$\Delta z(t) = \Delta z_{equilibrium} \left( 1 - \exp \left( - \frac{t - t_0}{T_{mor}} \right) \right) \quad (7.20)$$

It follows from Eq. 7.20 that  $T_{mor} = t(\Delta z = 0.63 \Delta z_{equilibrium})$ . Accordingly, the morphological time-scale was estimated from the results of the numerical model (Figure 7.8b). The morphological time-scale varied with the location along the river from around 55 years at point  $x_{end}$ , to some 85 years at point  $x_0$  (Figure 7.8c). This variation is due to the increasing sediment load from point  $x_0$  to  $x_{end}$ .

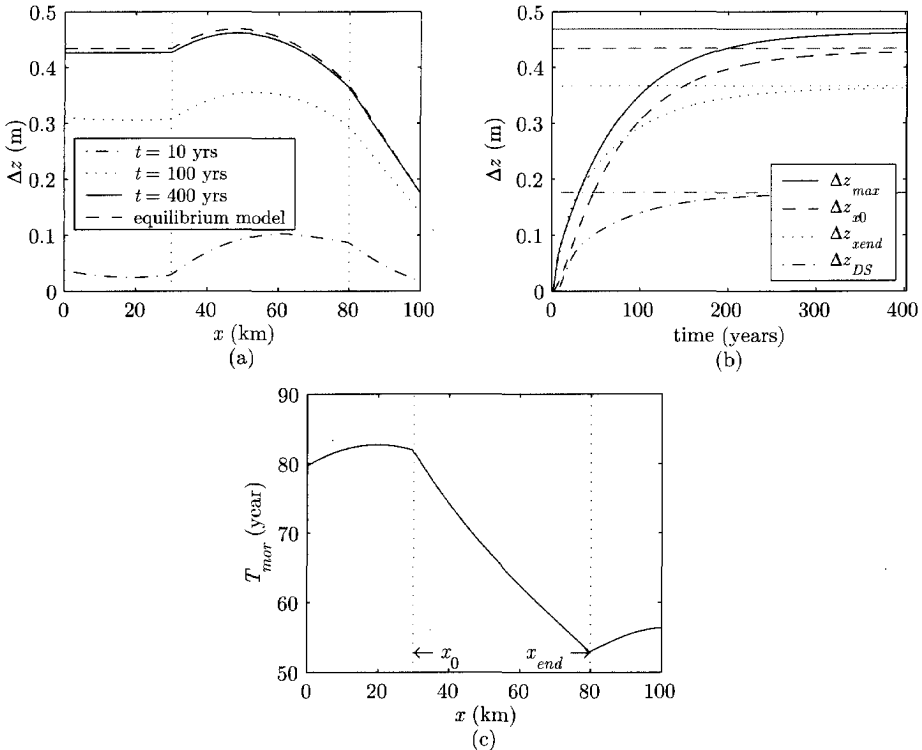


Figure 7.8: Result of the numerical model compared with analytical model; (a) equilibrium and intermediate states of the longitudinal profile, (b) temporal development at some locations along the river, horizontal lines are equilibrium values, and (c) morphological time-scale as a function of the location along the river.

#### 7.4.2 Morphodynamic behaviour

The variable discharge that is inherent to reality and, more importantly, the alternation between emerged and submerged groyne situations produces a dynamic behaviour, in which an equilibrium state as defined in the foregoing formally may exist, but will never be reached. In this case, studying the variations around this so-called equilibrium state becomes more relevant. To that end, a time-dependent morphodynamic model has to be used. Here, we apply the dynamic model to two cases. In the first case, we use a rather simple hydrograph composed of a low-flow – high-flow sequence. In the second case study, we utilise the historical discharge time-series of the Rhine River.

In either case, the model was initially run without including the interaction with the groyne fields, in order to establish the natural dynamic behaviour of the bed under variable discharge. In a subsequent run, the lateral exchange component is introduced; the natural variations as estimated from the initial run are subtracted from the results, in order to isolate the effect of the interaction with the groyne fields.

### Case 2: low-flow – high-flow sequence

The purpose of this case study is to have insight into the seasonal variations of the bed level in the main channel due to the interaction with the groyne fields. Therefore, three different sub-cases were considered, each comprising a simplified hydrograph composed of two discharges (Figure 7.9 lower panels). The duration of the low-flow condition varied between one year (Case 2a), five years (Case 2b) and ten years (Case 2c). To compensate for the long dry period, the magnitude of the flood varied correspondingly between 3000, 5000, and 6000 m<sup>3</sup>/s. Each run covered a period of 200 years, through which the lateral sediment exchange component was guaranteed to yield no net erosion or deposition to the groyne fields on the long run i.e.  $\sum_{\text{large time}} q_{s_{lat}} = 0$ ; note that the peak discharge increases with the interval between floods to satisfy this condition.

During low-flow periods, the sediment coming from the groyne fields is deposited in the main channel. This sediment is brought back to the groyne fields during the high-flow period. Such a behaviour induces temporal variations in bed level. Figure 7.9 (upper panels) presents an example of these variations at some locations along the river. The effect of the extent of the dry period is visible in the amplitude of changes in  $\Delta z$  (cf. Figure 7.9a and Figure 7.9c).

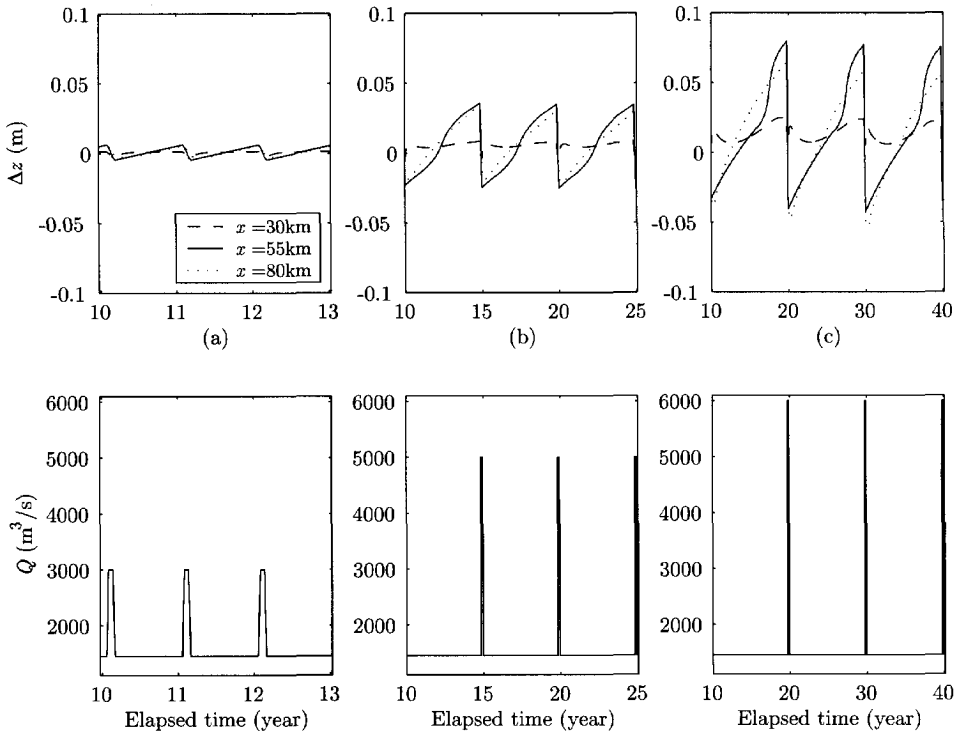


Figure 7.9: Schematic hydrographs used in Case 2 (lower panels), and corresponding bed level variations at some locations along the river (upper panels);  $\Delta z$  does not include natural bed variations.

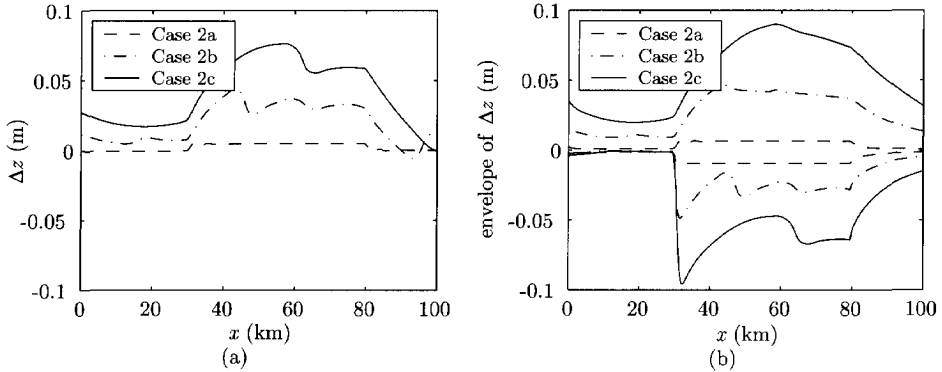


Figure 7.10: Longitudinal profile of bed level changes  $\Delta z$  at the end of the dry period (a), and the envelope of these changes during the whole simulation period ( $\Delta z_{\max}$  &  $\Delta z_{\min}$ ) (b).

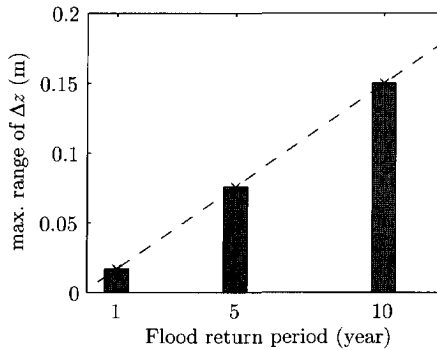


Figure 7.11: Effect of a long dry period on the range of bed level changes; dashed line is an indication of the trend of  $(\Delta z_{\max} - \Delta z_{\min})_{\max}$  versus the return period of flood.

The longitudinal profile of bed level changes  $\Delta z$  at the end of the dry period is presented in Figure 7.10a, where we can see a tendency to reach a new equilibrium state based on dry season conditions (cf. Figure 7.8a). However, this tendency is interrupted by the subsequent flood. Unlike the results presented in Figure 7.8a for a constant discharge, we can now distinguish the morphological effects of the variable discharge, viz. the existence of migrating bedforms downstream of point  $x_0$ . The envelope of these changes is presented in Figure 7.10b, from which the maximum range of variation was estimated. The result, as presented in Figure 7.11, reveals the effect of extended duration of dry conditions on the range of bed level variations. For a dry period of less than a decade, the range of variations is nearly linear (dashed line in Figure 7.11). A longer dry period shows a relaxation behaviour hence, the result presented in Figure 7.8b is more relevant.

### Case 3: discharge time-series from 1945 to 2005

In this case study, we utilise the actual discharge time-series of the Waal River for the last 60 years from 1945 to 2005 (Figure 7.12, lower panel). We assume the bed level variations in the groyne fields to be small enough for the lateral sediment exchange rate not to be affected.

Figure 7.12 (upper panel) presents the temporal changes of bed level at some locations along the morphologically active reach. The result shows that the morphodynamic behaviour of the river bed comprises two different time-scales. The first is in the order of one year and the second in the order of a decade. The short morphological time-scale results from the seasonal discharge variations that give rise to submerged groyne conditions with a return period of one year. The amplitude of changes at this time-scale is quite small and can be estimated from the simplified case of low-flow – high-flow sequence with a flood return period of one year (Case 2a, Figure 7.9a).

The long morphological time-scale results from the long-term discharge variations with relatively long dry/wet periods (periods with low/high flood intensity). Such a behaviour induces an imbalance between the erosion and deposition in the groyne fields. A relatively dry period causes an imbalance in favour of erosion from the groyne fields, yielding

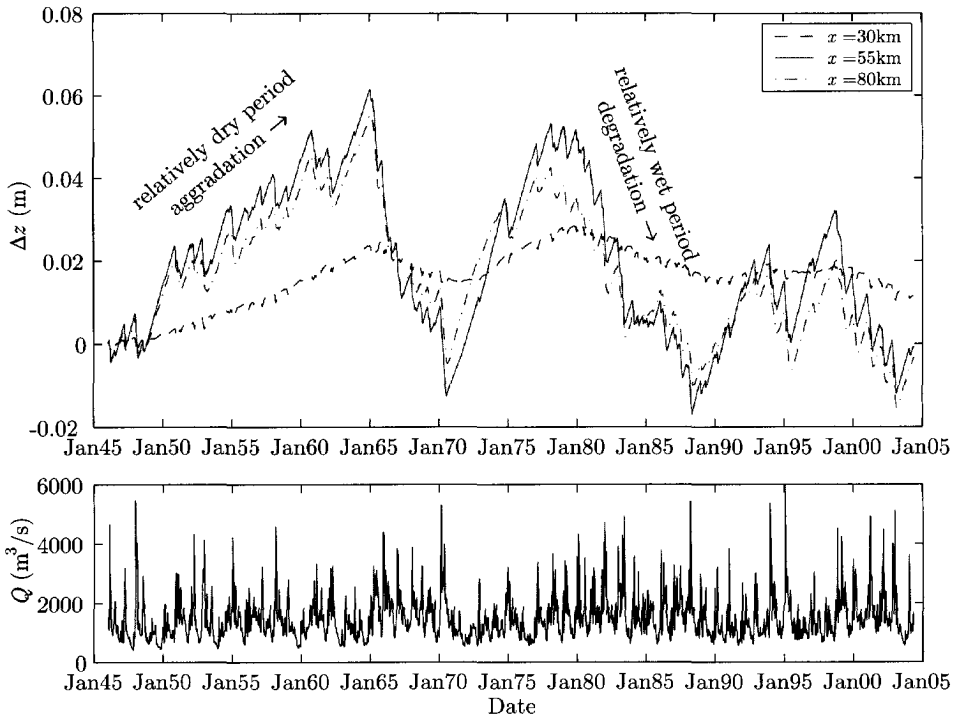


Figure 7.12: Temporal changes in  $\Delta z$  of the main channel due to the interaction with groyne fields at some locations along the river (upper panel), and discharge time-series (lower panel).

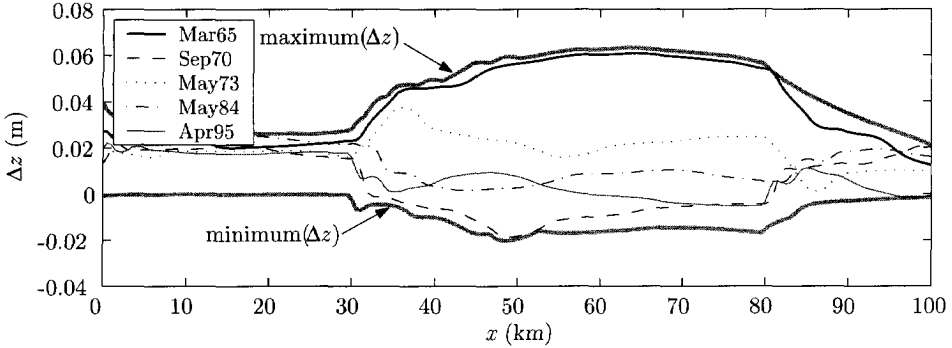


Figure 7.13: Some realisations for variations in the bed level of the main channel due to the interaction with groyne fields, and the envelope of all realisations for the period 1945-2005.

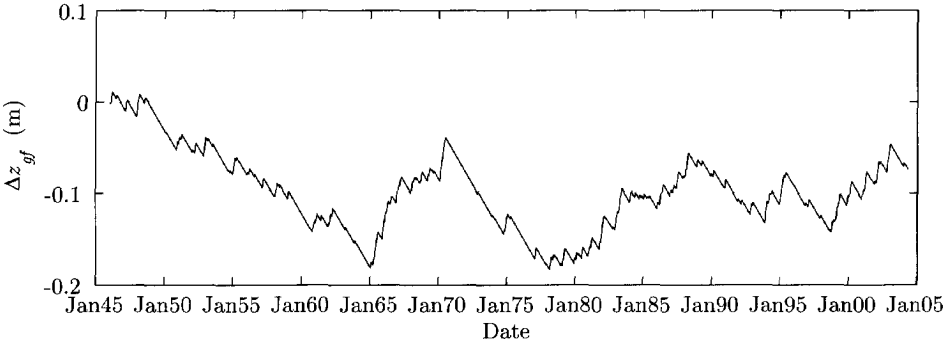


Figure 7.14: Temporal variations of the bed level of the groyne fields in the period 1945-2005.

a tendency to general aggradation in the main channel. Conversely, a relatively wet period causes an imbalance in favour of deposition into the groyne fields, yielding a tendency to general degradation in the main channel. The amplitude of variations at this time-scale is larger than at the yearly scale. It can also be estimated from a simplified case of low-flow – high-flow sequence with a reduced exchange rate. The exchange rate in this case should be equivalent to the net imbalance between erosion and deposition rates and the flood return period is meant to be equivalent to the extended dry period.

The case study shows that during the past 60 years the range of bed level changes due to the interaction between the main channel and the groyne fields is about 8 cm (Figure 7.13). Such a small variation can hardly be detected in the natural system. If it were only the natural variation in bed level due to discharge variations is usually higher.

Since sediment is continuously transported in the downstream direction, variations in the sediment content of the groyne fields do not necessarily mirror those in the main channel. Figure 7.14 represents the bed level variation in the groyne fields during the period 1945-2005, from which we see that there has been up to 20 cm of degradation. These variations are too small to significantly influence the sediment exchange rates.

Similar to the effect on the main channel, we can detect the effect of the imbalance between the inflow and outflow parts of  $qs_{lat}$  on the changes in the bed level of the groyne fields. For instance, in the relatively dry period 1970-1980, the bed in the groyne fields degrades by 20 cm. In the relatively wet period 1980-1990, however, the bed in the groyne fields aggrades by a similar amount. During the last decade, the range of bed level variations in the groyne fields amounts to only 10 cm.

## 7.5 LOWERING THE GROYNES

Lowering the groynes will alter both the discharge passing through the main channel and the sediment exchange with the groyne fields. Firstly, we investigate the morphological effect of reducing the discharge passing through the main channel due to increasing the conveyance capacity of the groyne fields region. The effect is analogous to that of lowering the floodplain. This effect is first evaluated without including sediment exchange with the groyne fields (Case 4), subsequently, including the lateral sediment exchange component  $qs_{lat}$  (Case 5).

### 7.5.1 Effect of reduced discharge in the main channel

#### Case 4: lowering the groynes; $qs_{lat} = 0$

In this case study we use the schematic channel described in Section 7.2 with the groynes lowered by one metre in the reach from  $x_0$  to  $x_{end}$ . To explore a possible new equilibrium state, we repeat the discharge time-series of 1945-2005, 4 times to cover an extended period of 240 years. Lowering the groynes is modelled by reducing the roughness of the groyne fields in the designated region in accordance with the findings of Chapter 3 (Eq. 3.8, Section 3.6). Such an action will reduce the discharge passing through the main channel section (see Figure 7.3).

Eqs. 7.13 & 7.14 show that in the equilibrium state the slope of the lowered-groynes reach will be steeper and the flow depth shallower than in the initial state. Between points  $x_0$  and  $x_{end}$ , the river will therefore aggrade while getting steeper. Upstream of point  $x_0$ , the river bed slightly aggrades without any change in slope. The result of the analytical equilibrium state model clearly indicates this behaviour (dashed line in Figure 7.15).

The results of the morphodynamic simulation indicates that the river tends towards a new dynamic equilibrium state (Figure 7.16) of which the mean bed level changes during the last simulated 10 years coincide fairly well with those resulting from the equilibrium model. Clearly, the agreement between the dynamic model and the equilibrium model in this case is not perfect as in the case of a constant discharge. The dynamic model yields a steeper bed than the equilibrium model (Figure 7.15). The 90% confidence interval based on the statistics of the last 10 years of simulation, i.e. after the river has already reached the new equilibrium state, indicates the natural variability of the bed level due to discharge variations (Figure 7.15). Such a variability is inherent to nature, due to the inherent variability of the discharge time-series.



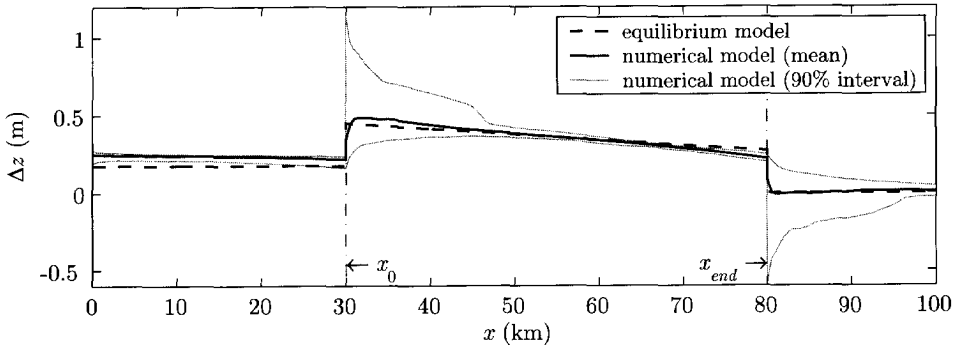


Figure 7.15: Bed level changes due to the decreased discharge in the main channel because of lowering the groynes; comparison between analytical equilibrium state model (Eqs. 7.13 & 7.14), and numerical model (statistics are based on the results of the last 10 years).

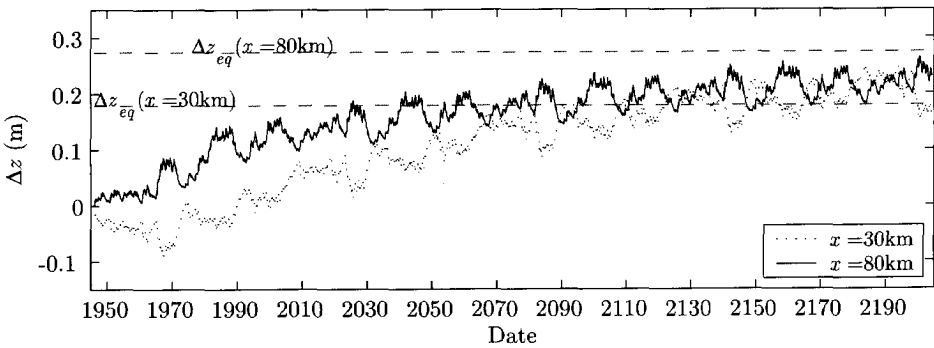


Figure 7.16: Temporal development at the upstream and downstream ends of the lowered-groynes reach compared with the equilibrium value.

In summary, the bed aggradation in the reach upstream of point  $x_0$  amounts to some 0.25 m. In the lowered-groynes reach, the mean aggradation can reach some 0.50 m at point  $x_0$  and 0.20 m at point  $x_{end}$ . Due to the abrupt change in the conveyance at points  $x_0$  and  $x_{end}$ , the range of variability at these two locations is relatively large.

### 7.5.2 Effect of sediment exchange

#### Case 5: lowering the groynes; $qs_{lat} = f(Q)$

Due to lowering the groynes, not only the discharge through the main channel is reduced but also the lateral exchange of sediment between the main channel and the groyne fields ( $qs_{lat}$ ) is altered. The effect of the latter is introduced in this case study. The morphological effect of lowering the groynes is modelled in accordance with the findings of Chapter 5 by adapting  $qs_{lat}(Q)$  to the new situation. On the one hand, the groyne fields' filling component of  $qs_{lat}$  during the submerged conditions is reduced. On the other hand, the

groynes are going to be submerged more often, which reduces the time fraction of erosion due to navigation and increases the time fraction of deposition due to high flow. Groyne lowering will therefore disturb the long-term balance between erosion and deposition processes, leading to a new equilibrium bed level in the groyne fields. This will develop during the first years after lowering the groynes, after which, again, the long-term balance of  $qs_{\text{net}}$  will prevail again. The morphological effect of that new balance is similar to that of the original one (see Section 7.4).

The new equilibrium bed level for the groyne fields, and hence, the morphological time-scale, are very much dependent on how the navigation-induced erosion process responds to the bed level changes in the groyne fields. Such information cannot be obtained from the data available at present. Therefore, we will run the model for a long period of time without changing the effect of navigation, in order to have an impression of the rate of change during the transition period. Again, we utilise the discharge time-series of 1945–2005, repeated 4 times to cover a period of 240 years.

The effect on the bed level in the groyne fields is presented in Figure 7.17 where we can see a lower deposition rate due to the lowering of the groynes, apparently, this dominates the effect of the larger time fraction of submergence. This causes an imbalance in favour of eroding the beaches of the groyne fields and leads to an ongoing degradation over the years. Noticeably, it is a very slow process that has an average erosion rate of 0.28 cm/year (dashed line in Figure 7.17). Needless to say that the linear behaviour in Figure 7.17 is a result of ignoring the feedback between the actual bed level and the rate of sediment exchange. Allowing feedback would reduce the long-term erosion rate with time, yielding a relaxation-type behaviour for the bed level of the groyne fields. For reference, a hypothetical curve with a morphological time-scale of 100 years with the same initial rate of erosion (0.28 cm/year) is presented by the dotted line in Figure 7.17.

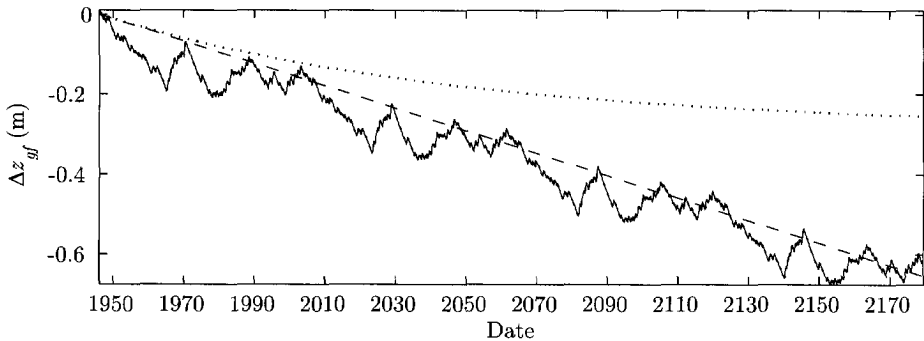


Figure 7.17: Temporal variations of the bed level of the groyne fields due to lowering the groynes; the dashed line is a linear fit to the estimated  $\Delta z_{gf}$ , the dotted line is a relaxation model with a hypothetical morphological time-scale of 100 years.

The sediment becoming available from the ongoing large-scale degradation of the groyne fields, is laterally supplied to the main channel, a situation similar to Case 1 (cf. Figure 7.18b & Figure 7.8a). Consequently, the equilibrium mean bed level in the main channel is slightly higher in this case than when disregarding any lateral exchange of sediment (Figure 7.18a). The difference between the equilibrium profiles in Figure 7.18a, is only due to the additional sediment supply from the groyne fields (Figure 7.18b). Once equilibrium bed level has been reached in the groyne fields, however, the balance in  $qs_{lat}$  has been restored and the equilibrium mean bed level in the main channel will be the same in either case similar to that of Case 4. The principal effect of the initial imbalance of  $qs_{lat}$  is therefore a reduction of the morphological time-scale of the aggradation process in the main channel (Figure 7.19). The morphological time-scale of this aggradation process was evaluated for either cases: 75 years for Case 5, as opposed to 125 years for Case 4.

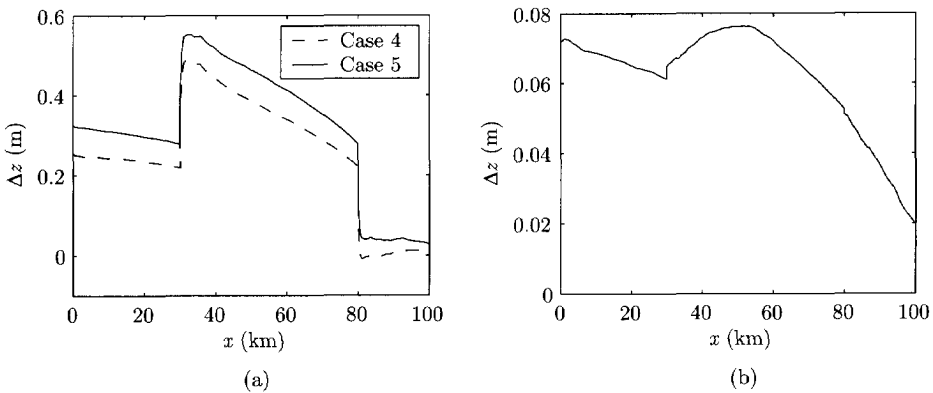


Figure 7.18: The mean bed level changes over the last 10 years of simulation due to lowering the groynes; (a) comparison between Case 4, and Case 5, (b) isolated effect of including the exchange between the main channel and the groyne fields.

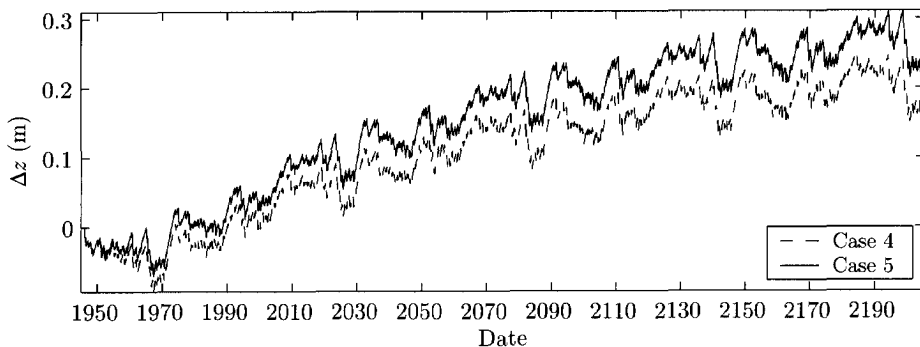


Figure 7.19: Comparison between the temporal development in Case 4 and Case 5 for the main channel bed level at the upstream end of the lowered-groyne reach.

## 7.6 SUMMARY AND DISCUSSION

In this chapter, the large-scale morphological effect of the interaction between the main channel and the groyne fields of a river has first been investigated for the current situation. Subsequently, the effect of lowering the groynes has been investigated. Three cases were considered to analyse the morphodynamics of the current situation, and two additional cases to study the situation upon lowering the groynes.

### Analysis of current situation

**Case 1:** A constant supply of sediment from the groyne fields to the main channel was assumed in the analysis of the analytical equilibrium state model, and in the sensitivity analysis. The results from the analytical model can be considered as the maximum possible changes under a certain discharge condition. We have to realise, however, that, for several reasons, such changes will never take place in real-life situations. Firstly, due to the nature of the discharge hydrograph, such a long period of constant low discharge will never occur. As soon as a flood takes place, sediment will be brought back into the groyne fields. Even if we alter the natural hydrograph, e.g. by creating a secondary channel to dampen flood peaks, the amount of sediment available between the groynes is not enough to sustain such a supply rate for a time long enough to reach equilibrium in the main channel. Moreover, feedback from the decreasing bed level of the groyne fields onto the erosion rate will sooner or latter become an important factor that should be taken into account. If such a change in the hydrograph is to take place, the groyne fields will tend to erode completely before the main channel reaches its equilibrium state. If such a scenario is practically relevant, it should be subject to additional investigation.

**Case 2:** Three different sub-cases, each comprising a simplified hydrograph composed of a regular low-flow – high-flow sequence, were used to investigate the seasonal variations of the main channel bed level due to the morphological interaction with the groyne fields. The range of variations at a time scale less than a decade was found to be linearly proportional to the flood return period. This indicates that the time scale of adjustment to the new equilibrium state must be much longer than a decade. The results from this case study also show the importance of including the interaction with the groyne fields when studying scenarios that involve long dry or wet periods.

**Case 3:** Utilising the actual discharge time-series 1945-2005, this case was used to analyse the morphodynamics of the existing situation before lowering the groynes. With respect to the main channel, the effect of the interaction with the groyne fields was found to be relatively small. The maximum range of variation of the bed level was less than 0.1 m. The bed level of the groyne fields showed a wider range of variation. Two different morphological time scales were detected, in the main channel and the groyne fields. The first is associated with the seasonal discharge variations, and the second is due to the residual sediment transport in certain direction due to the long-term imbalance of the lateral sediment exchange component associated with considering long periods of relatively high and low discharges.

Validation of this morphodynamic behaviour of the main channel with field data is not possible, since the natural variability of the bed level is usually larger than the calculated

variations due to the groyne fields effect. The morphodynamic behaviour of the groyne fields, however, conforms to field observations.

The sand supplied from the groyne fields was evenly distributed over the cross-section of the main channel. If we allow for an uneven distribution over the cross-section, the local morphological changes will be more pronounced. Nevertheless, the aim of this model is to study the large-scale morphological impact on the whole river. Analysis of the local morphological features near groynes requires the use of a multi-dimensional model (two- or even three-dimensional, see Chapter 6).

### Lowering the groynes

**Case 4:** The effect of the reduced discharge in the main channel was investigated in this case without including the lateral exchange with groyne fields. The bed aggradation upstream of the lowered-groynes reach amounted to 0.25 m, whereas the mean aggradation in the lowered-groynes reach reached some 0.5 m at the upstream end and 0.2 m at the downstream end. Due to the abrupt change in conveyance at the upstream and downstream ends, the range of variability at these two locations could reach 1.0 m. In reality, such large variations are not likely to occur, as the intrinsically discrete arrangement of the groynes makes the changes in cross-section at these locations rather gradual.

The 90% confidence interval indicated in Figure 7.15 is meant to describe the natural bed variation due to the discharge variation. This confidence interval was estimated from a single ‘deterministic’ model run, with a predefined hydrograph. Nonetheless, it is comparable to the uncertainty in the bed level due to discharge variation as indicated by Van Vuren *et al.* (2002) and Van der Klis (2003), where they used a Monte Carlo simulation to quantify the uncertainty in the morphological changes. The estimated confidence interval in our case contains most of the uncertainty in bed level due to discharge variation. What a Monte Carlo simulation offers more, is the confidence interval of the percentile, which is a relatively narrow band around it (cf. Van Der Klis, 2003). Here, we will adhere to the term ‘variability’ rather than ‘uncertainty’ as the uncertainty is mostly associated with stochastic modelling, whereas, the resulting variability is due to a single deterministic run.

**Case 5:** The exchange of sediment was introduced in this case to investigate the effect of changing the lateral exchange component from its current situation. The effect on the morphology of the main channel was minor compared to the effect of the reduced discharge. The principal effect is a reduction of the time scale of adaptation to a new equilibrium state. The model yields a monotonous degradation of the beaches of the groyne fields at a rate of 0.28 cm/year. In the absence of detailed information on the response of the navigation-induced sediment transport to the lowering of the bed level of groyne fields, it is not possible to model the feedback between the exchange flux and the state of the groyne fields, hence the time scale of adaptation to the new equilibrium state.

## 7.7 CONCLUSIONS

From the case studies presented in this chapter, the following conclusions can be drawn:

- In the present situation, the large-scale effect of the sediment exchange between the groyne fields and the main channel on the morphology of the main channel is small and can be ignored. However, in scenarios that involve a long dry period followed by a high flow flood, this effect should be taken into account.
- The primary morphological impact of lowering the groynes is due to the reduced discharge passing through the main channel.
- The sediment exchange with the main channel does not affect the ‘equilibrium’ state of the main channel, but it reduces the morphological time scale and accelerates the aggradation process in the main channel.
- Lowering the groynes causes a slow but persistent erosion of the groyne fields, caused by a disturbance of the long-term balance between the erosion and deposition of sediment in the groyne fields.
- The bed level variations in the groyne fields are small; in order to be able to detect them, measurements should be made consistently and over an extended period of time.

## Chapter 8

# CONCLUSIONS AND RECOMMENDATIONS

### 8.1 GENERAL

The effects of groynes on a river were investigated in this thesis, with primary focus on the morphological interaction between the groyne fields and the main channel. The thesis involved analyses on a range of spatial and temporal scales. At the small scale level, the governing sediment exchange processes between the groyne fields and the main channel of a river were identified. At the intermediate scale level, the effects of the groynes on the navigation channel were investigated. At the large scale level, the effects of the groynes on the morphology of the whole river were considered and the morphological impact of lowering the groynes was assessed. Various methodologies were utilised in accordance with the scale level considered, viz.,

- a fixed-bed flume experiment, to study the details of the hydrodynamics in the vicinity of a series of groynes,
- a mobile-bed flume experiment, to study the sediment exchange process between the main channel and the groyne fields,
- a two-dimensional process-based model (DELFT3D), to study the intermediate-scale morphological effect of a series of groynes on a river, and
- an analytical model and a one-dimensional numerical model (SOBEK), to study the morphological effects of groynes on the river at large.

The objectives of this thesis were formulated in Section 1.3 as follows:

- With respect to the hydrodynamics:
  - to identify the flow pattern in the vicinity of groynes in detail,
  - to estimate the resistance of the groynes to the flow when they are submerged.
- With respect to the morphodynamics:
  - to identify the transport mechanisms that govern the sediment exchange process between the river and its groyne-fields,

- to quantify the sediment budget of a single groyne field.
- With respect to modelling:
  - to devise feasible strategies for detailed modelling of rivers with groynes, and
  - to be able to aggregate the detailed small-scale behaviour to the large-scale level.
- With respect to river management:
  - to quantify the effect of lowering the groynes on the design flood level,
  - to identify the effect of the morphological interaction between the main channel and the groyne fields, and
  - to identify the morphological impact of lowering the groynes,

This thesis concerns groynes in a straight river reach without taking into consideration the interaction with the floodplain. The analysis presented in Chapter 5 as well as the case studies presented in Chapters 6 and 7 were based on schematic channels. The conclusions based on these case studies are to be interpreted within this context. These conclusions are summarised in the following section. The final section gives some recommendations for implementation and future research.

## 8.2 CONCLUSIONS

The following conclusions are drawn from this thesis:

### 8.2.1 Hydrodynamics near a series of groynes

- When the groynes are not submerged, the flow inside the groyne fields can be characterised by a primary eddy that forms in the downstream part of the groyne field, a secondary eddy driven by the primary one with an opposite sense of rotation, and a dynamic eddy that frequently sheds from the tip of the upstream groyne. The whole circulation is driven by the main stream via exchange of momentum through the interfacial mixing layer. In the submerged stage, the flow in the groyne fields region does not show the circulation pattern as observed in the emerged condition, yet, it can be characterised as a low velocity region. The mixing layer in this case shows an alternate accelerating and decelerating pattern between flow over and around the groynes.
- The mixing layer between the main channel and the groyne fields differs between the emerged and submerged flow stages. In the emerged situation, it originates from the tip of the groyne and grows in width towards the next groyne downstream. In the submerged situation, it has a rather constant width due to the continuous generation of turbulence by the successive groynes, which keep the total turbulence intensity along the normal line at a high level.
- To estimate the sediment budget of a single groyne field during the submerged situation, the flow near the groynes was parameterised as follows:



- the mixing layer between the river and the groyne fields was treated as a mixing layer with a constant width,
  - the mean velocity across the mixing layer was represented by a self-similar profile,
  - the large-scale fluctuating component of the velocity was represented by a 'perfect' sine wave,
  - the large-scale velocity fluctuations are in phase in the centre of the mixing layer and out of phase at its boundaries,
  - the amplitude of the fluctuations is proportional to the velocity difference across the mixing layer,
  - the velocity fluctuations are maximum in the centre of the mixing layer and negligible on its boundaries, and
  - the flow periodicity is a function of the mixing layer width and the velocity in its centre.
- A relation between the blockage by a groyne and its resistance to the flow has been reached (see Section 3.6). In this relation the resistance of the groynes region was represented by a drag formula, in which the drag coefficient is proportional to the blockage by a groyne to the flow. This led to an expression of an effective Chézy coefficient that is representative of the resistance in the groynes region (Eq. 3.8). Such an expression allows for estimating the conveyance capacity of the groynes region and hence the effect of lowering the groynes. This expression can be further utilised in numerical models (mainly one-dimensional models) where groynes will have to be schematised.

### 8.2.2 Morphological interaction between the river and its groyne fields

- In the absence of navigation, there is always a net import of sediment into the groyne fields from the main channel. In heavily navigated rivers, this is balanced by the navigation-induced sediment transport, yielding a state of dynamic equilibrium inside the groyne fields.
- The mechanisms of sediment transport into the groyne fields differ according to the flow stage. In the emerged situation, the sediment is mainly advected towards the groyne fields following the direction of the primary circulation cell. In the submerged situation, the sediment is transported to the groyne fields across the whole length of the normal line, primarily by residual advective transport by large-scale coherent structures. Diffusion through the mixing layer and secondary flow circulation play a minor role in this case.
- Groyne height, as such, does not affect the deposition volume into the groyne fields; it is primarily the submergence ratio that plays an important role. The lateral sediment transport component into the groyne fields normalized by that of the main channel decreases as the submergence level increases. However, due to the increase of sediment content in the main channel with increasing submergence, the net import of sediment into the groyne fields increases as the submergence level increases.
- A PIV-technique has been utilised to measure bedform celerity in the mobile-bed experiments. This method is suited for laboratory conditions with concentrations low

enough to allow sufficient visibility. The measured bedform celerity obtained with this PIV-technique confirmed the trend highlighted in the previous paragraph.

- The vertical suspended sediment concentration profiles in the vicinity of the groynes are not primarily governed by diffusion. There is additional sediment entrainment in this region, due to the high turbulence intensity and the existence of vortical motions. This is revealed by the deviation of the concentration profiles from their equilibrium shape. The equilibrium profile appears to form the lower envelope of the actual ones.
- The sediment budget of a single groyne field for different discharge conditions has been obtained by evaluating the influx and efflux components across the normal line. The sediment influx was obtained by analytically modelling the relevant sediment transport mechanisms. The efflux component was obtained from the balance between the deposition in the absence of navigation and the navigation-induced erosion. Information about navigation-induced erosion was primarily based on available literature. This exercise revealed that, indeed, the groyne fields are in a state of dynamic equilibrium. The morphological time-scale of the deposition process during flood conditions is an order of magnitude shorter than that of the erosion process.

### 8.2.3 Modelling rivers with groynes

With respect to intermediate-scale modelling, the following conclusions can be drawn:

- In the case of a river with groynes or similar structures, it is important to use a model that has the capacity to resolve large-scale time-dependent turbulence structures.
- A mathematical model that has the capacity to resolve large horizontal eddies (in this case: DELFT3D with HLES) yielded a flow field (in the case of emerged groynes) that compares well to that measured in the laboratory. Consequently, it was possible to reproduce the morphological features associated with groynes (groyne flames). In this case, the bed morphology computed when using HLES, as well as its associated time-scale, is comparable to what has been observed in a field case. When using a mean-flow model without HLES, the bed morphology was less realistic and the morphological time-scale was larger, by lack of the strong velocity fluctuations associated with the time-varying eddy formation (remember that  $Q_s(\bar{u}) \neq \overline{Q_s(u)}$ ). This implies that large eddies which form at the interface between the main channel and the groyne fields are an important mechanism underling the typical groynes-induced bed pattern.
- If large-scale flow structures exist, the time span for transport computations should be taken long enough to cover the large-scale structures. A snapshot or an average flow field would not necessarily yield the same result as a long time sequence. The transport direction, and hence the sediment flux into the groyne fields, is strongly affected by the contribution of the fluctuating lateral velocity component.
- The net advective sediment transport by large-scale structures could be modelled as diffusive transport by enhancing the sediment-mixing coefficient in the mixing layer. The obtained horizontal eddy viscosity from the sub-grid model is to be enhanced by

a factor  $\mathcal{O}(5)$  in order to account for the increased exchange in the mixing layer. Yet, the use of an eddy-resolving model is recommended.

- The simulation presented in Chapter 6, and several others not included herein, as well as those carried out by Rupprecht (2004), did not yield any morphodynamic response in the groyne fields. This shortcoming of the numerical model is primarily due a deficiency of the transport model, which does not account for the increased turbulence level in the mixing layer, nor for the role of vortical motions in picking up sediment and keeping it in suspension over large distances.

With respect to large-scale modelling, the following conclusions can be drawn:

- When schematising a river with groynes in a one-dimensional model, a drag-formulation is preferred over a weir-formulation to represent the groynes. In this case, the groyne region should have an equivalent roughness coefficient that is a function of the blockage by the groynes. Accordingly, if the groynes are lowered, only the effective roughness in the groynes region will be reduced.
- The morphological interaction between the main channel and the groyne fields can be represented by a discharge-dependent lateral supply/extraction of sediment to/from the main channel, in accordance with the small-scale morphodynamic behaviour of the groyne fields under different discharge conditions.
- The above is based on a quantitative description of the small-scale behaviour and its aggregation to a forcing (boundary condition) of the system. In the absence of a model that can reproduce the small-scale behaviour correctly, this is a suitable approach to large-scale prediction.

#### 8.2.4 Groyne lowering

- In order to estimate the conveyance capacity of the groynes region, using a one-dimensional model, two methods are available to represent the groynes, viz. a weir-formulation and a drag-formulation. The difference between the two lies in the assumption that in the former the water surface slope is zero (horizontal surface) between the groynes, whereas in the later it is equal to the water surface slope in the main channel. Besides, in the case of a weir-formulation, by definition, the flow control-section lies on top of the groynes, whereas in the drag-formulation the control-section lies between the groynes. Having the flow control-section on top of the groynes makes the estimate of the discharge capacity of the groynes region sensitive to changes in the crest level of the groynes. Using a drag-formulation, the conveyance capacity of the groynes region is less sensitive to the exact height of the groynes. Since the flow control-section in this case is not affected by changes in the groyne, only the drag coefficient is a function of the groyne geometry. In addition, due to the momentum exchange along the normal line, the slope in the groynes region is more likely to be similar to that in the main channel. Therefore, a drag-formulation is preferred. Note that, both methods of representing the groynes (weir or large obstacle) can be calibrated to reproduce a given situation. However, when attempting to evaluate the effect of changing the geometry of the groynes, they will deviate from

one another, such that a weir representation will yield a more pronounced effect than a drag formulation.

- If the drag-resistance approach is adopted, the effect of lowering the groynes on the design flood level is rather small: lowering the groynes by 1.0 m will reduce the design flood level by approximately 4 cm. The effect of lowering the groynes on moderate floods is more significant. The insensitivity of the water level to groyne lowering under design flood conditions is due to the fact that the blockage by the groynes in this case is relatively small and the resistance of the groynes is proportional to the blockage.
- In the present situation, the large-scale effect of the sediment exchange between the groyne fields and the main channel on the morphology of the main channel is small and can be ignored. Nevertheless, in scenarios that involve a long dry period,  $\mathcal{O}(\text{decade})$ , followed by a high flood, this effect should be taken into account. The range of variation of the bed level in the main channel due to the interaction with the groynes was found to be in the order of 6 cm.
- The yearly variations in the bed level of a groyne field are rather small; on a larger-scale,  $\mathcal{O}(\text{decade})$ , these variations can reach some 20 cm; at a yet larger scale, the groyne fields are in a state of dynamic equilibrium and the variations are small, again. In order to be able to detect bed level variations in a groyne field, measurements should be made consistently and over an extended period.
- The primary morphological impact of lowering the groynes is due to the reduced discharge passing through the main channel. In the reach where the groynes are to be lowered, the bed slope will become steeper and large-scale aggradation will take place.
- The sediment exchange with the main channel does not affect the 'equilibrium' state of the main channel, but it reduces the morphological time-scale and accelerates the aggradation process in the main channel.
- Lowering the groynes causes a slow but persistent erosion to the groyne fields, caused by a disturbance of the long-term balance between the erosion and deposition of sediment in the groyne fields. If the groynes are to be lowered by 1.0 m, the average erosion rate in the groyne fields will amount to some 0.3 cm/year.

### 8.3 RECOMMENDATIONS

- The large-scale analysis was based on a schematic river. It is recommended to use the procedures presented in this thesis in a real-life situation e.g. in the Rhine branches model. In this case, the behaviour of the groynes is not only a function of the discharge, but also is of the location along the river. Groyne fields located in a straight reach behave differently from those located in a bend.
- The best representation of the resistance of groyne fields needs to be further evaluated. We believe that the drag-formulation is preferable to the weir-formulation. However, an extensive comparison between the two approaches was not conducted in this thesis. Assessment of the best representation of groynes can be made through a desk study, and if necessary laboratory experiments. For the specific case of lowering the groynes in the Waal, the effect on the design flood level can be evaluated by a physical model test that runs for the design flood situation.
- In this thesis, we focused on groynes in a straight river reach without including the effect of the floodplain. It is recommended to study the effect of non-parallel flow (e.g. oblique flow into floodplain) on the sediment balance of the groyne fields.
- Field observations indicate that there is a substantial difference in sediment size between the groyne fields and the main channel. In this thesis, we considered only uniform sediment. It is recommended to include graded sediment transport in modelling rivers with groynes using the procedures presented in this thesis.
- The navigation-induced erosion from groyne fields remains to be further investigated. We recommend carrying out a detailed laboratory experiment to study the navigation-induced erosion from the groyne fields. Upscaling of the results of such a model is by no means straightforward. Therefore, such an experiment should involve detailed measurements to calibrate a process-based model that can be further utilised to model the prototype situation.
- With the current performance of the hydrodynamic models in general and DELFT3D in particular, it appears that the development in sediment transport modelling is lagging behind. It is time to invest into the improvement of our sediment transport models, especially the incorporation of vortical motion and increased turbulence levels.



## BIBLIOGRAPHY

- ALVAREZ, J. A. M. (1989). "Design of groins and spur dikes" *In: Proc. 1989 National Conf. On Hydraulic Engineering*, New Orleans, 296-301.
- AYA, S., FUJITA, I., and MIYAWAKI, N. (1997). "2-D Models for flows in river with submerged groins" *In: Proc. 27<sup>th</sup> IAHR Congress*, San Francisco, CA. USA, 829-837.
- BASTIAANS, R. J. M., VAN DER PLAS, G. A. J., and KIEFT, R. N. (2002). "The performance of a new PTV algorithm applied in super-resolution PIV" *Experiments in Fluids*, 32(3), 346-356.
- BERG, M. H., and UIJTTEWAAL, W. S. J. (2002). *Anticiperend onderzoek kribben*, (measurements report). Delft University of Technology, Delft, the Netherlands.
- BHOWMIK, N. G., XIA, R., MAZUMDER, S., and SOONG, T. W. (1995). "Return flow in rivers due to navigation traffic" *Journal of Hydraulic Engineering, ASCE*, 121(12), 914-918.
- BIJVELDS, M. D. J. P., KRANENBURG, C., and STELLING, G. S. (1999). "3D Numerical Simulation of Turbulent Shallow-Water Flow in Square Harbor" *Journal of Hydraulic Engineering*, 125(1), 26-31.
- BROLSMA, J. U. (1988). *Six-barge push-tow trials, Excerpt from bulletin 1988*, PIANC, Den Haag.
- CHEN, D., and JIRKA, G. H. (1995). "Experimental study of plane turbulent wakes in a shallow water layer" *Fluid Dynamics Research*, 16(1), 11-41.
- CHEN, F. Y., and IKEDA, S. (1997). "Horizontal separation in shallow open channels with spur dikes" *Journal of Hydroscience and Hydraulic Engineering*, 15(2), 15-30.
- COPELAND, R. R., ABRAHAM, D. D., NAIL, G. H., SEAL, R., and BROWN, G. L. (2001). *Entrainment and Transport of Sediments by Towboats in the Upper Mississippi River and Illinois Waterway, Numerical Model Study*, (ENV Report No. 37). Coastal and Hydraulics Laboratory, US Army Engineer Research and Development Center, Vicksburg, MS, USA.
- DE HAAS, A. D., and VAN ESSEN, J. A. F. (1987a). *Onderzoek naar de invloed van duwvaart op de water- en zandbeweging in het Kribvak Druten*, (Nota No. DBW/RIZA 87.007). RIZA, Arnhem, the Netherlands.
- DE HAAS, A. D., and VAN ESSEN, J. A. F. (1987b). *Onderzoek naar de invloed van duwvaart op de water- en zandbeweging in het Kribvak St. Andries*, (Nota No. DBW/RIZA 87.008). RIZA, Arnhem, the Netherlands.

- DE VRIEND, H. J. (1999). "Long-term morphodynamics of alluvial rivers and coasts." Environmental Applications of Mechanics and Computer Science, CISM courses and Lectures, G. BIANCHI, ed., Springer Wien, New York, 1-19.
- DE VRIES, M. (1993). *Use of models for river problems; prepared for the International Hydrological Programme within project M-3-5(a) (IHP-IV)*, Unesco, Paris.
- ELIASIEWICZ, R., ZEIDLER, R., ZBIKOWSKI, A., and ZELAZO, J. (1994). *River training techniques: fundamentals, techniques and applications; a literature survey. Part II: Fundamentals of river engineering and flood protection.*, Balkema.
- ETTEMA, R., and MUSTE, M. (2004). "Scale Effects in Flume Experiments on Flow around a Spur Dike in Flatbed Channel" *Journal of Hydraulic Engineering*, 130(7), 635-646.
- GALAPPATTI, G., and VREUGDENHIL, C. B. (1985). "A depth-integrated model for suspended sediment transport" *Journal of Hydraulic Research*, 23(4), 359-377.
- GHANI, B. A., and GILL, S. A. (1963). "River training" *West Pakistan Engrg. Congress*, pp.273-296.
- HAVINGA, F. (2001). "pers. comm." Delft University of Technology, Delft, the Netherlands.
- HAVINGA, H., SLOOTWEG, H., and ZEEKANT, J. (1984). *Kribvakmeting t.b.v. zesbaksduwvaart op de Waal bij Druten*, (Nota No. 84.9). Rijkswaterstaat, district Zuidoost, Arnhem, the Netherlands.
- HOCHSTEIN, A. B., and ADAMS, E., JR. (1989). "Influence of vessel movements on stability of restricted channels" *Journal of Waterway, Port, Coastal, and Ocean Engineering, ASCE*, 115(4), 444-456.
- ISHII, C., ASADA, H., and KISHI, T. (1983). "Shape of separation region formed behind a groyne of non-overflow type in rivers" *In: Proc. 20<sup>th</sup> IAHR Congress, Moscow, USSR*, 405-412.
- JAGERS, H. R. A. (2003). *Modelling planform changes of braided rivers*, Ph.D. Thesis, University of Twente, Twente, the Netherlands.
- JANSEN, P. P., VAN BENDEGOM, J., VAN DEN BERG, J. H., DE VRIES, M., and ZANEN, A. (1979). *Principles of river engineering - The non tidal alluvial rivers*, Delftse Uitgevers Maatschappij, Delft.
- JESSE, P., and KROEKENSTOEL, D. F. (2001). *1-D Morphodynamic Rhine branches model (text in Dutch)*, (rapport No. 2001.040). RIZA, Arnhem, the Netherlands.
- KAWAHARA, Y., NAKAGAWA, K., and KAN, K. (1995). "Experimental study of flows in embayments" *In: Proc. HYDRA 2000*, 391-396.
- KIM, J. J. (1978). *Investigation of Separation and Reattachment of a Turbulent Shear Layer: Flow over a Backward Facing Step*, Ph.D. Thesis, Stanford University, Stanford, CA, USA.
- KLAASSEN, G. J., and SLOFF, K. (2000). *Prediction of bed topography and recovery processes for dredging on the Waal River*, (Tech. Rep. No. Q2669). WL | Delft Hydraulics, Delft, the Netherlands.
- KLINGEMAN, P. C., KEHE, S. M., and OWUSU, Y. A. (1984). *Streambank erosion protection and channel scour manipulation using rockfill dikes and gabions*, (No. WRRI-98).



- Oregon State University, Water Resources Research Institute, Corvallis, Oregon, USA.
- KREBS, M., ZANKE, U., and MEWIS, P. (1999). "Hydro-Morphodynamic modelling of groin fields" *In: Proc. 28<sup>th</sup> IAHR congress*, Graz, Austria.
- KUHNLE, R. A., ALONSO, C. V., and SHIELDS, F. D. J. (1999). "Geometry of Scour Holes Associated with 90° Spur Dikes" *Journal of Hydraulic Engineering, ASCE*, 125(9), 972-978.
- KURZKE, M., WEITBRECHT, V., and JIRKA, G. H. (2002). "Laboratory concentration measurements for determination of mass exchange between groin fields and main stream" *In: River Flow 2002 - Proc. of the Int. Conf. on Fluvial Hydraulics*, Louvain-la-Neuve, Belgium, 369-376.
- LAUCLAN, C. (2004). "Experimental Investigation of Bed-load and suspended-load Transport over Weirs" *Journal of Hydraulic Research*, 42(5), 549-555.
- LESSER, G. R., ROELVINK, J. A., VAN KESTER, J. A. T. M., and STELLING, G. S. (2004). "Development and validation of a three-dimensional morphological model" *Coastal Engineering*, 51(8-9), 883-915.
- LIEK, G. A. (2000). *Horizontal large eddy simulation using Delft2D-Mor*, M.Sc. Thesis, Delft University of Technology, Delft, the Netherlands.
- LPR. (1996). "Towards a Balance in River Management" Landscape Planning River Rhine, RIZA and HKV, the Netherlands, CD-Supplement.
- MAYNORD, S. T. (2000). *Physical forces near commercial tows*, (ENV Report No. 19). US Army Engineer Research and Development Center, Vicksburg, MS, USA.
- MOSELMAN, E., and STRUIKSMA, N. (1992). *The effect of lowering groynes (text in Dutch)*, (Report No. Q1462). WL | Delft Hydraulics, Delft.
- MOSELMAN, E. (2000). "Technical memorandum on groyne length and spacing", Personal communication, Delft.
- MUSTE, M., and PATEL, V. C. (1997). "Velocity Profiles for Particles and Liquid in Open-Channel Flow with Suspended Sediment" *Journal of Hydraulic Engineering*, 123(9), 742-751.
- MUTO, Y., IMAMOTO, H., and ISHIGAKI, T. (2000). "Turbulence characteristics of a shear flow in an embayment attached to a straight open channel" *In: Proc. Advances in Hydro-Science and Engineering*, Seoul, Korea, 232.
- MUTO, Y., BABA, Y., and FUJITA, I. (2002). "Velocity measurements in rectangular embayments attached to a straight open channel" *In: River Flow 2002 - Proc. of the Int. Conf. on Fluvial Hydraulics*, Louvain-la-Neuve, Belgium, 1213-1219.
- NAKAGAWA, H., and NEZU, I. (1987). "Experimental investigation on turbulent structures of back-ward facing step flow in open channel" *Journal of Hydraulic Research*, 25(1).
- NASSIRI, M., BABARUTSI, S., and CHU, V. H. (1999). "Wall boundary conditions on recirculating flows dominated by bottom friction" *In: Proc. 28<sup>th</sup> IAHR congress*, Graz, Austria.
- NEZU, I., and NAKAGAWA, H. (1993). *Turbulence in open channel flow*, A. A. Balkema, Rotterdam.

- NIELSEN, P. (1992). *Coastal bottom boundary layers and sediment transport*, World Scientific, Singapore.
- NIELSEN, P., and TEAKLE, I. A. L. (2004). "Turbulent diffusion of momentum and suspended particles: A finite-mixing-length theory" *Physics of Fluids*, 16(7), 2342-2348.
- OUILLOU, S., and DARTUS, D. (1997). "Three-dimensional computation of flow around groyne" *Journal of Hydraulic Engineering, ASCE*, 123(11), 962-970.
- PARCHURE, T. M., MCANALLY, W. H., and TEETER, A. M. (2001). *Wave-Induced Sediment Resuspension near the Shorelines of the Upper Mississippi River System*, (ENV Report No. 20). Coastal and Hydraulics Laboratory, US Army Engineer Research and Development Center, Vicksburg, MS, USA.
- PENG, J., KAWAHARA, Y., and TAMAI, N. (1997). "Numerical analysis of three-dimensional turbulent flows around submerged groynes" *In: Proc. 27<sup>th</sup> IAHR congress*, San Francisco, USA.
- PRZEDWOJSKI, B., BLAZEJEWSKI, R., and PILARCZYK, K. W. (1995). *River training techniques- fundamentals, design and application*, A.A. Balkema, Rotterdam.
- RICHARDSON, E. V., STEVENS, M. A., and SIMONS, D. B. (1975). "The design of spurs for river training" *In. Proc. 16<sup>th</sup>, IAHR congress*, Sao Paulo, Brazil, 382-388.
- ROELVINK, J. A., and VAN BANNING, G. K. F. M. (1994). "Design and development of Delft3D and application to coastal morphodynamics" *In: Hydroinformatics 94; Proc. of the 1<sup>st</sup> Int. Conf. on Hydroinformatics*, Delft, Netherlands, 451-455.
- RUPPRECHT, R. (2004). *Modelling of the morphological interaction between a river and its groyne fields - using Delft3D-flow with online-sediment and HLES*, M.Sc. Thesis, Delft University of Technology, Delft, the Netherlands / University of Karlsruhe, Karlsruhe, Germany.
- SCHANS, H. (1998). *Representativiteit van kribvakmetingen uit 1996 en 1997 ten opzichte van de hele Waal*, (Report No. ICG 98/15). Universiteit Utrecht, Fysische Geografie, Utrecht.
- SISTERMANS, P. G. J. (2002). *Graded sediment transport by non-breaking waves and a current*, Ph.D. Thesis, Delft University of Technology, Delft, the Netherlands.
- STELLING, G. S. (1984). *On the construction of computational methods for shallow water flow problems*, Ph.D. Thesis, Delft University of Technology, Delft, the Netherlands.
- STRIUKSMA, N. (1985). "Prediction of 2-D Bed Topography in Rivers" *Journal of Hydraulic Engineering, ASCE*, 111(8), 1169-1182.
- STRIUKSMA, N., OLESEN, K. W., FLOKSTRA, C., and DE VRIEND, H. J. (1985). "Bed Deformation in Curved Alluvial Channels" *Journal of Hydraulic Research*, 23(1), 57-79.
- SUKHODOLOV, A., ULJTTEWAAL, W. S. J., and ENGELHARDT, C. (2002). "On the correspondence between morphological and hydrodynamical patterns of groyne fields" *Journal of Earth Surface Processes and Landforms*, 27(3), 289-305.
- SUKHODOLOV, A., ENGELHARDT, C., KRUGER, A., and BUNGARTZ, H. (2004). "Case Study: Turbulent Flow and Sediment Distributions in a Groyne Field" *Journal of Hydraulic Engineering, ASCE*, 130(1), 1-9.
- TAAL, M. (1999). *Waal Project - Experimental morphology*, (CD-version 2.0, October 1999). RWS-DON department of river engineering, Arnhem, the Netherlands.

- TAAL, M. (2000). *Waal Project - Experimental morphology*, (CD-version 3.0, February 2001). RWS-DON department of river engineering, Arnhem, the Netherlands.
- TEN BRINKE, W. B. M., KRUYT, N. M., KROON, A., and VAN DEN BERG, J. H. (1999). "Erosion of sediments between groynes in the River Waal as a result of navigation traffic" *Spec. Publs int. Ass. Sediment*, 28, 147-160.
- TEN BRINKE, W. B. M., BOLWIDT, L. J., SNIPPEN, E., and VAN HAL, L. W. J. (2001). *Sedimentbalans Rijntakken 2000*, (Report No. 2001.043). RIZA, Arnhem, the Netherlands.
- TEN BRINKE, W. B. M., and GÖLZ, M. (2001). *Bed level changes and sediment budget of the Rhine near the German Dutch boarder*, (Report No. 2001.044). RIZA, Arnhem, the Netherlands.
- TEN BRINKE, W. B. M. (2003). *De Sedimenthuishouding van kribvakken langs de Waal*, (Report No. 2003.002). RIZA, Arnhem, the Netherlands.
- TEN BRINKE, W. B. M., SCHULZE, F. H., and VAN DER VEER, P. (2004). "Sand exchange between groyne-field beaches and the navigation channel of the Dutch Rhine: the impact of navigation versus river flow" *River Research and Applications*, 20(8), 899-928.
- TERMES, A. P. P., VAN DER WAL, M., and VERHEIJ, H. J. (1991). *Waterbeweging door scheepvaart op rivieren en in kribvakken*, (Report No. Q1046). WL|Delft Hydraulics, Delft.
- TINGSANCHALI, T., and MAHESWARAN, S. (1990). "2-D depth averaged flow computation near groyne" *Journal of Hydraulic Engineering, ASCE*, 116(1), 71-85.
- TOMINAGA, A., IJIMA, K., and NAKANO, Y. (2001). "Flow structures around submerged spur dikes with various relative height" *In: Proc. 29<sup>th</sup> IAHR Congress*, Beijing, China, 421-427.
- TOOBY, P. F., WICK, G. L., and ISAACS, J. D. (1977). "The motion of a small sphere in a rotating velocity field: A possible mechanism for suspending particles in turbulence" *Journal of Geophysical Research*, 82(C15), 2096-2100.
- UIJTTEWAAL, W. S. J. (1999). "Groyne field velocity patterns determined with particle tracking velocimetry" *In: Proc. 28<sup>th</sup> IAHR congress*, Graz, Austria.
- UIJTTEWAAL, W. S. J., and BOOIJ, R. (2000). "Effects of shallowness on the development of free-surface mixing layer" *Physics of Fluids*, 12(2), 392-402.
- UIJTTEWAAL, W. S. J., LEHMANN, D., and VAN MAZUIK, A. (2001). "Exchange process between a river and its groyne fields - Model experiments" *Journal of Hydraulic Engineering, ASCE*, 127(11), 928-936.
- UIJTTEWAAL, W. S. J., BERG, M. H., and VAN DER WAL, M. (2002). "Experiments on physical scale models for submerged and non-submerged groynes of various types" *In: River Flow 2002 - Proc. of the Int. Conf. on Fluvial Hydraulics*, Louvain-la-Neuve, Belgium, 377-383.
- UIJTTEWAAL, W. S. J., and VAN SCHIJNDEL, S. (2004). "The complex flow in groyne fields: numerical modelling compared with experiments" *In: River Flow 2004 - Proc. of the 2nd Int. Conf. on Fluvial Hydraulics*, Naples, Italy, 1331-1338.

- UITTENBOGAARD, R. E., and VAN VOSSEN, B. (2003). "Subgrid-scale model for Quasi-2D turbulence in shallow water" *In: Proc. of the Int. Symposium on Shallow Flows*, Delft, the Netherlands, 169-176.
- USACE. (2004). *Integrated feasibility report and programmatic environmental impact statement for the UMR-IWW system navigation feasibility study*, [http://www2.mvt.usace.army.mil/umr-iwwsns/documents/Main\\_report\\_6may.pdf](http://www2.mvt.usace.army.mil/umr-iwwsns/documents/Main_report_6may.pdf).
- VAN DER KLIS, H. (2003). *Uncertainty analysis applied to numerical models of river bed morphology*, DUP Science, Delft.
- VAN PROOIJEN, B. C. (2004). *Shallow mixing layers*, Ph.D. Thesis, Delft University of Technology, Delft, the Netherlands.
- VAN RIJN, L. C. (1984a). "Sediment Transport, Part I: Bed Load Transport" *Journal of Hydraulic Engineering, ASCE*, 110(10), 1431-1456.
- VAN RIJN, L. C. (1984b). "Sediment Transport, Part II: Suspended Load Transport" *Journal of Hydraulic Engineering, ASCE*, 110(11), 1613-1641.
- VAN RIJN, L. C. (1987). *Mathematical modelling of morphological processes in the case of suspended sediment transport*, Ph.D. Thesis, Delft University of Technology, Delft, the Netherlands.
- VAN RIJN, L. C. (1993). *Principles of sediment transport in rivers, estuaries and coastal seas*, Aqua Publications, Amsterdam.
- VAN SCHIJNDEL, S., and JAGERS, B. (2003). "Complex flow around groynes, computations with Delft3D in combination with HLES" *In: Proc. of the Int. Symposium on Shallow Flows*, Delft, the Netherlands, 213-219.
- VAN URK, G., and SMIT, H. (1989). "The Lower Rhine geomorphological changes." *Historical Changes of Large Alluvial Rivers: Western Europe*, G. E. PETTES, ed., John Wiley & Sons. Ltd, 167-182.
- VAN VUREN, S., VAN DER KLIS, H., and DE VRIEND, H. J. (2002). "Large-scale floodplain lowering along the River Waal: a stochastic prediction of morphological impacts" *In: River Flow 2002 - Proc. of the Int. Conf. on Fluvial Hydraulics*, Louvain-la-Neuve, Belgium, 903-912.
- VISSER, P. J. (2000). *Bodemontwikkeling Rijnsysteem*, (Report). Delft University of Technology, Hydraulic and Offshore Engineering Section, Delft.
- WL | DELFT HYDRAULICS. (1987). *Kribvakerosie door zes- en vierbaksduwvaart op de Waal*, (Report No. Q 93/Q 576). WL | Delft Hydraulics, Delft.
- WL | DELFT HYDRAULICS. (2001a). *Delft3D-MOR user manual*, (Manual). WL | Delft Hydraulics, Delft.
- WL | DELFT HYDRAULICS. (2001b). *SOBEK River/Estuary user manual*, (Manual). Sobek help desk, WL | Delft Hydraulics, Delft.
- WWF. (1993). *Living Rivers*, (Report). World Wide Fund for Nature, Zeist, the Netherlands.
- YOSSEF, M. F. M. (2002). *The Effect of Groynes on Rivers - Literature review*, (Report No. DC 03.03.04). Delft University of Technology c/o Delft Cluster, Delft, The Netherlands.

- YOSSEF, M. F. M., and KLAASSEN, G. J. (2002). "Reproduction of groynes-induced river bed morphology using LES in a 2-D morphological model" *In: River Flow 2002 - Proc. of the Int. Conf. on Fluvial Hydraulics*, Louvain-la-Neuve, Belgium, 1099-1108.
- YOSSEF, M. F. M. (2003). *Sediment exchange between the main channel and the groyne fields of a river - Design of a mobile-bed experiment*, (Report No. DC 01.334.04). Delft University of Technology c/o Delft Dcluster, Delft, The Netherlands.
- YOSSEF, M. F. M., and ULTTEWAAL, W. S. J. (2003). "On the dynamics of the flow near groynes in the context of morphological modelling" *in: XXX IAHR Congress*, Thessaloniki, Greece, 361-368.
- YOSSEF, M. F. M. (2004). "The effect of the submergence level on the resistance of groynes - an experimental investigation" *In: Advances in Hydro-science and -Engineering, Proc. of the 6<sup>th</sup> Int. Conf. on Hydro-science and -Engineering CD-ROM*, Brisbane, Australia.
- YOSSEF, M. F. M., and DE VRIEND, H. J. (2004). "Mobile-bed experiments on the exchange of sediment between main channel and groyne fields" *In: River Flow 2004 - Proc. of the 2nd Int. Conf. on Fluvial Hydraulics*, Naples, Italy, 127-133.



# Appendix A

## RESULTS FROM THE MOBILE-BED EXPERIMENT

This appendix gives the results of the mobile-bed experiment presented in Chapter 4. The results are given for the following measured quantities:

- 1- Velocity
- 2- Suspended sediment concentration
- 3- Bed level
- 4- PIV-measurements

### A.1 VELOCITY

Horizontal velocities in two-dimension ( $u$  &  $v$ ) in ( $x$  &  $y$ ) were measured along Sections S1 & S2 (Figure 4.6), after 10 hours from the start of the experiment, at  $0.6h$  from the water surface. Figures A.1 to A.24, give the transverse distribution of the time-averaged velocity (upper panels), and the turbulence intensity (standard deviation) (lower panels).

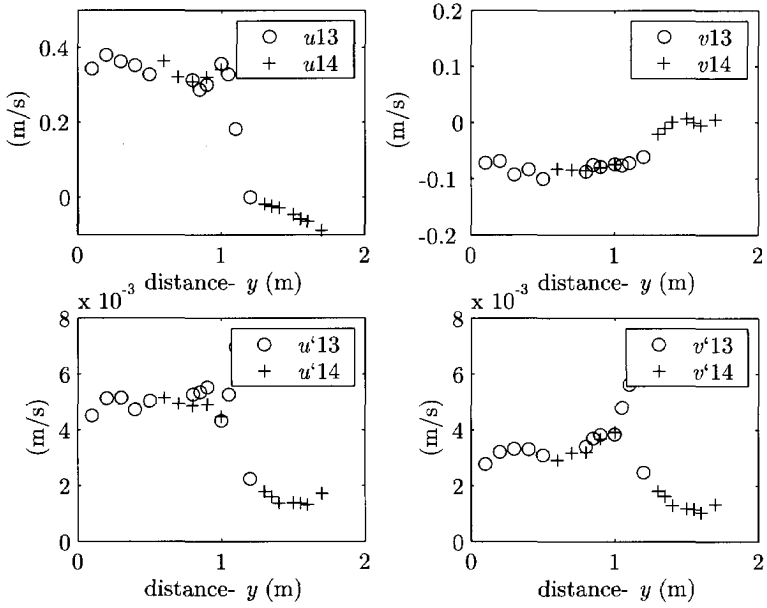


Figure A.1: Distribution in the transverse direction of  $u$  &  $v$  (upper panel), and  $u'$  &  $v'$  (lower panel); for G1i-S1.

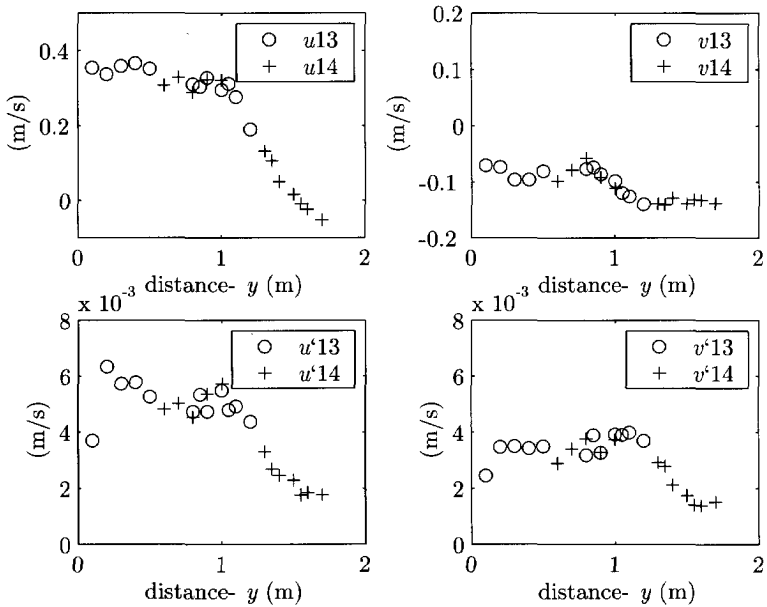


Figure A.2: Distribution in the transverse direction of  $u$  &  $v$  (upper panel), and  $u'$  &  $v'$  (lower panel); for G1i-S2.



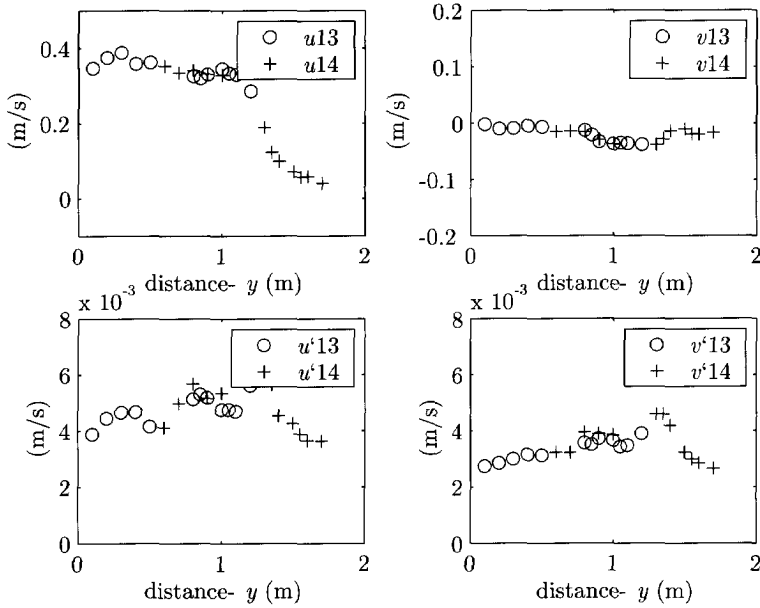


Figure A.3: Distribution in the transverse direction of  $u$  &  $v$  (upper panel), and  $u'$  &  $v'$  (lower panel); for G1a-S1.

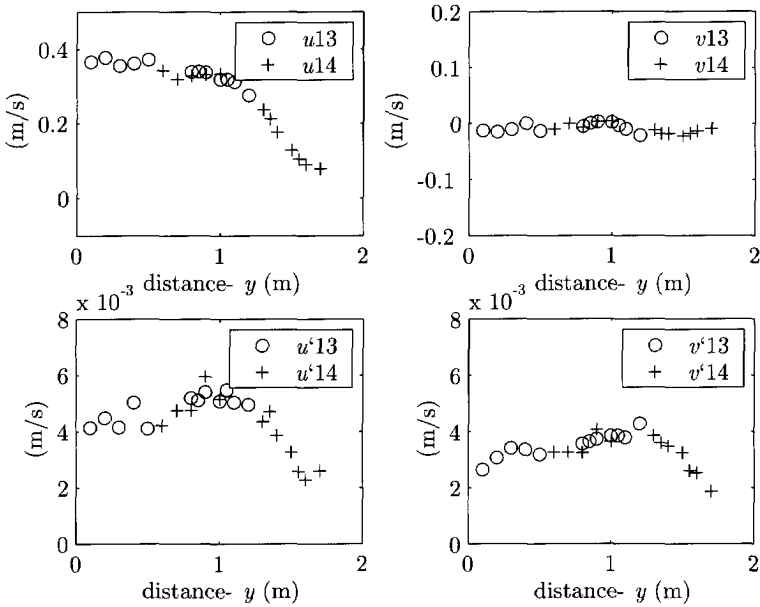


Figure A.4: Distribution in the transverse direction of  $u$  &  $v$  (upper panel), and  $u'$  &  $v'$  (lower panel); for G1a-S2.

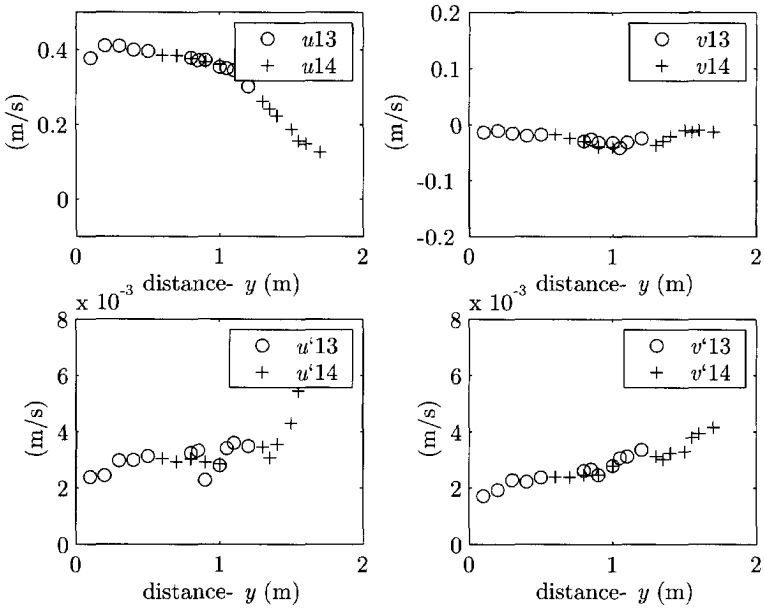


Figure A.5: Distribution in the transverse direction of  $u$  &  $v$  (upper panel), and  $u'$  &  $v'$  (lower panel); for G1b-S1.

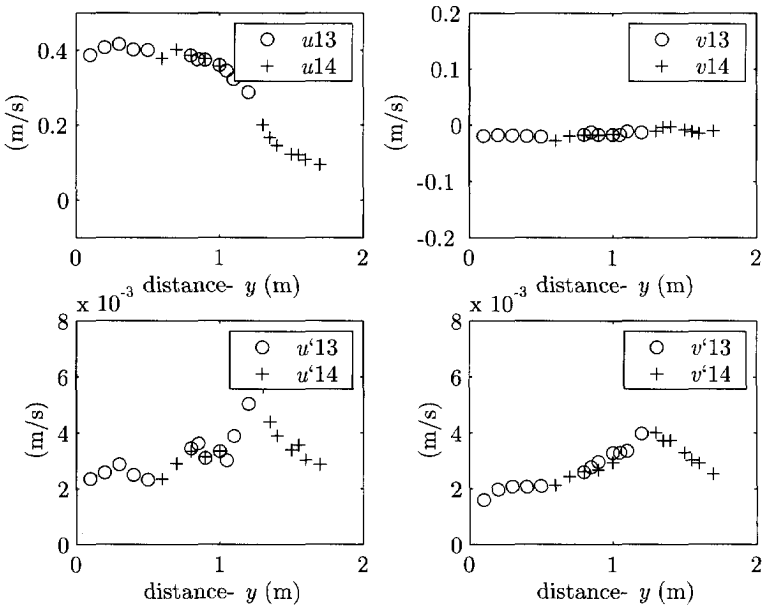


Figure A.6: Distribution in the transverse direction of  $u$  &  $v$  (upper panel), and  $u'$  &  $v'$  (lower panel); for G1b-S2.

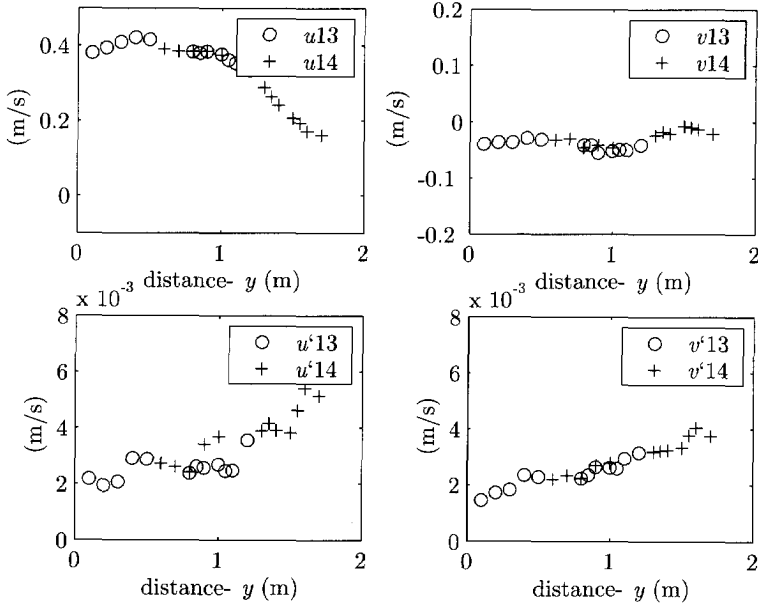


Figure A.7: Distribution in the transverse direction of  $u$  &  $v$  (upper panel), and  $u'$  &  $v'$  (lower panel); for G1c-S1.

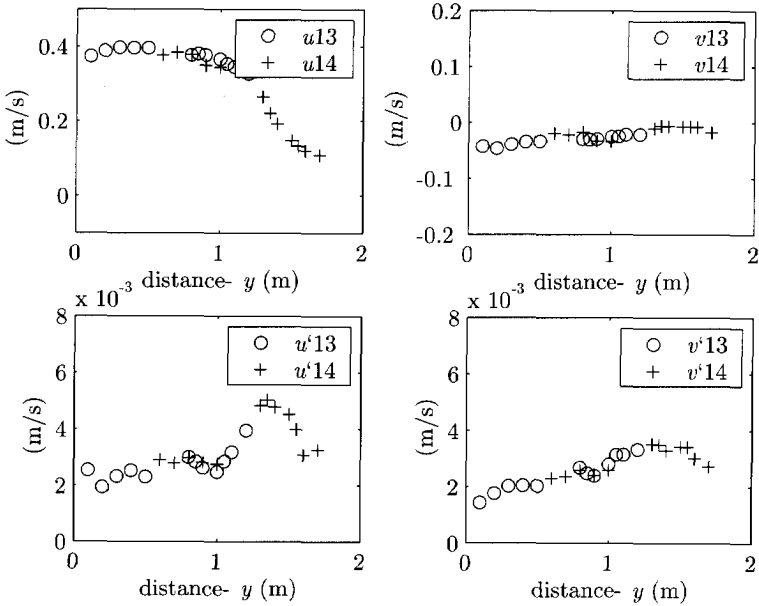


Figure A.8: Distribution in the transverse direction of  $u$  &  $v$  (upper panel), and  $u'$  &  $v'$  (lower panel); for G1c-S2.

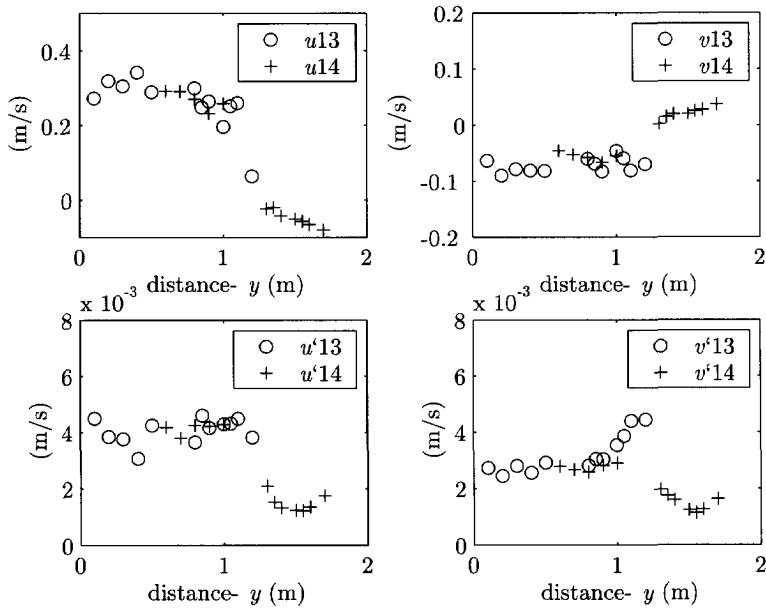


Figure A.9: Distribution in the transverse direction of  $u$  &  $v$  (upper panel), and  $u'$  &  $v'$  (lower panel); for G2i-S1.

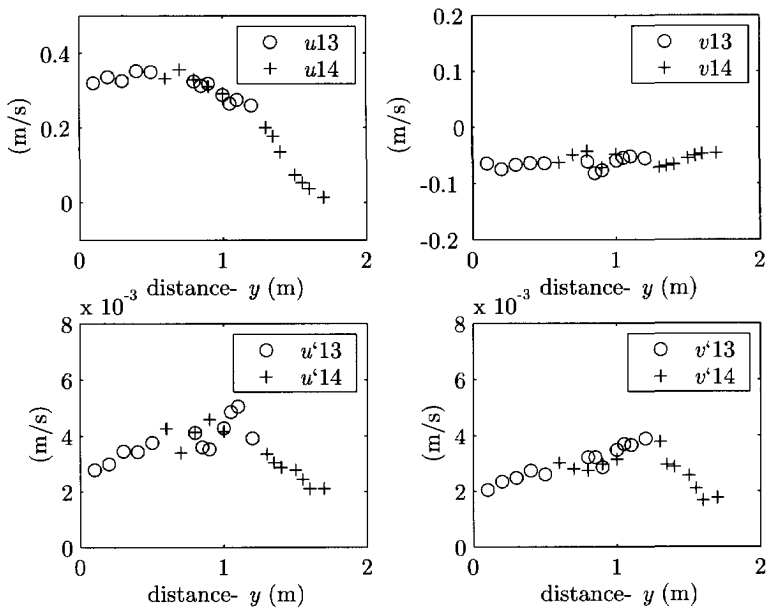


Figure A.10: Distribution in the transverse direction of  $u$  &  $v$  (upper panel), and  $u'$  &  $v'$  (lower panel); for G2i-S2.

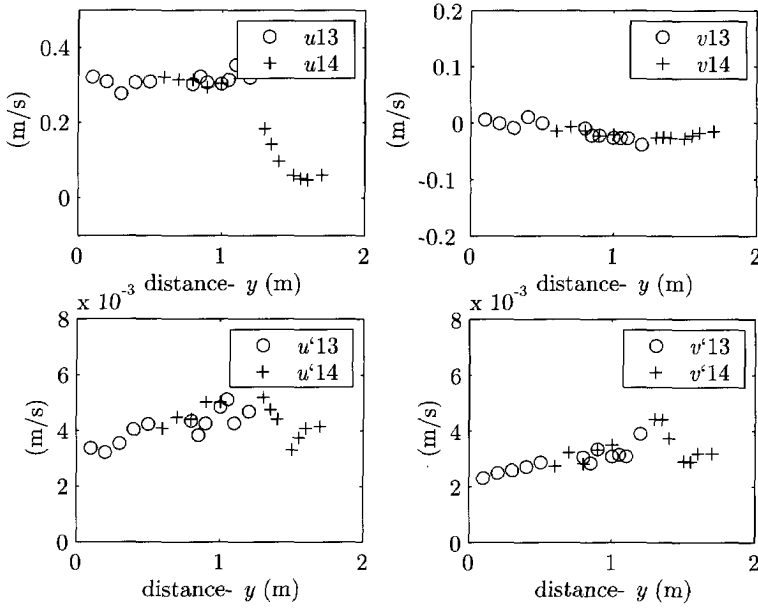


Figure A.11: Distribution in the transverse direction of  $u$  &  $v$  (upper panel), and  $u'$  &  $v'$  (lower panel); for G2a-S1.

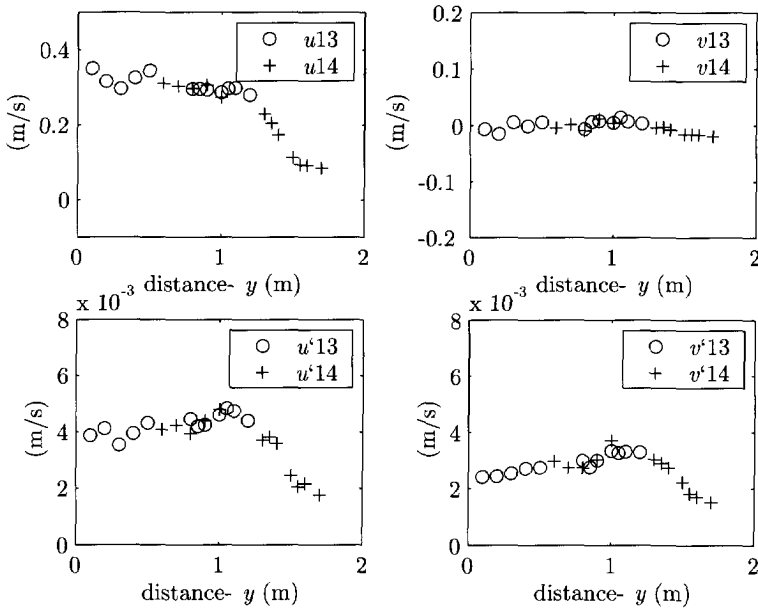


Figure A.12: Distribution in the transverse direction of  $u$  &  $v$  (upper panel), and  $u'$  &  $v'$  (lower panel); for G2a-S2.

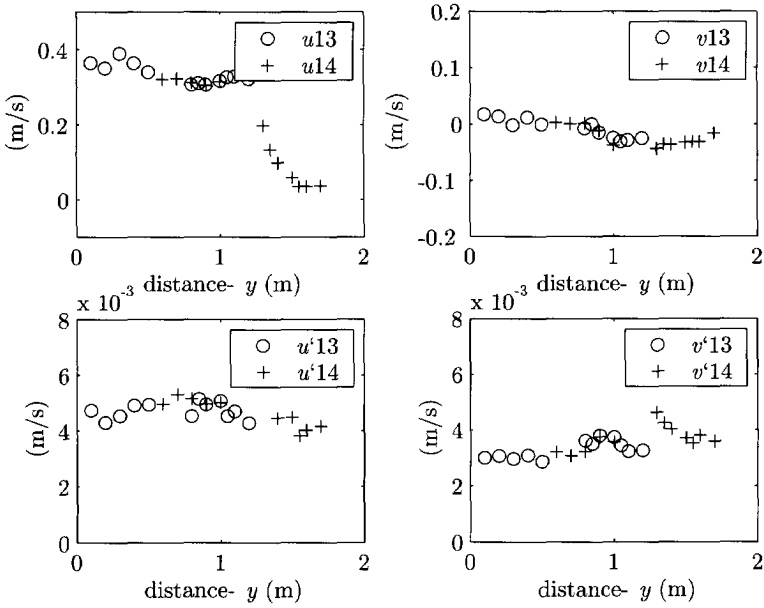


Figure A.13: Distribution in the transverse direction of  $u$  &  $v$  (upper panel), and  $u'$  &  $v'$  (lower panel); for G2b-S1.

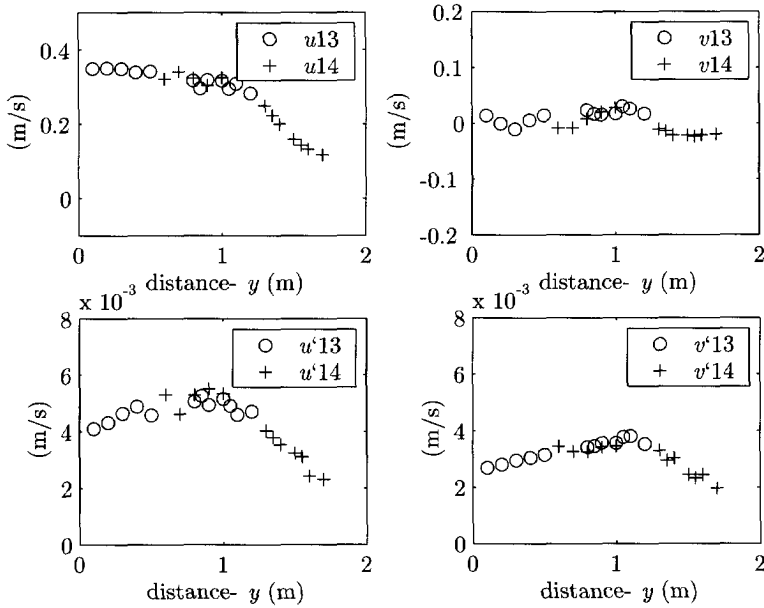


Figure A.14: Distribution in the transverse direction of  $u$  &  $v$  (upper panel), and  $u'$  &  $v'$  (lower panel); for G2b-S2.

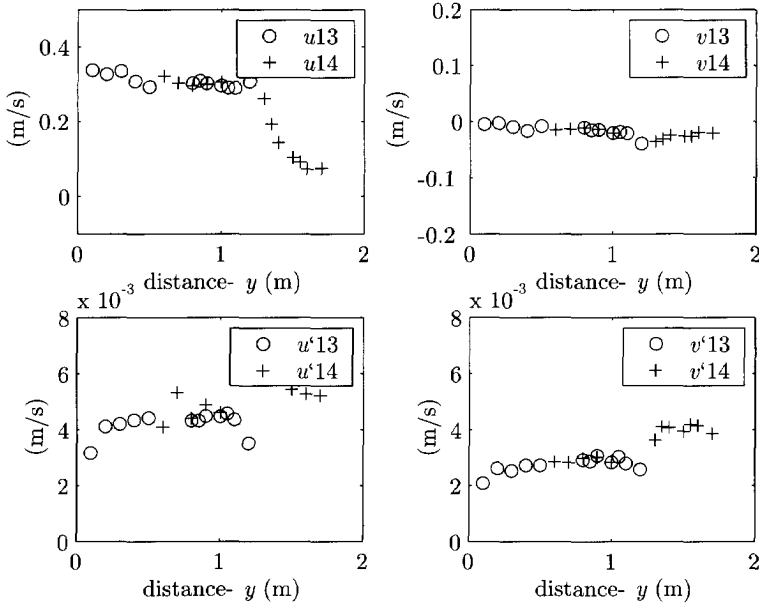


Figure A.15: Distribution in the transverse direction of  $u'$  &  $v'$  (upper panel), and  $u''$  &  $v''$  (lower panel); for G2c-S1.

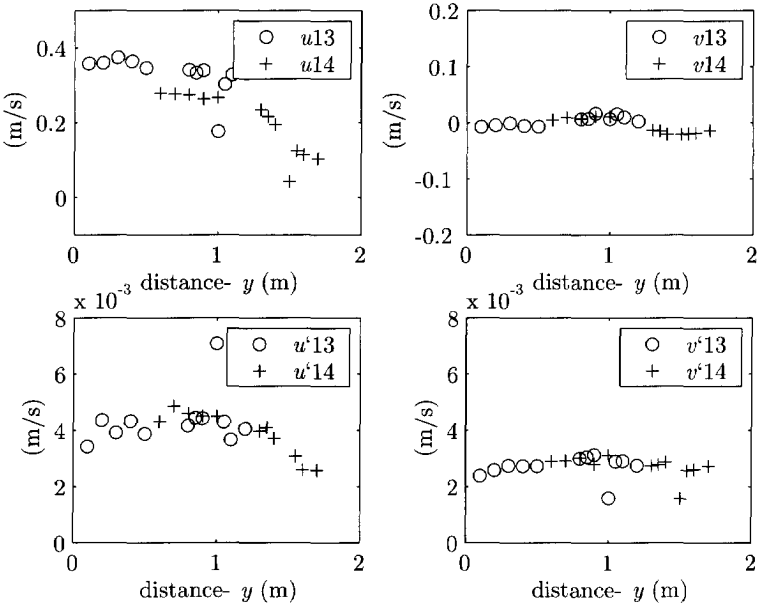


Figure A.16: Distribution in the transverse direction of  $u'$  &  $v'$  (upper panel), and  $u''$  &  $v''$  (lower panel); for G2c-S2.

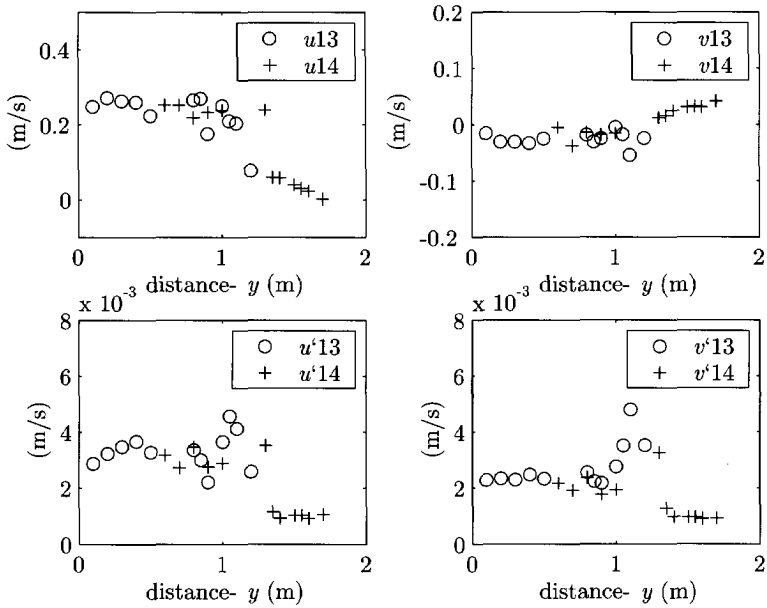


Figure A.17: Distribution in the transverse direction of  $u$  &  $v$  (upper panel), and  $u'$  &  $v'$  (lower panel); for G3i-S1.

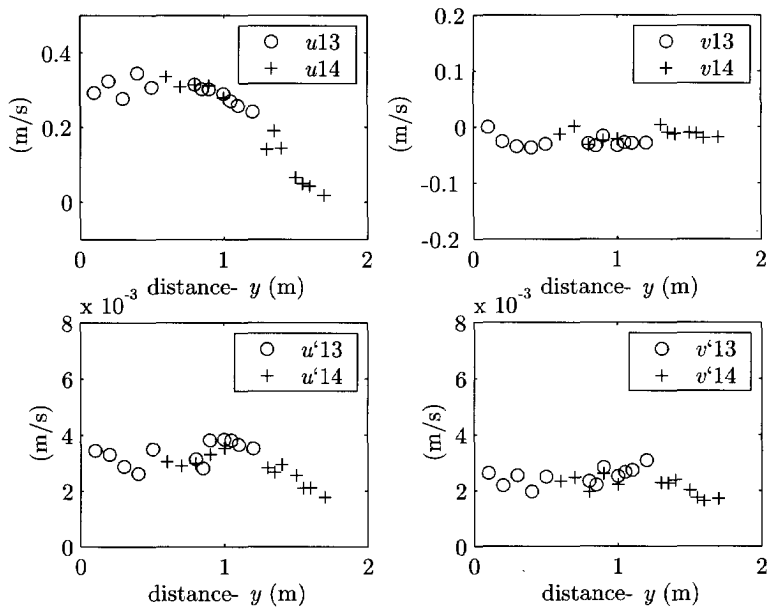


Figure A.18: Distribution in the transverse direction of  $u$  &  $v$  (upper panel), and  $u'$  &  $v'$  (lower panel); for G3i-S2.



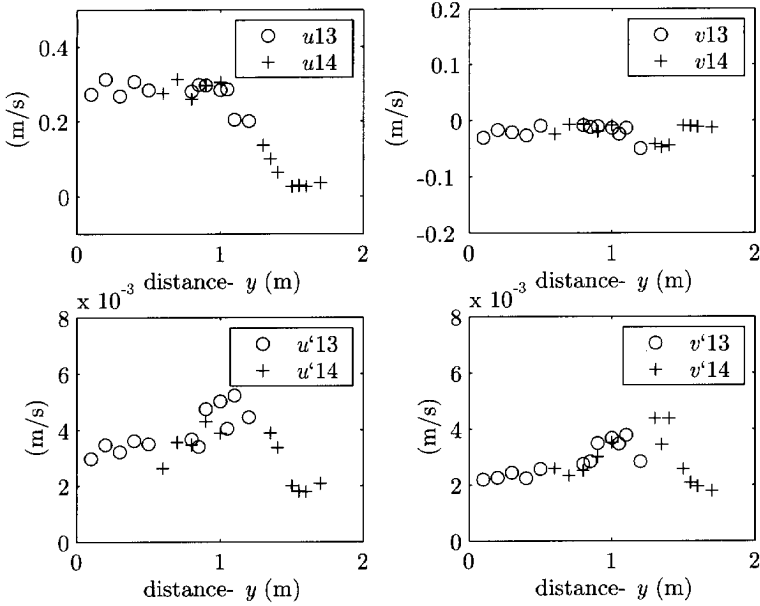


Figure A.19: Distribution in the transverse direction of  $u$  &  $v$  (upper panel), and  $u'$  &  $v'$  (lower panel); for G3a-S1.

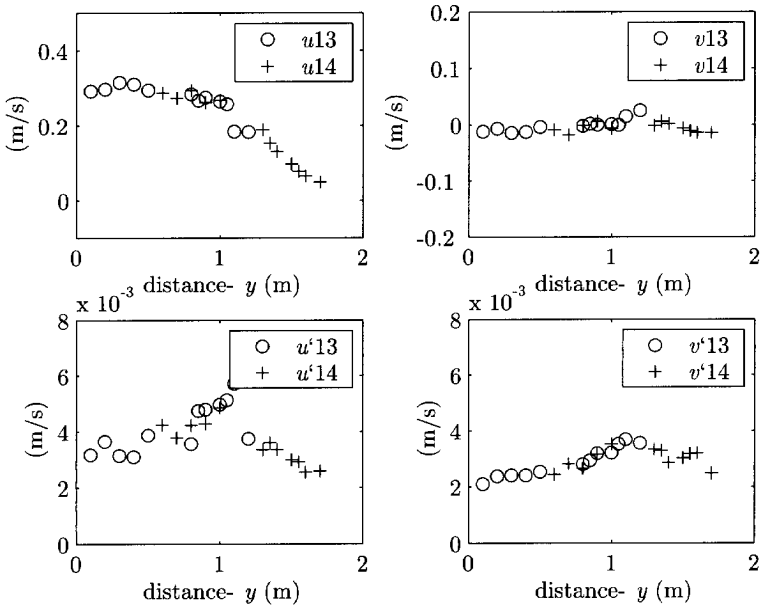


Figure A.20: Distribution in the transverse direction of  $u$  &  $v$  (upper panel), and  $u'$  &  $v'$  (lower panel); for G3a-S2.

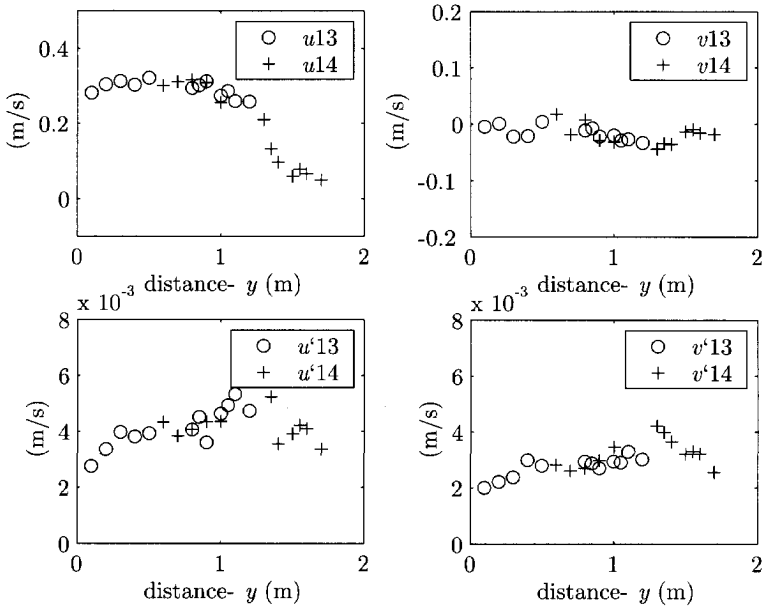


Figure A.21: Distribution in the transverse direction of  $u$  &  $v$  (upper panel), and  $u'$  &  $v'$  (lower panel); for G3b-S1.

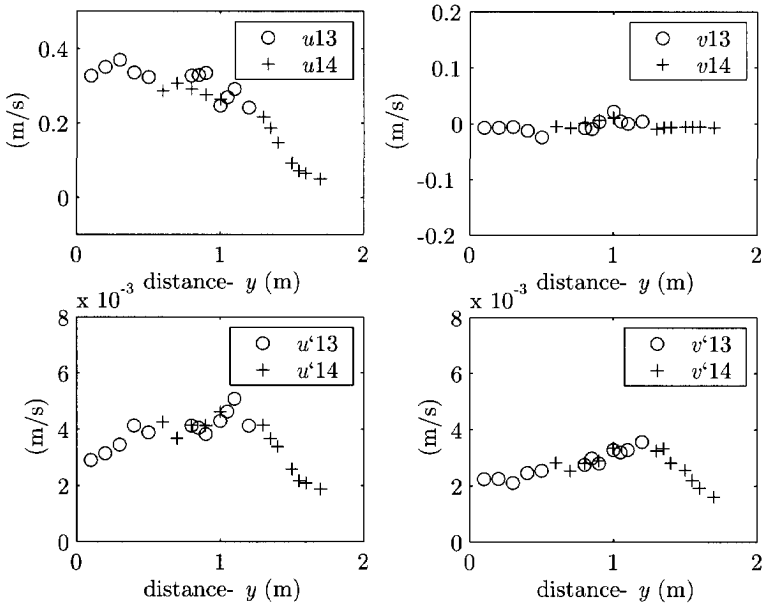


Figure A.22: Distribution in the transverse direction of  $u$  &  $v$  (upper panel), and  $u'$  &  $v'$  (lower panel); for G3b-S2.

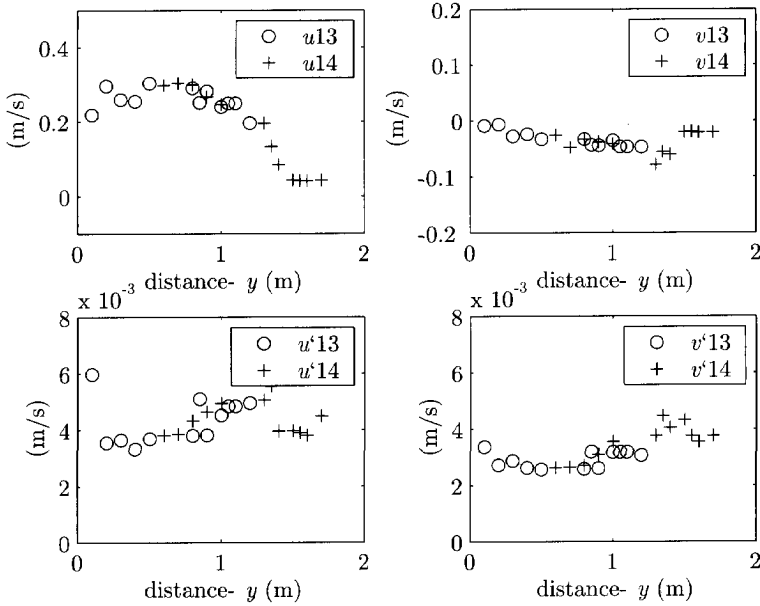


Figure A.23: Distribution in the transverse direction of  $u$  &  $v$  (upper panel), and  $u'$  &  $v'$  (lower panel); for G3c-S1.

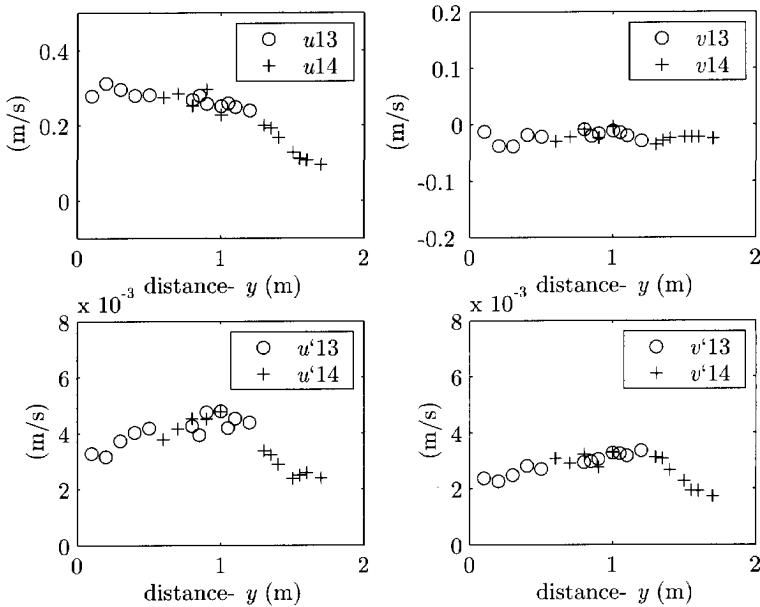


Figure A.24: Distribution in the transverse direction of  $u$  &  $v$  (upper panel), and  $u'$  &  $v'$  (lower panel); for G3c-S2.

## **A.2 SUSPENDED SEDIMENT**

Vertical concentration profiles were measured along Sections S1 & S2 (Figure 4.6) in the transverse locations indicated by the legend, after 10 hours from the start of the experiment. Figures A.25 to A.27, give the vertical concentration profiles for all tested cases.

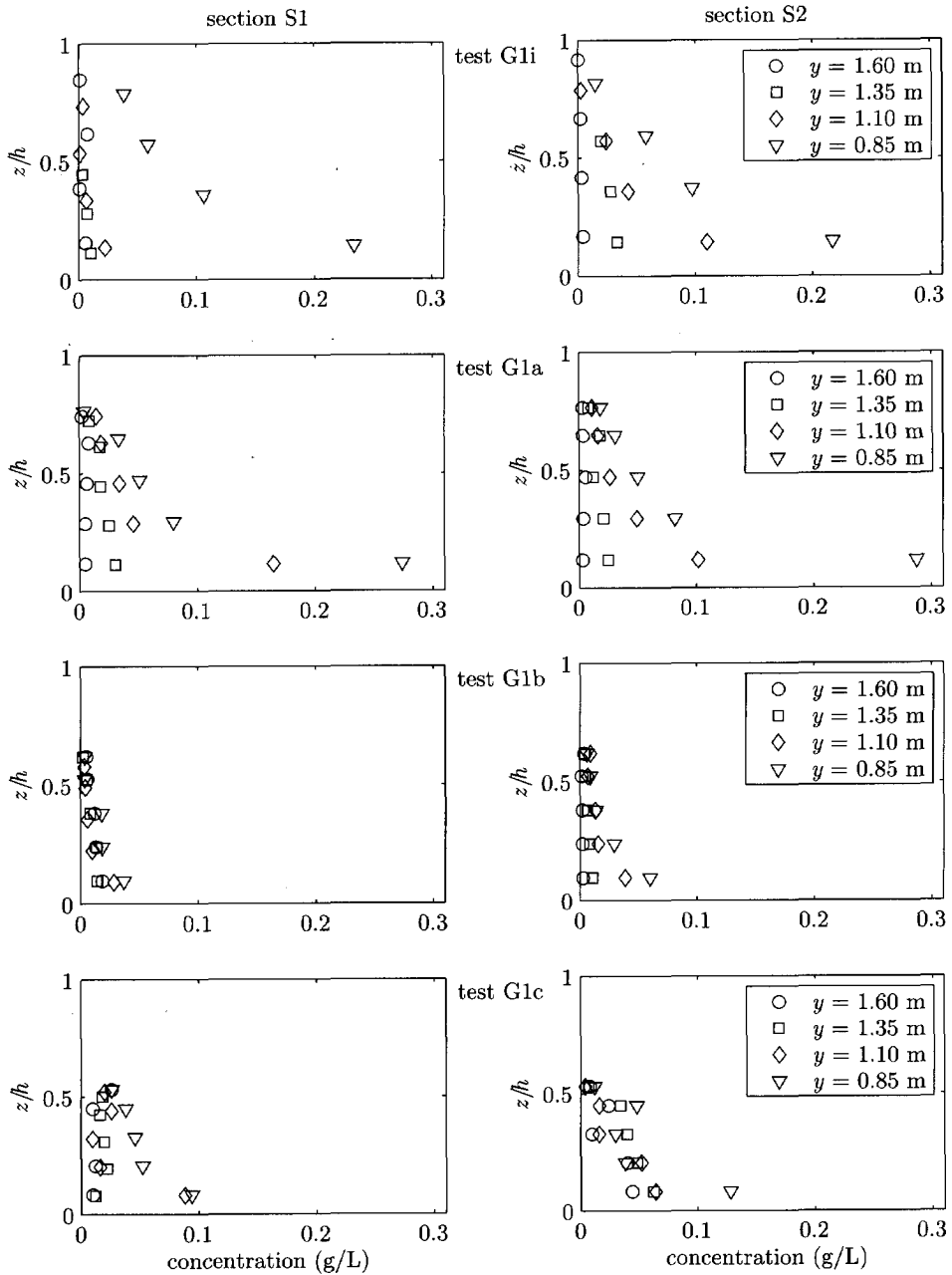


Figure A.25: Suspended sediment concentration profiles for all cases in G1, section S1 (left column) and section S2 (right column); profiles are measure at transverse locations  $y$  indicated by legend.

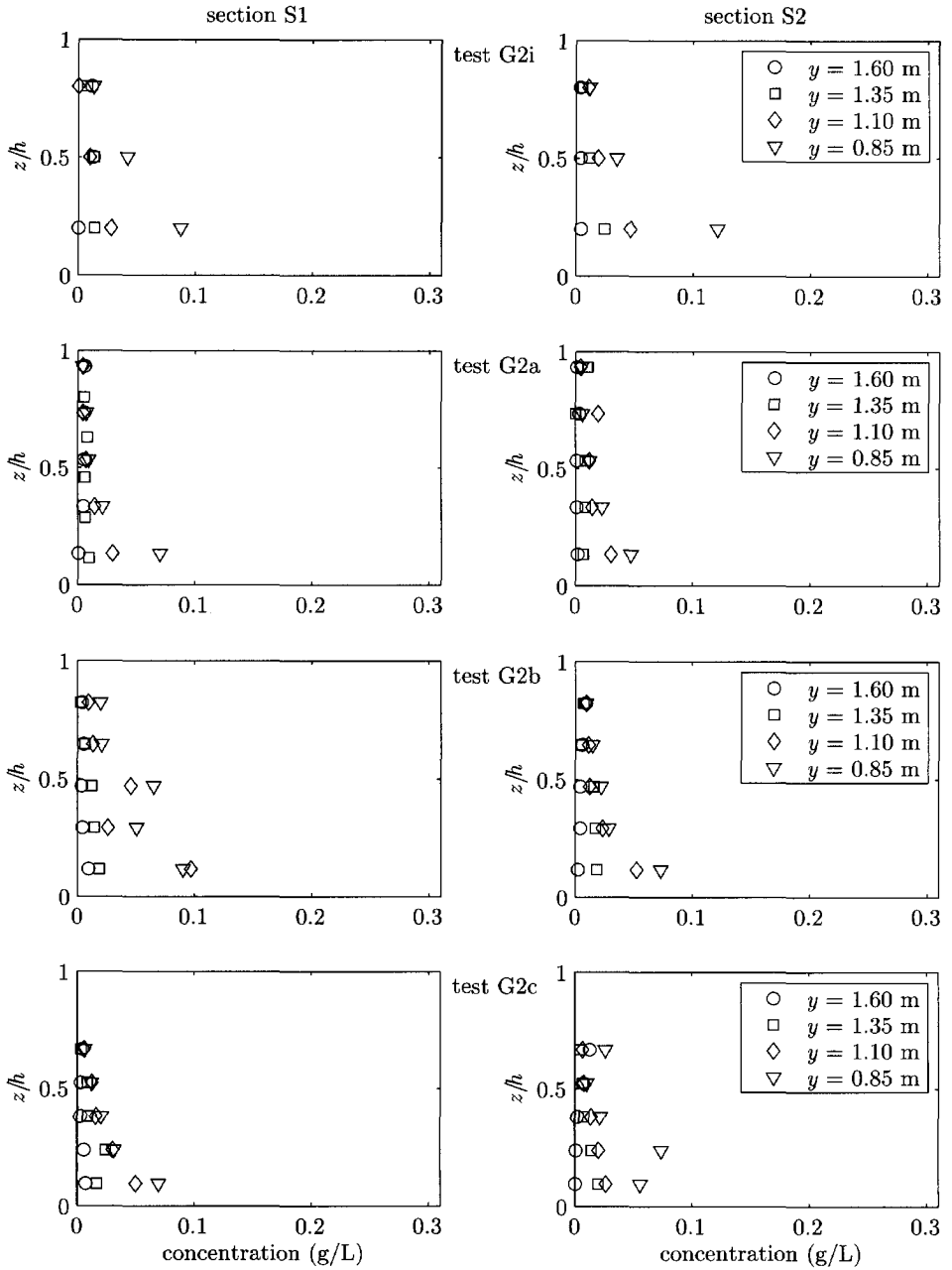


Figure A.26: Suspended sediment concentration profiles for all cases in G2, section S1 (left column) and section S2 (right column); profiles are measure at transverse locations  $y$  indicated by legend.

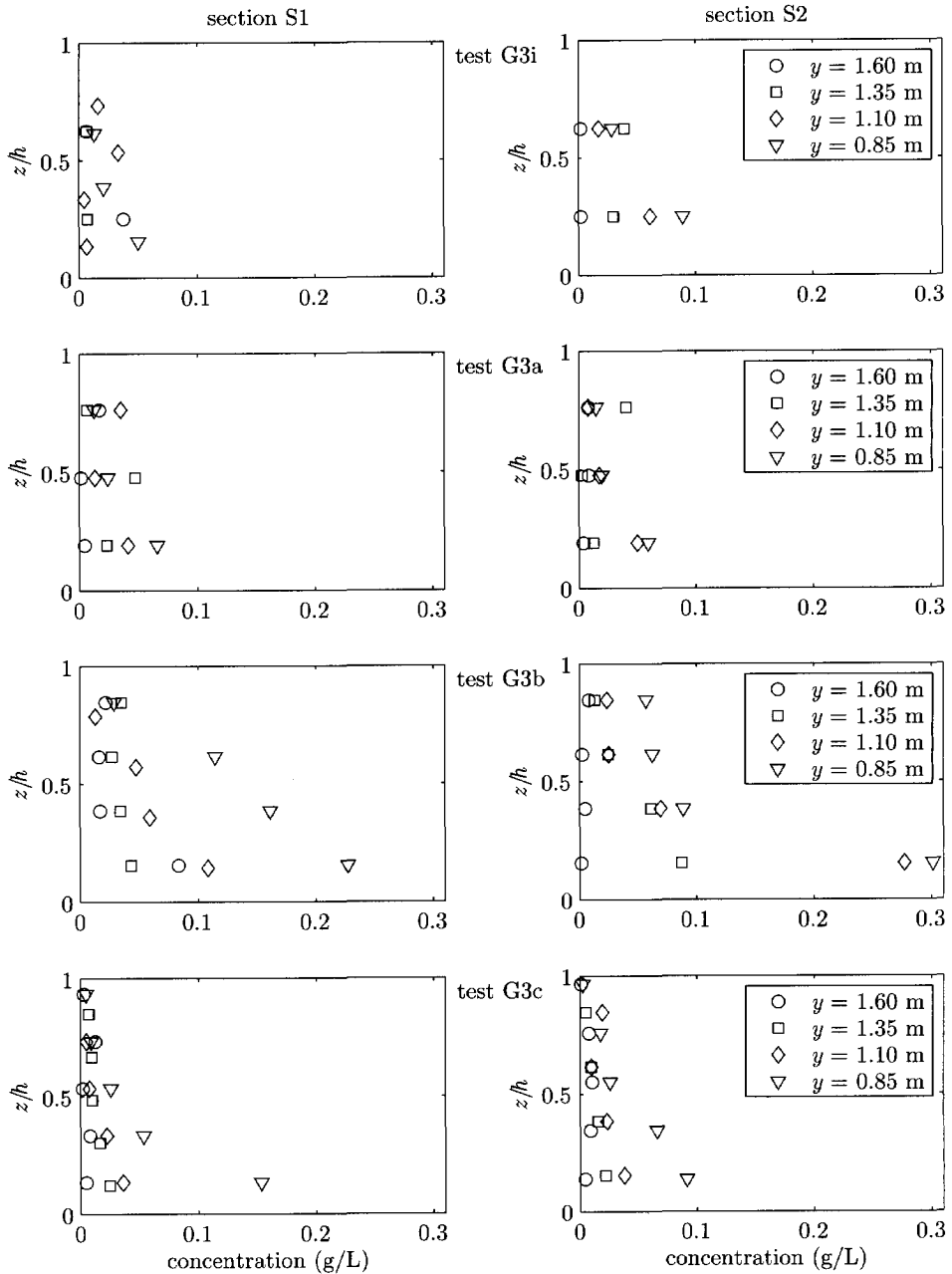


Figure A.27: Suspended sediment concentration profiles for all cases in G3, section S1 (left column) and section S2 (right column); profiles are measure at transverse locations  $y$  indicated by legend.

### **A.3 BED LEVEL**

Bed levels were measured between groynes #5 & #8 (Figure 4.6), at 10, 20, 30 and 40 hours from the start of the experiment. Figures A.28 to A.39, give the bed level (left column), and the erosion/deposition pattern (right column).



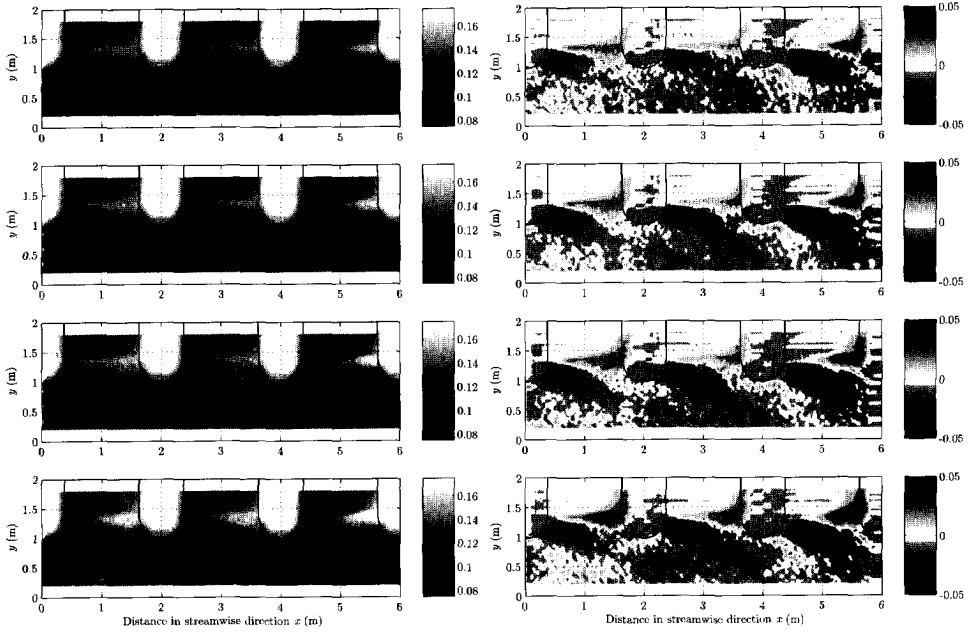


Figure A.28: Bed level (left column) and erosion/deposition pattern (right column) measured after: 10, 20, 30 and 40 hours consecutively (from top to bottom) – Case G1i.

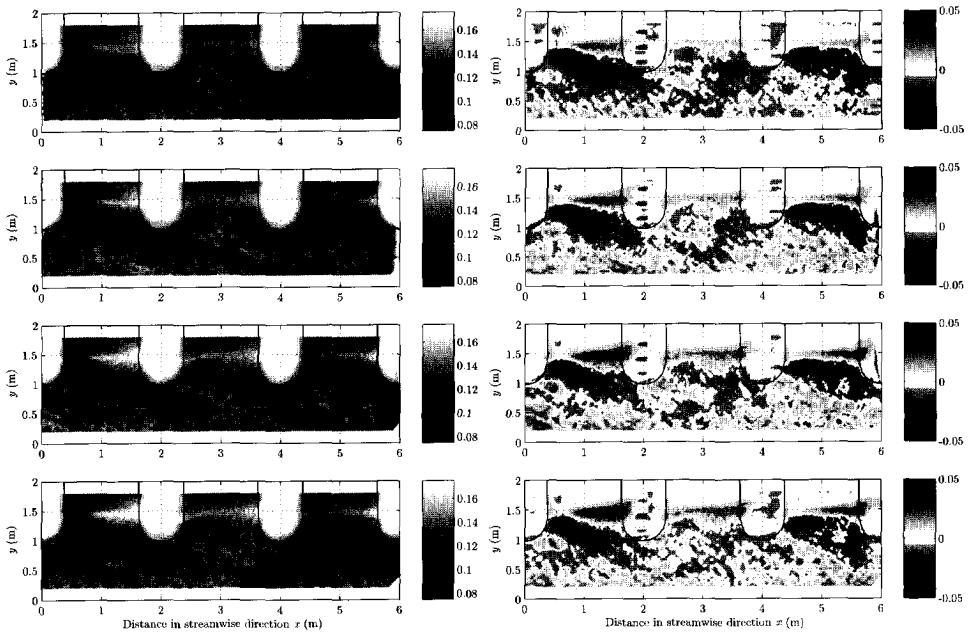


Figure A.29: Bed level (left column) and erosion/deposition pattern (right column) measured after: 10, 20, 30 and 40 hours consecutively (from top to bottom) – Case G1a.

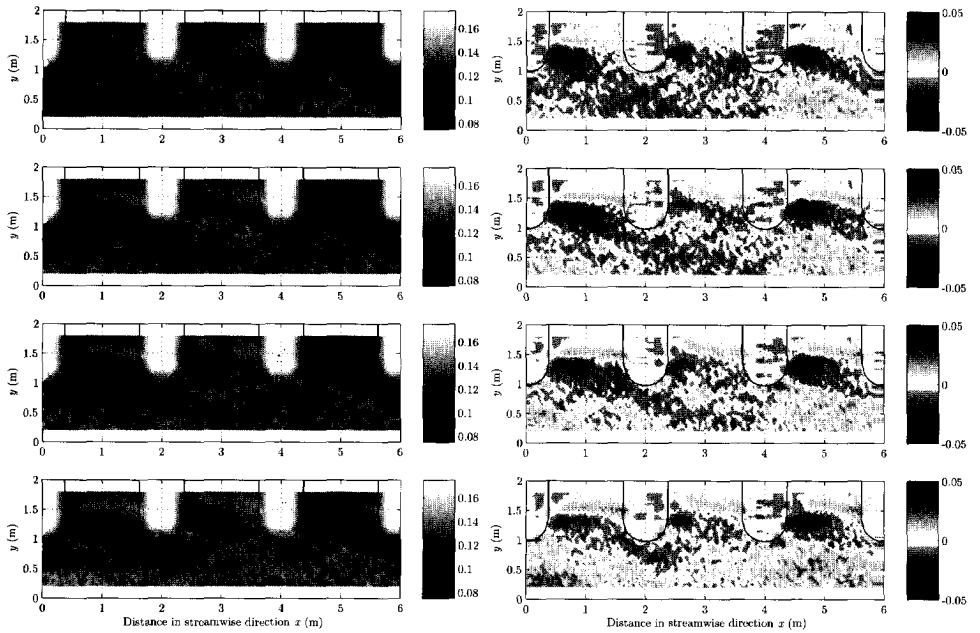


Figure A.30: Bed level (left column) and erosion/deposition pattern (right column) measured after: 10, 20, 30 and 40 hours consecutively (from top to bottom) – Case G1b.

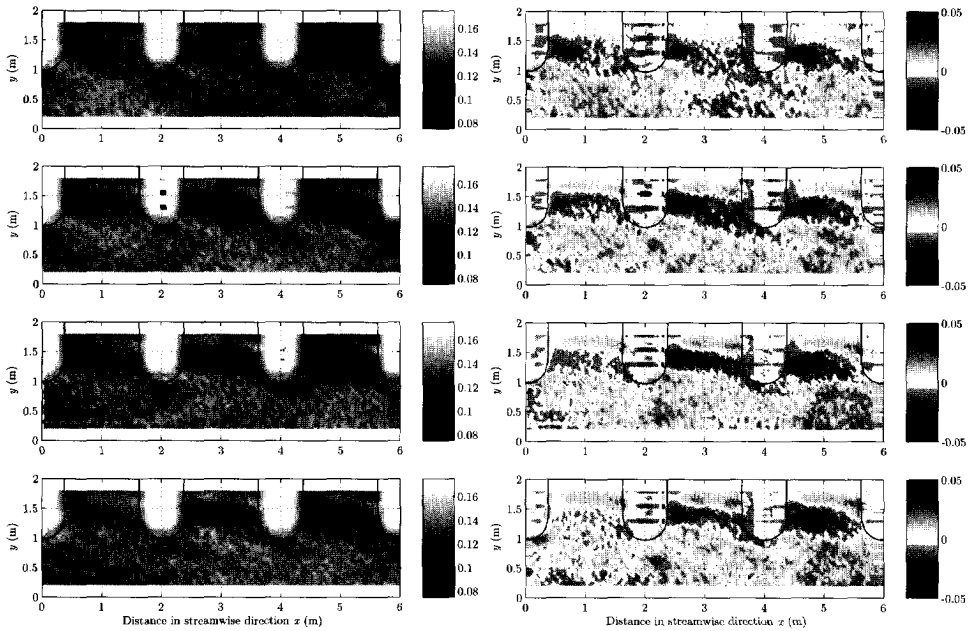


Figure A.31: Bed level (left column) and erosion/deposition pattern (right column) measured after: 10, 20, 30 and 40 hours consecutively (from top to bottom) – Case G1c.

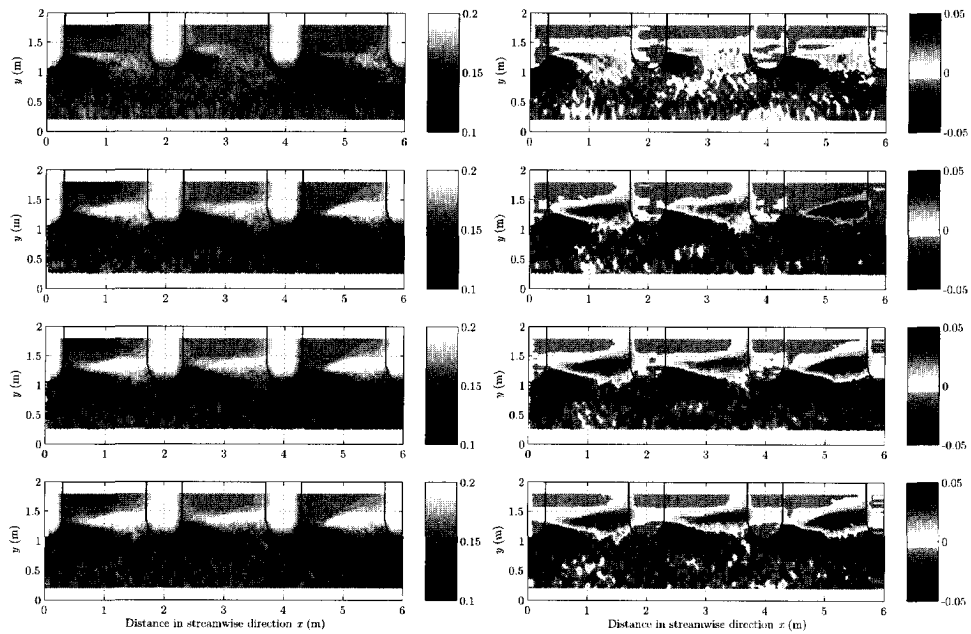


Figure A.32: Bed level (left column) and erosion/deposition pattern (right column) measured after: 10, 20, 30 and 40 hours consecutively (from top to bottom) – Case G2i.

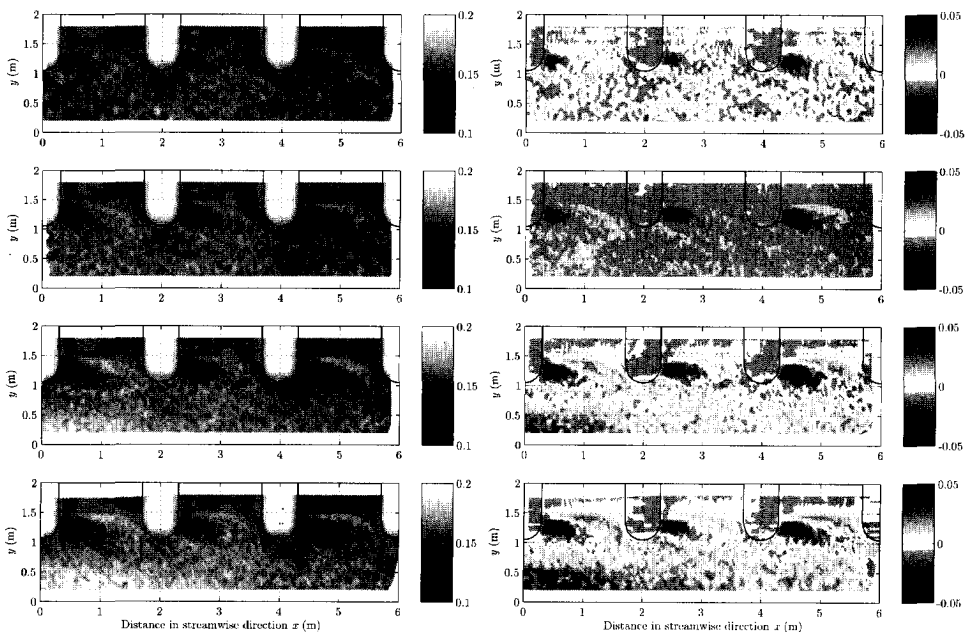


Figure A.33: Bed level (left column) and erosion/deposition pattern (right column) measured after: 10, 20, 30 and 40 hours consecutively (from top to bottom) – Case G2a.

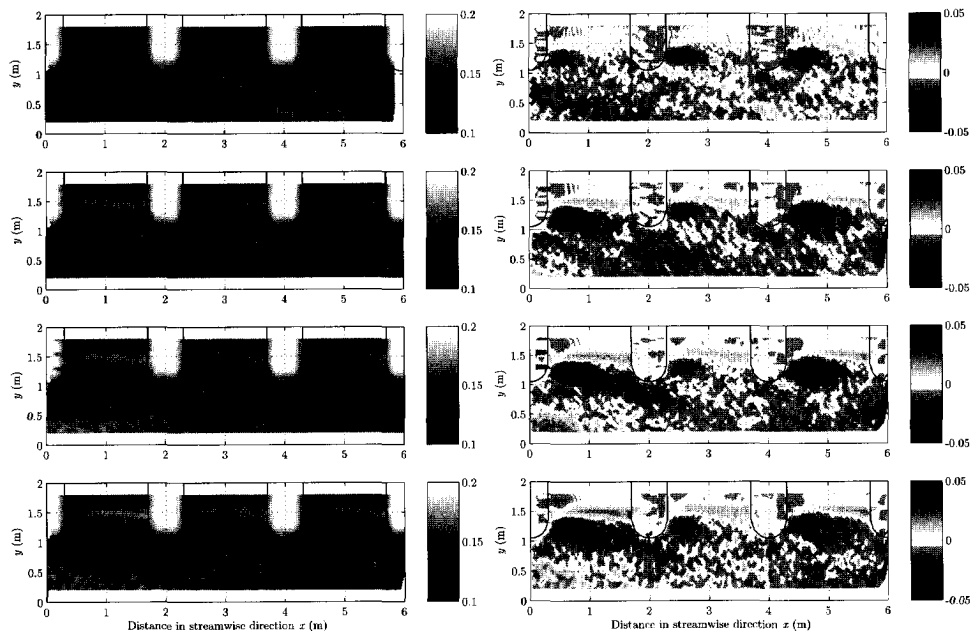


Figure A.34: Bed level (left column) and erosion/deposition pattern (right column) measured after: 10, 20, 30 and 40 hours consecutively (from top to bottom) – Case G2b.

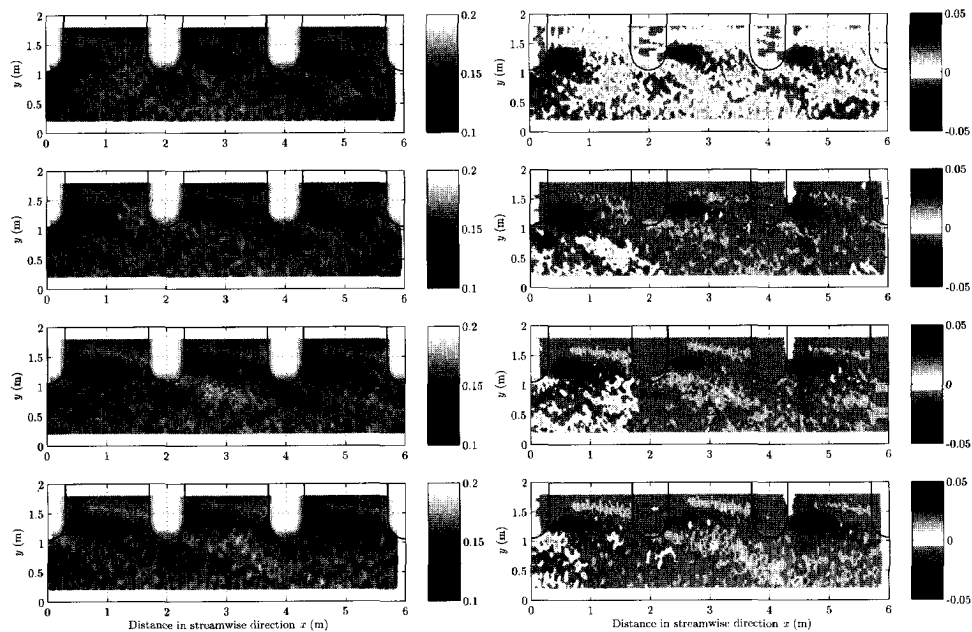


Figure A.35: Bed level (left column) and erosion/deposition pattern (right column) measured after: 10, 20, 30 and 40 hours consecutively (from top to bottom) – Case G2c.

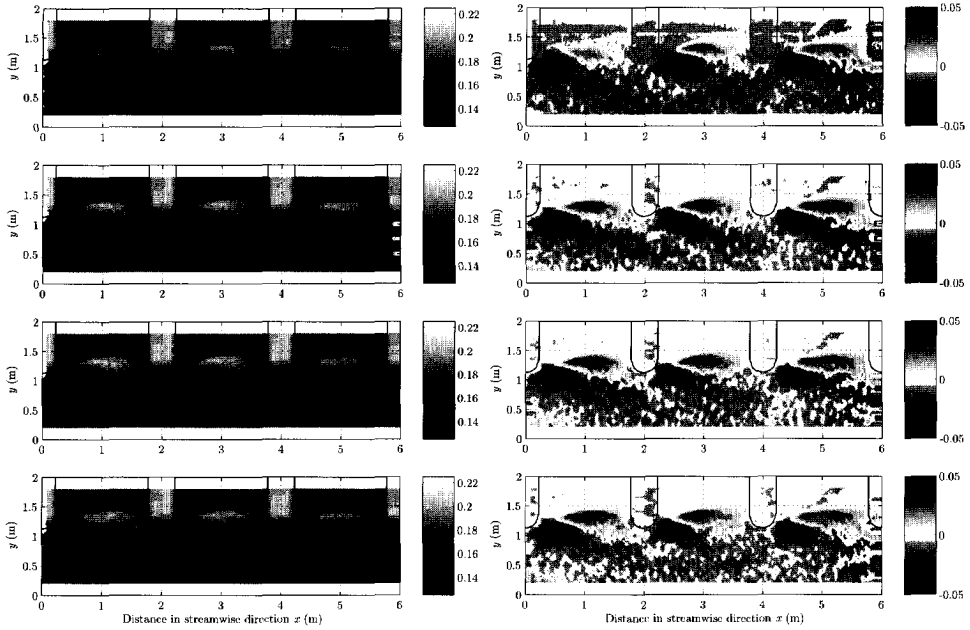


Figure A.36: Bed level (left column) and erosion/deposition pattern (right column) measured after: 10, 20, 30 and 40 hours consecutively (from top to bottom) – Case G3i.

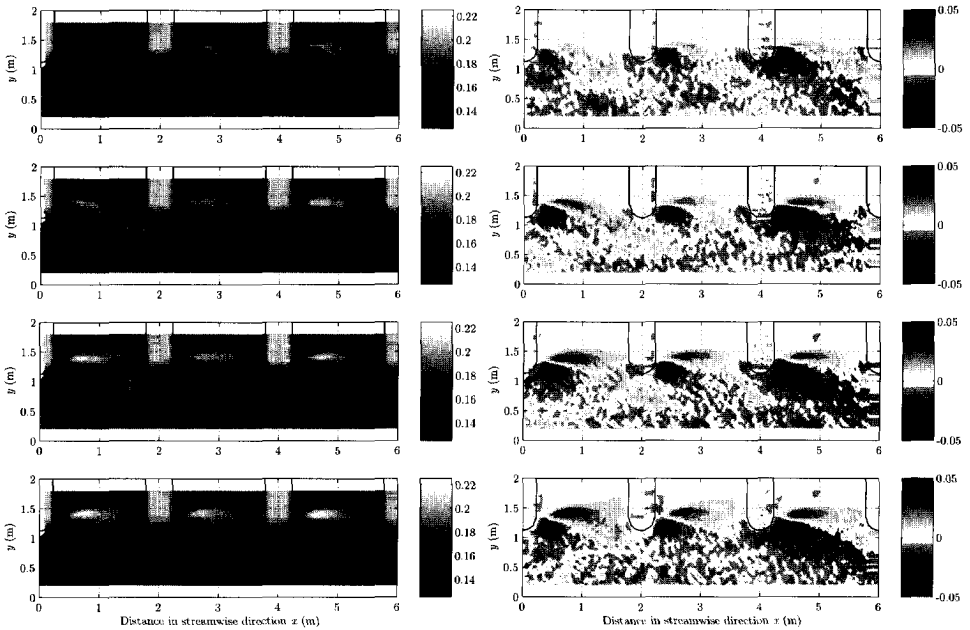


Figure A.37: Bed level (left column) and erosion/deposition pattern (right column) measured after: 10, 20, 30 and 40 hours consecutively (from top to bottom) – Case G3a.

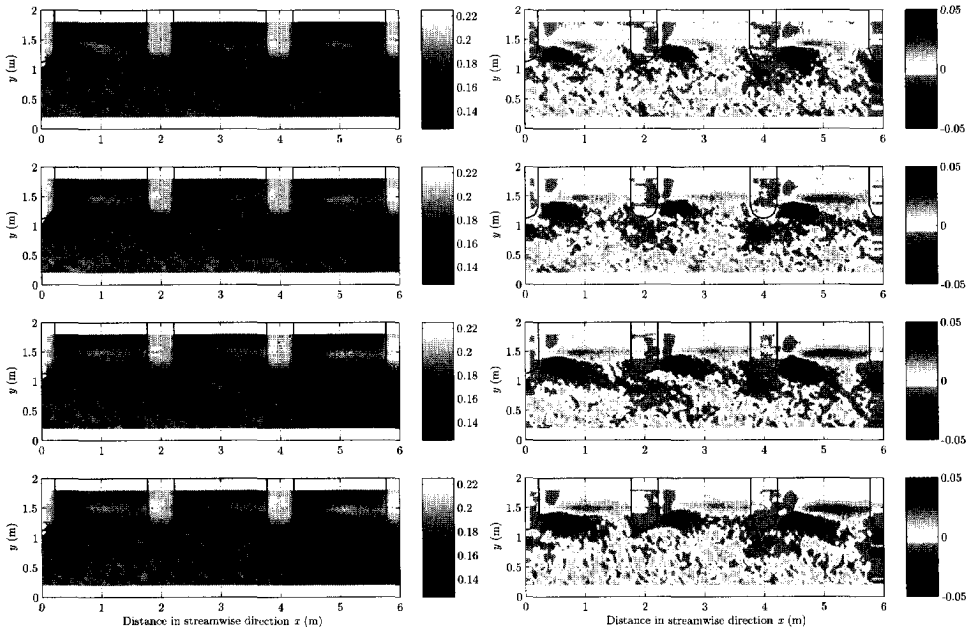


Figure A.38: Bed level (left column) and erosion/deposition pattern (right column) measured after: 10, 20, 30 and 40 hours consecutively (from top to bottom) – Case G3b.

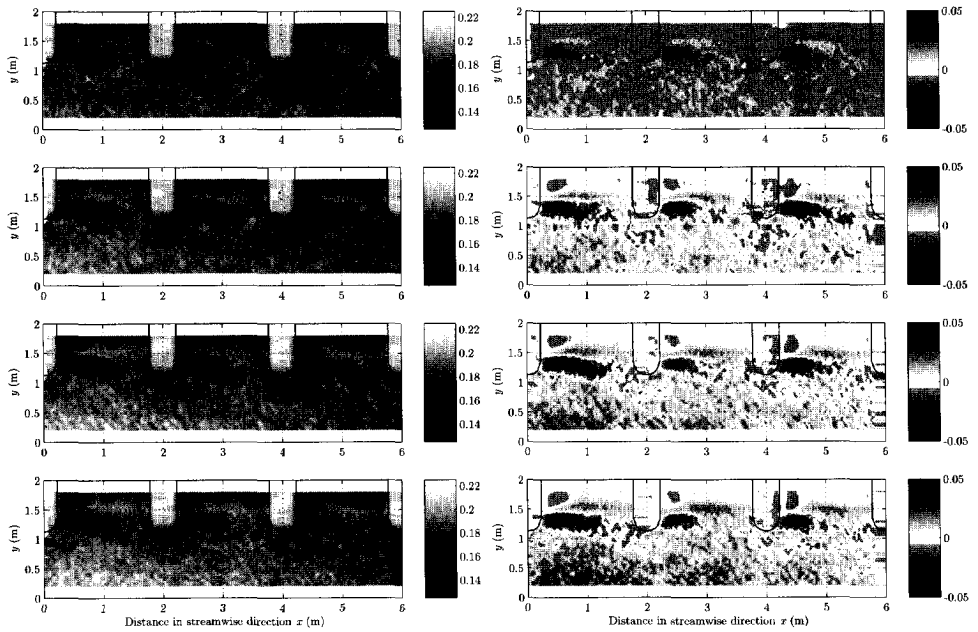
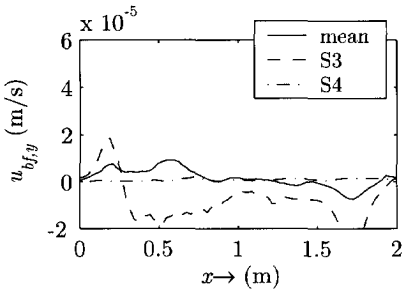
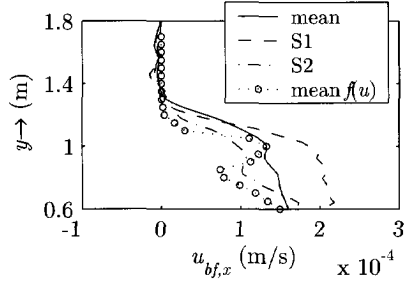
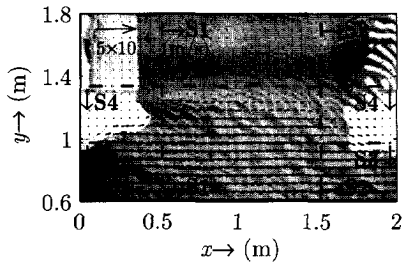


Figure A.39: Bed level (left column) and erosion/deposition pattern (right column) measured after: 10, 20, 30 and 40 hours consecutively (from top to bottom) – Case G3c.

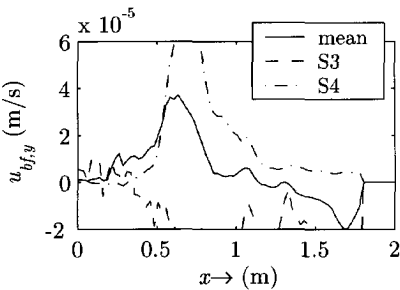
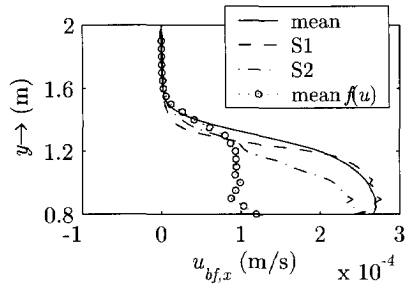
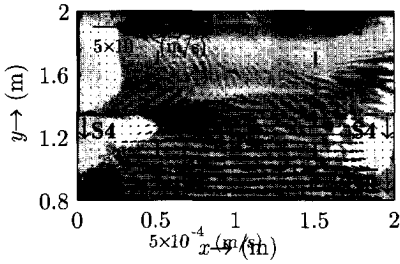
#### A.4 PIV-MEASUREMENTS

PIV-measurements were carried out in the area between groynes #5 and #6 (Figure 4.6). Measurements and processing details are given in Section 4.2.5. Figures A.40 to A.51, give the time-averaged bedform celerity vector field (upper left panel), celerity in streamwise direction  $u_{bf,x}$  (upper right panel), celerity in transverse direction  $u_{bf,y}$  (lower left panel).



case: gl1  
 $\Delta t = 60$  s  
 (upper left) bedforms celerity - vector field  
 (upper right)  $u_{bf,x}$  celerity in streamwise direction  
 (lower left)  $u_{bf,y}$  celerity in transverse direction

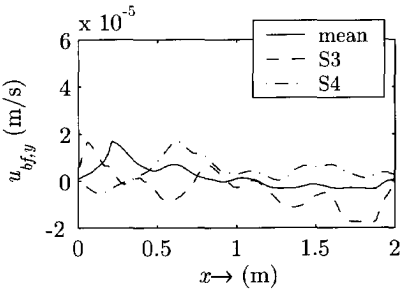
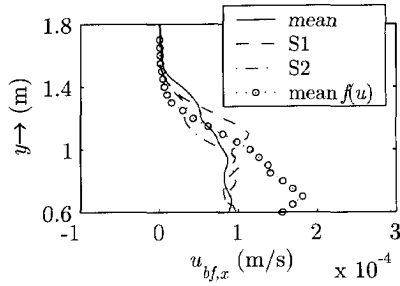
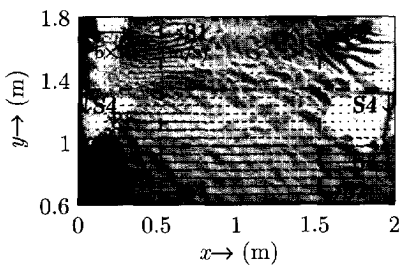
Figure A.40: Time-averaged bedform celerity computed from images taken with image-interval of 60 s, background is an unprocessed image; case G1i.



case: gl1a  
 $\Delta t = 60$  s  
 (upper left) bedforms celerity - vector field  
 (upper right)  $u_{bf,x}$  celerity in streamwise direction  
 (lower left)  $u_{bf,y}$  celerity in transverse direction

Figure A.41: Time-averaged bedform celerity computed from images taken with image-interval of 60 s, background is an unprocessed image; case G1a.





case: g1b

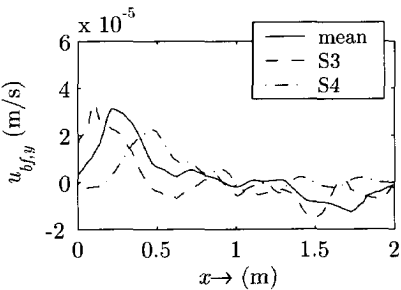
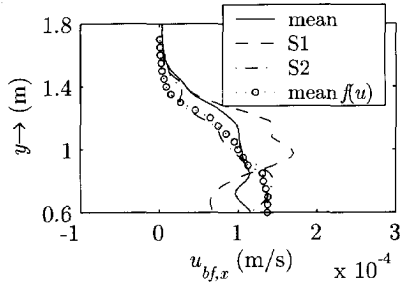
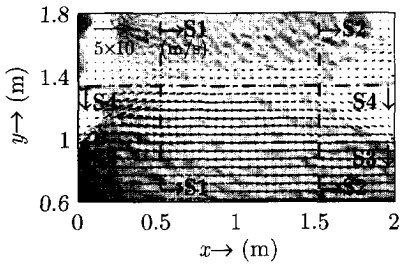
$\Delta t = 60$  s

(upper left) bedforms celerity - vector field

(upper right)  $u_{bf,x}$  celerity in streamwise direction

(lower left)  $u_{bf,y}$  celerity in transverse direction

Figure A.42: Time-averaged bedform celerity computed from images taken with image-interval of 60 s, background is an unprocessed image; case G1b.



case: g1c

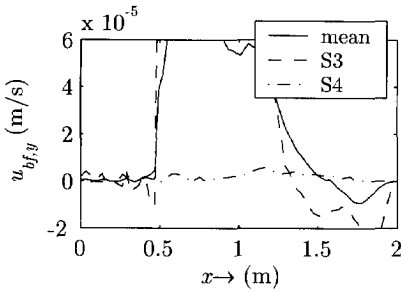
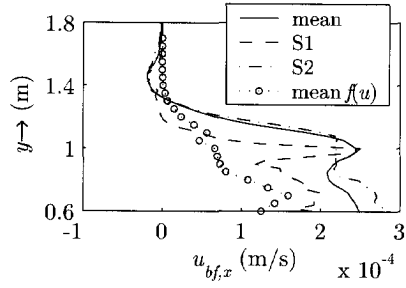
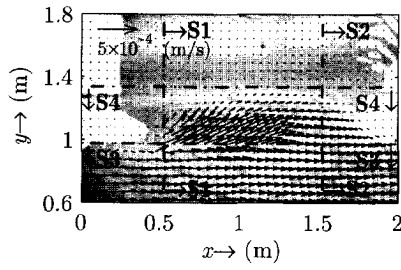
$\Delta t = 60$  s

(upper left) bedforms celerity - vector field

(upper right)  $u_{bf,x}$  celerity in streamwise direction

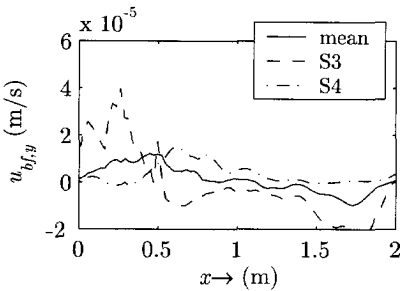
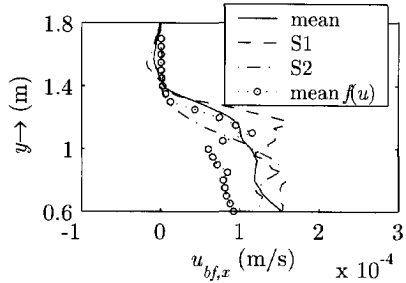
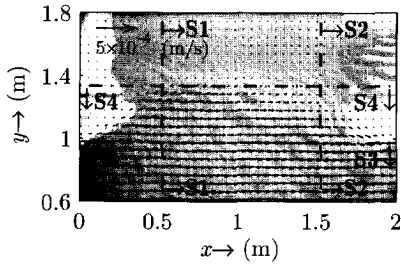
(lower left)  $u_{bf,y}$  celerity in transverse direction

Figure A.43: Time-averaged bedform celerity computed from images taken with image-interval of 60 s, background is an unprocessed image; case G1c.



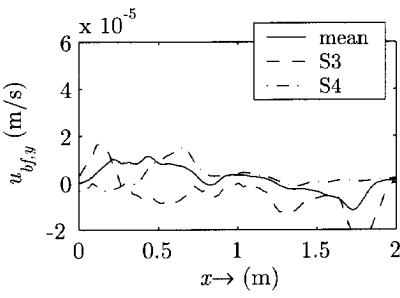
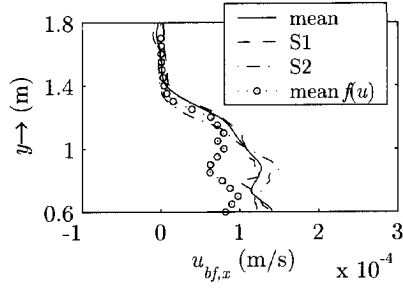
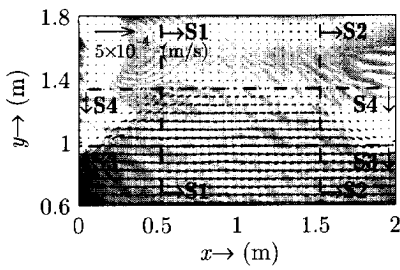
case: g2i  
 $\Delta t = 60$  s  
 (upper left) bedforms celerity - vector field  
 (upper right)  $u_{bf,x}$  celerity in streamwise direction  
 (lower left)  $u_{bf,y}$  celerity in transverse direction

Figure A.44: Time-averaged bedform celerity computed from images taken with image-interval of 60 s, background is an unprocessed image; case G2i.



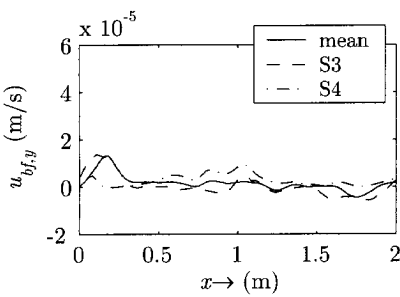
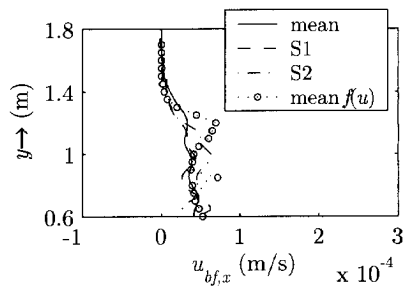
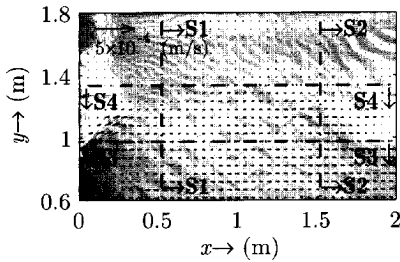
case: g2a  
 $\Delta t = 60$  s  
 (upper left) bedforms celerity - vector field  
 (upper right)  $u_{bf,x}$  celerity in streamwise direction  
 (lower left)  $u_{bf,y}$  celerity in transverse direction

Figure A.45: Time-averaged bedform celerity computed from images taken with image-interval of 60 s, background is an unprocessed image; case G2a.



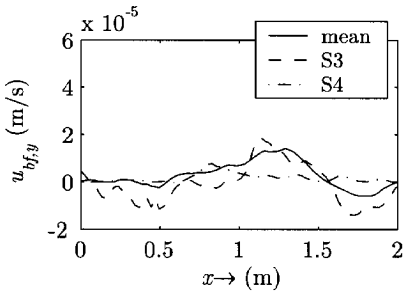
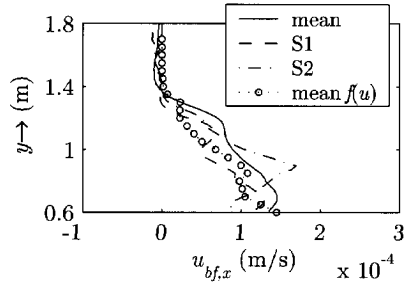
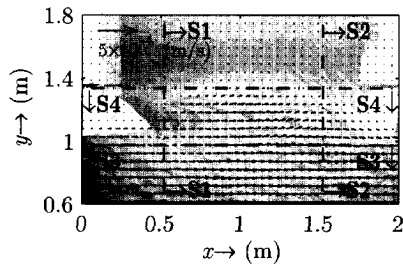
case: g2b  
 $\Delta t = 60$  s  
 (upper left) bedforms celerity - vector field  
 (upper right)  $u_{bf,x}$  celerity in streamwise direction  
 (lower left)  $u_{bf,y}$  celerity in transverse direction

Figure A.46: Time-averaged bedform celerity computed from images taken with image-interval of 60 s, background is an unprocessed image; case G2b.



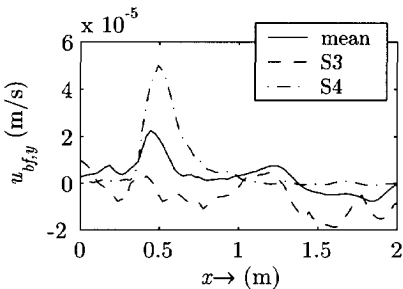
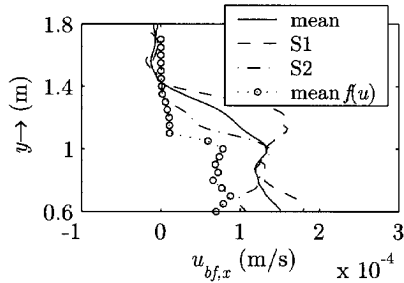
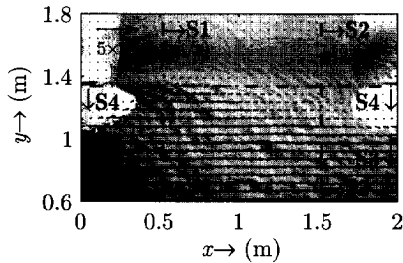
case: g2c  
 $\Delta t = 60$  s  
 (upper left) bedforms celerity - vector field  
 (upper right)  $u_{bf,x}$  celerity in streamwise direction  
 (lower left)  $u_{bf,y}$  celerity in transverse direction

Figure A.47: Time-averaged bedform celerity computed from images taken with image-interval of 60 s, background is an unprocessed image; case G2c.



case: g3i  
 $\Delta t = 60$  s  
 (upper left) bedforms celerity - vector field  
 (upper right)  $u_{bf,x}$  celerity in streamwise direction  
 (lower left)  $u_{bf,y}$  celerity in transverse direction

Figure A.48: Time-averaged bedform celerity computed from images taken with image-interval of 60 s, background is an unprocessed image; case G3i.



case: g3a  
 $\Delta t = 60$  s  
 (upper left) bedforms celerity - vector field  
 (upper right)  $u_{bf,x}$  celerity in streamwise direction  
 (lower left)  $u_{bf,y}$  celerity in transverse direction

Figure A.49: Time-averaged bedform celerity computed from images taken with image-interval of 60 s, background is an unprocessed image; case G3a.

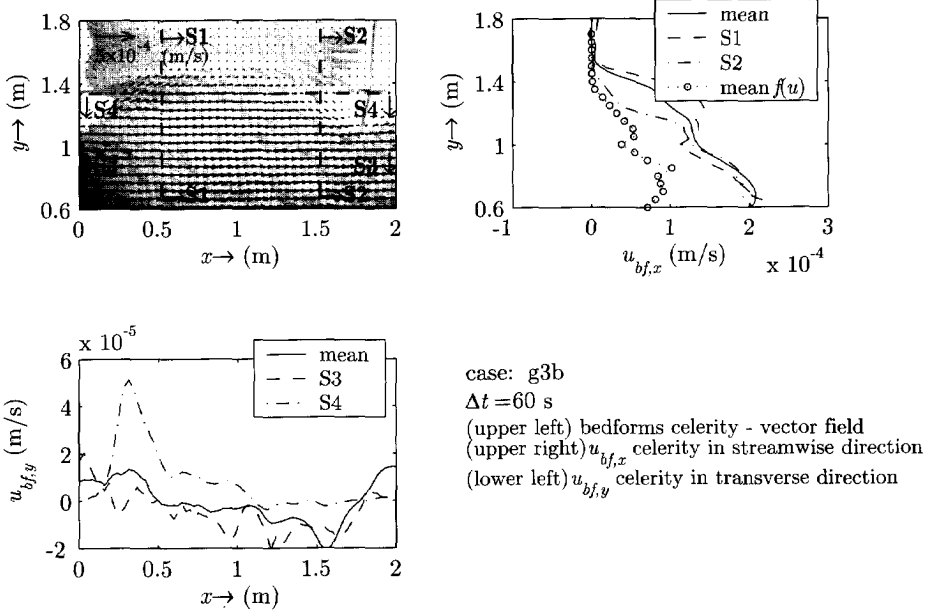


Figure A.50: Time-averaged bedform celerity computed from images taken with image-interval of 60 s, background is an unprocessed image; case G3b.

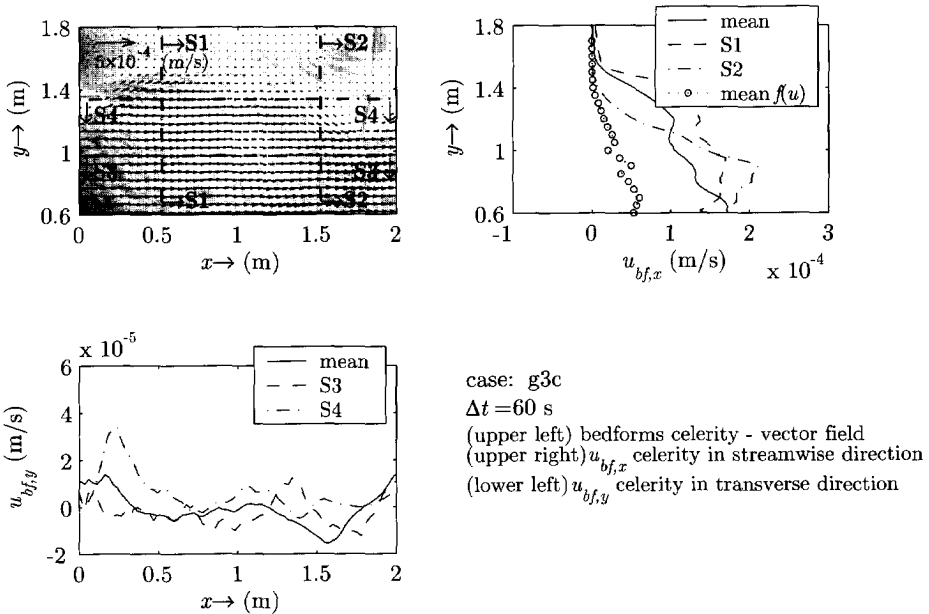


Figure A.51: Time-averaged bedform celerity computed from images taken with image-interval of 60 s, background is an unprocessed image; case G3c.



## LIST OF FIGURES

Figure 1.1:	River engineering measures as proposed in <i>LRP</i> report to achieve a decrease of the water levels at peak discharges (source: LPR, 1996) ..	2
Figure 1.2:	Scale cascade of morphological process according to De Vriend (1999) .....	5
Figure 1.3:	Overview of the various forcings and processes that affect the interaction between the groyne-fields and the main channel.....	6
Figure 1.4:	Graphical representation of the thesis layout. ....	8
Figure 2.1:	Rhine branches in the Netherlands – key-map .....	13
Figure 2.2:	The Waal River near km 899-901 showing the channel changes over a period of about 200 years (source: Van Urk and Smit, 1989).....	14
Figure 2.3:	The Waal River near km 892-894 showing the channel changes since the 18 <sup>th</sup> century (source: Van Urk and Smit, 1989).....	14
Figure 2.4:	Aerial photographs showing the present situation for some locations along the Waal (courtesy of Rijkswaterstaat).....	16
Figure 2.5:	Definition sketch for the dimensions of arbitrary groyne fields.....	17
Figure 2.6:	Statistical representations for the spacing between the groynes ( $S$ ), and the length of groynes ( $L$ ), in the Waal River. ....	18
Figure 2.7:	Different types of flow pattern in a groyne field, (source: Klingeman <i>et al.</i> , 1984). ....	19
Figure 2.8:	Flow pattern in a groyne field during passage of a pushtow unit, (source: Brolsma, 1988). ....	22
Figure 2.9:	Flow velocities during a pushtow passage (source: Brolsma, 1988)...	23
Figure 2.10:	Example of the field records showing the navigation effect on current velocities, water level, and sediment concentration, (after: Ten Brinke, 2003). ....	24
Figure 2.11:	A straight part of the River Waal (a) near Druten; and a curved part (b) near St. Andries.....	26
Figure 3.1:	Experimental set-up with indication to the fourth groyne field where the measurements were taken; the set-up comprises five identical groynes. Co-ordinates are given in Figure 3.3. ....	30
Figure 3.2:	Cross-sectional view, showing the details of groyne type-A (not to scale). ....	31
Figure 3.3:	Measurement locations with respect to the co-ordinate system; shadow areas P1 to P4 indicate areas where PTV is applied.	

	Points #1 to #4 are selected points for future illustration, sections A to D are located at 0.75, 1.50, 2.25, 3.50 m from the tip of the groyne.....	31
Figure 3.4:	Relation between discharge, and Froude number ( $F_r$ ) for series-S (note that test SB has only two cases; see Table 3.2).....	34
Figure 3.5:	Sample time signals of the velocity records observed at section-A for cases (A1: emerged groynes), (A2 & A3: submerged groynes).....	37
Figure 3.6:	Velocity distribution in the transverse direction of ( $\bar{u}$ ), along sections A to D for cases (A1: emerged groynes), (A2 & A3: submerged groynes).....	37
Figure 3.7:	Total turbulence intensity $\sqrt{u'^2 + v'^2}$ extracted from PTV-data, for cases (A1: emerged groynes), (A2 & A3: submerged groynes); the solid line represents the crest of the groyne, dashed lines are imaginary lines for mixing layer shape. ....	38
Figure 3.8:	Transverse profiles of transverse shear stress $\tau_{xy}$ , along sections A to D for cases (A1: emerged groynes), (A2 & A3: submerged groynes).....	38
Figure 3.9:	Flow pattern in a groyne field during emerged flow situation. ....	39
Figure 3.10:	Autocorrelation functions of transverse velocity fluctuations ( $v'$ ) at sections A&D (case A1: emerged groynes); (a) point #1 inside the groyne field, (b) point #2, (c) point #3, (d) point #4 in the main channel. ....	40
Figure 3.11:	Energy density spectra of transverse velocity fluctuations ( $v'$ ) at sections A&D (case A1: emerged groynes); (a) point #1 inside the groyne field, (b) point #2, (c) point #3, (d) point #4 in the main channel. ....	40
Figure 3.12:	Autocorrelations function for velocity fluctuations in the transverse direction at sections A&D (cases A2, A3: submerged groynes); (a) point #1 inside the groyne field, (b) point #2, (c) point #3, (d) point #4 in the main channel.....	42
Figure 3.13:	Energy density spectra at sections A, D (cases A2: submerged groynes); (a) point #1 inside the groyne field, (b) point #2, (c) point #3, (d) point #4 in the main channel.....	42
Figure 3.14:	Transverse velocity profile for all test cases of series-S; velocities are normalised by the main channel velocity ( $\bar{u}_{mc}$ ). ....	43
Figure 3.15:	Relation between drag coefficient and submergence stage of a groyne, for all test cases of series-S; legend indicates the different test cases (see Table 3.2). ....	45
Figure 3.16:	Relation between the blockage by a groyne and its drag coefficient normalised by $F_r^2$ ; solid line is a data fit line for $[y = a_1 x^{a_2}]$ , with $a_1 = 76.4$ , and $a_2 = 3.7$ ; legend indicates the different test cases (see Table 3.2). ....	46
Figure 3.17:	Comparison between the total turbulence intensity $u'$ and the large-scale and small-scale turbulence intensities, separated at a cut-off frequency of 1.0 Hz.....	47



Figure 3.18: Relation between turbulence intensity $u'$ at the centre of the mixing layer and the velocity deficit $\Delta u$ for all test cases. ....	48
Figure 3.19: Relation between $u'$ and $v'$ in the centre of the mixing layer for all test cases. ....	48
Figure 3.20: Cross-energy spectra (upper panel) for velocity fluctuations and phase relation (bottom panel) for $u'$ and $v'$ components ( $u', v'$ is the cross-spectra); near the centre of the mixing layer. ....	51
Figure 3.21: Cross-energy spectra (upper panel) for velocity fluctuations and phase relation (bottom panel) for $u'$ and $v'$ components at a point on the boundary of the mixing layer inside the groyne fields ( $u', v'$ is the cross-spectra). ....	51
Figure 3.22: Cross-energy spectra (upper panel) for velocity fluctuations and phase relation (bottom panel) for $u'$ and $v'$ components at a point on the boundary of the mixing layer from the main channel side ( $u', v'$ is the cross-spectra). ....	52
Figure 3.23: Example of a random phase relation between $u'$ and $v'$ outside the mixing layer. ....	52
Figure 4.1: Picture of the flume looking upstream. ....	58
Figure 4.2: Schematic drawing for the experimental set-up; upper panel is a side view, lower panel is a top view (drawing is not to scale). ....	58
Figure 4.3: Cross-section view through a groyne; empty flume. ....	59
Figure 4.4: Particle size distribution curve. ....	59
Figure 4.5: Details of the inflow section. ....	61
Figure 4.6: Test section and coordinate system. ....	63
Figure 4.7: Movable carriage with two EMF units, and three bed profilers. ....	64
Figure 4.8: Bed profile followers (PROFOS) in action. ....	64
Figure 4.9: Suspended sediment sampling using transverse suction system (TSS). ....	65
Figure 4.10: Image correction using a square grid with a spacing of 0.20 m; a pre-processing step. ....	66
Figure 4.11: Distribution of depth-averaged velocity in the transverse direction $y$ , for all cases in G1, G2 and G3 (1 <sup>st</sup> , 2 <sup>nd</sup> and 3 <sup>rd</sup> row consecutively), measured at section S1 (left column) and section S1 (right column). ....	68
Figure 4.12: Distribution of depth-averaged suspended sediment concentration in the transverse direction $y$ , for all cases in G1, G2 and G3 (1 <sup>st</sup> , 2 <sup>nd</sup> and 3 <sup>rd</sup> row consecutively), measured at section S1 (left column) and section S1 (right column). ....	69
Figure 4.13: Suspended sediment concentration profiles for all cases. Profiles are measured at transverse locations indicated by legend. Lines represent equilibrium (Rouse) concentration profiles at different values of suspension number $Z$ (deduced from measured velocity), solid-lines represent profiles at $y = 0.85$ m (main channel), dotted-	

	lines represent profiles at $y = 1.60$ m (groyne field), dashed-lines at $y = 1.10$ m, and dash-dot-lines at $y = 1.35$ m. ....	70
Figure 4.14:	Bedforms celerity computed over eight consecutive minutes from case G3i; background is an unprocessed reference image.....	72
Figure 4.15:	Time-averaged bedform celerity computed from images taken with image-interval of 60 s, o-points in upper right panel is $u_{bf,x}$ resulting from EMF velocity measurements; background is an unprocessed image; case G3i. Complete results are given in Appendix A.4.....	73
Figure 4.16:	Behaviour of $u_{bf,y}/u_{bf,x}$ versus the submergence ratio $h/h_g$ deduced from the vector fields of all test cases; $u_{bf,y}$ is across the normal line and $u_{bf,x}$ is in the main channel. The solid line is an indicative exponential decay function. ....	73
Figure 4.17:	Bed level (left column) and erosion/deposition pattern (right column) measured after: 10, 20, 30 and 40 hours consecutively (from top to bottom) – Case G1i (emerged groynes).....	75
Figure 4.18:	Erosion/deposition pattern after 40 hours, averaged over one groyne field; Case G1I (emerged groynes).....	75
Figure 4.19:	Bed level (left column) and erosion/deposition pattern (right column) measured at: 10, 20, 30 and 40 hours consecutively (from top to bottom) – Case G1a (submerged groynes).....	77
Figure 4.20:	Erosion/deposition pattern after 40 hours, averaged over one groyne field; Case G1a (submerged groynes). ....	77
Figure 4.21:	Morphological features for emerged groynes with indications to the flow pattern (dashed-lines); picture taken at the end of case G1i.....	79
Figure 4.22:	Morphological features for submerged groynes; picture taken at the end of case G1c.....	79
Figure 4.23:	Deposition volume inside a single groyne field after 40 hours for all tested cases.....	80
Figure 4.24:	Distribution of deposited material inside groyne fields per unit length (left column) and per unit width (right column), grouped by submergence ratio.....	81
Figure 4.25:	Sediment influx into a single groyne field upscaled to prototype condition.....	83
Figure 5.1:	Mechanisms governing the sediment exchange between the groyne fields and the main channel of a river.....	88
Figure 5.2:	Distribution of time-averaged inflow velocity $\overline{v_m(x)}$ during emerged condition; comparison between result from numerical computation for emerged groynes (Rupprecht, 2004), and Eq. 5.3.....	90
Figure 5.3:	Pushtow unit in the River Waal near Ewijk, sailing downstream; (courtesy: Wim Uijttewaal, 2004).....	91
Figure 5.4:	Distribution of the outflow velocity from a groyne field during a ship passage.....	92
Figure 5.5:	Bed development of a groyne field during emerged situation for conditions similar to the Waal River (no floods were considered), measured from main channel level.....	94

Figure 5.6: Representation for the mixing layer due to groynes. (a) distribution of the velocity in the transverse direction, (b) large-scale velocity fluctuations  $u'$  and  $v'$  with  $\pi/2$ -phase difference (c) distribution of the phase difference angle (d) distribution of the amplitude of fluctuations..... 96

Figure 5.7: The effect of the phase difference ( $\phi_0$ ) between  $u$  and  $v$  on the transverse component of the sediment transport ( $qs_{net}$ ,  $qs_m$ ,  $qs_{out}$ ); values are divided by  $qs_{net}(\phi_0 = 0)$ ..... 98

Figure 5.8: Sediment transport rate to the groyne fields due to advection by large-scale coherent structures (solid line), diffusion by small-scale turbulence (dash-dot line), and diffusion by large-scale turbulence for two different values of  $\beta_{s,LS}$  (dash lines); distribution in the transverse direction corresponding to a discharge of 3000 m<sup>3</sup>/s in the Waal River. .... 100

Figure 5.9: Behaviour of  $\beta_{s,LS}(qs_{diff,LS} = qs_{y,LS})$  versus normalised velocity difference for different values of  $U_{mix,c}$  ..... 101

Figure 5.10: Comparison between the transverse component of the sediment transport over one wave period with and without secondary flow correction; values are calculated for  $\phi_0 = 0$ . Dash-dot line is the corrected transport using equilibrium values of secondary flow intensity..... 103

Figure 5.11: Schematic cross section..... 105

Figure 5.12: Sediment transport rate to the groyne fields verses (a) the river discharge, and (b) the height of the groynes; normalised by the transport rate of the main channel (c) & (d)..... 106

Figure 5.13: Contour plot for (a)  $qs_y$  and (b)  $qs_{y,r} = qs_y / qs_{mc}$ , verses the discharge ( $Q$ ), and the submergence ratio ( $h/h_g$ )..... 107

Figure 5.14: Relative contribution of advective transport to the total sediment influx to the groyne fields..... 107

Figure 5.15: Effect of lowering the groynes; (upper panel) contour plot of the change in flow depth  $\Delta h = h(h_{g,new}) - h(h_{g,0})$  as a function of  $Q$ , and  $\Delta h_g$  (the reduction of the groynes height form its current situation of  $h_g = 7$  m); (lower panel)  $\Delta h$  for the design discharge. . 109

Figure 5.16: Contour plot for (a)  $qs_y$  and (b)  $qs_{y,r} = qs_y / qs_{mc}$ , verses the discharge ( $Q$ ), and the height of the groynes ( $h_g$ )..... 110

Figure 5.17: Effect of lowering the groynes; (upper panel) contour plot of the change in relative sediment supply rate to groyne fields  $\Delta qs_{y,r}$  as a function of  $Q$ , and  $\Delta h_g$ ; (lower panel)  $\Delta qs_{y,r}$  for some chosen values of  $\Delta h_g$  ..... 111

Figure 5.18: Discharge of the River Waal; probability density  $p\{Q\}$  estimated from daily records in the period from 1945 to 1997 (with  $dQ = 100$  m<sup>3</sup>/s). .... 111

Figure 5.19: Relative change in sediment supply to the groyne fields due to lowering the groynes. .... 112

Figure 6.1:	Structure of Delft3D-Mor; (a) conventional morphological procedures, (b) eddy resolving procedures.....	121
Figure 6.2:	Model layout.....	122
Figure 6.3:	Overview of the model grid. ....	122
Figure 6.4:	Channel cross-section through a groyne-field.....	123
Figure 6.5:	Flow field in a groyne-field, snapshot picture; (a) experimental result (after Uijttewaal, 1999), (b) model results.....	124
Figure 6.6:	Computed time varying flow field in a groyne field (over a period of 6 minutes). ....	124
Figure 6.7:	Velocity fluctuations for some points along the normal line, $u$ -component (upper panel) and $v$ -component (lower panel).....	125
Figure 6.8:	Energy density spectra for velocity fluctuations, $u$ -component (upper panel) and $v$ -component (lower panel).....	125
Figure 6.9:	Comparison between sediment transport rate along the normal line using different values of $T_p$ as averaging period. Streamwise component $S_x$ (upper panel) and transverse component $S_y$ (lower panel) +ve $S_y$ , is towards the groyne fields. ....	127
Figure 6.10:	Comparison between sediment transport rate along the normal line using a multiple of $t_p$ ( $T_p = 4 \times t_{p1}$ ), and $T_p = 4 \times t_{p1} \pm 2$ minutes....	127
Figure 6.11:	Bed topography after two months; (bed level is measured from water surface; flow from left to right).....	128
Figure 6.12:	Erosion deposition pattern after one month (upper panel) and after two months (lower panel); (computation <i>with</i> HLES).....	129
Figure 6.13:	Erosion deposition pattern after: one month (upper panel), three months (lower panel); (computation <i>without</i> HLES). ....	130
Figure 6.14:	Comparison between bed level development with and without HLES, at the point with coordinates (1665,90). ....	130
Figure 6.15:	Key map for Rhine branches in the Netherlands (a); discharge record of the River Waal for year 2000 (b).....	131
Figure 6.16:	Bed morphology for the reach near Druten for three consecutive months (flow from East to West) .....	132
Figure 6.17:	Distribution of: total turbulence intensity (upper panel), and vorticity (lower panel) .....	135
Figure 7.1:	Schematic planform and cross section of the case study. ....	138
Figure 7.2:	Schematic representation for the exchange of sediment between the groyne fields and the main channel as a function of the discharge. ....	139
Figure 7.3:	Comparison between the total discharge of the river and the discharge of the main channel (a), and cumulative probability distribution of the discharges (b); subscripts 0 and <i>new</i> refer to current situation and the situation with lowered groynes. ....	142
Figure 7.4:	Changes in slope and depth due to sediment supply rate $qs_{lat} = 0.1 \times 10^6$ m <sup>2</sup> /s from the groyne fields (left panel), and corresponding changes in bed and water levels (right panel).....	144

- Figure 7.5: Sensitivity to changes in  $Qs_s$ ; longitudinal profiles of  $\Delta z$  for different values of  $Qs_s$  (left panel), and relative changes in  $\Delta z$  verses relative changes in  $Qs_s$  at different locations along the river. 145
- Figure 7.6: Sensitivity to changes in length of morphologically active reach ( $L = x_{end} - x_0$ ); longitudinal profiles of  $\Delta z$  (left panel) and effect on  $\Delta z$  at some locations along the river (right panel). ..... 145
- Figure 7.7: Sensitivity to changes in  $x_0$ ; longitudinal profiles of  $\Delta z$  (left panel), and effect on  $\Delta z$  at different locations along the river (right panel). 145
- Figure 7.8: Result of the numerical model compared with analytical model; (a) equilibrium and intermediate states of the longitudinal profile, (b) temporal development at some locations along the river, horizontal lines are equilibrium values, and (c) morphological time-scale as a function of the location along the river. .... 147
- Figure 7.9: Schematic hydrographs used in Case 2 (lower panels), and corresponding bed level variations at some locations along the river (upper panels);  $\Delta z$  does not include natural bed variations... 148
- Figure 7.10: Longitudinal profile of bed level changes  $\Delta z$  at the end of the dry period (a), and the envelope of these changes during the whole simulation period ( $\Delta z_{max}$  &  $\Delta z_{min}$ ) (b). .... 149
- Figure 7.11: Effect of a long dry period on the range of bed level changes; dashed line is an indication of the trend of  $(\Delta z_{max} - \Delta z_{min})_{max}$  verses the return period of flood..... 149
- Figure 7.12: Temporal changes in  $\Delta z$  of the main channel due to the interaction with groyne fields at some locations along the river (upper panel), and discharge time-series (lower panel). .... 150
- Figure 7.13: Some realisations for variations in the bed level of the main channel due to the interaction with groyne fields, and the envelope of all realisations for the period 1945-2005. .... 151
- Figure 7.14: Temporal variations of the bed level of the groyne fields in the period 1945-2005..... 151
- Figure 7.15: Bed level changes due to the decreased discharge in the main channel because of lowering the groynes; comparison between analytical equilibrium state model (Eqs. 7.13 & 7.14), and numerical model (statistics are based on the results of the last 10 years)..... 153
- Figure 7.16: Temporal development at the upstream and downstream ends of the lowered-groynes reach compared with the equilibrium value. ... 153
- Figure 7.17: Temporal variations of the bed level of the groyne fields due to lowering the groynes; the dashed line is a linear fit to the estimated  $\Delta z_{gf}$ , the dotted line is a relaxation model with a hypothetical morphological time-scale of 100 years. .... 154
- Figure 7.18: The mean bed level changes over the last 10 years of simulation due to lowering the groynes; (a) comparison between Case 4, and Case 5, (b) isolated effect of including the exchange between the main channel and the groyne fields..... 155

Figure 7.19: Comparison between the temporal development in Case 4 and Case 5 for the main channel bed level at the upstream end of the lowered-groynes reach. ....	155
Figure A.1: Distribution in the transverse direction of $u$ & $v$ (upper panel), and $u'$ & $v'$ (lower panel); for G1i-S1. ....	176
Figure A.2: Distribution in the transverse direction of $u$ & $v$ (upper panel), and $u'$ & $v'$ (lower panel); for G1i-S2. ....	176
Figure A.3: Distribution in the transverse direction of $u$ & $v$ (upper panel), and $u'$ & $v'$ (lower panel); for G1a-S1. ....	177
Figure A.4: Distribution in the transverse direction of $u$ & $v$ (upper panel), and $u'$ & $v'$ (lower panel); for G1a-S2. ....	177
Figure A.5: Distribution in the transverse direction of $u$ & $v$ (upper panel), and $u'$ & $v'$ (lower panel); for G1b-S1. ....	178
Figure A.6: Distribution in the transverse direction of $u$ & $v$ (upper panel), and $u'$ & $v'$ (lower panel); for G1b-S2. ....	178
Figure A.7: Distribution in the transverse direction of $u$ & $v$ (upper panel), and $u'$ & $v'$ (lower panel); for G1c-S1. ....	179
Figure A.8: Distribution in the transverse direction of $u$ & $v$ (upper panel), and $u'$ & $v'$ (lower panel); for G1c-S2. ....	179
Figure A.9: Distribution in the transverse direction of $u$ & $v$ (upper panel), and $u'$ & $v'$ (lower panel); for G2i-S1. ....	180
Figure A.10: Distribution in the transverse direction of $u$ & $v$ (upper panel), and $u'$ & $v'$ (lower panel); for G2i-S2. ....	180
Figure A.11: Distribution in the transverse direction of $u$ & $v$ (upper panel), and $u'$ & $v'$ (lower panel); for G2a-S1. ....	181
Figure A.12: Distribution in the transverse direction of $u$ & $v$ (upper panel), and $u'$ & $v'$ (lower panel); for G2a-S2. ....	181
Figure A.13: Distribution in the transverse direction of $u$ & $v$ (upper panel), and $u'$ & $v'$ (lower panel); for G2b-S1. ....	182
Figure A.14: Distribution in the transverse direction of $u$ & $v$ (upper panel), and $u'$ & $v'$ (lower panel); for G2b-S2. ....	182
Figure A.15: Distribution in the transverse direction of $u$ & $v$ (upper panel), and $u'$ & $v'$ (lower panel); for G2c-S1. ....	183
Figure A.16: Distribution in the transverse direction of $u$ & $v$ (upper panel), and $u'$ & $v'$ (lower panel); for G2c-S2. ....	183
Figure A.17: Distribution in the transverse direction of $u$ & $v$ (upper panel), and $u'$ & $v'$ (lower panel); for G3i-S1. ....	184
Figure A.18: Distribution in the transverse direction of $u$ & $v$ (upper panel), and $u'$ & $v'$ (lower panel); for G3i-S2. ....	184
Figure A.19: Distribution in the transverse direction of $u$ & $v$ (upper panel), and $u'$ & $v'$ (lower panel); for G3a-S1. ....	185
Figure A.20: Distribution in the transverse direction of $u$ & $v$ (upper panel), and $u'$ & $v'$ (lower panel); for G3a-S2. ....	185

Figure A.21: Distribution in the transverse direction of  $u$  &  $v$  (upper panel), and  $u'$  &  $v'$  (lower panel); for G3b-S1. .... 186

Figure A.22: Distribution in the transverse direction of  $u$  &  $v$  (upper panel), and  $u'$  &  $v'$  (lower panel); for G3b-S2. .... 186

Figure A.23: Distribution in the transverse direction of  $u$  &  $v$  (upper panel), and  $u'$  &  $v'$  (lower panel); for G3c-S1. .... 187

Figure A.24: Distribution in the transverse direction of  $u$  &  $v$  (upper panel), and  $u'$  &  $v'$  (lower panel); for G3c-S2. .... 187

Figure A.25: Suspended sediment concentration profiles for all cases in G1, section S1 (left column) and section S2 (right column); profiles are measure at transverse locations  $y$  indicated by legend. .... 189

Figure A.26: Suspended sediment concentration profiles for all cases in G2, section S1 (left column) and section S2 (right column); profiles are measure at transverse locations  $y$  indicated by legend. .... 190

Figure A.27: Suspended sediment concentration profiles for all cases in G3, section S1 (left column) and section S2 (right column); profiles are measure at transverse locations  $y$  indicated by legend. .... 191

Figure A.28: Bed level (left column) and erosion/deposition pattern (right column) measured after: 10, 20, 30 and 40 hours consecutively (from top to bottom) – Case G1i. .... 193

Figure A.29: Bed level (left column) and erosion/deposition pattern (right column) measured after: 10, 20, 30 and 40 hours consecutively (from top to bottom) – Case G1a. .... 193

Figure A.30: Bed level (left column) and erosion/deposition pattern (right column) measured after: 10, 20, 30 and 40 hours consecutively (from top to bottom) – Case G1b. .... 194

Figure A.31: Bed level (left column) and erosion/deposition pattern (right column) measured after: 10, 20, 30 and 40 hours consecutively (from top to bottom) – Case G1c. .... 194

Figure A.32: Bed level (left column) and erosion/deposition pattern (right column) measured after: 10, 20, 30 and 40 hours consecutively (from top to bottom) – Case G2i. .... 195

Figure A.33: Bed level (left column) and erosion/deposition pattern (right column) measured after: 10, 20, 30 and 40 hours consecutively (from top to bottom) – Case G2a. .... 195

Figure A.34: Bed level (left column) and erosion/deposition pattern (right column) measured after: 10, 20, 30 and 40 hours consecutively (from top to bottom) – Case G2b. .... 196

Figure A.35: Bed level (left column) and erosion/deposition pattern (right column) measured after: 10, 20, 30 and 40 hours consecutively (from top to bottom) – Case G2c. .... 196

Figure A.36: Bed level (left column) and erosion/deposition pattern (right column) measured after: 10, 20, 30 and 40 hours consecutively (from top to bottom) – Case G3i. .... 197

Figure A.37: Bed level (left column) and erosion/deposition pattern (right column) measured after: 10, 20, 30 and 40 hours consecutively (from top to bottom) – Case G3a.....	197
Figure A.38: Bed level (left column) and erosion/deposition pattern (right column) measured after: 10, 20, 30 and 40 hours consecutively (from top to bottom) – Case G3b. ....	198
Figure A.39: Bed level (left column) and erosion/deposition pattern (right column) measured after: 10, 20, 30 and 40 hours consecutively (from top to bottom) – Case G3c.....	198
Figure A.40: Time-averaged bedform celerity computed from images taken with image-interval of 60 s, background is an unprocessed image; case G1i.....	200
Figure A.41: Time-averaged bedform celerity computed from images taken with image-interval of 60 s, background is an unprocessed image; case G1a.....	200
Figure A.42: Time-averaged bedform celerity computed from images taken with image-interval of 60 s, background is an unprocessed image; case G1b.....	201
Figure A.43: Time-averaged bedform celerity computed from images taken with image-interval of 60 s, background is an unprocessed image; case G1c.....	201
Figure A.44: Time-averaged bedform celerity computed from images taken with image-interval of 60 s, background is an unprocessed image; case G2i.....	202
Figure A.45: Time-averaged bedform celerity computed from images taken with image-interval of 60 s, background is an unprocessed image; case G2a.....	202
Figure A.46: Time-averaged bedform celerity computed from images taken with image-interval of 60 s, background is an unprocessed image; case G2b.....	203
Figure A.47: Time-averaged bedform celerity computed from images taken with image-interval of 60 s, background is an unprocessed image; case G2c.....	203
Figure A.48: Time-averaged bedform celerity computed from images taken with image-interval of 60 s, background is an unprocessed image; case G3i.....	204
Figure A.49: Time-averaged bedform celerity computed from images taken with image-interval of 60 s, background is an unprocessed image; case G3a.....	204
Figure A.50: Time-averaged bedform celerity computed from images taken with image-interval of 60 s, background is an unprocessed image; case G3b.....	205
Figure A.51: Time-averaged bedform celerity computed from images taken with image-interval of 60 s, background is an unprocessed image; case G3c.....	205



## LIST OF SYMBOLS

### Roman Symbols

$a_{1,2}$	constants in Eq. 3.9	
$A_f$	cross-sectional flow area	$m^2$
$A_t$	total cross-sectional area	$m^2$
$B_{fp}$	Width of the floodplain	$m$
$B_{gf}$	width of the groyne fields	$m$
$B_{mc}$	width of the main channel	$m$
$c$	sediment concentration	--
$C$	Chézy coefficient	$m^{1/2}/s$
$c_a$	reference concentration	--
$C_{base}$	base Chézy coefficient in the groynes region (without groynes)	$m^{1/2}/s$
$C_D$	drag coefficient	--
$c_e$	equilibrium depth-averaged concentration	--
$C_{effective}$	effective Chézy coefficient in the groynes region	$m^{1/2}/s$
$C_{gf}$	Chézy coefficient of the groynes region	$m^{1/2}/s$
$D_{50}$	median sediment grain size	$m$
$E_u$	energy density spectra of streamwise velocity	$(m/s)^2/Hz$
$E_u$	energy density spectra of streamwise velocity	$(m/s)^2/Hz$
$E_{uv}$	cross-energy spectra	$(m/s)^2/Hz$
$F$	flatness (kurtosis)	
$f$	frequency	$Hz$
$f_{fp}$	spatial low-pass filter coefficient	
$f_r$	dominant frequency in Eq. 3.16	$Hz$
$F_r$	Froude number; $F_r = \frac{\mathcal{L}}{\sqrt{g \cdot \mathcal{U}}}$	
$G$	orientation of a groyne (with respect to the line $\perp$ thalweg)	$deg.$
$g$	acceleration of gravity $g = 9.81 \text{ m/s}^2$	$m/s^2$
$h$	water depth	$m$
$h_e$	equilibrium water depth	$m$

$hg$	height of the groynes	m
$i$	bed level slope	--
$i_e$	equilibrium bed level slope	--
$I_s$	intensity of secondary flow	m/s
$I_{s,c}$	Equilibrium value of the secondary flow intensity	m/s
$k_{1,2,3}$	correction factors in Eq. 2.1	--
$k_s$	bed roughness height	m
$k_t$	truncation wave number	
$\mathcal{L}$	length scale	m
$L, L_g$	length of groynes	m
$L_{a,s}$	adaptation length-scale of secondary flow	m
$L_{gf}$	length of groyne field	m
$L_{gfw}$	groyne field length along the waterline	m
$L_{r1}$	active inflow length in Eq. 5.3	m
$L_{r2}$	active outflow length in Eq. 5.7	m
$m$	constant in Englund & Hansen sediment transport formula;	
	$m = \frac{0.05}{(1-p)\sqrt{g}C^3\Delta^2D_{50}}$	
$m_1$	side slopes of the groyne	m
$n$	power in Englund & Hansen sediment transport formula	
$n_X$	scale factor of parameter $X$ ( $n_X = X_{prototype}/X_{model}$ )	--
$p$	porosity of bed material	--
$Q$	water flow rate (discharge)	m <sup>3</sup> /s
$q$	water flow rate (specific discharge)	m <sup>2</sup> /s
$Q_s$	sediment transport rate	m <sup>3</sup> /s
$qs$	sediment transport rate	m <sup>2</sup> /s
$Qs_0$	sediment transport rate upstream of the morphologically active groynes region	m <sup>3</sup> /s
$Qs_b$	bed load sediment transport rate	m <sup>3</sup> /s
$qs_{lat}$	lateral sediment exchange component between the main channel and the groyne fields	m <sup>2</sup> /s
$Qs_r$	relative contribution of the lateral sediment exchange component per unit length of the normal line ( $qs_{lat}/Qs_0$ )	1/m
$Qs_s$	suspended load sediment transport rate	m <sup>3</sup> /s
$qs_y$	sediment transport rate in y-direction	m <sup>2</sup> /s
$qs_{y,LS}$	sediment transport rate in y-direction due to large-scale coherent structures	m <sup>2</sup> /s
$R_e$	Reynolds number; $R_e = \frac{U \cdot \mathcal{L}}{\nu}$	
$R_s$	radius of curvature of streamlines	m

$R_{uu}$	auto-correlation function of the streamwise for velocity	--
$R_{vv}$	auto correlation function of the transverse velocity	--
$S$	spacing between groynes	m
$S^2$	sum of the horizontal component of the strain rate tensor in Eq. 6.11	
$S_K$	skewness	--
$St$	Strouhal number; $St = f_r \frac{\mathcal{L}}{U}$	
$t$	time	s
$T_a$	adaptation time for the vertical sediment concentration profile	s
$T_{a's}$	adaptation time-scale of secondary flow	s
$T_{mor}$	morphological time-scale	s
$T_P$	periodicity of velocity fluctuations	s
$T_s$	ship passage time	s
$U$	velocity scale	m/s
$u$	velocity in streamwise direction	m/s
$u\hat{u}$	velocity in streamwise direction	m/s
$u\bar{u}$	mean velocity in streamwise direction	m/s
$u_*$	shear velocity	m/s
$u'$	turbulence intensity of streamwise velocity	m/s
$u_{bf}$	bedform celerity	m/s
$u_{gr}$	velocity in the groyne fields	m/s
$u_i'$	fluctuating part of the streamwise velocity	m/s
$u_{mc}$	velocity in the main channel	m/s
$v$	velocity in transverse direction	m/s
$v'$	turbulence intensity of transverse velocity	m/s
$v_i'$	fluctuating part of the transverse velocity	m/s
$v_{in}$	inflow velocity into a groyne field across the normal line	m/s
$v_{out}$	outflow velocity from a groyne field across the normal line	m/s
$w_s$	fall velocity	m/s
$x$	horizontal coordinate in streamwise direction	m
$y$	horizontal coordinate in transverse direction	m
$y_c$	y co-ordinate of the centre of the mixing layer	m
$Y_{th}$	distance between the normal line and the thalweg	m
$Z$	suspension number	--
$z_{gf}$	bed level of a groyne field	m
$z_{gf0}$	initial bed level of a groyne field	m
$z_{gf,c}$	equilibrium bed level of a groyne field	m
$z_{mc}$	bed level of the main channel	m
$z_w$	water level	m

## Greek Symbols

$\alpha_1$	coefficient Eq. 5.4	
$\alpha_2$	calibration coefficient in Eq. 5.9	
$\alpha_s$	angle of sediment transport direction	
$\alpha_r$	angle of bed shear stress	
$\alpha_{v,SS}$	coefficient for small-scale turbulence in Eq. 5.26	
$\alpha_{v,LS}$	coefficient for large-scale turbulence in Eq. 5.26	
$\beta_{1,2,3}$	coefficients in Eqs. 3.12, 3.13 and 3.15	
$\beta_{in}, \beta_{out}$	coefficients in Eq. 6.20	
$\beta_s$	proportionality factor between the sediment mixing coefficient and the eddy viscosity	
$\delta$	mixing layer width	m
$\Delta$	specific density $(\rho_s - \rho)/\rho$	--
$\Delta u$	velocity difference across the mixing layer	m/s
$\Delta z$	bed level difference between groyne fields and main channel	m
$\varepsilon_s$	sediment-mixing coefficient	m <sup>2</sup> /s
$\varepsilon_{s,SS}$	sediment-mixing coefficient due to small-scale turbulence	m <sup>2</sup> /s
$\varepsilon_{s,LS}$	sediment-mixing coefficient due to large-scale turbulence	m <sup>2</sup> /s
$\phi_s$	turbulence damping factor	
$\phi_0$	phase difference between $u$ and $v$	rad.
$\gamma$	numerical coefficient depending on the dimensionality of the turbulence, in Eq. 6.9	
$\kappa$	Von Kármán constant $\kappa = 0.4$	
$\nu_t$	eddy viscosity	m <sup>2</sup> /s
$\nu_H$	horizontal eddy viscosity	m <sup>2</sup> /s
$\nu_{t,SS}$	horizontal eddy viscosity due to small-scale turbulence	m <sup>2</sup> /s
$\nu_{t,LS}$	horizontal eddy viscosity due to large-scale turbulence	m <sup>2</sup> /s
$\nu$	dynamic viscosity	m <sup>2</sup> /s
$\theta$	shields parameter	
$\rho$	density of fluid	kg/m <sup>3</sup>
$\rho_s$	density of sediment	kg/m <sup>3</sup>
$\sigma$	standard deviation	
$\sigma_T$	turbulent Prandtl-Schmidt number	
$\sigma_b$	Courant number for an explicit integration of SGS stress.	
$\sigma_{BT}$	Courant number for surface waves	
$\sigma_I$	Courant number for convection	
$\tau$	time shift	s
$\tau_b$	bed shear stress	N/m <sup>2</sup>

---

$\tau_{xy}$	transverse shear stress	N/m <sup>2</sup>
$\omega$	peak frequency of velocity fluctuations	rad/s
$\phi_0$	phase difference between $u'$ and $v'$	rad
$\zeta$	water level with respect to the reference level in Eqs. 6.1&6.2	m

### Abbreviations

EMF	ElectroMagnetic Flowmeter
HLES	Horizontal Large Eddy Simulation
LS	Large Scale
PIV	Particle-Image Velocimetry
PROFO	bed PROfile FOLlower
PTV	Particle-Tracking Velocimetry
SS	Small Scale
TSS	Transverse Suction System
RWS	Rijkswaterstaat



## ACKNOWLEDGMENTS

I have been always waiting for this day when I write this acknowledgement. It is a rare opportunity to 'officially' thank those whom you love, respect and appreciate.

Being away from my homeland, I would like first to thank my family, here and abroad. I thank my parents whom are bearing the anguish of their son being away. You always loved me, supported me, and gave me confidence. I thank also my parents in-law who are living the same feelings of their daughter being away. For my wife, Naze, without your support, motivation, and your sacrifices it would have been impossible to reach this day. Thank you very much for your love, support, patience, and for being a wonderful wife and mother for our son Kerim.

A sincere appreciation to Huib de Vriend, my promoter, for his guidance, encouragement and his active supervision during all stages of my research. Thank you for your 'always constructive' comments, your trust, and for allowing me the freedom in research. I have learned a lot more than river morphology from you.

I would like to show my gratitude to Gerrit Klaassen whom I knew since before my PhD, during my MSc. study in IHE. Thank you for recommending me to start this thesis and for your supervision especially during shaping the thesis in its early phases.

I thank Wim Uijttewaal for the long, friendly, and fruitful discussions that extended my knowledge about flow near groynes and turbulence in general. I will always remember the snow walk and sharing the same food table, as a vegetarian, in Japan.

I thank Erik Mosselman for his accurate comments and for passing his research wisdom. I learned a lot about doing a research from you.

I thank Kees Sloff for his support and help during some critical times of my research; you can really make modelling look very easy.

Many thanks go to Hendrik Havinga, Maarten van der Wal, Arjan Sieben, and Wilfried ten Brinke for their active participation in my steering committee and for the fruitful discussions during various stages of my research. In the meanwhile, I would like to acknowledge the role of DON in financing the fixed-bed experiment and the role of RIZA in supplying the field data used in this thesis.

Many thanks to all the staff members of the Laboratory for Fluid Mechanics of the Delft University of Technology for facilitating the experiments in all their stages; Harry Fontijn, Arie den Toom, Michiel van der Meer, and Fred van der Brugge.

I would like to thank Michelle Berg for her role in the fixed-bed experiment and Dirk Smolenaars and Sjoerd Dijkstra for their efforts during the setup and pilot tests of the

mobile-bed experiment. Thanks to Kenneth Thiemann for his incredible efforts during the mobile-bed experiment, and thanks to Rebekka Rupprecht for her efforts trying to model this experiment.

I thank my all my colleagues and friends in Delft University in the sections of Hydraulic Engineering and Environmental Fluid Mechanics. I enjoyed all those discussions about sports, politics and world matters in the coffee room. I will always remember the deep discussions with Martin Baptist about research, the long chats with Mark Klein in front of the coffee machine, the highly motivating music and non-stop, extremely fast, keyboard sound from Hessel Voortman, my first roommate, and the excursion to Luxembourg with Saskia van Vuren. Many thanks go to Mark Voorendt for all his support, and to Adeeba Ramdjan and Chantal van Woggelum.

A due thanks to all my friends which made my stay in Delft pleasant. I could always have the chance to speak Arabic during lunch breaks with Ahmed El-Kadi; it would have been lonely without you. Mustafa, Mohamed, Amr, Fahmi, Nur Ed-din, and Mustafa, the city of Delft is not the same without you all.

I would like to thank Ibrahim Eldsouky, director of HRI; I will not forget the first day that I joined; you convinced me to stay, in fact you made me like hydraulic modelling. Thanks to Dr. Mustafa Gawesh and Dr. Bahaa, for giving me the permission to do my PhD in Delft.

Finally, I would like to thank all my new work colleagues in WL | Delft Hydraulics especially Rashid Thabet who has been like an older brother to me.



## CURRICULUM VITAE

Mohamed Fathy Mohamed Yossef was born on 22 June 1969 in Giza, Egypt. There, he studied primary and secondary education. In 1987 Mohamed started his engineering studies in Cairo University where he graduated from the Faculty of Engineering, Civil Engineering department in 1991. Shortly after, in 1992 he started his employment as a research engineer in the Hydraulics Research Institute, HRI-Egypt. Running parallel, Mohamed played volleyball and joined the Egyptian national team in the period from 1990 to 1996. By the end of 1996, he started studying hydraulic engineering in IHE Delft (now UNESCO IHE) where he obtained his MSc degree, with distinction, in 1998. Moving between Turkey, where he worked in STFA Marine Construction Co., and HRI-Egypt, late 2000 he came back to Delft to start his PhD study in Delft University of Technology, Faculty of Civil Engineering and Geosciences, Hydraulic Engineering Section. As of the 1<sup>st</sup> of April 2005, Mohamed started a new assignment as a Researcher/Advisor in WL | Delft Hydraulics.

